STRUCTURAL AND MORPHOLOGICAL CHARACTERIZATION OF MODEL ELASTOMERIC ION CONTAINING POLYMERS

by

Lakshmi Narayan Venkateshwaran

Dissertation submitted to the Faculty of the

Virginia Polytechnic Institute and State University

in partial fulfillment of the requirements for the degree of

DOCTOR OF PHILOSOPHY

in

CHEMICAL ENGINEERING

APPROVED:

Prof. Garth L. Wilkes, Chairman

Prof. James E. McGrath

Prof. Donald G. Baird

Prof. Thomas C. Ward

Prof. William L. Conger

June 18, 1989

Blacksburg, Virginia

STRUCTURAL AND MORPHOLOGICAL CHARACTERIZATION OF MODEL ELASTOMERIC ION CONTAINING POLYMERS

by

Lakshmi Narayan Venkateshwaran

Prof. Garth L. Wilkes, Chairman

CHEMICAL ENGINEERING

(ABSTRACT)

Over the last several years, there has been widespread interest in the structure property behavior of ion containing polymers. Of particular interest are those materials termed ionomers which contain ionic groups that are typically less than 15 mole percent. These ionic interactions provides an additional means of controlling polymer structure and properties. In the conventional ionomers, the ionic groups are placed randomly along the polymeric backbone resulting in a network structure that is rather poorly defined. An alternate approach is to prepare ionomers where the ionic groups are placed at well defined locations along the polymer backbone such as the telechelic ionomers, block ionomers, or the segmented ionomers where the ionene polymers serve as an example. The structure-property behavior of all these three type of ionomers have been investigated in this study.

The telechelic ionomers were based on either a polyisoprene (PIP) or polybutadiene (PBD) backbone. The PIP ionomers have been neutralized with various cations and neutralized to different levels. The bulk properties were found to be highly dependent on the nature of the cation, its valency, and its ionic radius. A series of sulfonated and carboxylated ionomers of similar molecular weight have been studied in order to compare the performance of sulfonated ionomers to that of the carboxylated counterpart. As expected, the nature of ionic association in the sulfonated ionomer was found to be much stronger than in the carboxylate ionomer. The extent of neutralization as well as variations in the non-ionic segment molecular was studied in the PBD telechelic ionomers. For the first time, a bimodal type of SAXS peak was observed for 2000 $\overline{M}_n$ PBD ionomer.

In the segmented ionene polymers, the effect of the non-ionic segment (PTMO) molecular weight, the nature of the counterion (Cl vs. Br vs. I), and the architecture of the ionene segment were investigated. From SAXS analysis, a change in the morphology was indicated when the

PTMO segment molecular weight exceeded 3400 $\overline{M}_n$. It was estimated that the interfacial region was very sharp in all the materials investigated. One of the main limitations of the ionene polymers discussed herein is that the material undergoes irreversible degradation at elevated temperature. It has been shown that with the addition of an ionic plasticizer such as zinc stearate, the softening temperature of the ionene polymer is lowered which allows thermal processing without a major loss of properties.

A detailed morphological investigation of methacrylate based block ionomers was conducted. The effect of ionic block length, the architecture of the segments, and variations in the polarity of the glassy segments were investigated. Though the diblock materials exhibited poor tensile properties, the morphological features of these materials were very interesting. Multiple scattering peaks were observed in the diblock materials using SAXS. Both highly ordered as well as disordered regions were observed from TEM measurements. The spacing observed from TEM measurements correlates quite well with that observed from SAXS. Surprisingly, long range ordering was absent in the triblock ionomer with similar ion content. Finally, the spacing between the ionic domains were found to be a strong function of the ionic block length.

To

He who learns by Finding Out

has sevenfold

The Skill of him who learned by

Being Told

----- *Guiterman*

Acknowledgements

Over the years, there have been a number of people who have been instrumental in shaping my academic career. It is with great pleasure that I acknowledge their influence in my life:

I sincerely thank for encouraging me to enter the field of chemical engineering. His persuasive and enlightening arguments have been an "eye-opener" many a time. While at the Indian Institute of Technology, New Delhi, my interest in polymers was kindled by . He strongly encouraged me to pursue graduate study in this field. I am grateful to him for all his efforts. I would also like to thank at the University of Lowell in Massachusetts for providing me with the opportunity to pursue my Master' program under his guidance. He recruited me during his visit to India in 1983.

I would like to thank Professor Garth L. Wilkes for directing my research during my doctoral program. His unrestrained approach to research provided me with an opportunity to explore many avenues in the field of my research, to which I am very grateful. My special thanks to Dr. Richey M. Davis for all the "informal" discussions.

I sincerely appreciate and for collaborating in the "Block Ionomer Project". This association has been very fruitful and it has been a pleasure working with them. Furthermore, I wish to acknowledge the assistance provided by Dr. Dinshone Done and on the RMS, and Dr. Leo Lopez on the SEM. I would also like to thank the consultants

at User Services who have been very helpful with all my computer related problems. My sincere thanks to , and for all that they have done for me.

I wish to thank my family: my parents, , my sister and my brother-in-law, and , and my in-laws , for all their support, encouragement, and cooperation during my academic career. Lastly, but not the least, I am deeply grateful to my wife, , for without her love and support, none of this would have been possible. To her, I dedicate this dissertation.

Table of Contents

List of Illustrations

List of Tables

1.0 INTRODUCTION

The polymeric materials encompassed by the field of ion-containing polymers is extremely varied, ranging from naturally occurring biopolymers to synthetically modified polymers which have been used in a wide range of applications. Generally, ion containing polymers can be classified into two categories, ionomers and polyelectrolytes (shown in Figure 1.1). Of particular interest to the present study are the ionomers. The term ***ionomer,*** was originally coined by DuPont Co. as a generic description for their *Surlyn®* resins (1). However, the term has been generalized and is defined as ***a copolymer consisting of a polymer backbone with a minority of the repeat units carrying ionizable groups which are completely or partially neutralized to form salts*** (2). The ion content in these materials is typically less than 15 mole percent, whereas in polyelectrolytes the ion content is usually greater than 15 mole percent.

The unique mechanical and rheological properties exhibited by the ionomers, along with the possibility of engineering their properties toward a specific application(s) has greatly contributed to the widespread interest in this field. The utilization of the ionic interactions in these polymers provides the chemist with an added dimension in controlling the polymer structure and properties. The relationship between the properties of the ionomers and their corresponding microstructure has been the subject of many studies.

Earlier studies were primarily aimed at ionomers in which the backbone polymer was essentially non-elastomeric or glassy at ambient conditions. More recently, the emphasis has shifted to ionomers that are elastomeric in nature, due to the growing interest in utilizing these materials commercially as thermoplastic elastomers (i.e. materials that can flow at elevated temperatures yet retain their elastomeric character at ambient conditions). Such an application is feasible, since ionomers display extremely good elastomeric properties at ambient temperatures due to the association of ionic groups which form a pseudo-network. The network like structure is attributed to the formation of ***ionic crosslinks*** which results from the ionic interactions in the material. At higher

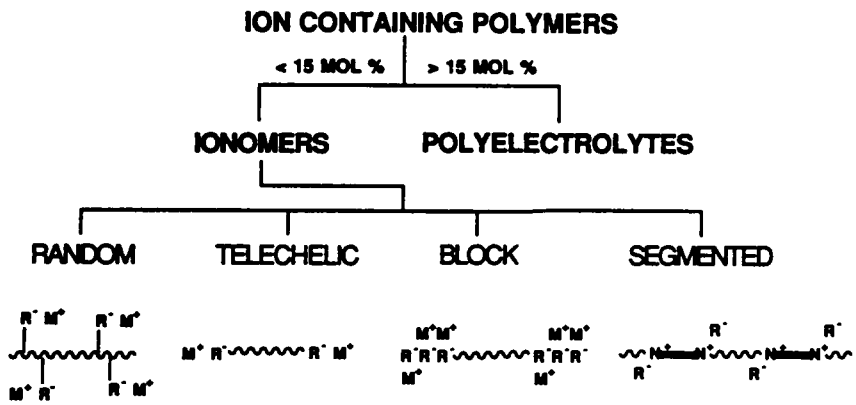

Figure 1.1. General classification of Ion Containing Polymers: as shown above R^-M^+ systems are anionomers while the N^+R^- systems are cationomers.

temperatures these same ionic interactions may become sufficiently labile such that the viscosity is reduced to the point where conventional processing techniques (such as injection molding or extrusion) could be utilized to "melt process" these materials.

The ionic groups in conventional ionomers are distributed randomly along the polymer backbone resulting in a poorly defined network structure. With recent advances in polymer synthesis, chemists have been able to selectively place the ionic groups at specific positions along the polymeric backbone. In contrast to random ionomers, the well defined positions of the ionic groups greatly simplify the task of relating the network microstructure to the properties of the ionomer. Essentially three synthetic routes have been utilized leading to three types of chain structures, namely, telechelic, block, and segmented ionomers. The various sub-classifications of ionomers are shown in Figure 1.1. In a telechelic ionomer, an ionic group is located at each of the chain ends. The block ionomers are a logical extension of the telechelic ionomers in which the ionic group at the chain ends is replaced by a block of ionic or partially ionizable groups. These materials are quite similar to the classical block copolymers of the ABA or AB type except that at least one of the blocks in these systems is ionic in character. The third route is through the synthesis of "segmented" ionomers, as for example, the polymeric ionenes or the polyurethane ionomers. In these materials the ionic groups can be located at well defined positions in the polymeric backbone. For example, in the ionenes, the quaternary amines (along with the counter ions) function as potential network points. The ability to control the intervening nonionic segment molecular weight is one of the attractive features in studying segmented ionene polymers. The ionenes that were synthesized earlier, were generally brittle in nature and often exhibited poor mechanical properties. Incorporation of flexible chains, such as polytetramethylene oxide (PTMO) or polypropylene oxide (PPO), as the intervening nonionic segment has greatly improved the flexibility and the mechanical properties of the ionene polymer. Consequently, these ionene polymers have the potential to become commercially viable thermoplastic materials. All three different routes lead to a more precisely defined network microstructure, particularly if the molecular weight between the ionic groups is controllable.

In order to place this research in an appropriate framework, the relevant literature pertaining to the structure and morphology of ionomers will be reviewed in Chapter 2. An exhaustive review

is not contemplated since several reviews have already appeared in the literature (3-8); however, emphasis is provided on those areas that are relevant to the objectives of this research.

The technique of small angle x-ray scattering has been extensively used to probe the microstructure in the materials under investigation. An overview of the relevant small angle x-ray scattering theory is, therefore, presented in Chapter 3. The purpose and the scope of the present investigation is discussed in Chapter 4 and the experimental methodologies are described in Chapter 5. The results of three different joint investigations with other researchers is described in Chapters 5-9. In Chapter 6, 7, and 9, the discussion relating to the structure-property relationships of telechelic ionomers, ionene polymers, and block ionomers, respectively, are discussed. The plasticization study on the segmented ionene polymers is reported in Chapter 8.

It should be noted that the materials considered for the present study were not synthesized in this laboratory but were obtained from different sources. The telechelic ionomers were synthesized in Professor Robert Jerome's laboratory at the University of Leige in Belgium. The block ionomers were synthesized in Professor James E. McGrath's laboratory in the Department of Chemistry at Virginia Polytechnic Institute and State University, Blacksburg, Virginia. The ionene polymers were synthesized in Dr. Charles E. Leir's laboratory in the Speciality Chemical Division at 3M Corporation, St. Paul, Minnesota.

2.0 LITERATURE REVIEW

An overview of the structural and morphological features of ionomers will be presented in this chapter. At the beginning, the chemical structure of ionomers will be presented followed by a discussion on the morphology of ionomers and its relationship to observed properties. The discussion will include both experimental and theoretical approaches that have been undertaken to reveal the nature of the ionic interactions in these materials.

The field of ion containing polymers has witnessed an explosive growth in recent years. There have been numerous efforts directed at studying the structure property relationship of ionomers. The degree of interest in these materials is evidenced by the rapidly growing body of literature relating to ion-containing polymers, especially ionomers. A number of review papers (3-8) and books (9-15) have appeared in the literature which are devoted to the subject of ion-containing polymers.

2.1 Chemical Structure and Morphology of Ionomers

The conventional ionomers usually contain acid groups which are randomly distributed along the polymeric backbone. Some of the commonly used acids include sulfonic, carboxylic, phosphonic, etc. In his study of carboxylated rubbers, Brown (16) was the first to propose that by neutralization of the acid groups, it was possible to produce materials which were inherently very different from the parent polymer. The resulting material appeared to contain crosslink junction points which were temporary in nature and which have since been aptly termed as "pseudo or ionic" crosslinks. This type of crosslink, which is formed due to the electrostatic interactions between the cations of the neutralizing species and the acid groups in the polymer chain can be effectively utilized to produce a network structure in an otherwise linear polymer. Therefore, the concept of an ionic crosslink is very important for understanding the structure of ionomers. Brown observed that upon neutralizing carboxylated elastomers by an appropriate cation such as zinc, resulted in mate-

rials quite similar to a cross-linked rubber. This behavior was explained in terms of the formation of an ionic crosslink with the divalent zinc cation that forms a bridge between two carboxylate ions as schematically depicted below

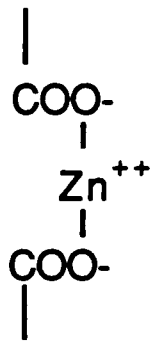

This rather simple model was widely accepted in the early literature, being the first effort to schematically represent ionic crosslinks in an otherwise non-polar environment. The model nevertheless ignores the coordinating tendencies of the zinc ion, the low polarity of the hydrocarbon environment and the potential influence of polar impurities such as water. On neutralization with a monovalent cation, quite similar results were obtained as that found for the divalent cation. Therefore, the simple "ionic crosslink" model above does not adequately explain the interaction mechanism of ions in the system. Otocka et al. (17) postulated that dipole-dipole interactions occur between the salt pairs, which can schematically be represented as;

This concept introduced the presence of "contact ion-pairs" in ionomers. Although both of the above simple models have proven to be quite useful in many instances, they are inadequate to completely account for the experimentally observed structural behavior.

Bonotto and Bonner (18) proposed that "ion aggregation" exists in ionomers. They believed that these ionic aggregates formed "ionic pockets" which behaved as crosslinks with a high level of functionality. A schematic representation of the model is given below.

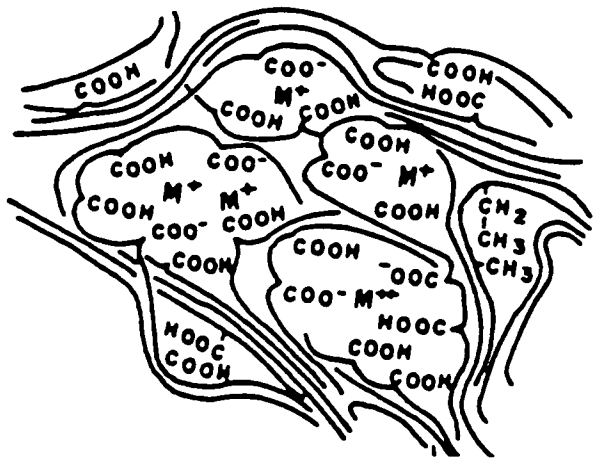

It was not clear whether microphase separation was implied by the model or the ionic domains were multiplets or clusters as later defined by Eisenberg (which will be addressed shortly).

The chemical microstructure of any polymer plays an important role in determining its final properties. Ionomers display rather unique properties which are a direct result of the ionic interactions between the ionic groups in the system. Varied opinions exist, however, regarding the state of aggregation of the ions. One viewpoint is that the ionic regions are of the order of 100 Å in which ions are clustered - evidence being mainly obtained from small angle x-ray scattering (SAXS) experiments. Another viewpoint (19) suggested that the ions to be dispersed throughout the matrix in a low state of aggregation, i.e. as ion pairs or higher order associations.

According to Eisenberg (19), both the opposing viewpoints can exist depending on the state of aggregation as well as conditions of the environment. In developing the most comprehensive theory that relates the state of aggregation of the ions, he assumed that the fundamental entity was that of a "contact ion-pair" in which the cation and the anion are separated by a distance equal to the sum of their respective ionic radii. The ionic regions termed multiplets, specifically exclude the

hydrocarbon or the non-ionic portions of the polymer chains. Multiplets are defined as small, tight aggregates of ionic groups containing little or no organic material (backbone polymer chain), i.e., the chains attached to the ions stay on the "outside" of the aggregates. The smallest size of a multiplet is a single ion-pair, where its maximum size is limited by steric considerations as well as the geometry of the multiplets. For a spherical geometry where the ion pair is restricted to the surface of the multiplet, the maximum size can be calculated from the relation,

$$r_m = \frac{3v_p}{S_{ch}} \tag{2.1}$$

where r_m is the radius of the multiplet, v_p is the volume of an ion pair, and S_{ch} is the area of the hydrocarbon chain in contact with the spherical surface of the multiplet. For an ethylene-sodium methacrylate copolymer, a multiplet radius of 3 Å was obtained which corresponds to a maximum of eight pairs for perfect volume occupation. If the multiplets exists as lamellar structures then there is essentially no limit to the size of the multiplets as steric considerations do not arise due to the nature of the geometry (7).

At higher ionic concentration, the multiplets may further associate to form clusters, in which the multiplets are separated by a hydrocarbon "skin" consisting of the nonionic portions of the chains. Eisenberg defined clusters as large, more loosely interacting aggregates, each containing a relatively large amount of organic chain material. Due to their large size, the clusters not only function as crosslinks, but also as a strongly interacting filler.

The formation of clusters is favored due to the electrostatic attraction between multiplets and opposed by forces arising from the elastic nature of the backbone chains. The size of these clusters is dependent upon the balance between the electrostatic forces within the clusters and the entropic (elastic) forces that tend to "pull" the multiplets apart from forming clusters. The elastic forces can be calculated from the theory of rubber elasticity while the electrostatic forces can be calculated by assuming that energy is released during cluster formation with the work done being dependent on both the geometry and the dielectric constant of the medium. The electrostatic forces have a weak dependence on temperature while the elastic forces scale directly with temperature. At low ion

concentrations, elastic forces dominate favoring multiplet formation while at higher concentration the electrostatic forces dominate favoring cluster formation. This suggests that there exists a critical ion concentration for cluster formation. This morphological transition has been experimentally supported from the studies of viscoelastic properties of ionomers which will be discussed later, in detail.

2.2 Morphological Studies

2.2.1 X-Ray and Neutron Scattering

Numerous studies have reported the effects of ions on the physical properties of ion containing polymers which provide evidence for the existence of clustering in an indirect way. Utilizing techniques such as x-ray diffraction and more recently neutron scattering there has been more direct evidence obtained for the existence of ionic clustering and associated phase separation. Some of the early x-ray scattering experiments showed that ionomers which are neutralized often display a distinct low angle scattering peak termed the "ionic peak" that is absent in the un-neutralized acid form of the polymer (20). Microphase separation is thought to occur because of the large differences in polarity between the hydrocarbon backbone and the pendant acid groups. Figure 2.1 shows the ionic peak for the sodium salt of an ethylene-metharylic acid copolymer together with the scattering profiles for the acid and low density polyethylene. The fact that the ionic peak was observed only for the neutralized ionomer suggests that considerable structural reorganization takes place in terms of a better definition of the microstructure upon neutralization or that the electron density difference becomes large enough for detection. The ionic peak has been the basis of many structural models which have been proposed by several investigators. The ionic peak, in addition, has the following general characteristic features (7);

- typically occurs in all ionomers irrespective of the nature of the cation,
- magnitude and location of the ionic peak depends on the nature of the counterion,
- relatively insensitive to temperature,

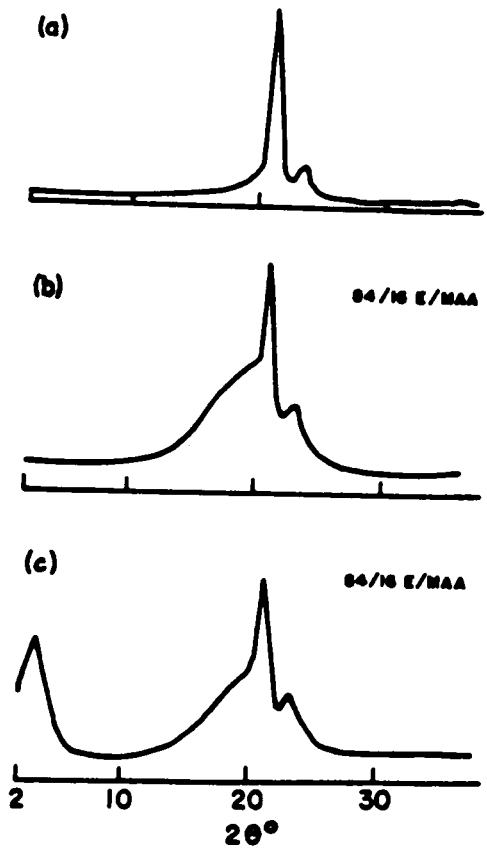

Figure 2.1. X-Ray Scattering Profiles of Polyethylene Based Materials: (a) low density polyethylene, (b) ethylene-methacrylic acid copolymer (5.8 mol % acid), and (c) 100 % neutralized sodium salt of (b). From Longworth (9).

- shows no evidence of orientation in cold drawn samples (no azimuthal dependence has been observed), and
- disappears or weakens in intensity when the ionomer is saturated with water.

There are many microstructural models that have been proposed to explain the characteristic features observed from scattering experiments. However, only the salient features of some of the important morphological models will be discussed in the next section.

2.2.2 Proposed Models for Ionomer Morphology

Longworth and Vaughan (20) assumed that the ionic peak was a Bragg diffraction maximum whose periodic spacing was about 20 Å. They attributed this spacing to the average multiplet spacing within the cluster where the clusters themselves were about 100 Å in size. According to MacKnight and Earnest (7), the limitations of the proposed model were;

- difficulty in envisioning a potential capable of producing a periodic spacing of 20 Å between multiplets when the ionic groups are randomly placed along the polymer chain,
- inadequacy in accounting for the intensity differences in the ionic peak for different cations,
- failure to explain the lack of changes in the morphological features of the crystallites present in the sample especially with the presence of clusters of such large dimensions.

Marx, Caulfield and Cooper (21) proposed an "aggregate model" based on their studies of carboxylated butadiene. They assumed that no phase separation occurs between the hydrocarbon matrix and the neutralized acid groups with the latter existing as "aggregates" homogeneously dispersed in the amorphous phase. The aggregates contained two or more acid groups depending on the concentration of the copolymer and the amount of water present. In this "aggregate model", the ionic peak is assumed to arise from the electron density difference between the metal cations and the hydrocarbon matrix. The cations were considered as point scatterers distributed on a paracrystalline lattice. According to this model, the maximum number of acid groups that can associate even for the highest concentration is about seven. Hence, this model rejects the concept of aggregation of multiplets to form larger clusters which is contrary to Eisenberg's theory. MacKnight and Earnest (7) pointed out, however, that the "aggregate model" clearly leaves some unanswered

questions such as the origin of a potential capable of arranging the scattering entities in a paracrystalline lattice in an amorphous, random copolymer. The model does not explain the presence of an ionic peak in lithium neutralized material and its absence in the corresponding acid form, despite the small differences in electron density between lithium carboxylate and the corresponding acid.

MacKnight, Taggart and Stein (22) proposed a model which was radically different from the earlier models. They assumed that the origin of the ionic peak was due to some structural features in the ionomer system imposed by the presence of salt groups. The model not only addresses the question of the size of the scattering particles but also attempted to gain insight into the internal structure of the ionic clusters. The model is based on the radial distribution function (RDF) analysis of the x-ray diffraction data of the wide as well as small angle regions of ethylene based ionomers of either acrylic or methacrylic acid, ranging in concentration from 2 to 7 mole percent. Details regarding the RDF analysis and the interpretation of the small angle x-ray scattering data are not provided here but only the results obtained will be discussed. It was shown using RDF analysis that the ionic peak does not arise from the interparticle interference since from previous knowledge of the ionomer composition the average distance between the scattering centers (clusters) would have to be several hundred angstroms.

Based on the x-ray studies, MacKnight et al. (22) proposed a model which assumes ionic clusters 8-10 Å in radius are formed that are shielded from the surrounding matrix ions by a shell of hydrocarbon chains. Matrix ions are those ions that are not incorporated in the clusters. They assumed the fundamental structural entity to be a coordinated metal ion and that there was a tendency toward charge imbalance within the cluster. The surrounding matrix ions were attracted toward the cluster due to electrostatic forces, but could not approach the inner core any closer than that allowed by the hydrocarbon shell surrounding the cluster. Therefore, a preferred distance of about 20 Å is established between the inner core of the cluster and the matrix ions. This preferred distance has been thought to be the origin of the ionic peak. These authors also suggest that water molecules tend to congregate in the neighborhood of the inner cluster upon saturation thereby raising the local dielectric constant. Hence, the preferred distance and the resulting ionic peak is

destroyed yet at the same time leaving the cluster intact. This provides the explanation for the disappearance of the low angle scattering peak upon saturation with water. A schematic representation of MacKnight, Taggart and Stein model is shown in Figure 2.2.

Fujimura, Hashimoto and Kawai (23) suggested a model which is a slight variation from the core-shell model of MacKnight, Taggart and Stein. In this model it is assumed that the hydrocarbon shell is depleted of any ions while the surrounding matrix had a finite ion concentration as shown in Figure 2.3.

Yarusso and Cooper (24) proposed a different model in which they attributed the small angle x-ray scattering (SAXS) peak to the interparticle interference between small ionic aggregates arranged with a liquid-like order within the material. The model is depicted in Figure 2.4. The proposed model was a variation to the classical model of Debye for the interparticle interference for a system of hard spheres (25). In their model the distance of closest approach between two scattering centers was larger than the sum of the radius of the two individual spheres. It was assumed that each ionic aggregate is coated with a layer of hydrocarbon material which is attached to the aggregate and whose electron density is the same as the matrix but which provides a barrier for the closest approach between ionic aggregates. The authors have estimated that, on the average, about half of the ionic groups are incorporated in the microphase separated clusters. The remaining groups are randomly dispersed in the hydrocarbon matrix as ion pairs. This theory is consistent with the prediction made earlier by Eisenberg wherein he proposed that the two ionic environments - i.e. multiplets and the clusters can coexist. Yarusso and Cooper have been able to theoretically fit the experimental scattering curves of zinc neutralized polystyrene ionomers over much of the angular region (26). One of the main limitations of the model, however, was its inability to fit the very low or the zero-angle scattering region where an increase in intensity was observed for all ionomers they studied. The discussion on the upturn in intensity at very low angles will be presented shortly.

More recently, Lee et al. (27) proposed the bead-spring micronetwork model. This model is based on a liquidlike distribution of the bead-spring micronetwork - see Figure 2.5. The ionic multiplets are represented as beads while the hydrocarbon chains are represented as a springs. The cluster size is dependent on the number of branches emanating from the central multiplet. The

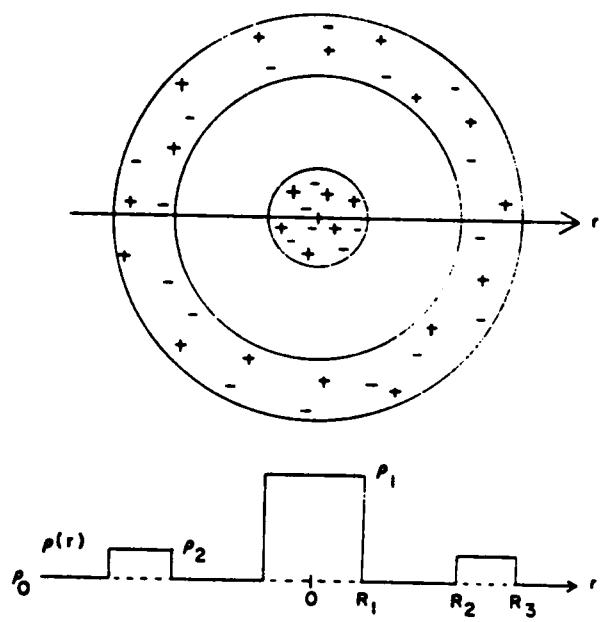

Figure 2.2. Schematic Representation of the MacKnight, Taggart, and Stein Model: From (22).

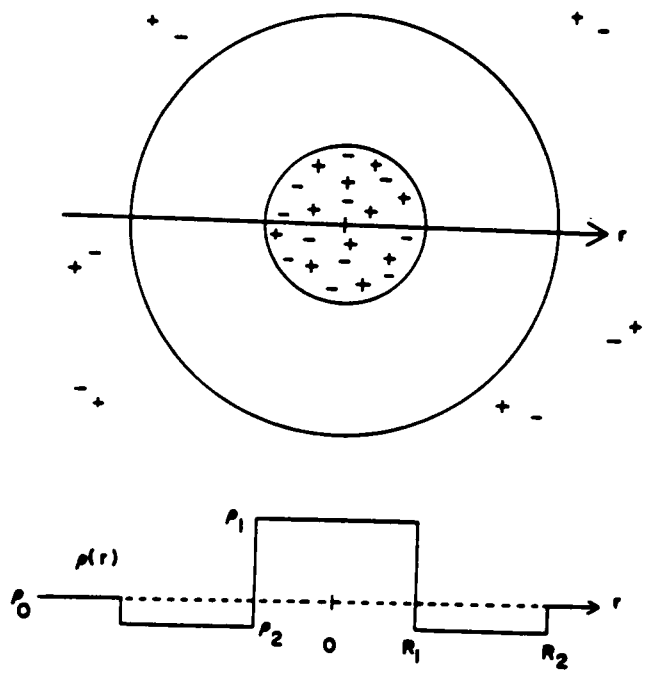

Figure 2.3. Schematic representation of the Fujimura, Hashimoto, and Kawai Model: From (23).

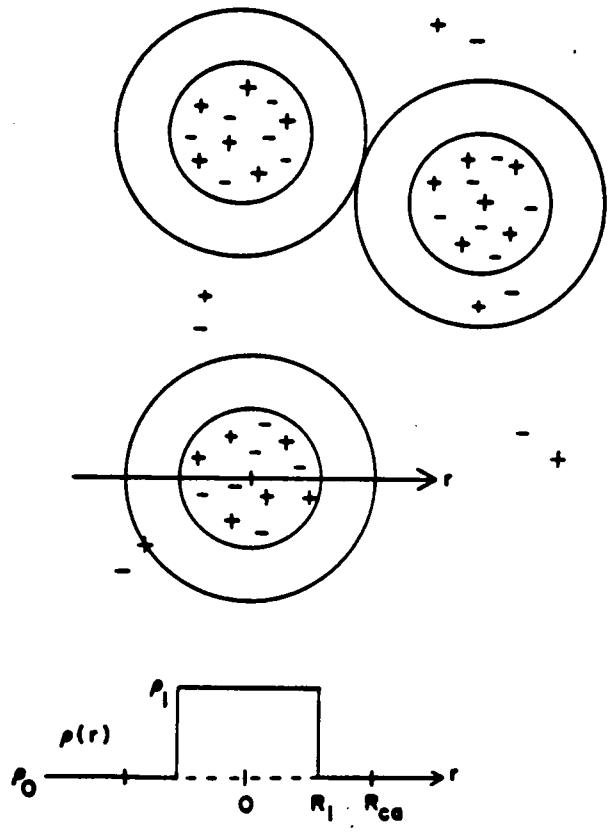

Figure 2.4. Schematic Representation of the Yarusso and Cooper Model: From (22).

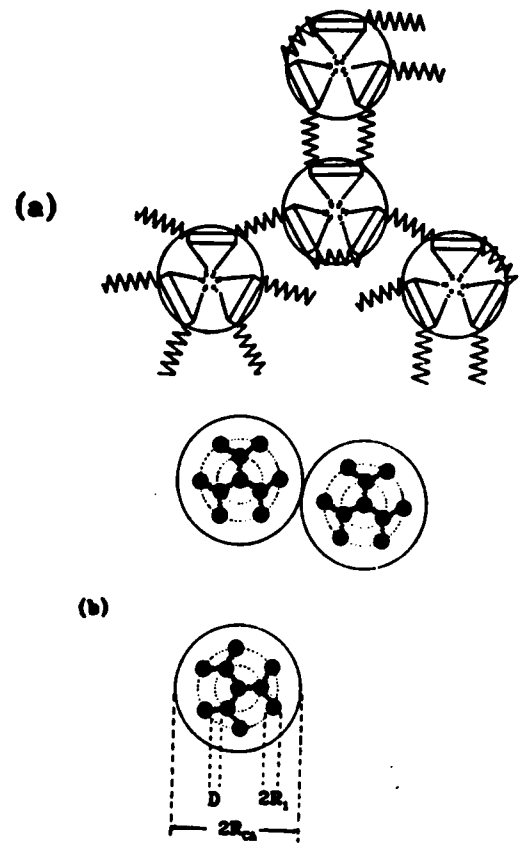

Figure 2.5. Schematic Representation of the Lee et al. Seven Parameter Model: From (27).

number of branches is related to the crosslink functionality of the central multiplet or bead. The model utilizes seven parameters which have been used to fit the experimental data of a MDI-based polyurethane segmented ionomer that exhibited a distinct SAXS shoulder in addition to the prominent ionic peak. The seven parameters of the model are the electron density difference between the multiplets and the matrix, multiplet (or bead) radius, the distance between multiplets, the average crosslink functionality of the multiplets, the effective cluster radius, the volume fraction of the clusters in the material, and the number of shells per micronetwork. The bead-spring network model does not predict the upturn in the scattered intensity near zero angle. But the model can be easily modified by including an additional source of scattering to account for the upturn in the scattered intensity at low angles once the origin for the upturn is well established.

It has been shown by Chu et al. (28) that the ionic peak intensity is about 100 times smaller that the scattered intensity extrapolated to zero angle in the region where the upturn in the scattering curve occurs. Therefore, the contribution from the zero angle scattering region cannot be ignored in any morphological model and the determination of its origin is important in understanding the microstructural arrangement of the ionic groups in ionomers. Recently, there have been many studies directed at studying the upturn phenomenon in the low angle region. Some have attempted to explain the upturn phenomenon by attributing it to the presence of voids or impurities (24). From anomalous small angle x-ray scattering experiments (ASAXS) experiments, Ding et al. (30) rejected the earlier notion that the upturn may be due to the presence of voids or impurities. They showed that the upturn is related to the neutralizing cation and may be caused by an inhomogeneous distribution of isolated ion pairs in the system.

Galambos et al. (31) in a recent study on solution cast films of sulfonated polystyrene have suggested that the upturn in the low angle region may be due to random multiplets (or ion pairs) that have not been incorporated into any cluster regions. They observed that the intensity in the low angle region decreases at elevated temperatures due to the formation of clusters which occur at the expense of multiplets. The decrease in the zero angle intensity is a result of the depletion of the multiplets. It should be noted that the data does not represent an equilibrium behavior and thermal annealing of the sample may considerably affect the behavior. Lantman et al. (32) suggested that

the low angle upturn is directly related to a non-equilibrium distribution of material. Based on results obtained from SAXS and SANS studies, they concluded that the inhomogeneities which are responsible for the upturn includes both the ionic entities as well as the polymer chains. The magnitude of the upturn and hence the extent of inhomogeneity was shown to be strongly dependent upon the annealing conditions.

Sample preparation and thermal history significantly affect the morphology of ionomers (33). The ion content at which cluster formation occurs is still an unresolved question. Peiffer et al. (34) did not observe a SAXS peak in sulfonated polystyrene ionomers for zinc salts below ionic content of 6.5 mol %. However, Fitzgerald and Weiss (9) have observed a SAXS peak at sulfonation levels as low as 0.9 mol %.

2.2.3 Electron Microscopy

Electron microscopy is perhaps the only technique by which one can directly view heterogeneities of the order of 10 Å, the size of ionic clusters. It would appear to be a particularly useful technique to study ionomer structure because neutralization with a heavy cation produces substantial contrast between the ionic domains and the nonionic hydrocarbon matrix. However, the structural features obtained are generally quite difficult to interpret. One of the main limitations of utilizing this technique to investigate ionic domains is the difficulty in getting film sections thicknesses which are of the order the domain size. The thinnest sections obtained even after cryogenic microtoming are typically in the range of 500 Å. The differentiation of a domain from the one below it is therefore difficult under these circumstances due to overlapping effects.

Handlin et al. (35) have attempted to image ionic domains in four different ionomers using transmission electron microscopy (TEM). They concluded that no reliable information about the ionic domains can be obtained from solvent cast films. The inability to image the ionic domains have been attributed to the fact that the ionic domains in the ionomers are typically small (compared to the thickness of the microtomed sections) and this prohibits an accurate measurement of the domain shape and size distribution. They suggest that previously observed structures in ionomers may have been due to the presence of artifacts in the microscopy results.

Graiver, Litt and Baer (36) have been the first to distinctly observe ionic microdomains using TEM. Their effort has attracted very little attention in the literature. They observed a regular a layered structure in polysiloxane dizwitterionomers stained with uranyl aceate. Since the solubility parameter differences between polydimethylsiloxane and the zwitterions is large, the phase separation process is highly favored thermodynamically. Their SAXS data complement the dimensions observed from the TEM micrographs. The ionic domains were only observed when the domains planes were parallel to the electron beam.

Feng et al. (37) have observed a lamellar or a rodlike morphology in segmented ionene polymers using TEM. Such an occurrence was surprising since the ionic groups represent only 6.4 % of the all the volume occupied. From block copolymer studies the transition from a spherical to a cylindrical morphology occurs at ca. 20 vol. % (38). The ordering phenomenon has been suggested to be promoted by a strong driving force for the ionic groups to microphase separate due to high level of coulombic interactions in these systems. The observed spacings from the TEM studies were consistent with that obtained from small angle x-ray scattering studies on the same system. A detailed analysis of the SAXS data of these ionene systems, which is a part of a joint effort, will be discussed in Chapter VI of this dissertation.

Pineri and coworkers (39-42) have used other techniques such as small angle neutron scattering (SANS), electron microscopy, electron spin resonance (ESR) and Mössbauer (γ ray) spectroscopy in addition to x-ray scattering to elucidate the structure of ionomers. Meyer and Pineri (42) studied Fe(II) complexes of random terpolymer of butadiene-styrene-vinylpyridine whose composition was 85% butadiene, 10% styrene and 5% vinylpyridine. From the SAXS and SANS experiments they determined that more than 82% of the clusters were less than 30 Å in radius and the most probable size was around 10 Å which is in good agreement with the model proposed by MacKnight et al. (22). The results from Mössbauer spectroscopy revealed that the ions exist in three types of distinct environments or level of aggregation. They were:

- dimers which account for about 20% of the iron, consisting of two asymmetrical Fe(III) complexes which are anti-ferromagnetic,

- "qausi-isolated" complexes which account for less than 20% of the iron, having a weak ferromagnetic coupling that could either be very small multiplets or be preferentially located in the vicinity of the clusters, and
- clusters which contain 40-60% of the iron with 90% of these clusters being less than 30 Å in radius and contain an average of 30 complexes.

The studies strongly suggest that the basic structural unit which was thought to be an ion-pair may actually be a coordination complex.

Even after numerous efforts utilizing a battery of techniques, a complete understanding of the state of aggregation of ions in ionomers is still elusive though the efforts being made appear to be heading in the right direction.

2.2.4 Theoretical Models

There have been numerous efforts to understand the nature of the ion aggregation in ionomers from a theoretical perspective. The first theoretical approach which attempted to elucidate the phase separation of ions in a non-polar matrix was put forth by Eisenberg (19). He proposed that the ion aggregation occurred in two steps. At low ion concentration, the ions exist as ionic aggregates or multiplets. With increasing ion content, these multiplets themselves aggregate to form ion clusters. This concept was introduced earlier on page 8.

Forsman (43,44) proposed a theory for ion-pair association based on the statistical mechanics of chain-like molecules and the energetics of ionic interactions. He calculated critical ion contents below which ion clusters would not form. He also calculated critical equilibrium cluster sizes as a function of interaction parameter. For realistic values of the interaction parameter, he calculated that the number of ion-pairs or multiplets in a cluster could range from 6 to 30 ionic groups depending on the concentration of the ionic moieties. Dreyfus (45) developed a model in which a cluster was built from the center of the closest packing, resulting in a charge distribution which decreases monotonically from the center. More recently, Painter and coworkers (46) proposed a model that predicts the equilibrium distribution of cluster sizes. In their study they reassessed the energetic terms that were used in previous studies and concluded that the chain extension term

could be neglected for ionomers with a truly random distribution of clusters, linked by subchains that obey Gaussian statistics. In a recent review of the different theoretical studies, Mauritz (47) discusses the various merits and limitations of the various theoretical models that have been proposed.

2.3 Physical Properties Of Ion Containing Polymers

In view of the considerable amount of work relating to the morphology of ionomers, the effect of morphology on the physical properties of the system is important. Surprisingly, there is little direct experimental evidence correlating multiplet and cluster formation to physical properties. However, indirect evidence relates selected physical properties to the nature of ion aggregation.

2.3.1 Ionomers in the Glassy State

The presence of ionic groups in the polymeric backbone does not result in major changes in the viscoelastic response of a system in the glassy state except that the dynamic mechanical behavior is somewhat altered. Drzewinski and MacKnight (48) in their study of sulfonated polysulfone observed that the sulfonated portion of the chain gives rise to a new loss peak (β transition) which tends to move to higher temperatures with increasing level of sulfonation. The absorption of water significantly also affects the low temperature transitions. The β transition shifted to lower temperatures and increased in intensity with moisture content. However, the γ transitions shifted to lower temperatures with moisture content but with decreasing intensity - an antiplastization effect.

There is little data that has been reported regarding the effect of ionic groups on the properties in the glassy state such as impact, stress-strain characteristics, etc. Hara and Jar (49,50) have reported that the fatigue performance initially decreases with ion content up to ca. 5 mol %. This is attributed to the crosslinking effect of the multiplets. The crosslinking reduces chain mobility, dissipates less energy, and makes the ionomer more brittle. However, the fatigue performance increases with ion content above 5 mol %. The increased fatigue resistance is considered to arise from an increased resistance to crack propagation due to the presence of clusters. It appears that additional

studies in the area of glassy ionomers would open new avenues for a better understanding of the structure-property behavior of ionomers.

2.3.2 *Ionomers in the Glass Transition Region*

The glass transition temperature T_g, is perhaps one of the most fundamental properties of polymers. Materials below T_g are usually hard, glassy solids while the materials above T_g are leathery or rubbery in nature. The transition from the vitreous or the glassy state to that of a rubbery state is characteristic of many polymeric solids (an exception being that of a crosslinked material), and depends upon the thermal energy of the polymer molecules. Therefore, the T_g of a material relative to the application temperature is an important parameter.

The effect of ion content on the glass transition temperatures of ethylene and styrene has been investigated by Eisenberg (51) using differential scanning calorimetry (DSC) and dynamic mechanical analysis (DMA). The data were observed to be linear within the narrow concentration range studied, although a linear relationship over a wide concentration range is not expected. The increase in T_g with ion content is due to two effects, (a) a copolymerization effect, i.e. incorporation of glassy ionic groups into the polymer and (b) restriction placed on backbone mobility by the "ionic crosslinks". Thus a higher thermal energy is required to induce the same backbone mobility and this results in an increase in T_g.

Numerous studies have confirmed that the glass transition temperature is greatly influenced by the presence of ionic interactions in polymers. Eisenberg and co-workers (52-54) have shown that the increase in T_g is related to the nature of the anion-cation interactions. A stronger interaction places a greater restriction to backbone motion which results in a higher T_g . Matsuura and Eisenberg (53) developed a simple relationship wherein $\Delta T_g \sim \frac{q}{a}$, where q is the cation charge (the anion charge is assumed to be constant for a given series) and "a" is the inter-nuclear distance between the anion and the cation. In Figure 2.6, T_g is plotted against $\frac{cq}{a}$, where c is the concentration of ionic groups. Multiplication of $\frac{q}{a}$ with c serves to cancel out the effect of cation type and produces a rather unusual "sigmoidal" master curve. The T_g initially rises linearly with increasing ion content followed by a non-linear rise of T_g observed between $\frac{q}{a}$ values of 0.05 to 0.1. At higher

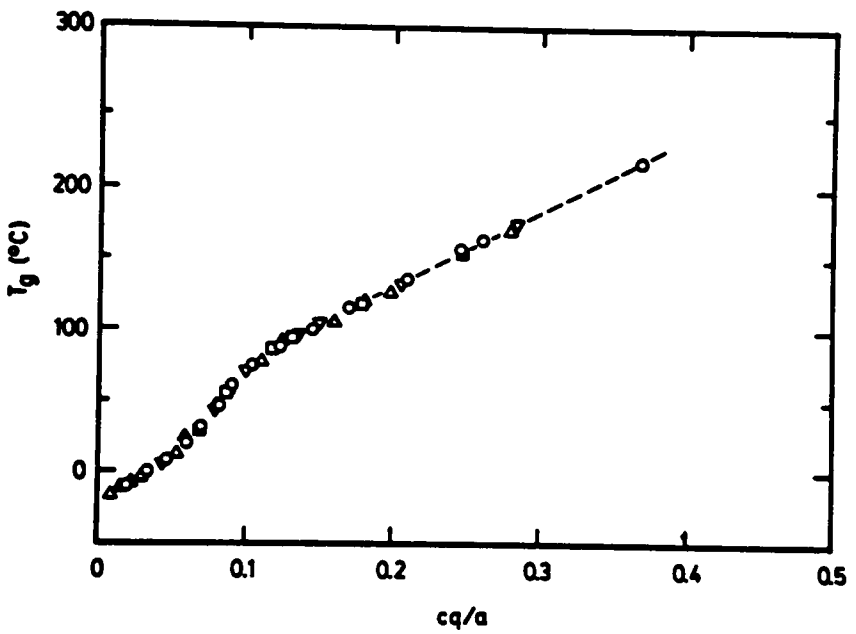

Figure 2.6. **Plot of the Glass Transition Temperature versus cq/a:** From Matsuura and Eisenberg (53).

ionic content, T_g again rises linearly. The concentration at the hump corresponds to the onset of non-superposability of the time-temperature superposition principle in the viscoelastic studies and is attributed to the onset of cluster formation. Multiplet formation is believed to have a dominating influence in the linear region prior to the hump.

The glass transition temperature is also significantly affected by moisture or other highly polar liquid species which are preferentially sorbed into the ionic domains (either multiplets or clusters), producing a plasticization effect. Such additives termed "ionic plastizers" can solvate the ionic domain thereby significantly affecting the T_g of the ionomer. Again, the degree to which the T_g is shifted is dependent upon the level of sorption, concentration of ionic species and backbone stiffness.

In summary, ionic moieties when incorporated in polymeric matrices often tend to raise the glass transition temperature. They have a significant influence on the viscoelastic response of a material provided that these ionic associations have a sufficiently long relaxation time relative to the backbone relaxation time associated with glass transition phenomenon. However, if the average relaxation time of the backbone is longer than the relaxation time associated with ionic associations, then the influence of ionic associations would be negligible.

2.3.3 Viscoelastic Properties of Ionomers

The examination of the viscoelastic properties of ionic polymers has been the principal but an indirect method by which the presence of unusual structural features has been revealed. The relaxation behavior of ethylene-methacrylic acid ionomers partly supported by x-ray and electron microscopy measurements have provided some evidence for the formation of clusters (20,55). Stress relaxation and dynamic mechanical studies have been primary techniques used and the objective of the investigation being to correlate the mechanical behavior with the molecular structure of the polymer.

2.3.3.1 Stress-Relaxation

Incorporation of ionic groups into polymers alters the molecular relaxation process. The effect of increasing the ion content as well as neutralization of the ionic groups results in shifting the relaxation times of the ionomers to longer times. Eisenberg and Navratil (56-59) have studied the styrene copolymers of methacrylic acid in considerable detail and have provided indirect evidence of cluster formation from studies of viscoelastic properties. They have shown that incorporation of acid groups into polystyrene increases T_g due to hydrogen bonding. Neutralization of the acid groups had a dramatic effect in that the relaxation curve of the ionomer which was shifted to much longer times. The rubbery plateau is also greatly enhanced suggesting a significant increase in the crosslink density of the system which may probably be due to the "ionic crosslinks".

2.3.3.2 Time-Temperature Superposition

The William-Landel-Ferry (WLF) relationships have been widely used to predict the viscoelastic behavior of polymers in the transition region and they inter-relatate two important external variables of time and temperature together with T_g. The WLF relationship is generally used to predict changes in the properties over the range from T_g to T_g + 100 °C.

The time-temperature superposition is often used to construct master curves from experimental data carried out at shorter time scales but over a wide range of temperatures. The resulting shift factors should obey the WLF relation for thermorheologically simple materials. Any changes in molecular mechanism(s) controlling the response of a system, e.g. crosslinking crystallization, cluster formation etc, result in the failure of the time-temperature superposition principle.

In the literature, the observation of a deviation from WLF behavior or time-temperature superposition has been the main source of argument concerning the presence of clustered morphologies in ionomer systems (56-59). It has been a general observation that below a critical ion or salt concentration, the WLF or master curve can be utilized in ionomers but above this concentration one observes the failure of time-temperature superposition. Figure 2.7 illustrates the stress relaxation curves and the corresponding pseudo-master curves for six sodium neutralized poly

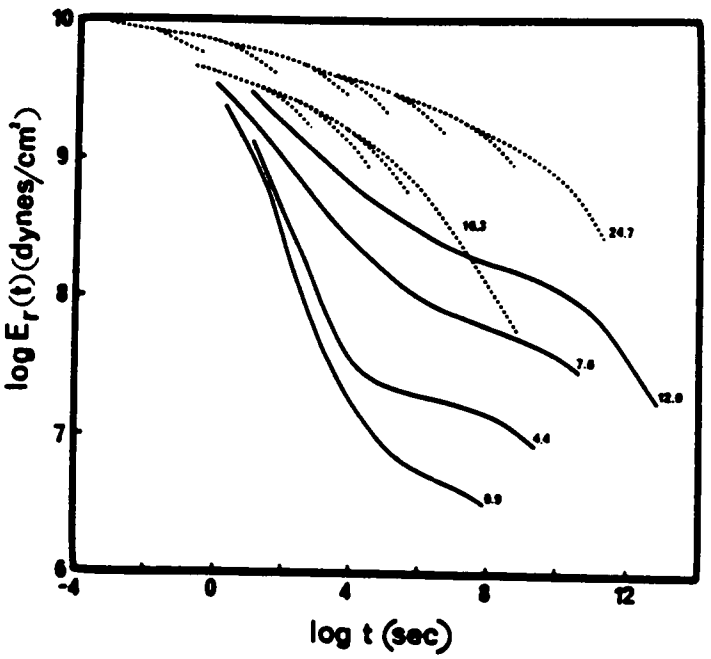

Figure 2.7. Stress-Relaxation Master Curves and Pseudomaster Curves for Six Ionomers: The numbers indicate ion concentration (mol %). From Eisenberg et al. (60).

(ethyl acrylate) ionomers obtained by Eisenberg et al. (60). Incorporation of the ions in the polymer broadens the relaxation behavior due to ionic associations. The time-temperature superposition principle is only valid at low ionic content and a single master curve is obtained upon shifting of relaxation curves up to 12 mol % ion content. At higher concentrations, however, shifting of the relaxation curves fail to produce a single master curve and a breakdown of time-temperature superposition is observed. A change in the relaxation mechanism is indicated in the ca. 12-16 mol % ion content range. This change may be due to morphological changes occurring at high concentration of ions in the ionomers - a transition from a multiplet morphology to a clustered morphology. The deviation from the time-temperature superposition principle is thought to be due to the onset of clustering which has a very different relaxation behavior. The time-temperature superposition which is typical of most nonionic and amorphous homopolymers breaks down for ionomers when the salt content is greater than ca. 6 mol % for the sodium methacrylate copolymers (56,57) and ca. 12-16 mol % for the ethyl acrylate-sodium methacrylate system (60). A difference by a factor of two in ion content is observed for the two systems to achieve the same result. This suggests that failure of time-temperature superposition may be used as a diagnostic tool to detect the presence of clusters at sufficiently high concentration (5). In other words one can expect a failure of time-temperature superposition in all system when clustering occurs. Also, there is a significant difference in water absorption for polymers with different ion contents (53). Navratil and Eisenberg (56) found that below 6 mol % of sodium acrylate in styrene, the ionomer samples could accommodate only one water molecule per ion pair with equilibrium being established in ca. 400-600 hrs. In contrast above 6 mol % the ionomer samples does not reach equilibrium and 3-6 water molecules are absorbed per ion pair.

2.3.3.3 Dynamic Mechanical Properties

Dynamic mechanical analysis is often used to study molecular relaxations in polymers. The results from DMA measurements, G′ and tan δ are often presented as a function of temperature, where G′ represents the dynamic storage modulus and tan δ (loss tangent) represents the energy lost relative to the energy stored (loss modulus / storage modulus) per deformation cycle. The

modulus will generally decrease with increasing temperature with a sharp drop occurring as various molecular relaxation mechanisms are activated at which temperatures the loss tangent will go through successive maxima. Conventionally, the transition occurring at the highest temperature experimentally accessible is labelled α, and subsequent transitions occurring at lower temperatures are labelled β, γ etc. In amorphous uncrosslinked polymers the α transition corresponds to T_g, the transition from a rubber to a glass.

The dynamic mechanical studies largely corroborate the results obtained from stress relaxation studies. Eisenberg and Navratil (58) in their study of styrene ionomers found considerable broadening of the relaxation response with increasing ion content and an increase in modulus at which the inflection point occurred. Similar results have been observed from stress relaxation experiments. The general features of all ionomers with ion concentration less than 6 mol % were nearly the same with appearance of two peaks in the loss tangent curves. The low temperature peak reflects the T_g of the matrix containing the multiplets and moves to higher temperatures with increasing ion content as expected but the higher temperatures peak occurs at approximately the same temperature, ca. 150 °C, and remains unaffected by ion concentration. This peak has been suggested to be due to softening of the multiplet structures (58). The second peak is considerably reduced for the samples of 6 mol % and above this value no definitive peaks were discerned, although an increase in tan δ was observed. This increase in tan δ is likely due to the softening of clusters (58), a phenomenon which occurs over a broad range of temperatures thus indicating a continuous change in structure with temperature. The increase in tan δ was also observed to shift to higher temperatures with increasing ion content, as opposed to the fact that for ion concentration below 6 mol % the higher temperature peak remained at nearly the same temperature. The absence of the high temperature peak for any concentration range in polyethylene lends further support to the conclusion that the ethylene ionomers experience clustering at very low concentrations.

Rigdahl and Eisenberg (61) studied the viscoelastic properties of sulfonated styrene ionomers and have compared their properties with those of the previously studied carboxylated styrene ionomers. They found the high temperature peak of carboxylated systems of styrene ionomers were considerably lower than that for the sulfonated system. Re-establishment of time-temperature

superposition has been observed in carboxylated styrene ionomers above 180 °C but was not observed for the sulfonated ionomers. This further indicates that the clusters in sulfonated materials are more stable in nature and do not break up into multiplets even at elevated temperatures.

Since the high temperature peak has been associated with the transition in the ion-rich clusters, this suggests that the clusters in sulfonated materials are more thermally stable and the interactions within the clusters are greater than that present in carboxylated systems. Both sulfonated and carboxylated materials exhibited thermorheological simplicity below 6 mole % ion content but a failure of the time-temperature superposition principle was observed above the critical concentration of 6 mole %.

The effects of partial neutralization of ionomers have been investigated by Navratil and Eisenberg (57). They found that ions cease to act as crosslinks for degrees of neutralization below ca. 50% since the upper inflection point related to presence of ionic crosslinks disappears. Above 50% neutralization the position of the upper inflection point increase with increasing degree of neutralization. Furthermore, calculations based on the theory of rubber elasticity indicate that the apparent cross-link density is significantly less than that expected on the basis of neutralization. For example, 80% neutralized ionomer contains only half the number of equivalent crosslinks contained in the fully neutralized ionomer, and the 60% ionomer contains only one fourth this number. Also, the partially neutralized samples generally relaxed more rapidly than the corresponding fully neutralized materials, which suggests that the free carboxyl groups are incorporated into the ionic clusters and in effect, plasticize them.

2.3.4 Elastomeric Ionomers

It must now be clear that incorporation of low levels of neutralized ionic groups profoundly alters the structure-property behavior of the parent material. With a few exceptions, most of the earlier discussions have focussed on non-elastomeric, rigid polymer backbone based ionomers since much of the early work had been conducted on these systems. Moreover, most of the theories and fundamental concepts relating to ionomers have been developed from studies conducted on non-elastomeric systems.

The rubbery region of the viscoelastic spectrum of ionomers is particularly of great commercial importance since ionic interactions could be utilized to produce thermoplastic elastomers. The ionic interactions form "physical" or pseudo crosslinks which at elevated temperatures become sufficiently labile to allow melt processing. One of the severe limitations encountered in classical elastomers such as polybutadiene, polyisoprene, etc. was their inability to be reprocessed.

A review of the earlier work on elastomeric ionomers has been presented by Jenkins and Duck (62). Carboxylic acid groups were initially introduced into the polymer matrix as a means of controlling polarity. The first such commercial product was a butadiene-styrene acrylic acid terpolymer latex (trade name Hycar 1571) marketed by B.F. Goodrich in 1949 (17). It was Brown who first neutralized carboxylated elastomers with metal oxides in the 1950's thus actually forming ionically crosslinked elastomer. His work catalyzed the development of a whole new class of materials.

Following the pioneering work of Brown, the field of ionomers grew rapidly but there was a shift in emphasis toward non-elastomeric ionomers. This was probably due to the poor elastomeric properties exhibited by carboxylated ionomers. At that time it was not realized that ionic crosslinks were thermally reversible. With the advent of sulfonated ionomers the focus has shifted toward elastomeric ionomers since it was found that they have much better mechanical properties than the carboxylated materials (63). Esso patents (64-66) in the early to mid-seventies have revitalized the effort towards understanding elastomeric ionomers. However, it was not until 1978 that the first data on EPDM based ionomers were published in open literature. Since then numerous studies have been reported which were directed toward ionomeric thermoplastic elastomers.

2.3.4.1 Sulphonated EPDM

The EPDM systems are terpolymers of ethylene, propylene, and non-conjugated diene monomer (e.g., ethylidene norbornene, ENB) which are polymerized by a Ziegler-Natta or coordination mechanism. Details regarding the synthesis, sulfonation and neutralization procedures have been described by Makowski et al. (67). Agarwal et al. (68) have studied the effect of sulfonation and cation on the viscoelastic properties of sulfonated EPDM (SEPDM) materials. Figure 2.8 illustrates the effect of sulfonate content on the storage modulus as a function of temperature. For

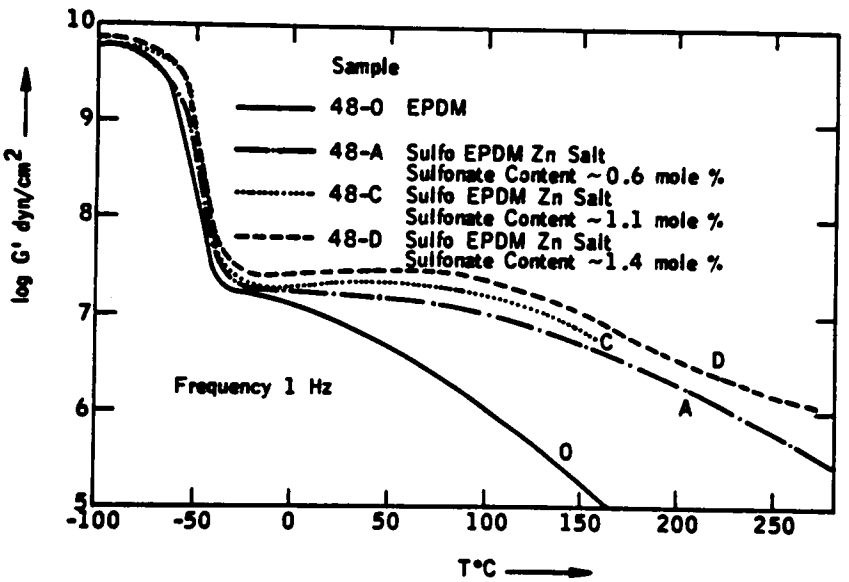

Figure 2.8. Storage Modulus G′ versus Temperature for Zinc Sulfonated EPDM Ionomers of Varying Sulfonate Content: From Agarwal et al. (68).

the unmodified polymer only a short rubbery plateau was observed near room temperature indicating an absence of a developed network structure. With increasing levels of sulfonation, a small but an apparent increase in T_g was observed. A more noticeable feature was the development of a well defined rubbery plateau at sulfonation levels as low as 0.6 mol %. The increase in sulfonate content also results in an increase in the magnitude of the rubbery plateau. An interesting feature observed at higher sulfonate levels (1.1 and 1.6 mol %) is an increase in G′ with increasing temperature in the rubbery plateau region which is in accordance to the rubbery elasticity theory (69). It was also observed that time-temperature superposition principle was valid for these ionomers suggesting that the behavior of these materials is thermorheologically simple. This suggests that a multiplet morphology may exist in these systems.

The effect of the cation on the viscoelastic behavior of SEPDM was also studied (68). The cations studied were Li, Na, Cs, Ba and NH_4. Small differences in the rubbery modulus were observed for the metal sulfonates. However, the viscous flow region in the NH_4 salt ionomer was approached at lower temperature. This may be attributed to the bulkiness of the NH_4 which provides steric hindrance to a stronger association of the ionic groups. Very little change in the T_g of the material was observed with the different cations.

Makowski et al. (67) have studied the effect of cations on the tensile and flow behavior of EPDM based sulfonated ionomers. Nine different cations studied were Mg, Ca, Co, Li, Ba, Na, Pb, Hg, and Zn. Zinc neutralized materials displayed the highest melt index (0.75 g/10 min at 190 °C, and 478 psi) followed by Pb (0.1), while the rest of the materials had a melt index of zero (did not flow). The tensile strength of Zn neutralized materials was found to be greater or at least comparable to the other materials. This combination of good tensile strength along with the low melt viscosity makes Zn neutralized material an ideal candidate for use as thermoplastic elastomer. The melt viscosity can greatly be reduced using ionic plasticizer such as zinc stearate. It has been shown that on cooling zinc stearate crystallizes out and acts as a filler enhancing the mechanical properties.

2.3.4.2 Telechelic Ionomers

The unique feature of telechelic ionomers is that the ionic groups are located only at the chain ends unlike in random ionomers where these groups are randomly distributed along the polymer chain. This greatly simplifies the task of relating microstructure of the ionomer to the properties. Recently, telechelic ionomers have attracted considerable attention, especially as model ionomer or model network systems. Extensive research on carboxylated telechelic materials have been studied by Otocka et al. (17), Pineri et al. (39) and Broze et al. (70-82).

Carboxylated Telechelic Ionomers

Otocka et al. (18) studied the bulk and the solution viscosity of carboxylic-acid-terminated polybutadiene using this novel telechelic approach. They observed that the viscosity increased markedly upon neutralization with both monovalent and divalent cations.

Broze et al. have studied linear carboxylated telechelic ionomers based on polybutadiene (PBD) and polyisoprene (PIP). The carboxy-telechelic PBD's used are commercially available with a $\overline{M}_n$ of 4600, polydispersity and functionality close to 1.8 and 2.0, respectively. However, the carboxy-telechelic PIP's were prepared anionically with a variety of molecular weights, a polydispersity close to 1.2 and a functionality greater than 1.9. The carboxy-telechelic ionomers have been extensively characterized in terms of thermal (69,70), dilute solutions (5,71-73), morphology (74), and viscoelastic (69,70,75,76,82) properties. Figure 2.9 shows the viscoelastic behavior of both un-neutralized carboxy-telechelic PBD and the corresponding magnesium neutralized material. It is clear from Figure 2.8 that the material undergoes a transformation from a viscous fluid at low frequencies (where $G''>G'$) to a material displaying a network character which is indirectly deduced from the presence of a plateau within G' curve at higher frequencies. The time-temperature superposition principle was found to be valid over the entire frequency range for the magnesium neutralized ionomer, but the shift factors, a_T's do not obey the WLF type of temperature dependence. However, the shift factors seem to fit an Arrhenius type relationship. The materials neutralized with Zn and Ca displayed similar viscoelastic behavior. The crossover fre-

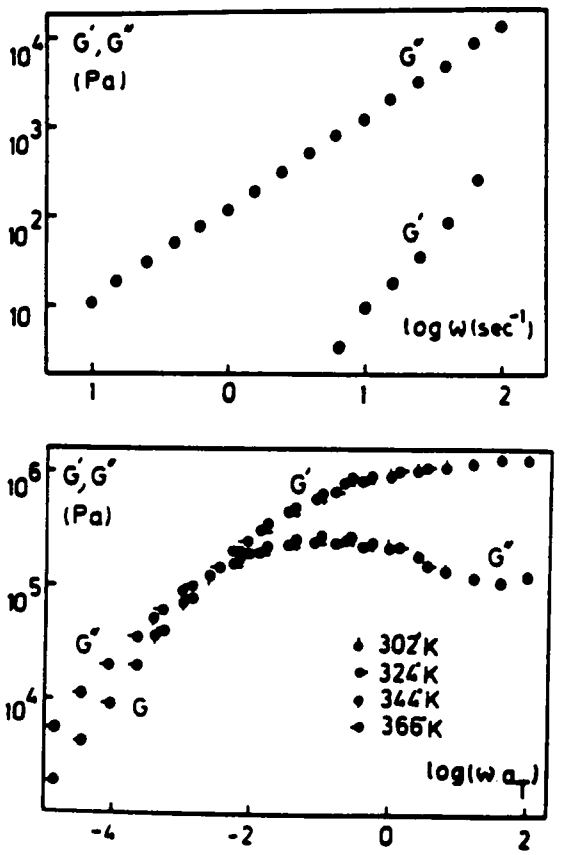

Figure 2.9. **Dynamic Mechanical Behavior of Carboxy-telechelic PBD Ionomer (Mn = 4600) at 302 K:** (a) un-neutralized form, (b) master curve for the same material neutralized with Mg. From Broze et al. (70).

quency (where $G''/G' = 1$) for Zn neutralized materials occurs at much higher frequency due to the greater covalent nature of zinc which results in a weaker network and a broader flow region. Materials neutralized with Ba and Be exhibit a network character spanning a wider range of frequency and temperature but for fundamentally very different reasons. The Be carboxylates are believed to form small and a very tight aggregates due to high electrostatic interactions, while the Ba carboxylates which interact to a lesser extent favor a larger extension of the two-dimensional growth of multiplets into layered structures. They also found that T_g was independent of the concentration of the ionic groups (70).

In the study of carboxylated polyisoprenes, the prepolymer molecular weight was varied from 7,000 to 70,000. The effect of increasing the molecular weight results in a corresponding decrease in ionic content. Figure 2.10 depicts the effect of precursor molecular weight of PBD on the dynamic viscoelastic behavior for both un-neutralized material and magnesium neutralized materials. The unneutralized materials display a short pseudo-rubbery plateau which disappears as $\overline{M}_n$ reduces to 15,500. Moreover, it was not possible to characterize the 7,000 material due to its higher fluidity at the test temperature. Upon neutralization, the development of a well defined rubbery plateau is observed with the 7,000 $\overline{M}_n$ material exhibiting a rubbery plateau spanning over a few decades of frequency. With increasing molecular weight (decreasing ion content), the rubbery modulus decreases and the terminal region is shifted to higher frequencies which is indicative of a weaker network being formed. However, for the 69,000 $\overline{M}_n$ material an increase in rubbery modulus is observed along with the terminal region shifting to lower frequencies. This behavior is due to the development of a more extensive entanglement network (82).

Tant et al. (83) have studied the mechanical properties of carboxylato-telechelic polyisoprene neutralized with various cations. Figure 2.11 shows the effect of cation valence at nearly constant molecular weight. The modulus of Zr and Al neutralized materials are nearly the same while it is substantially lower for Ba neutralized material. This suggests that the crosslink density or crosslink functionality may be similar for the Zr and Al materials but lower for the barium material. At higher elongations, the stresses decrease in the order Zr > Al > Ba. The authors attribute the higher stresses observed for Zr material to the bonds being more covalent than ionic and it also possesses a higher

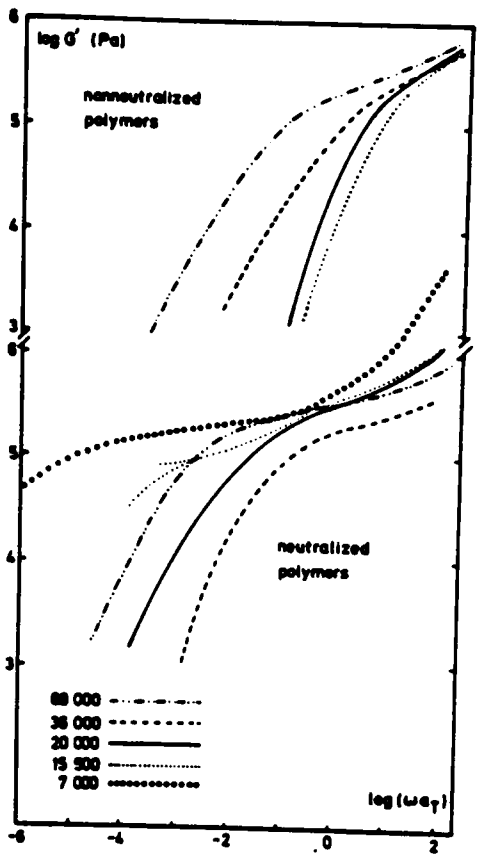

Figure 2.10. G′ Master Curves for Carboxy-telechelic PIP Ionomer (ref. T = 296 K): Effect of molecular weight and neutralization with Mg. From Broze et al. (82).

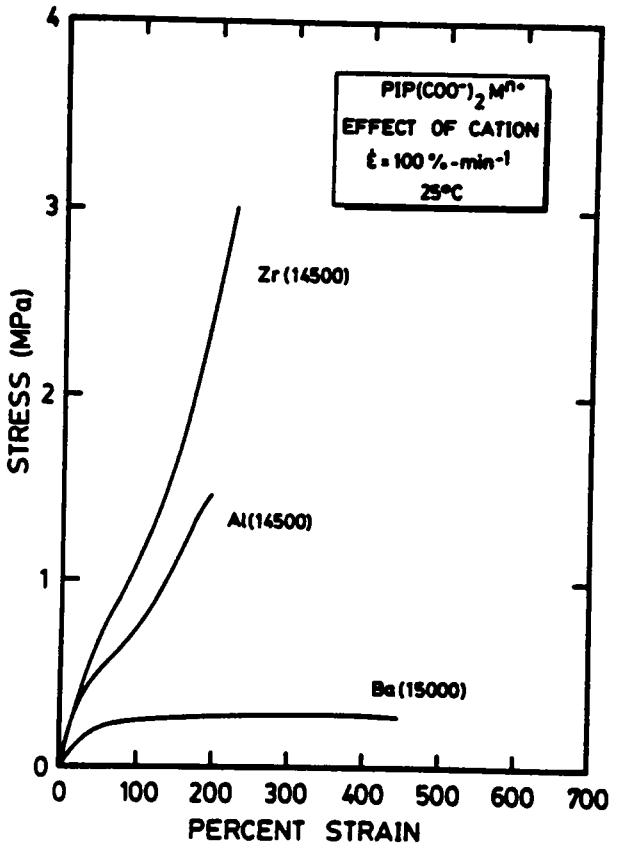

Figure 2.11. Effect of Cation Valence on the Stress-Strain Behavior of PIP Ionomers in the Molecular Weight Range 14500-15000: From Tant et al. (83).

functionality because of the cation valence and neutralization pathway. The differences between Al and Ba materials have been attributed to the differences in cation valence. From stress relaxation experiments, it was found that Ba material displays a rapid decrease in stress suggesting a poor network character. The Zr material, especially the 14,500 $\overline{M}_n$ system, maintained stress levels over a long period of time indicating a more permanent network structure.

Williams et al. (84) have studied a series of model telechelic ionomers based on PBD and PIP backbone which have been neutralized with various cations. From their SAXS studies, they concluded that the characteristic spacing between the ionic domains was principally governed by the configuration of the backbone polymer whereas the nature of the cation only plays a secondary role. They have observed that there is a sharp phase separation between the ionic domains and the non-polar polymer matrix. This was determined from the analysis of the tail region of the SAXS intensity profile.

Laleg et al. (85) studied the influence of the cation valence on the viscoelastic transition parameters and microphase separation in carboxy-telechelic PBD. Differential scanning calorimetry was used to determine the amount of polybutadiene in the matrix away from the ionic aggregates. The heat capacity change ΔC_{p_2} during the glass transition of the PBD matrix was measured and compared with ΔC_{p_1} of the pure PBD. It was assumed that the polymer chain in the ionic aggregates do not have sufficient mobility to undergo a transition. Therefore, the heat capacity variation of ΔC_{p_2} during the glass transition of the PBD phase will always be lower than the ΔC_{p_1} of pure PBD. Thus, the ratio of $\Delta C_{p_2}/\Delta C_{p_1}$ can be assigned to the degree of phase separation of the PBD phase, and the difference $(\Delta C_{p_1}-\Delta C_{p_2})$ is related to the amount of PBD chains which are in the ionic aggregates (multiplets or clusters) or in the interphase between the ionic aggregates and the PBD matrix. The degree of microphase separation was found to decrease with increasing cation radius or by a decrease in the molecular weight of the precursor.

Sulfonated Telechelic Ionomers

Wilkes, Kennedy and coworkers (86-93) have extensively studied the properties of polyisobutylene (PIB) telechelic ionomers. These materials have several advantages over the

carboxylated-telechelic ionomers. It has already been shown that sulfonate groups provide a much stronger interaction than the carboxylate groups (94), thus the mechanical properties are considerably improved over those of the carboxylated materials. Moreover, the polyisobutylene chain is saturated and is therefore more stable than polybutadiene or polyisoprene polymers. Also, a variety of chain architecture was developed - specifically, linear monofunctional, linear difunctional and the three-arm trifunctional materials.

Bagrodia et al. (93) have investigated the effect of molecular architecture and have found that the tri-arm trifunctional materials possess the best mechanical properties. This is not surprising since each tri-arm trifunctional molecule possesses a permanent network junction point. Clearly, only an ion pair association would be required to form a three dimensional network for trifunctional materials while a similar association would only result in a chain extension in a difunctional material. In order for the difunctional materials to form a three-dimensional network a triplet or higher order association is necessary while it is impossible for the monofunctional materials to form a network structure. The trifunctional materials have been observed to reach stresses up to 7 MPa and elongations up to 1000%, depending upon the molecular weight, neutralizing cation, and the extent of neutralization. By comparison, the linear difunctional materials reach stresses up to 1 MPa and elongations of only 300-400 %. As mentioned earlier, the linear monofunctional materials cannot form a network and hence characterization of these materials were difficult since the materials were tacky, viscous fluids at room temperature.

Bagrodia et al. (88) have also studied the effect of molecular weight of trifunctional materials neutralized with KOH to the stoichiometric end-point. It is observed that both stress and modulus increase with decreasing molecular weight. This can be explained from the fact that crosslink density increases with decreasing molecular weight, assuming only ion pair associations occur (88,93). An upturn above 600 % elongation was observed which is due to strain induced crystallization of the PIB segments which has been confirmed by wide angle x-ray scattering (87).

Wilkes and coworkers (89) have also studied the effect of excess neutralizing agent on the mechanical properties and have found that adding excess neutralizing agent significantly affects the mechanical properties of these ionomers. Figure 2.12 shows how this variable influences the

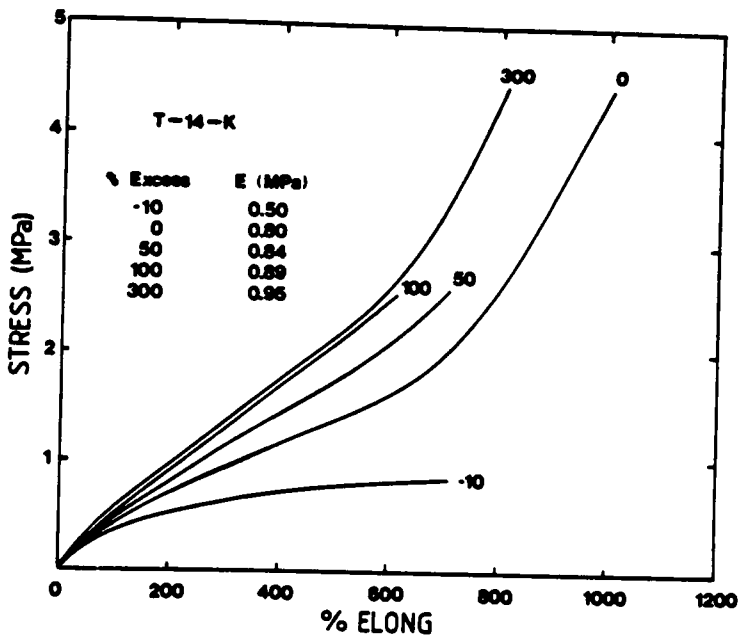

Figure 2.12. Stress-Strain Behavior of Sulfonated PIB Telechelic Ionomers: Effect of excess neutralizing agent. From Mohajer et al. (89).

stress-strain behavior of the T-14-K series. The T-14-K-(-10) material, which has been neutralized to only 90 % (-10 % excess neutralizing agent), displays poor mechanical properties where the stress does not reach 1 MPa and elongation being less than 800 %. Upon neutralization to stoichiometric amount, a significant change in properties results with stress values of almost 5 MPa and elongations up to 1000%. On the addition of excess neutralizing agent, both stress and modulus increase inspite of the fact that these materials, in solution, have been stream-stripped three times prior to the final precipitation, drying, and mechanical testing. This observed result discards an earlier popular assumption that washing removes excess neutralizing agent. The authors have proposed a model wherein the excess neutralizing agent is believed to be preferentially located at the ionic sites and they reinforce the ionic associations. A schematic representation of the model is illustrated in Figure 2.13. They have conclusively demonstrated the importance of excess neutralizing agent on the final properties in ionomers.

The effect of cations was studied on T-34 materials neutralized to the stoichiometric endpoint. It was found that the Zn neutralized materials performed nearly as well as the Ca neutralized materials. The observed result was surprising since Ca being highly ionic in character formed ionic bonds while Zn, a transition-metal formed bonds of a covalent character. The authors did not provide an explanation for the observed behavior.

So far, the discussions have emphasized the relevant literature related to the conventional as well as the telechelic ionomers. Another important class of ion containing polymers are block ionomers which will be discussed in the next section.

2.3.4.3 Block Ionomers

Block ionomers are a logical extension to the telechelic ionomers where ionic group at the chain ends is replaced by a block of fully ionized groups. These materials are quite similar to the classical block copolymers of the ABA or AB type, except that one of the blocks (such as block A) is fully ionized. This area of ionomers has received very little attention and very few publications have appeared in the available literature.

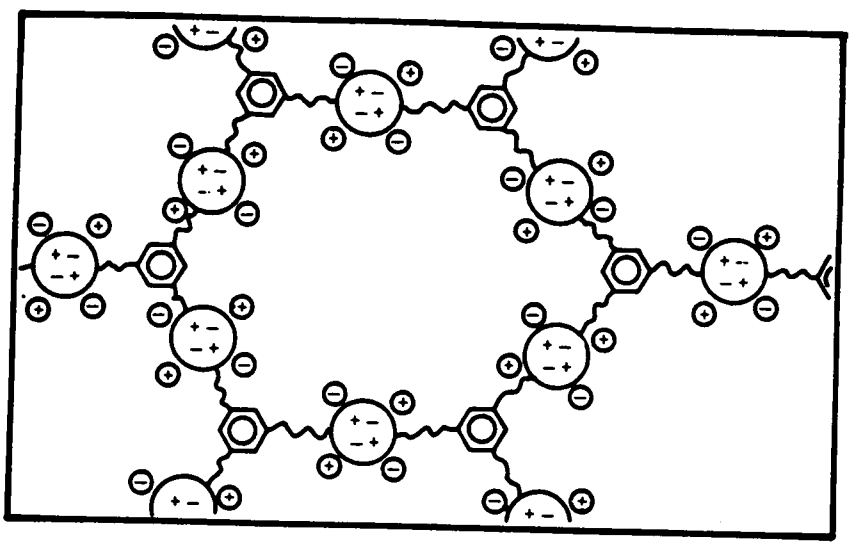

Figure 2.13. **Schematic Representation of Sulfonated PIB Telechelic Ionomer Structure:** The small circles represent the ions of the salt due to excess neutralizing agent. From Bagrodia et al. (89).

McGrath and coworkers (95-97) have pioneered the effort in this field introducing the concept of block ionomers. They have directed their attention toward synthesizing block copolymers where the ionomer block was prepared by the hydrolysis of poly (alkyl acrylates). But these systems have not been characterized in terms of their morphology.

Gauthier and Eisenberg (98) have reported the thermal and dynamic mechanical behavior of styrene-4-vinylpyridium ABA block ionomers. They observed only one T_g corresponding to the polystyrene phase from thermal analysis. The second T_g (ca. 200 °C) corresponding to the 4-vinylpyridium block was not accessible experimentally since the material dequaternized at a lower temperature (ca. 150 °C). The presence of water also tended to plasticize the T_g of the ionic blocks. This has been related to the method of preparation of these materials. There is another investigation which is presently being carried out on the same materials by Eisenberg et al. (99), the details of the which have not been reported in the literature.

2.3.4.4 Segmented Ionomers

An important class of ionomers where very little attention has been made are the "segmented" ionomers. The materials that mainly come under this category are the polyurethane ionomers and the ionene polymers. Of course, with the right type of chemistry the block ionomers can be extended to form a segmented system. A unique feature of these types of ionomers are that the ionic groups are located at well defined positions along the polymer backbone chain.

Polyurethane Ionomers

Over the last several years there has been a great deal of interest to study the structure property relationships in polyurethane (PU) elastomers. These materials are block copolymers of the $(A-B)_n$ type, consisting of alternating rigid segments and flexible chain extenders. Due to segmental incompatibility of the hard segments relative to the soft segments, the hard segments microphase separate to form domains which act as physical crosslinks. One method to enhance the degree of phase separation in these materials is by the introduction of ions in the hard segment units. Such materials are termed as polyurethane ionomers.

Traditionally polyurethanes have been widely used in coating applications. Due to environmental regulations there has been a drive toward the development of water-based materials. An interesting property of many polyurethane ionomers is their ability to emulsify or dissolve in water (100). Polyurethane ionomers due to its hydrophillic affinity has been widely considered as a potential candidate. The field of polyurethane ionomers is still in its infancy and only a small group of investigators have directed their effort in this field (2,101-105). Therefore, polyurethane ionomers are not only interesting from a scientific viewpoint but are also important commercially because of the potential of using them in solventless applications.

Cooper et al. (101,102) have studied the polyether-polyurethane zwitterionomers. It was found that increasing the sulfonation level tended to decrease the soft segment T_g due to improved phase separation. An enhancement of the rubbery plateau was also observed with increasing level of sulfonation from dynamic mechanical measurements. This is due to the hard segment cohesiveness being markedly enhanced by coulombic interactions among the ionic sites in the zwitterionomer.

Al-Salah et al. (2) have studied the influence of cations on the glass transition temperature and mechanical properties of polyurethane anionomers based on MDI hard segments. They observed a linear relationship exists between the glass transition temperature (T_g) and the ionic potential of the cation. This is in agreement with the observation of Matsuura and Eisenberg (53). The mechanical properties also improved with increasing ionic potential of the cation.

Ionene Polymers

In the early 1930's Marvel and co-workers (107) were the first to synthesize ionene polymers produced by the reaction of tertiary amines with difunctional electrophiles. But it was not until the late sixties with the work of Rembaum and coworkers (108-111) that ionenes found a renewed interest. Rembaum et al. (108) have defined ionenes as ***ionic amines in which cations based on quaternary amines form integral links in the polymeric backbone.*** The integral quaternary ammonium ions can be either on linear or cyclic (aliphatic or aromatic) species and they form an integral part of the polymer backbone. This definition of Rembaum et al. has been widely accepted and has been used to describe such materials. Ionene polymers have simple chemical structures and

typically consists of regular repeating units. A more attractive feature of studying ionenes is the ability to vary the number of chain segments between cationic sites which provides the opportunity to investigate systematically the effect of ion concentration on structure-property relationships in ion-containing polymers. The ionene polymers have been used in a wide range of applications. They are used as components in antimicrobials and antistats, in flocculants for water treatment, in photovoltiac cells and in biomedical applications (112).

The Menschutkin reaction between the dialkyl (or diallyl) halide and a ditertiary amine has been widely used in the synthesis of ionenes (108). The reaction scheme is given in Figure 2.14. Both symmetric and unsymmetric ionene structures have been synthesized. Furthermore, the distance between the cations can be changed almost at will so that one can tailor the hydrophilic and hydrophobic character of the ionene by altering the number of methylene groups (X or Y).

Due to the high ion content in the earlier prepared ionenes, they were essentially polyelectrolytes. In the dry state, these ionenes were often highly crystalline due to their high regularity in their methylene sequences. Hence, direct determination of the glass transition was very difficult. Also, because of the high ion content, these materials had a tendency to absorb moisture and therefore drying these materials completely without serious decomposition was often difficult. To overcome this problem, it was necessary to determine the T_g values of the ionene at several different concentrations of diluent and the true T_g is obtained by extrapolating to zero diluent concentration using the Gordon-Taylor copolymer equation:

$$T_g = w_1 T_{g1} + w_2 T_{g2} - \kappa w_1 w_2 \tag{2.2}$$

where w_i is the weight fraction of component i, T_{g_1} and T_{g_2} are the glass transition temperatures of the polymer and the diluent, and κ is a constant which is a function of the diluent.

It was found that diluent used had a significant effect on the T_g values of the ionenes (113). Figure 2.15 illustrates the effect on the T_g of 6,8 ionene by different diluents whose dielectric constant is plotted on the x-axis. The value of T_g is -4 °C with water while with glycerine it is -82 °C. Eisenberg et al. (113) have suggested this strange phenomenon may be due to a conformational change in the ionene backbone caused by a change in the dielectric constant of the diluent medium.

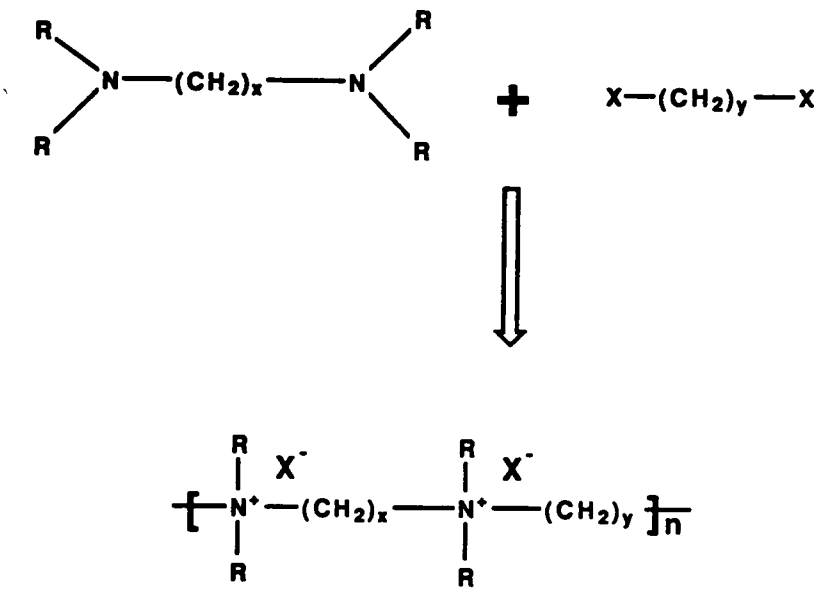

Figure 2.14. Schematic Representation of the Menschutkin Reaction

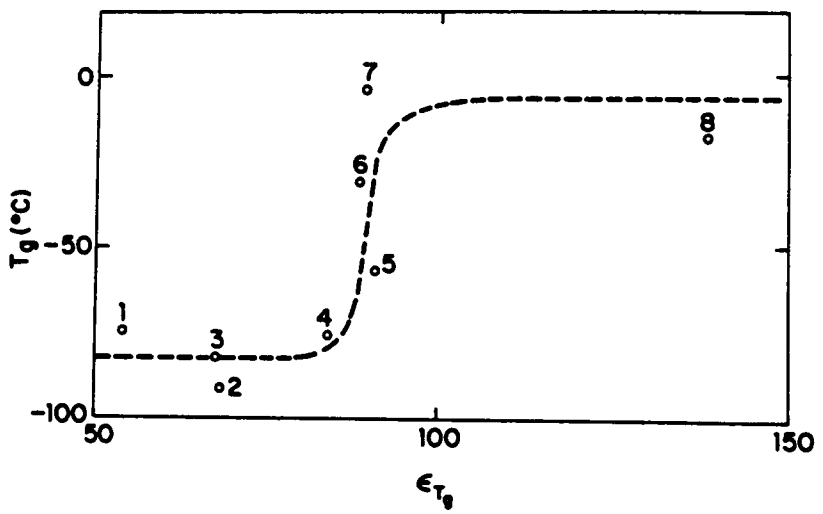

Figure 2.15. **Glass Transition of 6,8 Ionene versus the Dielectric Constant of Diluent:** (1) methanol; (2) ethylene glycol; (3) glycerine; (4) 4:1 glycerine-water; (5) 3:2 glycerine-water; (6) 2:3 glycerine-water; (7) water; and (8) formamide. From Eisenberg (113).

Tsutsui et al. (114) studied the dynamic mechanical properties of x, y - oxyethylene ionenes (x,y - OEI) using torsional braid analysis over a temperature range of -170 °C to 150 °C. The structure of x, y - OEI is shown below, x and y being varied from 2 to 5.

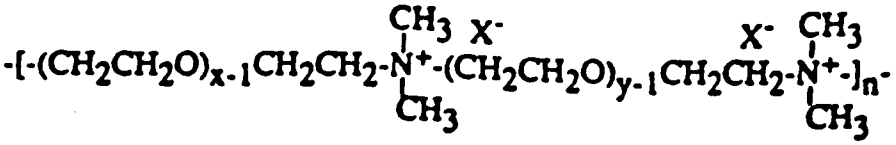

Two dispersions were observed for each polymer sample, except for 2, 2 - OEI. The temperature corresponding to the higher temperature dispersion T_α was identified with the T_g of the amorphous polymer and was found to be linearly dependent on the charge density along the ionene backbone. The lower temperature or β dispersion associated with a "local mode" dispersion showed no regular temperature dependence. It was also found that both relaxation regions were greatly affected by the presence of absorbed water.

2.3.4.5 Ionene Elastomers

Ionenes synthesized from low molecular weight dialkyl halides and ditertiary amines were generally brittle and often lacked mechanical strength. Knapick et al. (115) have observed that aliphatic ionenes behave as a polyelectrolyte when the quaternary N-alkyl groups is small and as a polysoap when the length of the N-alkyl increases. Polysoap behavior was indicated by a decrease in both the overall reduced viscosities and the steepness of the η_{red} curves. The charge density of the polyelectrolyte seems less important than the effect of length of the pendant alkyl group for the onset of polyelectrolyte-polysoap transition.

Elastometric ionenes have been prepared by the utilization of a flexible backbone such as polypropylene oxide (PPO) or polytetramethylene oxide (PTMO) as a chain extender. By careful control of the flexible chain length, ionenes with low ion content have been prepared (116-122).

Most of these materials can be classified as "ionomers" since the ion content is in the same range as conventional ionomers (less than 15 mol %).

Kohjiya et al. (120) have prepared elastomeric ionomers from the reaction of dimethylamino-terminated poly(tetramethylene) oxide (PTMO) and α, α'- dichloro-p-xylene using the Menshutkin reaction. The dimethylamino terminated PTMO was synthesized using the method of Smith and Hubin (123). The solution behavior of the poly (oxytetramethylene) ionene (PTI) ionenes is very interesting. These materials show an ordinary viscosity behavior in chloroform while behaving as a polyelectrolyte in methanol, i.e. reduced viscosity increases with decreasing concentration. According to the authors, this may be the first example that a polymer shows both electrolytic and non-electrolytic behavior depending on the solvent and without the addition of any salt. The PTI ionene displayed typical elastomeric behavior; low modulus, high ultimate tensile strength (27 MPa) and ultimate elongation (greater than 1000 %) for the ionene with PTMO molecular weight of 4400. Strain induced crystallization of the PTMO units in the backbone was observed at elongations over 500 %. However, the material exhibited poor recovery (in terms of reformation of the ionene linkages) on repeated cycling with instantaneous set values reaching up to 500 %.

Watanabe et al. (116-119) have studied elastomeric ionenes based on TCNQ (7,7,8,8 - tetracyanoquinodimethane) salts. Their hard segments were characterized by rigid polycation segments that contained 4,4'-bipyridium rings and the soft segments were based on flexible polypropyleneoxide (PPO). From the dynamic mechanical analysis they observed two distinct relaxation peaks which they have attributed to the T_g's of the respective hard and soft segments. Also the wide angle scattering measurements indicated that the ionene was amorphous. This clearly suggests that the ionene was microphase separated.

Klun et al. (112) studied a series of elastomeric ionene materials using the Menschutkin reaction of novel diamines and dihalides. A softening temperature of the ionenes ranged from 120 °C to 200 °C depending on the nature of the ionene segment. Many of the materials displayed typical elastomeric behavior viz. low modulus, high ultimate strength and elongation. They exhibited a phase separated morphology as studied by using thermal and dynamic mechanical analyses.

Yamashita et al. (124) investigated polybutadiene ionenes (PBI) based on the reaction of dimethyl-amino terminated polybutadiene and 1,4-dibromobutane. They have also compared the performance of PBI with a polybutadiene urethane (PBU). The solubility parameter of PBI was nearly the same as PBU but PBI attained about four times greater tensile strength at break than that of PBU at room temperature. The solubility parameters for PBI and PBU were obtained from swelling measurements in various solvents.

Lee (100) has investigated poly(tetrahyrofuran) based elastomeric ionenes. Two series of PTHF ionenes were prepared by the coupling reactions of "living" PTHF dioxonium ions with either 4,4'-bipyridine or 1,2-bis(4-pyridium)ethylene. These materials exhibited excellent mechanical properties with tensile strength over 30 MPa and elongation above 800 %. The 4,4'- bipyridine based ionenes exhibited superior thermal stability relative to the 1,2-bis(4-pyridium)ethylene based polymer. Also these materials exhibit reasonable thermal stability when compared to the ionenes based on benzyl dihalide prepared by Leir et al. (116).

Leir and Stark (116) studied the effects of dihalide structure on the polymerization rate of dimethylamino terminated poly(tetramethylene) oxide (PTMO), the reaction scheme is shown in Figure 2.16. They found that the reactivity of the dibenzyl halide can be enhanced by electron donating substituents on the benzene ring. However, the rate of polymerization and the ultimate polymer molecular weight increased drastically as the leaving group was varied from Cl to Br to I. All the ionene materials exhibited typical elastomeric behavior. From light scattering measurements of one of the ionenes it was observed that the overall molecular weight of these elastomers was quite high ($\overline{M}_w = 1.8 \times 10^6$). All the ionene materials displayed typical elastomeric behavior. Although these polymers show excellent mechanical (tensile strength ca. 30-40 MPa with elongations over 1000 %) and morphological properties at room temperature, their use as a thermoplastic elastomer is severely restricted due to an irreversible degradation mechanism occurring during thermal processing.

In one of the ionenes based on chloride as a counterion, the solution viscosity (inherent viscosity in chloroform) decreased considerably when the material was taken to elevated temperatures. This is an indication that the overall molecular weight of the ionene has drastically reduced.

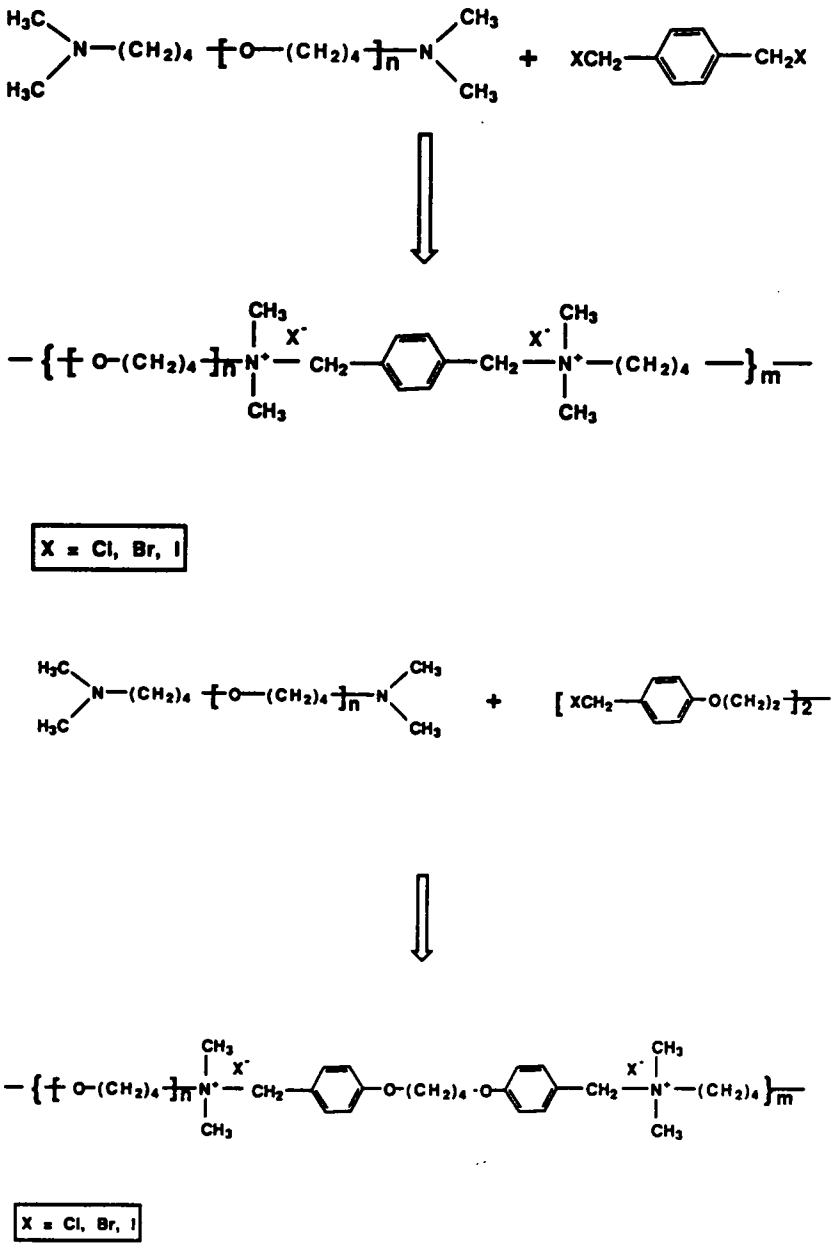

Figure 2.16. Schematic Representation of the Reaction used to Synthesize Ionene Polymers: From (116).

From standard organic chemistry it is well known that quaternary tetraalkylammonium salts at elevated temperatures decompose to yield an alkylhalide and a teriary amine. Based on this fact, Leir et al. (116) have suggested that the lowering of the solution viscosity in the ionene may be due to a depolymerization mechanism where the ionene polymer reverts back to the intial reactions. If this occurs then the melt viscosity of the ionene material is expected to be low thereby facilitating thermal processing of these materials by conventional techniques. On compression molding, however, this ideal scenario was not realized for reasons that have not yet been quantitatively provided.

Ionene polymers based in viologen chemistry have also been investigated. Paleos et al. (125) have studied ionene polymers bearing viologen groups which are separated by methylene sequences of varying length. Based on the data obtained from x-ray diffraction studies, electron microscopy and thermal analysis (mainly DSC), the authors have proposed a lamellar structure consisting of alternate polar layers, formed through the electrostatic interaction of quaternary nitrogens with bromides, and of the lipophilic layers of the methylene spacers.

2.3.5 Melt Rheology of Ionomers

Incorporation of small amounts of ionic groups in the polymeric backbone not only affects the mechanical and thermal properties but also the flow properties in the melt. It has generally been observed that dramatic increases in melt viscosities are displayed upon the introduction of ions into polymers. The extent of increase seems to depend primarily on ionic content or degree of neutralization, and to a lesser extent, on the nature of the counterion (5). Also, the zero shear viscosity increases with ion content in sulfonated polystyrene system (63). There have been fewer studies conducted on the melt rheological behavior of ionomers.

Shohamy and Eisenberg (126) have investigated the dynamic melt rheological properties of styrene-methacrylic acid polymers, their sodium salts and their methyl ester derivatives. In the range of conditions studied, the time-temperature superposition of the dynamic moduli was applicable for all materials up to 7.7 mol % ion content. Furthermore, it was also possible to superpose the master curves of the ester, acid and salt of a given ion content by selecting appropriate reference temperatures. This superposition suggests that the chain dynamics in all the three systems are

similar in the range studied. The temperature differences ΔT to which the shifts correspond were directly related to hydrogen bonding and ionic bonding in the acid and salt, respectively, relative to the ester. It was also found that the plot of ΔT as a function of ion concentration for the ester-salt pairs gave a sigmoidal curve in contrast to the linear relation observed for ester-acid ΔT's. There was an upswing near ca. 5 mol % ion content which is related to the onset of cluster formation which is in close agreement with that observed in stress-relaxation experiments (52).

Sakamoto, MacKnight and Porter (127) investigated the melt rheology of ethylene methacrylic acid ionomers (4.1% acid, ionized to 56-59%) for two different counterions, sodium and calcium. It was found that time-temperature superposition was applicable to the unionized copolymer but not to its corresponding salt. The relaxation spectra obtained from the dynamic shear moduli exhibited a rubbery plateau region and a flow region for the two ionized polymers, while the unionized material exhibited only the flow region. This result indicates the existence of structure in the molten copolymer above the crystalline melting point, which is associated with the ions. Evidently, the ions are able to move from one domain to another (ion-hopping) during flow. This hopping motion becomes easier with increasing temperature and more difficult with increasing frequency, or shorter time scale. At higher frequencies the characteristic relaxation time of this hopping motion is larger than the time scale of the experiment and therefore cannot be detected. The values of steady shear viscosity versus shear rate for the unionized copolymer were remarkably small compared to those of the two salts. The zero shear viscosity of the Ca salt was found to be significantly higher than that for the Na salt. This result is not very surprising because Ca being divalent forms a tighter network.

Earnest and MacKnight (128) studied the dynamic melt rheology of ethylene-methacrylic acid copolymer (3.5 mol %), its methyl ester derivative, and a 70% neutralized sodium salt. In the temperature (120 °C to 180 °C) and frequency range (over five decades) studied, it was found that shifting the loss modulus G'' of the salts using the same shift factors as that obtained from G' resulted in a failure of time-temperature superposition principle for G''. It is known that for thermorheologically simple materials both G' and G'' satisfy the superposition principle in the same

way (129). Based on this concept, Earnest and MacKnight concluded that the results obtained were an indication of the thermorheological complexity of the ionomers studied.

Broze et al. (70,76,81) studied the melt rheology of polybutadiene (PBD) telechelic ionomer with carboxylic acid end groups. These PBD ionomers neutralized with various ions all exhibited thermorheological simplicity. However, in their study of polyisoprene (PIP) based telechelic ionomers in which the molecular weight of PIP was varied, the time-temperature superposition was applicable only when the number-average molecular weight, $\overline{M}_n$, was greater than 2×10^4. Thermorheological complexity sets in below this critical molecular weight. It has been proposed that above $\overline{M}_n = 2 \times 10^4$, the relaxations of the polymeric backbone dominate the rheological behavior where the ionic interactions essentially act like homogeneously distributed thermoreversible crosslinks which are responsible for greatly extending the rubbery plateau. With decreasing molecular weight (equivalent to increasing the ion content) phase separation sets in to form the ionic clusters. This gives rise to a secondary relaxation mechanism which is responsible for the thermorheological complexity.

Bagrodia et al. (130) investigated the viscoelastic behavior of sulfonated polyisobutylene telechelic ionomers in the melt flow region. Figure 2.17 shows the dynamic melt viscosity measured at 180 °C for a series of three-arm star trifunctional materials of varying molecular weight. The materials were neutralized with KOH, either to the stoichiometric amount or to twice that amount as indicated in the caption. Any excess neutralization agent present in the system were not stripped after the neutralization process. The sample designation used requires some explanation. Using the designation used by the authors, sample T-8.3-K-0 refers to a triarm trifunctional polymer (T) with a molecular weight of 8300, K refers to the cation (in this case potassium), and the "0" represents the percentage of excess neutralizing agent used. The unmodified telechelic polyisobutylene (PIB) was a viscous at room temperature but the neutralized sulfonate ionomer exhibited properties typical of a crosslinked network. It was observed that for endpoint neutralized materials the melt viscosity η^* at low shear increases as $\overline{M}_n$ increases from 8300 to 34000. Apparently at 180 °C the ionic interactions are sufficiently weakened and molecular entanglements dominate. However, on addition of 100% excess neutralizing agent, the ionic interactions are greatly

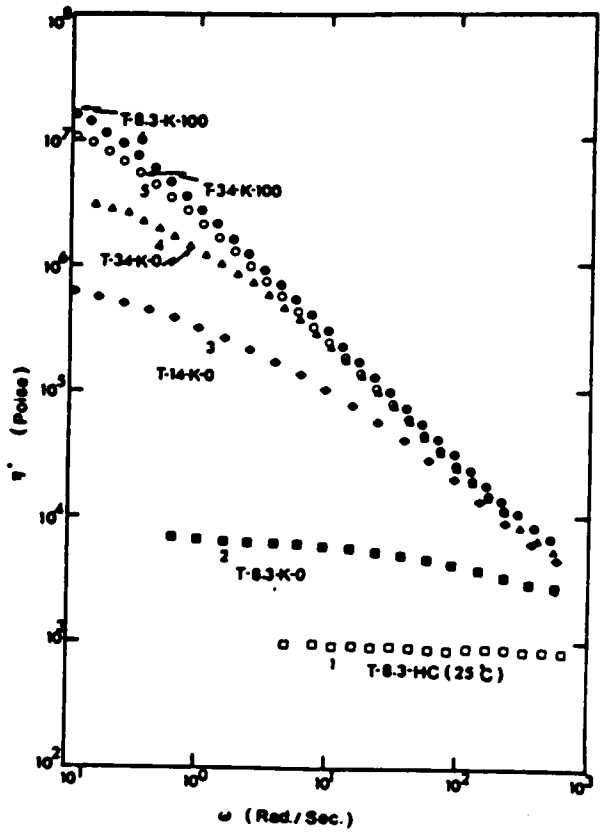

Figure 2.17. Dynamic Melt Viscosity versus ω for Sulfonated PIB Telechelic Ionomers: From Bagrodia et al. (130).

strengthened and a dramatic increase in η^* is observed at all frequencies. In fact, the value of η^* is higher for 8300 $\overline{M}_n$ material than for the 34,000 $\overline{M}_n$ material (the reverse was true for materials neutralized to stoichiometric amounts), indicating that ionic interactions have again become the dominant factor.

Bagrodia et al. (131) have studied the effect of molecular architecture of polyisobutylene telechelic ionomers. They found that the linear monofunctional sulfonated telechelic ionomer of 11,000 $\overline{M}_n$ was nearly independent of shear rate at 180 °C. On the other hand, the linear difunctional and the three-arm trifunctional materials displayed a shear thinning behavior with the trifunctional species showing a more pronounced reduction in viscosity with shear rate. This is not surprising since the monofunctional species is below the critical molecular weight for entanglements and also cannot form a network. The difunctional and trifunctional species can form a network through ionic interactions, but the network for the trifunctional species being the most extensive.

A comparison of the physical properties of polystyrene containing equal amounts of either carboxylate or sulfonate salts in a random ionomer has been carried out by Lundberg and Makowski (94). The softening behavior of the original polystyrene and polymers containing 5 mole % sodium carboxylate or sodium sulfonate salt groups is shown in Figure 2.18. There are two features which are evident from the TMA curves. The softening temperature of the sulfonate ionomer is higher than the carboxylate counterpart while the carboxylate ionomer exhibits a higher softening temperature than unionized polystyrene ionomer. Secondly, the T_g of the backbone shows similar trends. They also observed from the melt viscosity measurements that the melt viscosity of the sulfonated material was several orders of magnitude higher than the corresponding carboxylated material at the test temperature of 220 °C. Clearly, this suggests that the ions in the sulfonated materials are more strongly associated than in the corresponding carboxylated material. This is not surprising since the acid groups of the sulfonate ionomers are much stronger than the carboxylate counterpart, viz. carboxylic acid. The sulfonic acid groups, therefore, provide a much stronger interaction and therefore forms a much more stable network.

Due to the very strong interactions that occur in sulfonated ionomers, thermal processing of the neat ionomer often presents a potential problem. For example, the melt viscosity of the

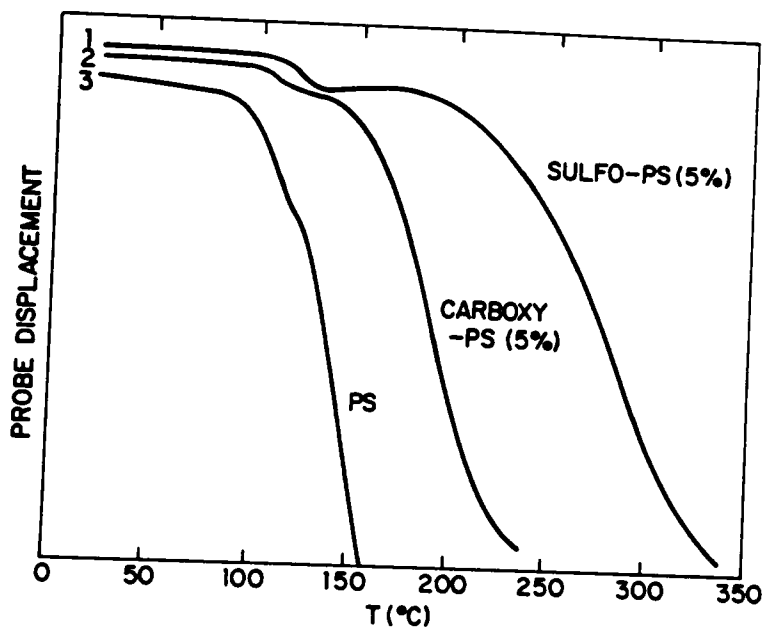

Figure 2.18. TMA Softening Behavior for PS, C-PS and S-PS: (load 10g; heating rate: 10 °C/min). From Lundberg et al. (63).

sulfonated polystyrene ionomer materials is very high, over 10^8 poise (10^7 Pa.s) at 220 °C. Often plasticizers are incorporated to facilitate processing of these materials. The effect of plasticizers on the ionic interactions in ionomers will be discussed in the following section.

2.3.5.1 Plasticization Behavior

Conventionally, the role of a plasticizer is to increase the free volume available to the polymer segments, lowering both the T_g and the melt viscosity of the polymer. Some of the desired features of a plasticizer are (132);

- compatibility with the base polymer,
- non-volatile or of low vapor pressure at the processing temperatures, and
- should not adversely affect the mechanical and/or chemical properties of the base resin.

There are essentially two types of plasticizers; those which uniformly increase the free volume of the backbone ("backbone plasticizers") and those which act ideally by diminishing the interchain association of the ionic groups on the polymer chain ("ionic plasticizer"). The latter class of plasticizers have been more effective in lowering the melt viscosity of ionomers than the former class. Lundberg et al. (133) have demonstrated that it is possible to selectively plasticize either the ion-rich phase or the nonpolar hydrocarbon phase of SPS ionomers Specifically, dioctyl pthalate (DOP) performed effectively as a backbone plasticizer, while glycerol - a polar additive, selectively plasticized the ionic groups. Figure 2.19 illustrates the differences in the resulting melt viscosity using the two types of plasticizers. For example, the addition of only 3.5 wt % glycerol was required to reduce the melt viscosity from 3.2 x 10^8 poise to 4 x 10^5 poise whereas 40 wt % of DOP was required to achieve the same effect. This difference is attributed to the differences in the plasticization mechanisms of the two plasticizers; glycerol preferentially solvates (or shields) the ionic interactions of the metal sulfonate groups in the ionic domains while DOP plasticizes the polymer backbone by lowering T_g (133). Though glycerol dramatically reduces the melt viscosity of the ionomer, it had very little influence on T_g. On the other hand, DOP reduces the melt viscosity by lowering T_g of the backbone material. This type of behavior is typical of a conventional plasticizer. Lundberg et al. (133) have demonstrated that by a judicious combination of both

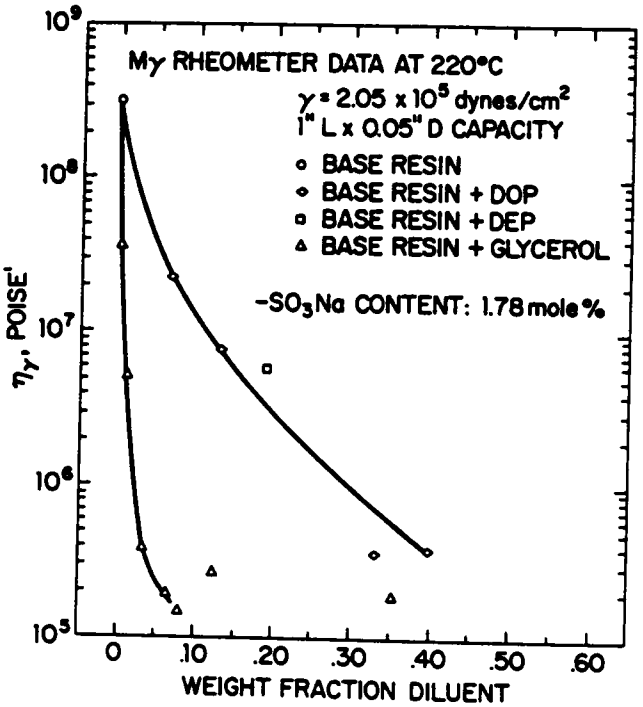

Figure 2.19. Melt Viscosity of 1.78 mol % Na-SPS versus Weight Fraction of Diluent: From Lundberg et al. (94).

plasticization approaches to sulfonated polystyrene, it is possible to prepare a flexible polymer similar to plasticized poly (vinyl chloride).

The principles of selective plasticization have also been applied by Makowski and Lundberg (132) to a number of sulfonated EPDM (S-EPDM) systems using stearic acid and its metal derivates. Addition of stearic acid resulted in significant reduction in the melt viscosity of these systems. However, the tensile properties were adversely affected at 70 °C (while an improvement was observed at 25 °C) alongwith an increase in water uptake. In contrast, incorporation of 30-90 meq/100 polymer of zinc stearate showed remarkable improvements in tensile properties at both 25 °C and 70 °C accompanied with a drastic reduction in melt viscosity. The improvement in mechanical properties are primarily due to microphase separation of zinc stearate into small crystallites (less than 5000 Å in size) which functions as a reinforcing filler. Also, materials incorporated with zinc stearate showed a reduction in water absorption (134).

Agarwal et al. (68) have proposed that zinc stearate above its melting point (120 °C) solvates or "dissolves" the ionic interactions permitting the flow of polymer segments at high temperatures. With the ionic interactions shielded, a structure very similar to amorphous high molecular weight polymers results where the polymer chain segments are free to undergo coordinated deformations at elevated temperatures. Another explanation that has been given is that the ionic plasticizers improve flow by promoting ionic bond interchange during deformation. The authors, however, are unable to distinguish between the two proposed mechanisms.

Recently, in a parallel study, Weiss et al. (135) have examined sodium-neutralized sulfonated polystyrene ionomers using dynamic mechanical analysis. They reported that DOP lowered the T_g of the backbone polymer and shifted the entire modulus versus temperature curve to lower temperatures, typical of a conventional plasticizer. However, no significant differences in the general modulus curves were observed. But glycerol substantially decreases the softening temperature while having little or no effect on the T_g of the backbone. The rubbery plateau and the high temperature loss peak also disappeared. These results clearly support the preferential plasticization of the two phases of an ionomer by polar and nonpolar diluents as earlier suggested by Lundberg et al (133).

In another study, Weiss and coworkers (136) utilized real time small-angle and wide-angle x-ray scattering to study the temperature-dependent microstructure of zinc stearate plasticized sufonated EPDM. Near 100 °C, they observed the development of a peak around 45 Å which disappears above 120 °C. They assigned this scattering peak to the formation of ionic clusters at elevated temperatures. This is an erroneous interpretation because the diffraction peak of crystalline zinc stearate in the small angle region occurs ca. 45 Å. However, it is surprising as to why they do not observe the zinc stearate diffraction peak at lower temperatures even with a zinc stearate loading level of 30 phr.

In summary, metal sulfonated ionomers can now be processed by conventional thermal processing techniques. This opens a wide range of potential applications for the sulfonated ionomers. Not only does an ionic plasticizer such as zinc stearate lower the melt viscosity but some of the physical properties are also enhanced from an application point of view.

2.4 Summary

It has been shown that the well defined architecture of the telechelic, block and segmented ionomers provide a unique route to understanding the effect of ion incorporation in polymers. The ionomers produced by any of these three routes have a well defined architecture and they ideally lend themselves to a detailed study in terms of the morphological arrangement of the ions in the system. In addition, very few investigations had directed their effort in studying the structure-property behavior of such well defined systems. A comparison of the performance of the ionomers from each of the three routes can now be investigated systematically.

3.0 SMALL ANGLE X-RAY SCATTERING REVIEW

The main focus of the present investigation is to study the microphase separation of elastomeric ion containing polymers. As this study entails extensive morphological investigation utilizing small angle x-ray scattering (SAXS), a comprehensive overview of the appropriate scattering fundamentals will be presented. There have been many excellent books (137-142) and review articles (143-148) that have appeared in literature which provide extensive background material on the subject.

3.1 Introduction

X-rays are electromagnetic radiation of exactly the same nature as light but of very much shorter wavelength. The commonly used x-rays that are utilized in diffraction studies have wavelengths lying in the range between 0.5 to 2.5 Å. For comparison, the wavelength of visible light is in the range between 4000 to 7000 Å. X-rays, therefore, occupy the region between gamma and ultraviolet rays in the complete electromagnetic spectrum (137).

The principal rheo-optical techniques that are used to characterize polymers are wide angle x-ray scattering (WAXS) and small angle x-ray scattering (SAXS). Wide angle x-ray scattering provides information regarding structural features whose dimensions are of the order of a few angstroms. It is widely used to study semi-crystalline polymers. Some typical structural features obtained are the lattice spacings in the crystalline region, degree of crystallinity, the size and "perfection" of crystals, as well as information regarding the orientation behavior of both crystalline and amorphous regions (more limited). These structural features have dimensions that are comparable with the wavelength of the x-rays (typically 1 to 20 about Å). The visible light on the other hand provides information regarding structural features that are of the order of its wavelength which are typically in the micron range (e.g., spherulites, molecular packing, or anisotropy differences over

large regions etc.). However, there are structural features of importance whose dimensions are intermediate between these two ranges, in the range of 20-1000 Å (e.g., lamellar structures or crystal domains, microvoids, local density fluctuations, etc.). Due to the high absorption characteristics of materials at several of the wavelengths comparable to its structural dimensions, it is not feasible to study these structures in a convenient angular region. To overcome this problem one is often forced to investigate these structures using x-rays of smaller wavelengths as dictated by the reciprocal nature of Fourier Transform theory, i.e., large structures scatter at small angles (149).

3.2 Interaction of X-Rays with Matter

As the x-rays passes through matter they interact with the atoms such that the dual particle wave nature of electromagnetic radiation is brought out. When the x-rays impinge on the electrons in an atom, these electrons become secondary emitters of x-rays and therefore the atoms act as "scatterers" of the incident x-rays. Since the information contained in the scattered radiation is of primary interest in the scattering experiments, the incident beam is often blocked using a beamstop.

There are essentially two types of scattering that take place - coherent or unmodified, and incoherent, or modified. The coherent scattering is better known as Thomson's effect or elastic scattering and the incoherent scattering is also known as Compton's effect or inelastic scattering. Fortunately, a major part of the energy emitted from these scatterers is due to elastic scattering (Thomson's effect). This scattered radiation can then be utilized for structural studies because it occurs without change of wavelength, and more importantly without loss of phase relationship between the incident and the scattered x-rays (139). In incoherent scattering (Compton's effect), a lack of phase relationship exists which contributes to the diffuse background that is often seen in an x-ray pattern (150).

When x-rays encounter any form of matter, they are partly transmitted and partly absorbed. The fractional decrease in the intensity of an x-ray beam as it passes through matter is proportional to the thickness of the medium, and is given by (137,139):

$$\frac{dI}{I} = -\mu dt \tag{3.1}$$

where I is the intensity, t being the thickness of the medium, and μ is the linear absorption coefficient and is dependent on the composition of the absorbing medium, its density, and the wavelength of the x-ray beam. Integration of the above expression results in,

$$I_x = I_0 e^{-\mu t} \tag{3.2}$$

where I_x = transmitted intensity and I_0 = the intensity of the incident x-ray beam.

Linear absorption coefficients of various elements have been tabulated for most commonly used x-ray wavelengths. For compounds, the linear absorption coefficient can be calculated from the mass absorption coefficient of the individual elements based on a weight average basis and is given by (139);

$$(\frac{\mu}{\rho})_{compound} = \sum_i w_i (\frac{\mu}{\rho})_i \tag{3.3}$$

where w_i = weight fraction of the i^{th} element and the ratio $(\frac{\mu}{\rho})_i$ is the mass absorption coefficient of the individual elements.

The intensity of the scattered radiation is dependent on the total number of electrons that interact with the primary incident beam. If thin sections are used the scattered intensity is low and long exposure times are required to obtain reliable data. However, with thicker sections, the scattered radiation from the initially encountered volume of electrons is absorbed by the remaining thickness of the sample, and again, the transmitted intensity is low. An optimum thickness therefore exists where the transmitted intensity is maximized and is given by (139);

$$t_{opt} = \frac{1}{\mu} \tag{3.4}$$

For metals and other elements with high atomic number (higher electron density) the optimal thickness is about 0.1 millimeters (mm) but for polymeric materials which primarily comprise of light elements (carbon, hydrogen, nitrogen and oxygen) the optimal thickness is around 0.5 to 3.0 mm (137).

3.3 Small Angle X-ray Scattering

As mentioned earlier, the technique of small angle x-ray scattering (SAXS) is used to study the structural features which are of the order of 20 to 1000 Å in size. It will be shown shortly that the amplitude of the scattered radiation is nothing but the three dimensional Fourier transform of the electron density distribution in the material. The morphological features of the material are revealed in terms of the magnitude and periodicity of the electron density distribution which are obtained from the analysis of the SAXS profile.

Small angle x-ray scattering is applicable to both dilute and dense systems. Analysis of the scattering profile in the dilute system provides information regarding the size, shape, and volume as well as the size distribution of the particles. For a dense system, however, the information regarding the various morphological features are contained in different parts of the scattering curve. For example, the interdomain spacing, if periodic, can be obtained from the angular position of the primary maxima in the scattering profile. The overall intensity is related to the degree of phase separation while the breadth of the scattering peaks is related to the size distribution of the inhomogeneities in the scattering medium. Finally, the tail region ($s > 0.3$ or $\theta > 0.23°$) generally provides information regarding the thickness as well as surface area of the transition zone between the system inhomogeneities. It should be kept in mind that the SAXS technique does not provide direct structural and morphological features of the material but rather the information is obtained indirectly by mathematical manipulation of the scattering profile.

The intensity profile which is observed in small angle x-ray scattering is a result of the interference phenomena that exists between the various scattered waves generated by the individual electrons present in the scattering volume. The scattered intensity at a given angle of observation

is obtained by taking the square of the amplitude of the composite wave obtained from the group of electrons at that point. This composite scattering amplitude is given by (140,141);

$$A(\vec{s}) = A_e \sum_{n=1}^{N} e^{-2\pi i (\vec{s} \cdot \vec{x}_i)} \tag{3.5}$$

where A_e is the maximum amplitude of the electric field scattered by the electrons at the origin, N is the total number of electrons, $\vec{x}_i$ is the vector from an arbitrary origin to the i^{th} element and $\vec{s}$ is the scattering vector which is equal to the difference between the unit vector along the incident direction and that of the scattered direction. The scattering vector is given by;

$$\vec{s} = \frac{2}{\lambda} \sin\theta \tag{3.6}$$

where the Bragg angle θ is the one half the angle between the scattering and the incident vectors, and λ being the wavelength of the scattered radiation. In equation 3.5, if N is large, the discrete vectors $\vec{x}_i$ that describe the positions of the scattering electrons can be replaced by a continuous distribution function $\rho(\vec{x})$. Then the integral form of the composite amplitude over the scattering volume is given by (151):

$$A(\vec{s}) = A_e \int_V \rho(\vec{x})\, e^{-2\pi i (\vec{s} \cdot \vec{x})}\, d\vec{x} \tag{3.7}$$

The above expression represents the three-dimensional Fourier transform of the electron density distribution function averaged over the whole scattering volume. The scattered intensity is obtained from the product of the scattering amplitude with its complex conjugate. For a system, with a center of symmetry in the electron distribution function, the scattering intensity is given by (151):

$$I(\vec{s}) = AA^* = I_e\left[\int_V \rho(\vec{x})\, e^{-2\pi i(\vec{s}\cdot\vec{x})}\, d\vec{x}\right]^2 \tag{3.8}$$

where V is the volume being irradiated by the x-rays and I_e is the Thomson's scattering constant for an electron. There are two significant features contained in the above equation. Firstly, the scattered intensity is directly proportional to the square of the electron density distribution function, $\rho(\vec{x})$. As a result, the scattered intensity is strongly dependent on both the number of electrons as well as their spatial distribution. Secondly, the scattered intensity is directly related to the scattering vector, "s", whose magnitude is inversely related to the wavelength, λ, and thus has reciprocal dimensions. The scattering profile is, therefore, just a representation of the real space structure projected in reciprocal or Fourier space. Although the Fourier transform is a completely invertible procedure, the electron density distribution function cannot be directly obatined from equation 3.8. This is due to the fact that squaring causes certain information regarding the electron density distribution function to be lost. This suggests that the intensity profile can, in principle, be calculated for any microstructure but the reverse procedure is not always possible. The morphological features contained in the electron density distribution function is obtained from the manipulation of scattering profiles utilizing mathematical analyses based on theoretical models. These methods will be discussed shortly.

Prior to discussing the various models, some background information regarding the treatment of the experimentally obtained scattering profile will be provided in the following section.

3.3.1 Treatment of Experimental Data

The scattering profile obtained from actual experimental measurements is quite often not identical to that expected from theoretical considerations (equation 3.8). There are a number of extraneous factors that affect the actual scattering profile of the system. Most often, the experimentally obtained scattering profile includes contributions from (152);

- polychromatic radiation

- parasitic scattering
- smeared intensity for slit collimation
- onset of wide angle scattering
- background or thermal scattering
- intradomain mixing

Therefore, a careful evaluation of the different contributions is necessary prior to manipulation of the data in order to obtain the structural parameters.

In the development of the different expressions for SAXS analysis, it will be assumed that the incident x-ray source is monochromatic. In practice, however, the radiation produced from a x-ray generator have a wide variety of wavelengths. The resulting intensity distribution often contain two peaks which are referred to as the K_α and K_β peaks (137,139). Due to K_α peak having higher intensity than the K_β peak, it is often desirable to use only the K_α radiation to conduct the scattering experiments. Differentiation between the peaks can achieved by using appropriate filters which selectively permit only certain wavelengths to pass through depending on the absorption edge of the filter material. For example, nickel filters are often be used to selectively obtain K_α radiation for the Cu target. To specifically obtain K_α radiation from a given metal target, a good rule of thumb is to choose the element which is positioned immediately to the right of the element under consideration in the periodic table since its absorption edge would generally fall between the K_α and K_β peaks of the selected target. However, not all of the low intensity polychromatic or "white" radiation in the vicinity of the K_α peak is removed by this method. In order to refine this procedure, metal filters have been used with a pulse height discriminator in conjunction with a proportional counter. A proportional counter essentially produces a pulse with the voltage height being proportional to the energy of the incident x-ray photon. Since the energy of the radiation is now related to its frequency, the pulse height discriminator allows only those pulses to pass through which have an energy level which satisfy a preset window for the desired energy levels (137).

A better alternative to monochromatization is to place a crystal or graphite monochromator in the path of the incident beam which enables the desired wavelength to be obtained by diffraction at a particular angle. This diffraction angle can be estimated using the Bragg's equation (equation

3.62). A radiation source which is entirely monochromatic in nature is obtained by setting up the scattering apparatus along the path of diffraction at an angle corresponding to the K_α radiation that is produced by the given target.

The scattering theory presented in the following sections applies to those systems which have a pinhole collimation (i.e. point source). It is often advantageous to use a slit collimation system over the pinhole collimation system because it provides higher intensity and therefore higher resolving power, and lower parasitic scattering but has the inherent disadvantage of "smearing" the resulting scattering profile. This results from the fact that more than one scattering angle is registered at any given point along the scattering profile. Mathematical manipulation of smeared intensities from slit collimation data provide desmeared intensities which are equivalent to scattered intensities obtained from pin-hole collimation (153).

In small angle x-ray scattering, the relation between slit smeared intensity, $\tilde{I}(s)$, and that expected from a pin hole collimation, I(s), is given by (153,154):

$$\tilde{I}(s) = 2\int_0^\infty W_l(u)\, I_{obs}(s^2 + u^2)\, du \tag{3.9}$$

where $W_l(u)$ is the slit length weighting function and u is an arbitrary variable of integration. In order to minimize the error due to slit collimation, infinite slit approximations (such as in a Kratky camera) are often used where the slit height is much smaller than the slit length. There are numerous methods available for desmearing the experimental scattering curves some of which are iterative methods (155,156), matrix inversion methods (157) or methods that require differentiation of the smoothed experimental curve followed by numerical integration (158-161). The desmearing procedure can be readily accomplished by means of computer analysis (162). If a scattering peak were to be present, the desmearing procedure generally moves the position of the scattering peak to higher scattering vectors (i.e. higher angles).

A large number of errors can be introduced into the desmearing procedure during the numerical analysis. The origin of these errors are primarily due to a magnification of the statistical errors and/or due to truncation errors introduced in the numerical evaluation. These errors are largest in

the Porod-law region where the scattered intensity is generally low and statistical variations high. To overcome this problem, it has been suggested that the relations developed for the unsmeared pin-hole collimated data be modified so that the smeared intensities from the slit collimated systems can be directly used. Of course, the desmearing procedure will still be required for evaluation of parameters such as Bragg spacing which is related to the interdomain spacing in the system.

In the development of different relations for the SAXS analysis it will assumed that the scattered intensity is obtained from a pin-hole collimated system. However, relevant expressions for the evaluation of certain morphological parameters for the slit-collimated system will be provided when needed.

The edges of the collimating slits also cause scattering of x-rays over the whole angular range even when the sample is not present. This parasitic scattering which is a characteristic feature of the instrument, can be routinely determined and subtracted from the experimentally determined scattering profile.

3.3.2 Correlation Function

The correlation function contains most of the information relating to the morphological features which can be obtained from SAXS analysis. It can be obtained through the manipulation of the electron density distribution function, $\rho(\vec{x})$, which was introduced earlier. For many systems, it is often difficult to uniquely determine the electron density distribution function from the scattered intensity profile. However, it is possible to evaluate the periodicity or the extent of inhomogeneity of $\rho(\vec{x})$ following the development of Debye and Bueche. They showed that $\rho(\vec{x})$ can be represented as (141,163):

$$\rho(\vec{x}) = \rho_0 + \Delta\rho(\vec{x}) \tag{3.10}$$

where ρ_0 is the average electron density of the medium and $\Delta\rho(\vec{x})$ accounts for the fluctuations in the electron density within the scattering volume. It should be noted that $\vec{x}$ is a 3-dimensional

vector in real space. Substituting equation 3.10 into the expression for scattering intensity, $I(\vec{s})$ as given in equation 3.8, results in (141):

$$I(\vec{s}) = AA^* = I_e \int_V \int_V [\rho_0 + \Delta\rho(\vec{x}_k)][\rho_0 + \Delta\rho(\vec{x}_j)]\, e^{[-2\pi\vec{s}\cdot(\vec{x}_j - \vec{x}_k)]} d\vec{x}_k d\vec{x}_j \qquad (3.11)$$

The above integration can be divided into a sum of four double integrals I_1, I_2, I_3, and I_4 over the irradiated volume, containing the terms ρ_0^2, $\rho_0\Delta\rho(\vec{x}_k)$, $\rho_0\Delta\rho(\vec{x}_j)$, and $\Delta\rho(\vec{x}_k)\Delta\rho(\vec{x}_j)$, respectively. Let us consider each term individually.

The first term being:

$$I_1 = I_e(s)\, \rho_0^2 \int_V \int_V e^{-2\pi i \vec{s}\cdot(\vec{x}_k - \vec{x}_j)}\, d\vec{x}_k\, d\vec{x}_j \qquad (3.12)$$

This can be interpreted as representing the scattered intensity of a "particle" of volume V with a uniform electron density, ρ_0 . It has been shown that the corresponding intensity, $I_1(s)$, is effectively zero for all observable angles (141).

The second and the third terms are complex conjugates and their sum is given by (141):

$$I_2 + I_3 = 2\, I_e(s)\, Re\left[\int_V \Delta\rho(\vec{x}_k)\, e^{-2\pi i(\vec{s}\cdot\vec{x}_k)}\, d\vec{x}_k \int_V \rho_0\, e^{2\pi i(\vec{s}\cdot\vec{x}_j)}\, d\vec{x}_j\right] \qquad (3.13)$$

The second integral is the complex conjugate of the expression for the amplitude of a particle with density, ρ_0 and volume V (compare with equation 3.7). This expression is essentially zero for all observable angles as was shown in evaluating I_1. The first integral in equation 3.13 will be of the same order of magnitude as the fourth integral, I_4. But, the sum of the second and third integrals

as determined by the product of the two integrals in equation 3.13 will be negligible in comparison to the fourth integral, I_4, of equation 3.11. It has been shown that I_1, I_2, and I_3 are all negligible in comparison to I_4. Hence, it is only necessary to evaluate the fourth term containing $[\Delta\rho(\vec{x}_k)][\Delta\rho(\vec{x}_j)]$ in order to evaluate $I(\vec{s})$ in equation 3.11.

$$I(\vec{s}) = I_4(\vec{s}) = I_e(s) \int_V \int_V \Delta\rho(\vec{x}_k)\, \Delta\rho(\vec{x}_j) e^{-2\pi i \vec{s} \cdot (\vec{x}_k - \vec{x}_j)}\, d\vec{x}_k\, d\vec{x}_j \tag{3.14}$$

Defining a position vector,

$$\vec{r} = \vec{x}_j - \vec{x}_k \tag{3.15}$$

and substituting for $\vec{x}_j$ from equation 3.15 in equation 3.14, results in:

$$I(\vec{s}) = I_e(s) \int_V \int_V \Delta\rho(\vec{x}_k)\, \Delta\rho(\vec{x}_k + \vec{r}) e^{2\pi i (\vec{s} \cdot \vec{r})} d\vec{x}_k\, d\vec{r} \tag{3.16}$$

The above equation consists of two parts. The first part of the integral being,

$$\int_V \Delta\rho(\vec{x}_k)\Delta\rho(\vec{x}_k + \vec{r})\, d\vec{x}_k \tag{3.17}$$

Evaluating the above equation at $|\vec{r}| = 0$, gives :

$$\int_V \Delta\rho(\vec{x}_k)\, \Delta\rho(\vec{x}_k + 0)\, d\vec{x}_k = \int_V [\Delta\rho(\vec{x}_k)]^2\, d\vec{x}_k = \overline{\Delta\rho^2}\, V = Q \tag{3.18}$$

This represents the mean square electron density fluctuations in the entire scattering volume and is often referred to as the scattering invariant. The scattering invariant represents the "scattering power" or the "scattering strength" of the medium. The term $\overline{\Delta\rho^2}$ is the mean square electron density fluctuation in the system and is defined as:

$$\overline{\Delta\rho^2}(r) = (\rho(r) - \overline{\rho})^2 \tag{3.19}$$

where $\rho(r)$ is the electron density at point r and $\overline{\rho}$ is the average electron density of the system.

The correlation function, $\gamma(\vec{r})$ has been defined by Debye and Bueche as (141,163):

$$\begin{aligned}\gamma(\vec{r}) &= \frac{1}{\overline{\Delta\rho^2}\, V}\int_V \Delta\rho(\vec{x})\,\Delta\rho(\vec{x}+\vec{r})\,d\vec{x} \\ &= \frac{< \Delta\rho_j \Delta\rho_k >_r}{\overline{\Delta\rho^2}}\end{aligned} \tag{3.20}$$

The correlation function represents the spatial correlation between the local fluctuations in electron density. This function can be viewed as a probability function for an imaginary stick of length r so that each of its ends are embedded in phases having the same electron density. Therefore, a peak or a maximum in the correlation function represents the greatest probability for such an occurrence and hence provides information regarding the periodicity or correlation distance in the local density fluctuations in the system (164). Incorporating the above definition for $\gamma(\vec{r})$ into equation 3.16, gives the following expression for the scattering intensity:

$$I(\vec{s}) = I_e(s)\,\overline{\Delta\rho^2}\, V \int_V \gamma(\vec{r})\, e^{2\pi i (\vec{s}\,.\,\vec{r}\,)} d\vec{r} \tag{3.21}$$

Equation 3.21 can be further simplified by making two simple assumptions. As $\vec{r}$ goes to infinity one can envision that the probability of finding any correlation in the electron density goes to zero. Hence, the integral over the volume can be replaced with an integral over an infinite region. Secondly, a spherical symmetry about $\vec{r}$ is assumed (i.e. system is statistically isotropic). It would then imply that $\gamma(\vec{r})$ depends only on the magnitude of $\vec{r}$ (i.e. $\vec{r}$ = r). The expression relating intensity to the correlation function is then given by (163,165):

$$I(s) = I_e(s)\,\overline{\Delta\rho^2}\,V\int_0^\infty \gamma(r)\,\frac{\sin(2\pi sr)}{(2\pi sr)}\,4\pi r^2 dr \tag{3.22}$$

where $\gamma(r)$ is a three dimensional correlation function.

It can be seen from equation 3.21 that the scattered intensity, $I(\vec{s})$, is the Fourier transform of the correlation function, $\gamma(\vec{r})$. Therefore, for an isotropic system, the correlation function can be determined experimentally from the scattered intensity profile by taking the inverse Fourier transform of equation 3.22;

$$\gamma(r) = \frac{4\pi}{\overline{\Delta\rho^2}V}\int_0^\infty s^2\left[\frac{I(s)}{I_e}\right]\frac{\sin(2\pi sr)}{(2\pi sr)}\,ds \tag{3.23}$$

For the limiting values of $r\rightarrow 0$, the above expression essentially represents the scattering invariant of the medium which was discussed earlier. Thus an expression for the scattering invariant, Q, can be obtained in terms of the scattered intensity profile (165):

$$Q = \overline{\Delta\rho^2}V = 4\pi\int_0^\infty s^2\left[\frac{I(s)}{I_e(s)}\right]ds \tag{3.24}$$

Incorporating equation 3.24 into 3.23, the resulting expression for the 3-D correlation function is (163,165):

$$\gamma(r) = \frac{\displaystyle\int_0^\infty s^2 I(s)\,\frac{\sin(2\pi rs)}{2\pi rs}\,ds}{\displaystyle\int_0^\infty s^2 I(s)\,ds} \tag{3.25}$$

There are some systems where the 3-D correlation function is not applicable. These are systems where the assumption of spherical symmetry is not valid. An example of which would be a

system containing cylindrical or lamellar domains. For such anisotropic systems, Vonk and Kortleve (166) have proposed a one dimensional colinear correlation function, $\gamma(x)$, where:

$$\gamma(x) = \frac{\int_0^\infty s^2 I(s)\ \cos(2\pi x s)\ ds}{\int_0^\infty s^2 I(s)\ ds} \tag{3.26}$$

A schematic representation of such a one dimensional colinear correlation function is shown in Figure 3.1. It is clearly seen from the figure that the first maximum is indicative of the periodicity between the phases and is often related to the average interdomain spacing in a phase separated system. A similar argument is also applicable for the 3-D correlation function in a truly isotropic, phase separated system.

In a dilute system, the integration of the 3-D correlation function gives the Porod's coherence length, $\bar{l}_c$, and it is a measure of the mean width of the correlation function (141):

$$\bar{l}_c = 2\int_0^\infty \gamma(r)dr \tag{3.27}$$

A system is considered dilute, by definition, when the contribution to the overall intensity is primarily due to intraparticle interference. Therefore, an analogous expression to equation 3.27 for a one-dimensional correlation function is (151) :

$$\bar{d}_c = 2\int_0^\infty \gamma(x)dx \tag{3.28}$$

where d_c is the 1-dimensional coherence length. The relation between the 3-dimensional coherence length and the 1-dimensional coherence length is given by (166):

$$\bar{l}_c = 2\,\bar{d}_c \tag{3.29}$$

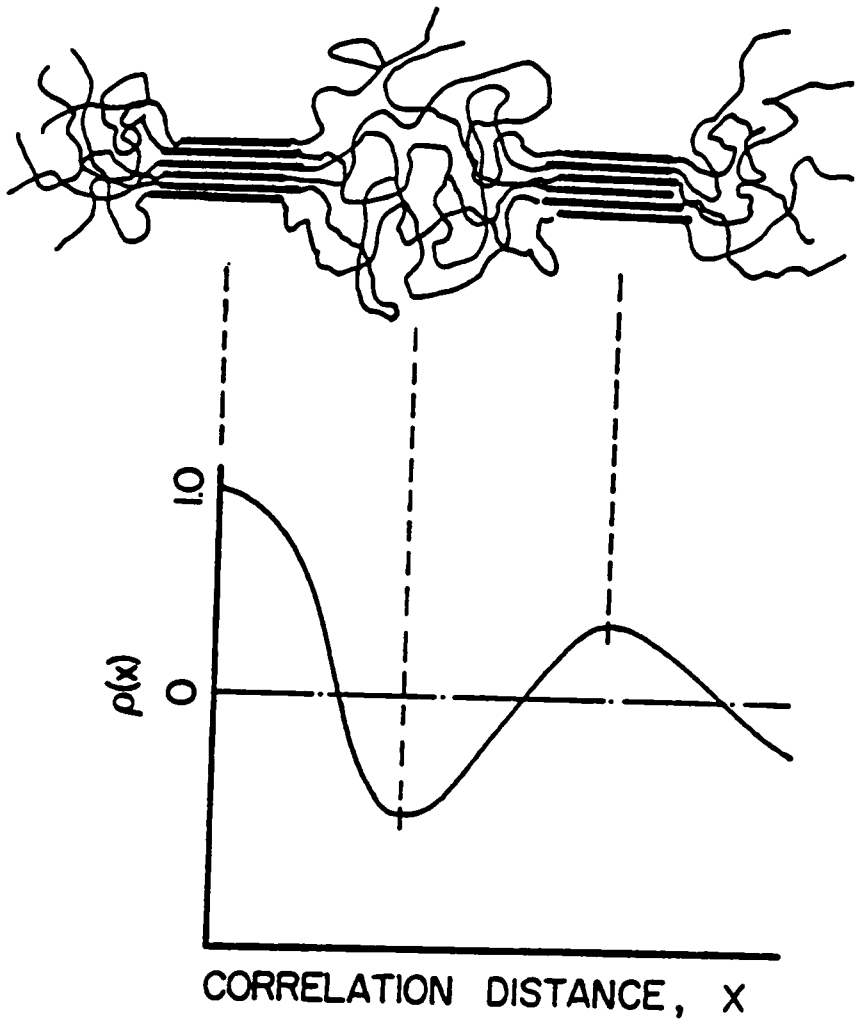

Figure 3.1. **Schematic Representation of the One-Dimensional Correlation Function:** showing the relation between the interdomain spacing and correlation distance corresponding to the first maxima (167).

For a completely random two phase system, Debye, Anderson and Brumberger (165) have proposed that the correlation function is exponential in form :

$$\gamma(r) = e^{-(\frac{r}{\bar{l}_p})} \tag{3.30}$$

where $\bar{l}_p$ is known as the correlation or the inhomogeneity length and is a measure of the average size of the inhomogeneities (or phase separated domains) in a dense two phase system. A system is considered to be a dense, by definition, when the contribution to the overall scattering intensity is primarily due to interparticle interference. Debye et al. have further shown that for such a dense two phase system, the initial slope of the correlation function is related to the specific surface area of the interface between the phases, and is given by (165):

$$\frac{d}{dr}\left[\gamma(r)\right]_{r=0} = -\frac{1}{4\phi_1\phi_2}\frac{S}{V} \tag{3.31}$$

where the ratio $\frac{S}{V}$ represents the specific surface area of the interfacial region between the phases and ϕ_i being the volume fraction of the respective phases. Using equations 3.30 and 3.31 in conjunction with equation 3.22, the inhomogeneity length can be shown to be (151):

$$\bar{l}_p = \frac{2}{\pi^2 K_p}\int_0^\infty s^2\left[\frac{I(s)}{I_e(s)}\right]ds \tag{3.32}$$

The inhomogeneity length, $\bar{l}_p$, is the harmonic average of the mean lengths $\bar{l}_1$ and $\bar{l}_2$ of the two phases comprising the inhomogeneity, and is given by:

$$\frac{1}{\bar{l}_p} = \frac{1}{\bar{l}_1} + \frac{1}{\bar{l}_2} \tag{3.33}$$

A schematic representation of the mean chord lengths, $\bar{l}_1$ and $\bar{l}_2$, in a two phase system is shown in Figure 3.2. These lengths represent the average length of random chords passing through the re-

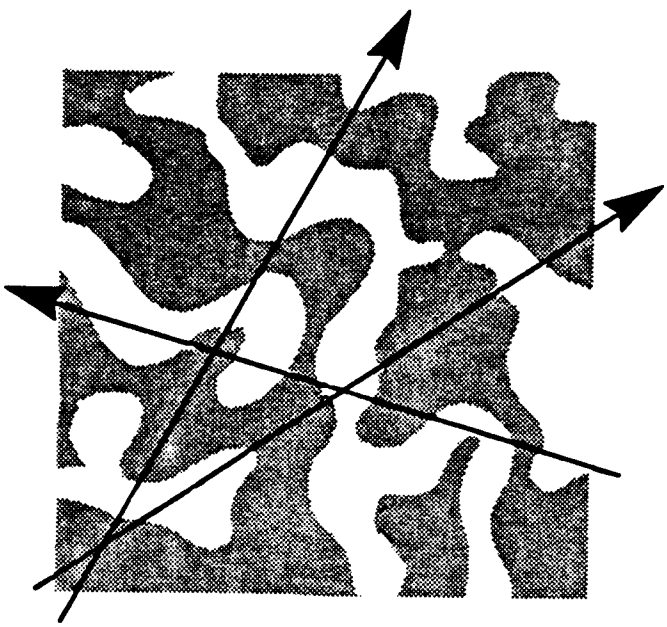

Figure 3.2. Physical Representation of the Mean Chord Length in a Two Phase System: From (139).

spective phases. Also, the relationship between the individual mean chord lengths with the average inhomogeneity of the system is given by (146):

$$\bar{l}_1 = \frac{\bar{l}_p}{\phi_2} \tag{3.34}$$

and

$$\bar{l}_2 = \frac{\bar{l}_p}{\phi_1} \tag{3.35}$$

The inhomogeneity length, $\bar{l}_p$, discussed above should not be confused with the coherence length, $\bar{l}_c$, discussed earlier. The former is applicable only to the dense systems whereas the latter is applicable to a dilute system.

The inhomogeneity length, $\bar{l}_p$, can be experimentally determined using equation 3.32. However, graphical techniques are a more convenient method of determination. A relation for the scattered intensity incorporating the incoherence length can be obtained by substituting equation 3.30 into equation 3.22, resulting in (145):

$$I(s) = A\left[\frac{\bar{l}_p}{(1+4\pi^2 s^2 \bar{l}_p^2)^2}\right] \tag{3.36}$$

where A is a constant. The inhomogeneity length, l_p, can be obtained from the ratio of the slope to intercept of the plot of $\frac{1}{\sqrt{I}}$ versus s^2 (commonly referred to as the Debye plot).

3.3.3 Porod's Law

Earlier it was shown that the correlation function and the scattered intensity are Fourier transforms of each other. Therefore, the high angle part of the intensity profile corresponds to those features of the correlation function at small distances. For small r, the correlation function can be represented by a power series (168):

$$\gamma(r) = 1 - ar + br^2 + cr^3 + \ldots\ldots \tag{3.37}$$

The initial slope of the correlation function has been shown by Guinier to be related to the specific surface area of the phases comprising the material. The first two terms of which being (141):

$$\gamma(r) = 1 - (\frac{S}{4V})r \tag{3.38}$$

Substituting equation 3.38 into the intensity expression (equation 3.22) and evaluating the integral gives (141,165):

$$\lim_{s\to\infty} [\, I(\vec{s}) \,] = \frac{\overline{\Delta\rho^2} S}{8\pi^3 \phi_1 \phi_2 s^4} = \frac{K_p}{s^4} \tag{3.39}$$

where K_p is the Porod's constant and ϕ_1 and ϕ_2 represent the volume fractions of the individual phases. The above equation is widely referred to in the literature as the Porod's law (169-171). Clearly from equation 3.39, the Porod's constant K_p, is closely related to the structural parameters of the system (154) :

$$K_p = \frac{\overline{\Delta\rho^2} S}{8\pi^3 \phi_1 \phi_2} = (\frac{S}{V}) \frac{Q}{8\pi^3 \phi_1 \phi_2} = \frac{Q}{2\pi^3 \bar{l}_p} \tag{3.40}$$

where the ratio $(\frac{S}{V})$ is the specific area of the interface between the phases. The inherent assumption in using equation 3.39 is that it is valid only at higher s values. Therefore, there exists a minimum value of s below which Porod's law is inapplicable. If a scattering peak is present, Ruland (172) has shown that the minimum value of the scattering vector for which the Porod's law is applicable is a function of the position of the primary scattering peak and generally the lower limit is approached by s values corresponding to the position of the secondary maxima in the long period.

It should be evident from equation 3.39 that the product of I^*s^4 should reach a constant value of K_p for an ideal two phase system. The Porod's law, if applicable, provides the means to extrapolate the scattered intensity to large scattering angles where experimental measurement of in-

tensity becomes impractical (154). Extrapolation of the experimental data beyond the measurable limits of the instrument provides an opportunity to compute the correlation functions from experimental data. Furthermore, Porod's law behavior can also be used to determine the morphological features, at least qualitatively, in phase separated systems. This is achieved by studying the degree as well as the nature of deviation of the system from the ideal Porod's law.

For an ideal two phase system with sharp phase boundaries, the plot of I^*s^4 versus s^2 (or s) [also referred to as Porod's plot] reaches a constant value as depicted in Figure 3.3. However, in most real systems, the product of I^*s^4 does not reach a constant value at higher scattering angles suggesting that deviations from ideal Porod behavior exists in the system. The factors that usually contribute to the positive deviation are those arising from thermal density fluctuations or from isolated mixing of one type of segment in the other (intradomain mixing) (154,172-174). A schematic representation of these effects along with their corresponding electron density profile is shown in Figure 3.4.

At the same time, there are other factors that contribute to a decrease in the overall scattered intensity profile which result in a negative deviation from ideal Porod behavior. One of the primary factors that is responsible for this negative deviation are those resulting from diffuse phase boundaries. This is due to the fact that a larger volume fraction of the material have their electron density closer to the mean density of the two phases. Hence, this volume of the material makes little or no contribution to the overall intensity profile (175). Figure 3.5 depicts the effect of the presence of a diffuse interface boundary between the phases which is responsible for the negative deviation from the ideal Porod behavior.

Ruland (176) has shown that the Porod's law could be modified to incorporate deviations that occur from the ideal Porod behavior, details of which will be discussed in the following sections. By incorporating the suggested modifications, an estimate of the diffuse boundary thickness can be determined. Measurement of the interfacial thickness is of considerable importance in the present study and therefore further discussions on the subject is presented.

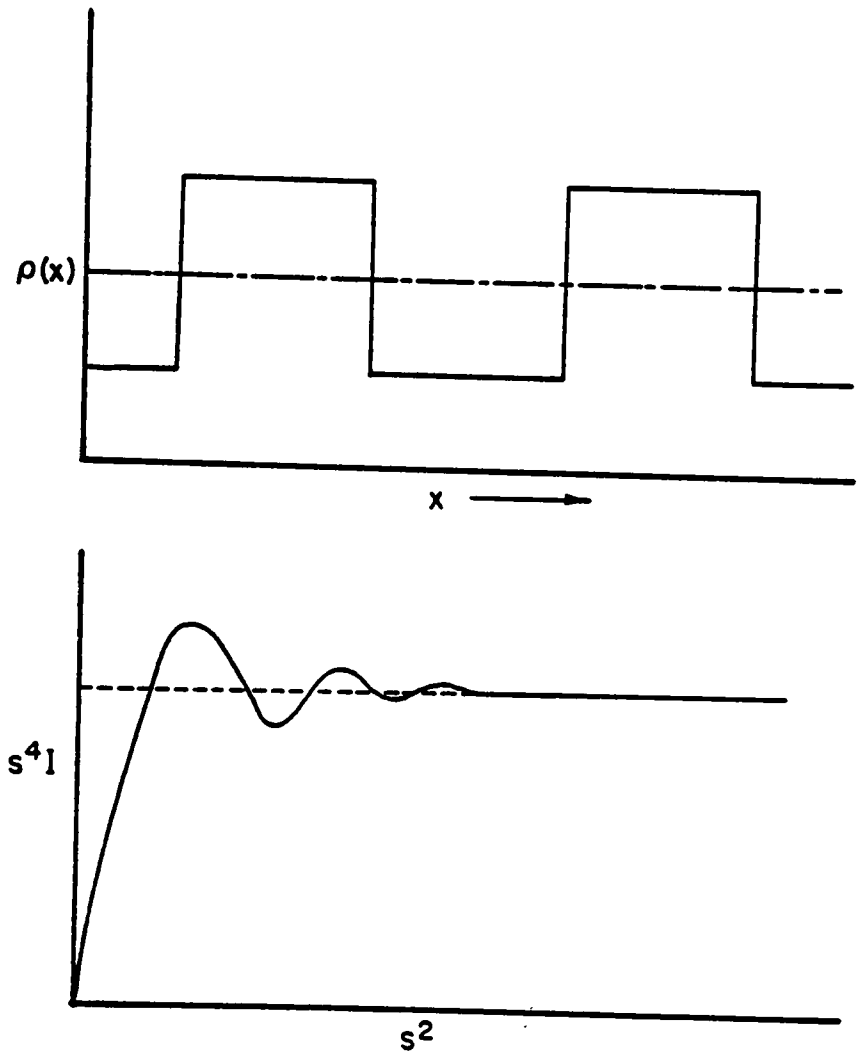

Figure 3.3. Ideal Two Phase Behavior - Schematic Representation of the Porod's law: From (139).

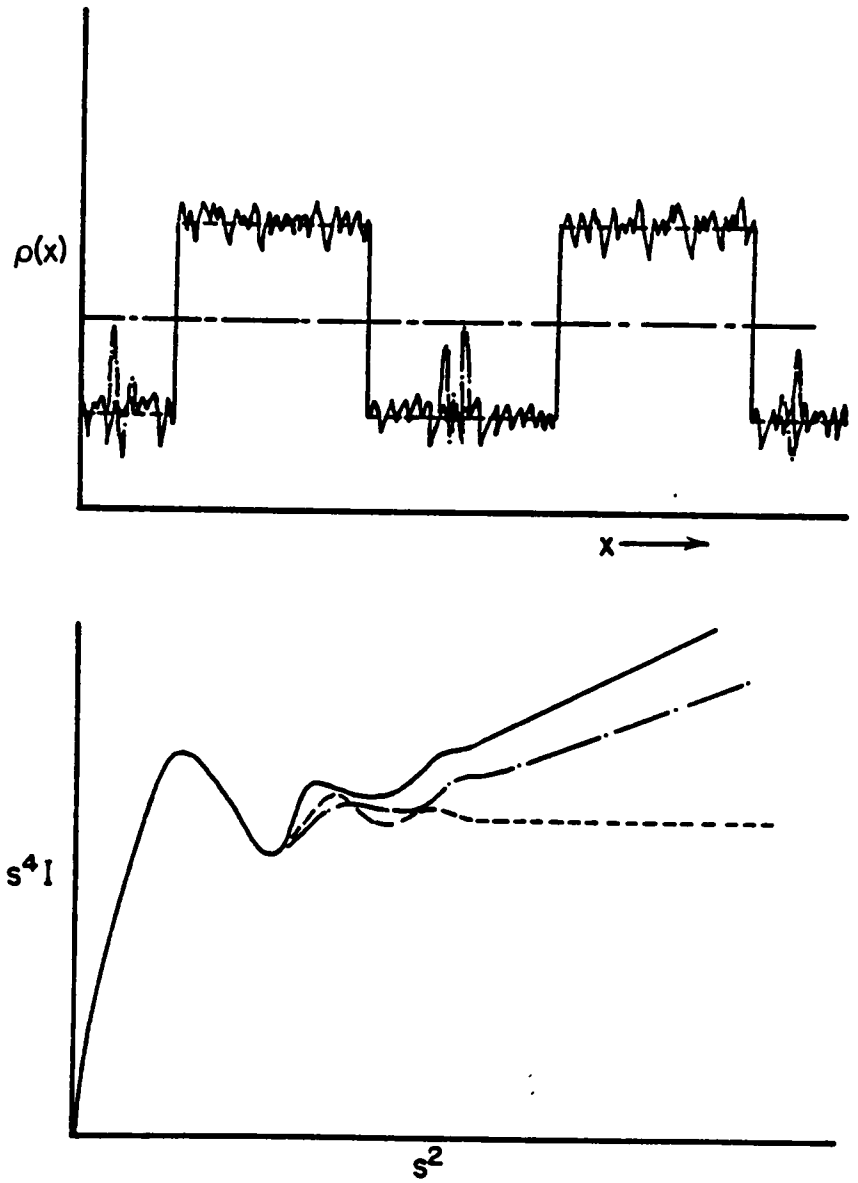

Figure 3.4. Positive Deviation from Ideal Behavior - A Schematic Representation: From (167).

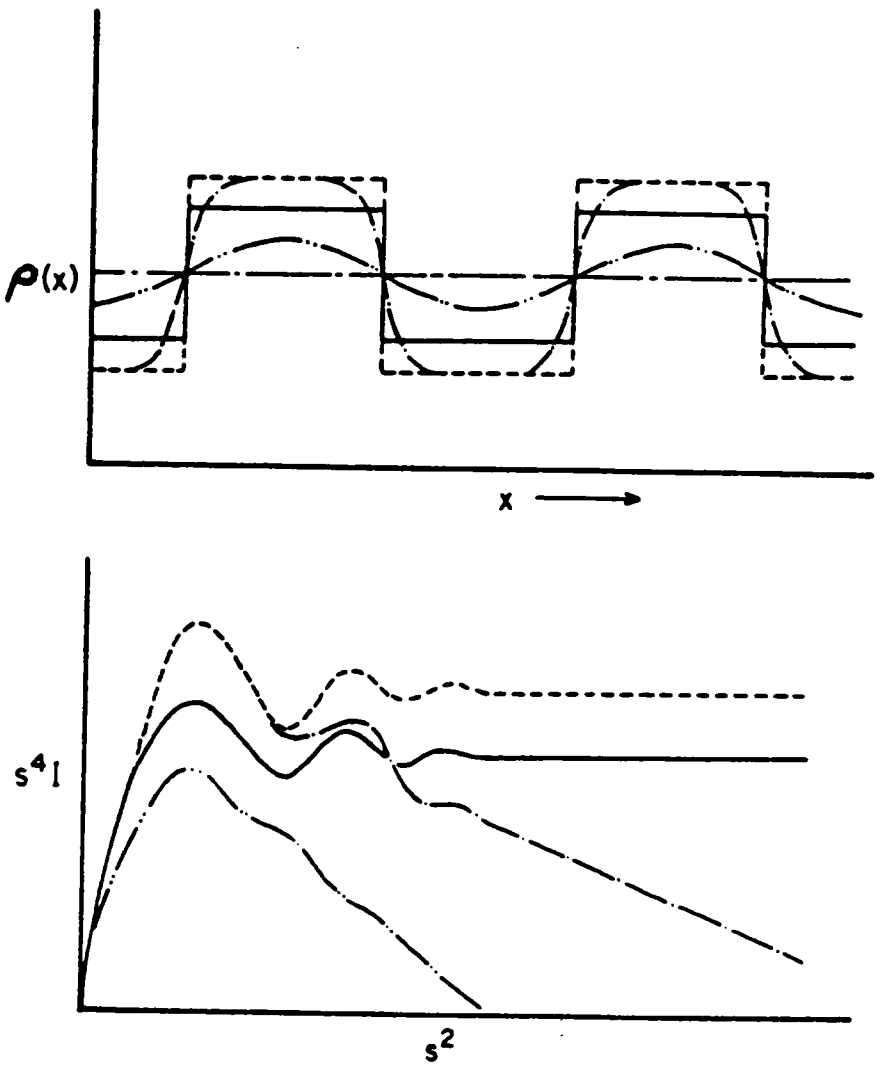

Figure 3.5. Negative Deviation from Ideal Behavior - A Schematic Representation: From (167).

3.3.4 *Interfacial Thickness Determination*

In the earlier discussions, the analyses were based on ideal systems having sharp interface between the phase boundaries. The scattering intensity for such a system is the Fourier transform of the electron density fluctuations in the system (154):

$$I_{ideal}(s) = \frac{K_p}{s^4} = \mathbf{F}\{\overline{\Delta\rho^2}\} \tag{3.41}$$

where **F** represents the three-dimensional Fourier transform of the mean square of the electron density fluctuations in the system.

However, if the electron density profile of the system is diffuse, the electron density can be modified to account for the deviation from the ideal behavior. Ruland has suggested that the finite width of the interfacial region can be conveniently represented by a convolution of the ideal electron density distribution function $\rho(r)$ with a smoothing function, h(r), as given below (176):

$$\rho_{obs}(r) = \rho(r)*h(r) \tag{3.42}$$

where * represents the convolution product. The nature of the smoothing function, h(r), depends on the type of interfacial gradient selected. Figure 3.6 depicts the two most frequently used interfacial gradient models, the sigmoidal gradient and the linear gradient. The sigmoidal gradient is a more realistic approximation to the real system whereas the linear gradient is much easier to visualize in terms of conceptualization of a model for the interfacial region. If the interface is represented as a sigmoidal gradient, then the smoothing function h(r) is gaussian in nature (154,176,177). However, if the interfacial region is modeled by a linear gradient at the interface, then the smoothing function h(r) is a box function or a square pulse of width, E, and height, 1/E (178,179).

It is known that the Fourier transform of a convolution product in real space is simply the product of the Fourier transforms in reciprocal space. Taking the Fourier transform of equation 3.42 results in :

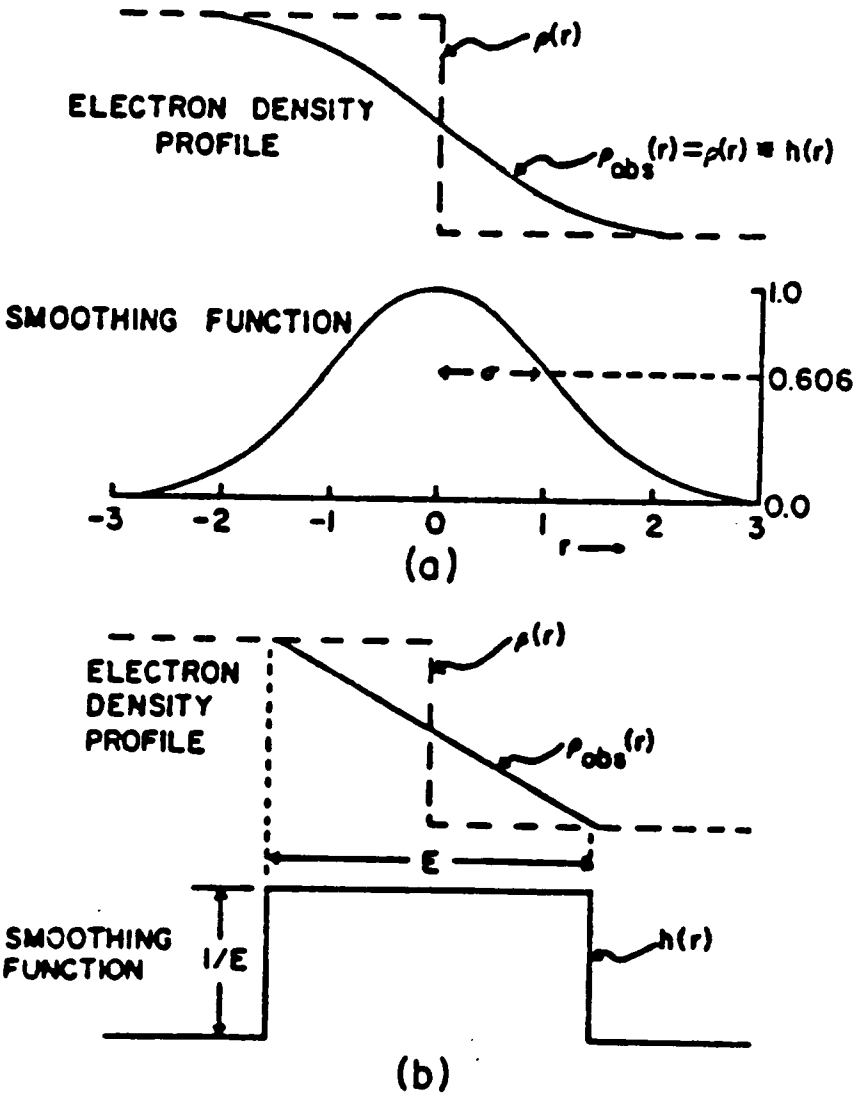

Figure 3.6. Schematic Representation of the Smoothing Function for Sigmoidal and Linear Gradient Across the Interface: From (154).

$$I_{obs}(s) = \mathbf{F}\left\{\overline{\Delta\rho^2}(r)\right\} \mathbf{F}\{h^2(r)\} = I_{ideal}(s)\, H^2(s) \tag{3.43}$$

where $H^2(s)$ is the Fourier transform of the autocorrelation of the smoothing function, h(r). At large values of s where Porod's law is applicable, I_{ideal} can be substituted by Porod's relation so that

$$I_{obs}(s) = \frac{K_p}{s^4} H^2(s) \tag{3.44}$$

Different forms of the term $H^2(s)$ have been reported in literature (141,154,162,176-180). The variations are dependent on the type of interfacial gradient selected, the collimation of the scattering apparatus and the approximations used to evaluate it. Tables 3.1 and 3.2 list the expressions used for the term $H^2(s)$ for pin-hole and slit collimated data, respectively. Direct evaluation of the interfacial thickness from the forms listed in Tables 3.1 and 3.2 for $H^2(s)$ often require iterative techniques which are often too cumbersome and hence graphical techniques are more suited for interfacial thickness determination. Tables 3.3 and 3.4 list the plotting variables and the parameters obtained from the plot which are then used to obtain the interfacial thickness parameter. By convention, the term σ is used to describe the interfacial thickness parameter for a sigmoidal gradient and the corresponding term for a linear gradient is E. The parameter σ represents the standard deviation of sigmoidal gradient in the direction normal to the interface. However, the term σ does not represent the actual interfacial thickness but the width of a gaussian function at 60.6% of the maximum value. Hence, σ differs from the actual interfacial thickness by a factor greater than two. The interfacial thickness for a linear gradient is denoted by E. The terms σ and E are obviously related and the relation that exists between them is

$$E = \sqrt{12}\,\sigma = 3.464\,\sigma \tag{3.45}$$

Table 3.1. Forms of $H^2(s)$ for Pin-Hole Collimation Assuming a Sigmoidal Gradient Across the Interface

Sigmoidal	$\exp(-4\pi^2\sigma^2 s^2)$
Expanded Sigmoidal	$(1 - 4\pi^2\sigma^2 s^2)$
Expanded Linear	$(1 - 1/3\pi^2 E^2 s^2)$

Table 3.2. Forms of $H^2(s)$ for Slit Collimation Assuming a Sigmoidal Gradient Across the Interface

Bonart	$\exp(-4\pi^2\sigma^2 s^2)$
Exponential	$\exp(-8\pi^2\sigma^2 s^2)$
Koberstein	$\exp(-38(\sigma s)^{1.81})$
Ruland	$(1 - 8\pi^2\sigma^2 s^2)$

Table 3.3. Estimation of the Interfacial Thickness Parameters for a Sigmoidal Gradient (Pin-Hole Collimation)

Density Gradient Model	Required Plot	Estimation of Parameters
Sigmoidal	$\ln[\, I_{obs}(s) - I_B(s)\,]^* s^4$ vs. s^2	$\sigma^2 = (-\text{ slope}/4\pi^2)$
Expanded Sigmoidal	$[\, I_{obs}(s) - I_B(s)\,]^* s^4$ vs. s^2	$\sigma^2 = (-\text{ slope}/4\pi^2 \text{ intercept})$
Expanded Linear	$[\, I_{obs}(s) - I_B(s)\,]^* s^4$ vs. s^2	$E^2 = (-\text{slope}/\pi^2 \text{ intercept})$

Table 3.4. Estimation of the Interfacial Thickness Parameters for a Sigmoidal Gradient (Slit Collimation)

Approximation	Required Plot	Estimation of Parameters
Bonart	$\ln[s^3*(\tilde{I}_{obs}(s) - \tilde{I}_B)]$ vs. s^2	σ^2 = (-slope/$4\pi^2$)
Exponential	$\ln[s^3*(\tilde{I}_{obs}(s) - \tilde{I}_B)]$ vs. s^2	σ^2 = (-slope/$8\pi^2$)
Koberstein	$\ln[s^3*(\tilde{I}_{obs}(s) - \tilde{I}_B)]$ vs. $s^{1.81}$	$\sigma^{1.81}$ = (-slope/38)
Ruland	$s^3*[\tilde{I}_{obs}(s) - \tilde{I}_B]$ vs. s^2	σ^2 = (-slope/$8\pi^2$ intercept)

3.3.5 *Background Determination*

As mentioned earlier, the real systems often do not obey the ideal Porod behavior as described by equation 3.41. Deviations from the ideal Porod behavior occur due to a variety of reasons. It was shown in the previous section that equation 3.41 can be modified to account for the presence of diffuse interface (equation 3.44). But this equation has not yet been corrected for those factors that contribute to the positive deviations in the system. These positive deviations occur due to the presence of thermal density fluctuations or "background scattering", intradomain mixing, or even an onset of wide-angle scattering. In order to correct for the background scattering, one needs to obtain data well beyond the small angle region. These data are then fitted to an empirical relationship which is then extrapolated back into the small angle region. The estimated background scattering is then subtracted from the observed scattered intensity profile so that the contribution from thermal density fluctuations is removed. Thus the Porod's law can further be modified to incorporate this additional contribution due to background scattering, and the resulting expression (177):

$$I_{obs}(s) = \frac{K_p}{s^4} H^2(s) + I_B(s) \tag{3.46}$$

where $I_B(s)$ is the contribution due to background scattering resulting from thermal density fluctuations. The function $H^2(s)$ has a value of one for small values of s but approaches zero at large s. Therefore, at large s values, the contribution to the overall intensity is essentially due to the background scattering. It is often difficult to determine where exactly the term $H^2(s)$ goes to zero since the interfacial thickness parameter (σ or E) which is unknown at this time is involved in its determination. Again, graphical techniques are used to determine the contribution due to thermal density fluctuations. The various methods require curve fitting at the high angle region of the scattering profile, where the term $H^2(s)$ essentially goes to zero and the contribution to the overall intensity is assumed to be due to background scattering, $I_B(s)$.

Estimation of the contribution due to background scattering term $I_B(s)$ has been carried out by several workers (176,179,181). The treatment of Bonart is perhaps the simplest method where

the contribution due to background scattering is assumed to be a constant (i.e. $I_B(s)$ = C, a constant) (181). The contribution of this term can be determined from the plot of I^*s^4 versus s^4. If the background contribution is nearly constant, the plot will be linear with slope, $I_B(s) = C$ (from equation 3.46). Such a simple treatment is adequate when the tail of the scattering profile is fairly flat.

Both Ruland and Vonk assume that the function $H^2(s)$ goes to zero at high scattering angles where the contribution to the overall intensity is essentially from the $I_B(s)$ term. The intensity at these angles (tail region) is fitted with an appropriate empirical expression and then extrapolated to lower angles to determine the background scattering for the entire angular range.

The Ruland method fits the tail of scattering profile with an exponential function (176).

$$I_B(s) = C \exp(as^n) \tag{3.47}$$

where "a" is a constant, C is the value of the intensity extrapolated to zero angle and "n" is an even integer, typically 2 or 4. Vonk suggested that the high angle tail of the scattering profile can be fitted using a power series with the first two of the series being (179):

$$I_B(s) = C + bs^n \tag{3.48}$$

where "b" is a constant and the value of n is restricted to even integers greater than 2. Both the Vonk's method as well as the Ruland's method can take into account the contribution due to the onset of wide angle x-ray scattering. It should be noted that the onset of wide angle x-ray scattering may be either be due to an intraparticle or an interparticle interaction of the polymer backbone. This contribution would then be dependent on the nature of the backbone polymer. The forms of the different treatments has been listed in Tables 3.5 and 3.6 for pin-hole collimation and slit collimation, respectively.

The expressions used to fit and extrapolate the background scattering intensity are at best empirical in nature. Therefore, there is no theoretical justification for preference of one method over the other. A proper choice of the method depends on the nature of the high angle tail as well as the goodness of fit of a particular method with respect to the experimental data. Subtraction of the

Table 3.5. Determination of Thermal Density Fluctuations (Background Scattering) For Pinhole-Collimation

Empirical Relatibn	Required Plot	Estimation of Parameters
Bonart : $I_B(s) = C$	$s^4 * I_B(s)$ vs. s^4	C = Slope
Vonk : $I_B(s) = C + bs^n$ n = 2,4, ...	$I_B(s)$ vs. s^n	b = slope; C = Intercept
Ruland : $I_B(s) = C \exp(as^2)$	$\ln [I_B(s)]$ vs. s^2	a = slope; C = exp (Intercept)

Table 3.6. Determination of Thermal Density Fluctuations (Background Scattering) For Slit-Collimation

Empirical Relation	Required Plot	Estimation of Parameters
Bonart : $\tilde{I}_B(s) = C'$	$s^3 * \tilde{I}_B(s)$ vs. s^3	C′ = Slope
Vonk : $\tilde{I}_B(s) = C' + b's^n$ n = 2,4, ...	$\tilde{I}_B(s)$ vs. s^n	b′ = slope; C′ = Intercept
Ruland : $\tilde{I}_B(s) = C' \exp(a's^2)$	$\ln[\tilde{I}_B(s)]$ vs. s^2	a′ = slope; C′ = exp (Intercept)

contribution due to background scattering does not alter the peak positions but they are important in those analyses which involve integration of the scattering profile or manipulation of the tail region (for interfacial thickness determination).

It was mentioned earlier that isolated segmental mixing (intradomain mixing) also contributed positively to the overall intensity. So far no modification of Porod's law has been suggested in literature which can estimate the contribution due to intradomain mixing.

3.3.6 Degree of Phase Separation

The mean square electron density fluctuation is related to the scattering invariant, Q, of the system (equation 3.24). This fluctuation or electron density variance is often used as a measure of the degree of phase separation in the system. In a multiphase system, the mean square electron density variance is given by (183):

$$\overline{\Delta\rho^2} = \sum_{i}^{N} \phi_i(\rho_i - \overline{\rho})^2 \tag{3.49}$$

where $\overline{\rho}$, the average electron density is given by

$$\overline{\rho} = \sum_{i}^{N} \phi_i \rho_i \tag{3.50}$$

where ϕ_i and ρ_i being the volume fraction and electron density of the i^{th} component, respectively. Comparing equation 3.49 along with the intensity expression 3.21, it should be apparent that the electron density variance provides the inherent contrast necessary for x-ray scattering. Therefore, if the electron density of a phase is equal to the average electron density, there is no contrast for that phase. In the absence of a contrast, a phase does not contribute to the observed scattering profile (183).

For a two phase system with a sharp phase interface boundary, the mean square variance of the electron density fluctuations (from equation 3.49) is given by:

$$\overline{\Delta\rho_c^2} = \phi_1\phi_2(\rho_1 - \rho_2)^2 \tag{3.51}$$

The term $\overline{\Delta\rho_c^2}$ can be calculated from the known chemical composition and densities of the component phases by assuming complete phase separation. A schematic representation of the electron density profile of an hypothetical ideal two phase system is shown in Figure 3.7c. However, the actual electron density variance obtained from experimental data is often less than ideal due to the presence of diffuse phase boundaries and/or thermal density fluctuations (background scattering). The schematic representation of such a system is shown in Figure 3.7a. These deviations can be estimated graphically by several different approaches by fitting the tail of the scattering intensity profile. The corrected electron density profile after the removal of thermal density fluctuations is shown in Figure 3.7b. The absence of a sharp transition in this profile is indicative of the presence of diffuse phase boundary between the phases. There may yet be another situation where the phase boundaries may be sharp but the average electron density of the medium may be altered due to mixing between the phases (intradomain mixing) which results in an increase in the average electron density of the medium and therefore lowering the scattering contrast as depicted by profile Figure 3.7d.

It is often difficult to obtain the electron density variance for systems where there is mixing within domains (due to the fact that the volume fraction and electron densities are not independent in these systems). However, for a special case where the gradient of the interfacial region between the two phases is linear, the electron density variance has been shown to be (179):

$$\overline{\Delta\rho^2} = (\phi_1\,\phi_2 - \frac{ES}{6V})(\rho_1 - \rho_2)^2 \tag{3.52}$$

Experimental electron density variances can be calculated for these profiles by employing the Porod-law relations which have been discussed in the earlier sections. The corresponding variance for background corrected profile depicted in Figure 3.7b is given by (180):

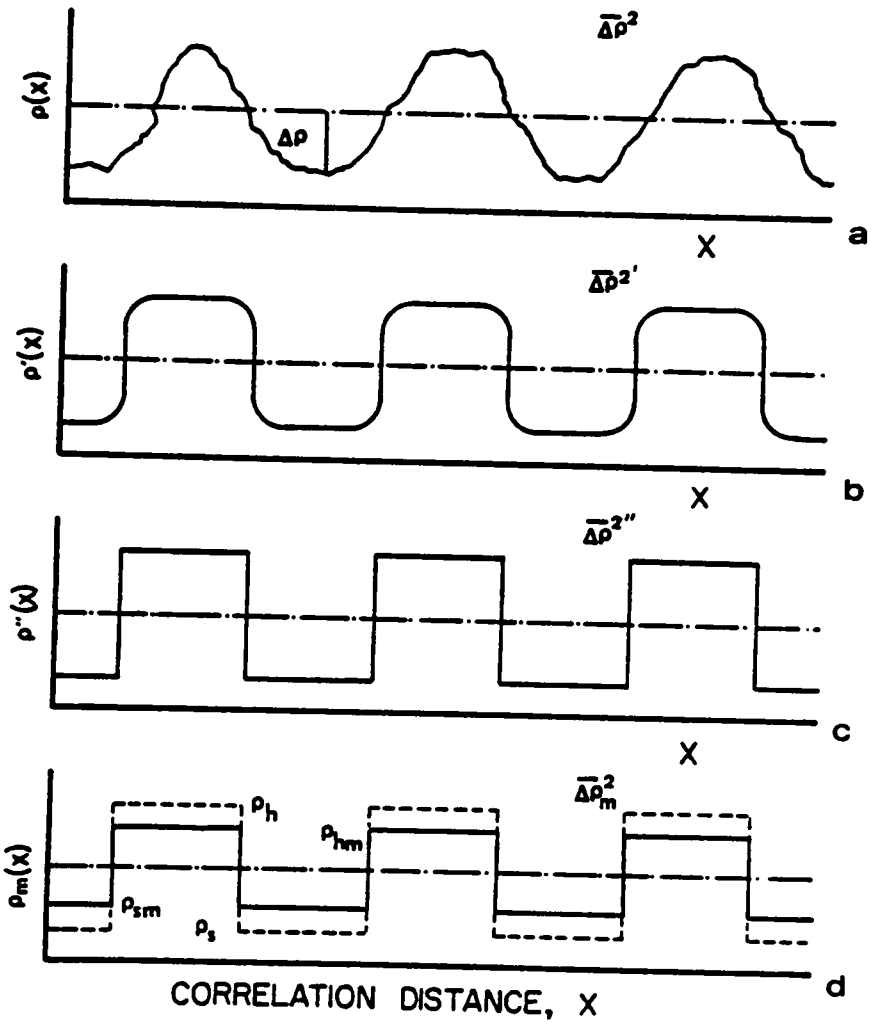

Figure 3.7. **Various Physical Forms of the Electron Density Profiles:** - in a two phase system. From (167).

$$\overline{\Delta\rho^{2'}} = \frac{4\pi}{VI_e}\int_0^\infty s^2\,[I_{corr}(s)]\,ds \tag{3.53}$$

where $I_{corr}(s) = I_{obs}(s) - I_B(s)$. The contribution to the overall scattering profile due to the presence of diffuse phase boundaries can be estimated by first determining the interfacial thickness, σ, of the system and then correcting the background corrected intensity for the diffuse interface using the $H^2(s)$ term. The resulting idealized profile is shown in Figure 3.7c. The corresponding variance, $\overline{\Delta\rho^{2''}}$, can be calculated from (180):

$$\overline{\Delta\rho^{2''}} = \frac{4\pi}{VI_e}\int_0^\infty s^2\left[\frac{I_{corr}(s)}{H^2(s)}\right]ds \tag{3.54}$$

Comparison of the estimated variances, $\overline{\Delta\rho^{2'}}$, $\overline{\Delta\rho^{2''}}$, to the variance of an ideal system, $\overline{\Delta\rho_c^2}$, provides valuable insight into the state and degree of phase separation in the system (180-182). An estimate of the degree of overall phase separation can be obtained from the ratio of

$$\frac{\overline{\Delta\rho^{2'}}}{\overline{\Delta\rho_c^2}} \tag{3.55}$$

The ratio approaches unity for a completely phase separated system and decreases with the occurrence of phase mixing. The value approaches zero for a completely phase mixed system (i.e., no distinct boundaries).

The amount of phase mixing within the domains irrespective of any boundary diffuseness is obtained from the ratio of

$$\frac{\overline{\Delta\rho_c^2}}{\overline{\Delta\rho^{2''}}} - 1 \tag{3.56}$$

The ratio has a value of zero in the absence of intradomain segmental mixing and increases with its occurrence.

A measure of the boundary diffuseness, irrespective of intradomain mixing, can be obtained from the ratio :

$$\frac{\overline{\Delta\rho^{2''}}}{\overline{\Delta\rho^{2'}}} - 1 \tag{3.57}$$

The value of the ratio is zero for systems with sharp phase boundaries and it increases with increasing domain boundary diffuseness.

The information obtained from the analysis of the electron density variances is only semi-quantitative but they provide valuable insight in assessing the degree and origin (within phases or at the phase boundary) of phase mixing (180). By this approach only qualitative comparisons can be made to compare different materials since a quantitative estimate would be questionable since a number of approximations are involved in the graphical techniques used to obtain the variances.

3.3.7 Radius of Gyration

One of the important parameters that can be sometimes be obtained from the scattered intensity profile is the radius of gyration of the dispersed phase. For an isotropic system, the scattered intensity in terms of the correlation function, $\gamma(r)$, is given by equation 3.22. If the $\frac{\sin\ (2\pi sr)}{2\pi sr}$ term in this equation is expanded in terms of a power series expansion, one obtains (141) :

$$\begin{aligned} I(s) &= 4\pi\, I_e(s)\overline{\Delta\rho^2}V\int_0^\infty \gamma(r)r^2\,[1-\frac{(2\pi sr)^2}{3!}+\frac{(2\pi sr)^4}{5!}+\ .....]dr \\ &= 4\pi\, I_e(s)\overline{\Delta\rho^2}V\int_0^\infty \gamma(r)r^2\,dr\left\{[1-\frac{(2\pi sr)^2}{3!}\frac{\int_0^\infty \gamma(r)r^4dr}{\int_0^\infty \gamma(r)r^2dr}+\ .....]\right\} \end{aligned} \tag{3.58}$$

The radius of gyration has been defined by Guinier as (141,184):

$$R_g^2 = \frac{\int_0^\infty \gamma(r) r^4 dr}{2\int_0^\infty \gamma(r) r^2 dr} \tag{3.59}$$

The first part of equation 3.58 is often referred to as the zero angle scattering and is usually represented as I_0. Substituting equation 3.59 in equation 3.58, results in the following expression for the scattered intensity :

$$\begin{aligned} I(s) &= I_0 \left[1 - \frac{R_g^2}{3} 4\pi^2 s^2 + ...\right] \\ &= I_0 \exp\left[- \frac{R_g^2}{3} 4\pi^2 s^2 \right] \end{aligned} \tag{3.60}$$

In the development of the above expression, there are two inherent assumptions that have been made; namely, the system under consideration is dilute and secondly, R_g would be determined only at small values of the scattering vector, s. In a dilute system, the value of R_g can be estimated from the slope of the plot of ln I versus s^2 [referred to as a Guinier plot].

The law of Guinier is not just restricted to spherical particles but is applicable to non-spherical dispersed particles as well (185). At small scattering vectors, the scattering profile approaches assymtotically the profile given by the Guinier relationship, however, deviations are encountered at higher s values depending on the particle shape (148). These deviations occur due to errors introduced when the higher order terms of equation 3.58 are truncated in the series simplification. If a distribution in the particle size exists in the material, then the radius of gyration determined using equation 3.60 will represent an average value, $\overline{R}_g$, given by (141):

$$\overline{R}_g^2 = \frac{\int_0^\infty m(r) r^5 dr}{\int_0^\infty m(r) r^3 dr} \tag{3.61}$$

where m(r) is the electronic mass distribution function. There are several different methods to determine the mass distribution function in a polydisperse system (185,186). It should be apparent the method of averaging using equation 3.59 favors those particles that have larger radii of gyration.

3.3.8 Bragg's Law

One of the simplest and perhaps the most routine analysis in x-ray analysis involves the application of the Bragg's equation to determine interdomain spacings. The interdomain spacing d is obtained from the position of a maximum in the scattering profile through the Bragg's equation

$$|s| = \frac{2}{\lambda}\sin\theta = \frac{n}{d} \tag{3.62}$$

where n = order of scattering, and the Bragg angle θ is one half the scattering angle. In small angle x-ray scattering, the presence of a maxima in the scattering profile is indicative of a long range ordering in the system.

For an isotropic system, the interdomain spacing can be obtained from the value of s_{max} obtained from the I(s) vs s plot. This value is generally larger than the interdomain spacing value obtained from the 3-D correlation function. This deviation can be attributed to the fact that the Bragg's law assumes a regular placement in one direction whereas the 3-D correlation function averages over the whole scattering volume. However, for anisotropic systems such as in a lamellar system, Lorentz corrections are often required to determine the interdomain spacing. This requires a plot of s^2*I vs s and the peak position corresponds to the interdomain spacing in the system. When the Lorentz correction is applied, the scattering curve represents a hypothetical system where all repeating structures are aligned along a common axis. The d spacing obtained in this manner should agree with the interdomain spacing obtained from the 1-D correlation function (152).

4.0 PURPOSE AND SCOPE OF THE PRESENT RESEARCH

From the discussions in the section on literature review it is evident that there has been considerable effort directed toward the investigation of ion-containing polymers with a major emphasis being placed toward random ionomers. Though a wide range of characterization techniques from nuclear magnetic resonance (NMR) to electron microscopy have been employed, the morphology of ionomers and its effect on the structure-property relationships are not yet been clearly elucidated and is still a topic of hot controversy.

The objectives of the present study is to achieve a better understanding of the morphology of model ionomers in terms of the ion aggregation, ion placement and the degree of phase separation existing in these systems. Structure-property relationship studies have been conducted on three model ionomers namely, telechelic ionomers and segmented ionene polymers and block ionomers. Unlike the random ionomers where the ions are located randomly along the polymer backbone, the placement of the ions in these three ionomer systems is well defined. This enables a systematic study to be conducted to investigate the influence of different variables on the morphology and the bulk properties of the materials. The discussions will relate the system variables based on the chemistry of the system to the observed behavior. A number of characterization techniques have been employed in order to gain insight regarding the nature of ionic interactions in these model ionomers.

4.1 Telechelic Ionomers

The unique feature of telechelic ionomers is that the ionic groups are located only at the chain ends. This well defined microstructure leads to a network whose structure is much better defined than those formed by traditional ionomers, thereby, simplifying the task of relating the structure to their properties. In prior work, the solution behavior and the bulk viscoelastic behavior of

carboxylated elastomeric telechelic ionomers have been studied extensively by Broze et al. (70-82). Tant et al. (83,187) have investigated the bulk properties of a series of carboxylated elastomeric telechelic materials based on polyisoprene backbone at large deformations. However, there has been very few studies conducted to relate the structural features to the nature of ionic associations in the telechelic ionomers. The aim of the present research is to obtain morphological information regarding the state of aggregation of the ions in the system and relate them to the observed bulk properties.

It has been shown in random ionomers that the sulfonated ionomers associate more strongly than the corresponding carboxylated ionomers (94). However, there has not been any study reported where a direct comparison is made between the performance of a sulfonated and carboxylated ionomer in a well defined network microstructure. For the first time, a direct comparison of the performance of a series of sulfonated telechelic ionomers is made with their corresponding carboxylated material.

4.2 Ionene Elastomers

As can be gleaned from the literature, there have been very few studies aimed at studying the structure-property relationships of ionene polymers. Much of the earlier work have focused on studying the dilute viscosity behavior of these materials (108-113,115,117-120). One of the attractive features in studying these segmented ionene materials is that the ionic groups are located at well defined positions along the polymer backbone. In addition, the synthesis of these segmented ionene materials is relatively simple which enables one to modify the chemical nature of these materials quite easily. The objective of the present research is to conduct a systematic study in order to explore the effect of different variables on the structure and morphology of the system and relate them to the observed bulk properties. There has been a joint effort in our laboratory where studies relating the mechanical, dynamic mechanical and electron microscopy has been studied by Feng (37,187,188) while the details relating to small angle x-ray scattering will be reported in this dissertation.

The effect of three important variables based on the chemistry of the ionene polymers has been studied in terms of the morphology of the system as they affect the final bulk properties. These variables are;

4.2.1 Effect of PTMO Segment Molecular Weight

The ability to control the molecular weight of the soft segment is one of the attractive features of studying polymers based on ionene chemistry. Polytetramethylene oxide (PTMO) has been widely used as a soft segment in many thermoplastic elastomers such as in the segmented urethanes and the segmented urethane-urea systems. The ionic content in these polymers can be controlled by varying the PTMO soft segment molecular weight. For example, increasing the PTMO molecular weight results in a decrease in the ionic content of the polymer. However, PTMO is well known to crystallize at ambient conditions, the rate depending on the length of the PTMO soft segment. Therefore, if the PTMO soft segment is of sufficient molecular weight, the tendency to crystallize may be viewed as a disadvantage (if the material is to be used an elastomer) since this would result in a loss of elastomeric character.

4.2.2 Effect of the Counterion of the Ionene hard segment

The counterion that has been widely used in the synthesis of ionenes is bromide ion. Other counterions that have also been considered are those of chloride, bromide (98) and triflate ion (100). The properties of the ionene elastomers can be significantly affected by the nature of the counterion. For example, electronegativity differences can alter the intersegment interactions that can affect the final mechanical properties. Also, differences in the size of the counterion will affect the packing arrangement and therefore the morphology of the ionene segments in the ionic domain since the coulombic forces of interactions is a function of the charge of the anion and the distance of closest approach (sum of the two ionic radii) between the anion and the quaternary ammonium ion. Microphase separation in these systems is largely promoted by the coulombic interactions between the ionene groups. Unlike in the segmented copolymer systems, it will also be shown that the

microphase separation in these systems is primarily driven by the ionic interactions in the system and not due to solubility parameter differences between the ionene hard segment and the PTMO soft segment. Hence, the morphology of the ionene polymers is greatly dependent on the counterion of the hard segment, and therefore, it is essential to study the effect of the counterion of the ionene polymer. The counterions considered for the study are chloride, bromide and iodide.

4.2.3 Effect of the Architecture of the Ionene Hard Segment

In conventional thermoplastic elastomers, the average hard segment generally contained more than one hard segment for establishing sufficient microphase separation necessary for enhancing physical properties. In the case of the ionene, however, sufficient microphase separation is observed with just a single unit of the ionene containing moiety. The aromatic nature of the hard segment was varied from a benzyl dihalide to that which is more aliphatic in character due to an aliphatic ether containing linkages placed between two benzyl units. Incorporation of an ether linkage in the ionene hard segment may likely promote a greater compatibility between the PTMO soft segment and the ether containing linkage due to their inherent aliphatic character. Hence, mixing effects can be studied by this variation in the architecture of the ionene hard segment.

4.2.4 Effect of Incorporation of an Ionic Plasticizer

Makowski and Lundberg (133) have shown that zinc stearate functions effectively as a plasticizer. In EPDM systems, zinc stearate selectively plasticizes the ionic domains significantly lowering the melt viscosity as well as improving the mechanical properties. The ionene polymers soften ca. 150-180 °C depending on the PTMO molecular weight and the nature of the counterion. One of the problems encountered in processing these materials at elevated temperatures is that of degradation occurring in the ionene polymer either in the ionene segments or in the PTMO soft segments. In order for these materials to be termed as a "thermoplastic elastomer", the processing temperature needs to be lowered in order to avoid the potential problem of degradation. Incorporation of an ionic plasticizer such as zinc stearate has been shown to sufficiently lower the softening

point enabling thermal processing of the ionene elastomers by conventional techniques. The effect of zinc stearate incorporation on the structure-property relationships in these ionene materials will be investigated.

4.3 Block Ionomers

The block ionomers are a natural extension to the telechelic ionomers. There are essentially two reasons for considering block ionomers. It has been shown in random ionomers that the network structure of sulfonated ionomers were much more stable than their carboxylated counterpart due to the stronger interactions existing between the sulfonate than in the carboxylated groups. This stronger interactions has been attributed to the fact that the corresponding acids, namely sulfonic acid is a much stronger acid than carboxylic acid (133). One potential limitations of the sulfonic acid based ionomers is if these groups are not neutralized, they can undergo thermal degradation at higher temperatures. By using a sequence of carboxylate groups, the network properties similar to that of the sulfonate ionomers might be mimicked. However, a higher ion content is required in the carboxylated block ionomers in order to achieve comparable properties as that of the sulfonate ionomer. If the higher ion content does not pose any potential problem, the carboxylated block ionomers can provide an equivalent performance of the sulfonated ionomers yet will not have any deleterious effects on the bulk properties at elevated temperatures. As a consequence, one may also be able to determine the number of carboxylate groups needed to match the performance of a single sulfonate unit. This knowledge would be useful in the design of carboxylate ionomers. So far, there has been only one other study in the literature based on styrene-4-vinylpyridium block ionomers in which the structure-property relationships have been investigated (99).

5.0 EXPERIMENTAL INVESTIGATION

5.1 Materials

As mentioned earlier, the telechelic ionomers were synthesized in the laboratory of Prof. Robert Jerome at the University of Leige in Belgium. The telechelic ionomers were either based on a polyisoprene or a polybutadiene backbone. The caboxy-telechelic polyisoprene (PIP) with a $\overline{M}_n$ = 33,000 was synthesized using anionic polymerization in THF at -78 °C. The molecular weight distribution is less than 1.2, with a 3,4/1,2 ratio of 65/35 and an average acid group functionality was ca. 1.95. This functionality was determined via potentiometric titration of the acid group ends with tetramethylammonium hydroxide in a 9:1 benzene-methanol mixture. The acid groups were essentially neutralized with four different cations namely, Na, Mg, Al and Ti to different levels of neutralization. The experimental details regarding the synthesis and neutralization of carboxy-telechelic polyisoprene can be found in previous publications (71,73,79). A commercial grade of telechelic polybutadiene (Hycar CTB 2000 x 156) from BF Goodrich was used to study the structural and morphological of carboxylated telechelic PBD ionomers. The material had a $\overline{M}_n$ = 4600, molecular weight distribution = 1.8, functionality = 2.01 and cis/trans/vinyl ratio = 20/65/15. The carboxylated polybutadiene telechelic acids were neutralized with a barium salt to different levels of neutralization (60 to 200%).

A systematic series of ionene polymers have been synthesized by Leir and Stark (116) based on the reaction of α,ω-bis (dimethlyamino) polytetramethylene oxide with specific benzyl dihalides. These materials have been kindly provided by Dr. Leir's group in the Specialty Chemicals Division at 3M company. Also, the architecture of the ionene segment was varied to study the effect of phase mixing in these systems. Details relating to the bis(dimethylamino) PTMO synthesis and its subsequent reaction to form the ionene polymer can be found elsewhere (116). The reaction scheme

for the synthesis of the ionene polymers is given in Figure 5.1. An uncharged "analogue" was also synthesized to address the feature of microphase separation and compare it to the above ionene materials. The non-ionene segmented polymer consists of a PTMO soft segment and a brominated aromatic hard segment; a schematic of the resulting polymer is given below.

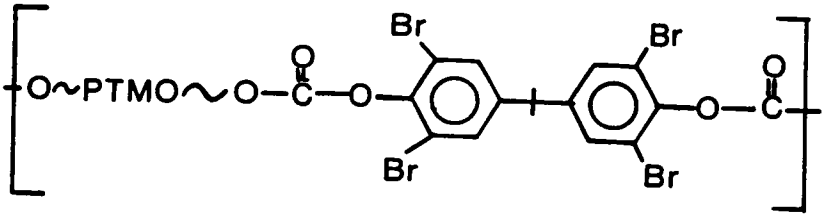

Determination of the overall molecular weight of these ionene polymers has been difficult due to the strong tendency of the ions to interact with GPC columns. Hence, only inherent viscosity (I.V.) data are available for these materials. The I.V. values obtained suggest that these materials are high molecular weight elastomers. This has been confirmed from limited experimentation conducted using low angle laser light scattering (LALLS) (116).

The carboxylated telechelic block ionomers based on alkyl methacrylates were synthesized in Prof. McGrath laboratory by Mr. C. D. DePorter in the Department of Chemistry at Virginia Polytechnic Institute & State University in Blacksburg, Virginia. The methacrylate precursors were synthesized using anionic polymerization techniques using an adduct of s-butyllithium and 1,1-diphenylethylene as the initiator using the mode of sequential addition. The rigid blocks were based on t-butyl methacrylate (TBMA, $T_g \sim 118°C$) while the elastomeric blocks were based on either n-hexyl methacrylate (NHMA, $T_g \sim -10°C$) or 2-ethylhexyl methacrylate (EHMA, $T_g \sim -27°C$). The methacrylate precursors were subsequently hydrolyzed using para-toluene sulfonic acid (PTSA) to obtain the corresponding acid form. This preferentially hydrolzes the TBMA block and does not affect the elastomeric segment (NHMA or EHMA). The hydrolyzed acid blocks are then neutralized using either KOH or CsOH (or Cs_2CO_3) to obtain the final block

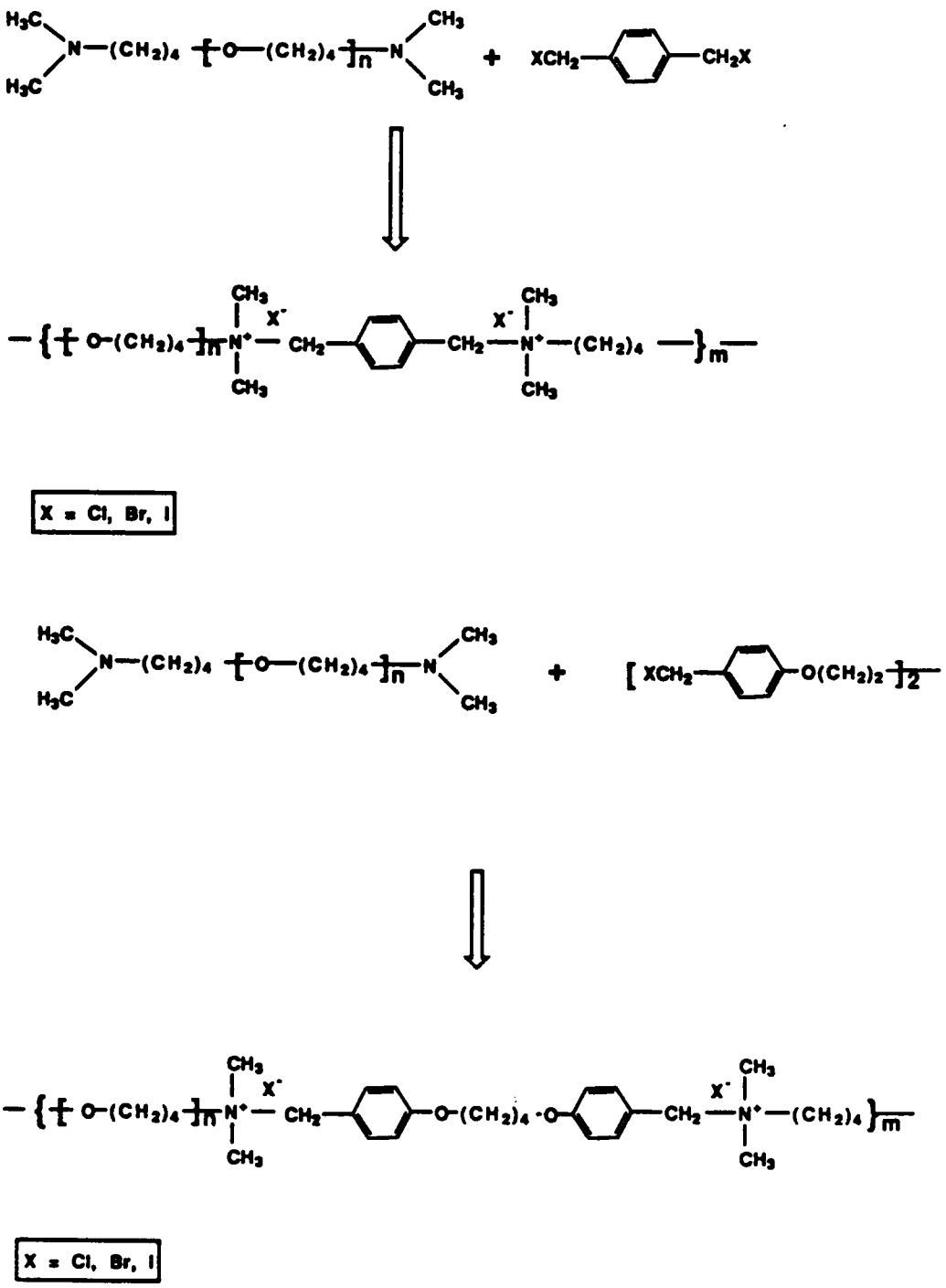

Figure 5.1. Reaction Scheme for the Synthesis of the Segmented Ionene Polymers: (a) dihalide xylene based ionenes; (b) benzyl dihalide butane based ionenes

ionomer. The details regarding the synthesis of the methacrylate esters, the process of hydrolysis and subsequent neutralization can be found elsewhere (97,189). The reaction scheme for the synthesis of the block copolymer, the hydrolysis and the neutralization procedures to obtain the final block ionomers are shown in Figures 5.2-5.4. The physical characteristics of both the diblock and the triblock ionomers are presented in Tables 5.1. The ion content in these block ionomers can be systematically varied by changing the sequence length of the TBMA blocks during the precursor synthesis. The apparent molecular weights and molecular weight distributions of the precursors were determined by size exclusion chromotography. A Waters 590 equipped with columns of 500 Å, 10^3 Å, 10^4 Å, 10^5 Å porosities in THF was used. Both poly(methyl methacrylate) and poly(styrene) standards from Polymer Laboratories were used in these characterizations.

5.2 Experimental Techniques

5.2.1 Film Preparation

The PIP ionomer samples were compression molded at 120 °C for two minutes to form films from which samples were cut for further testing. For materials with greater than stoichiometric amounts of neutralizing agent, slightly higher temperatures and/or molding times were used to obtain a uniform film. Uniform films of the ionene materials were solution cast slowly at ambient conditions from chloroform on a teflon surface. The block ionomers were directly cast on a teflon surface soon after the neutralization step. All the ionomer materials were maintained in a dry atmosphere (vacuum sealed desicator) prior to testing.

To prepare the plasticized ionene samples, required amounts of the zinc stearate powder were added to the ionene solution in chloroform. The resulting solution was cast on a teflon surface once a uniform suspension was obtained. The solution casting process was again carried out at ambient conditions. The plasticized ionene films that was obtained from the solvent casting process was later compression molded at 120 °C for 2 minutes giving a uniform film for further characterization.

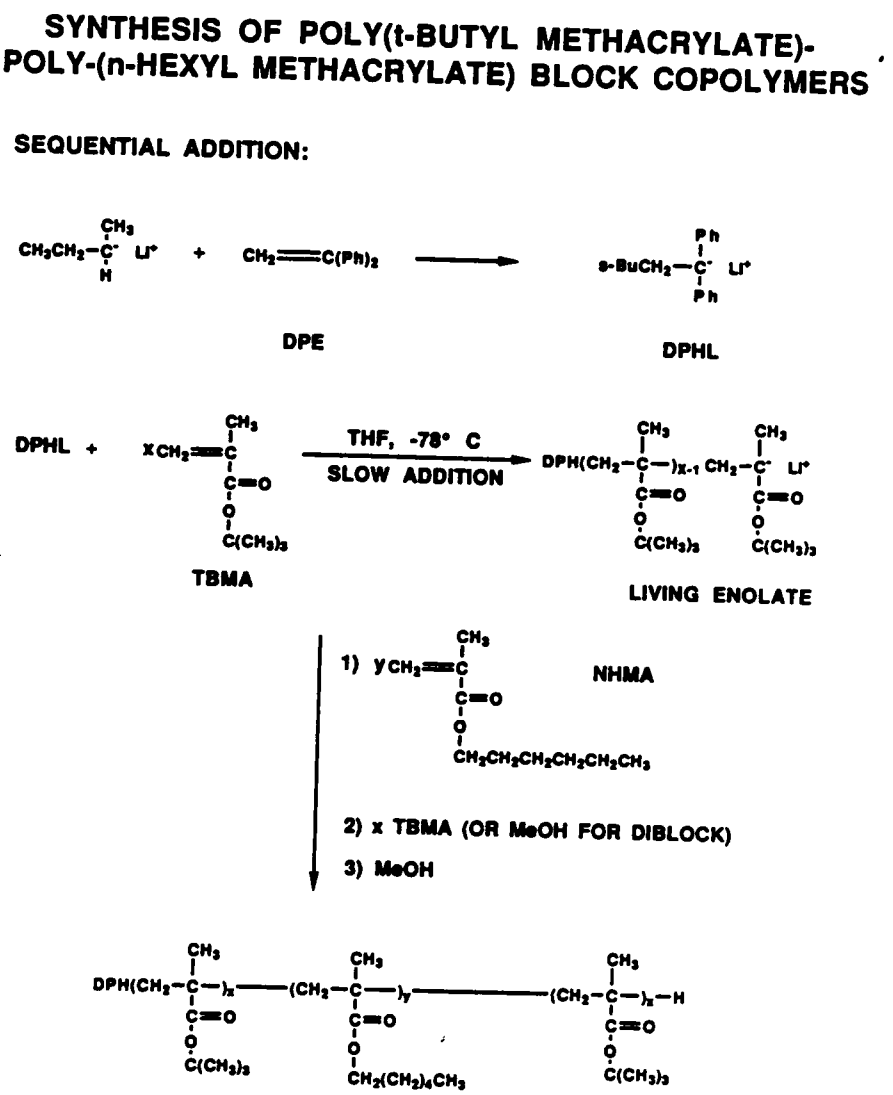

Figure 5.2. Reaction Scheme for the Synthesis of the NHMA-TBMA Block Copolymer: From (206).

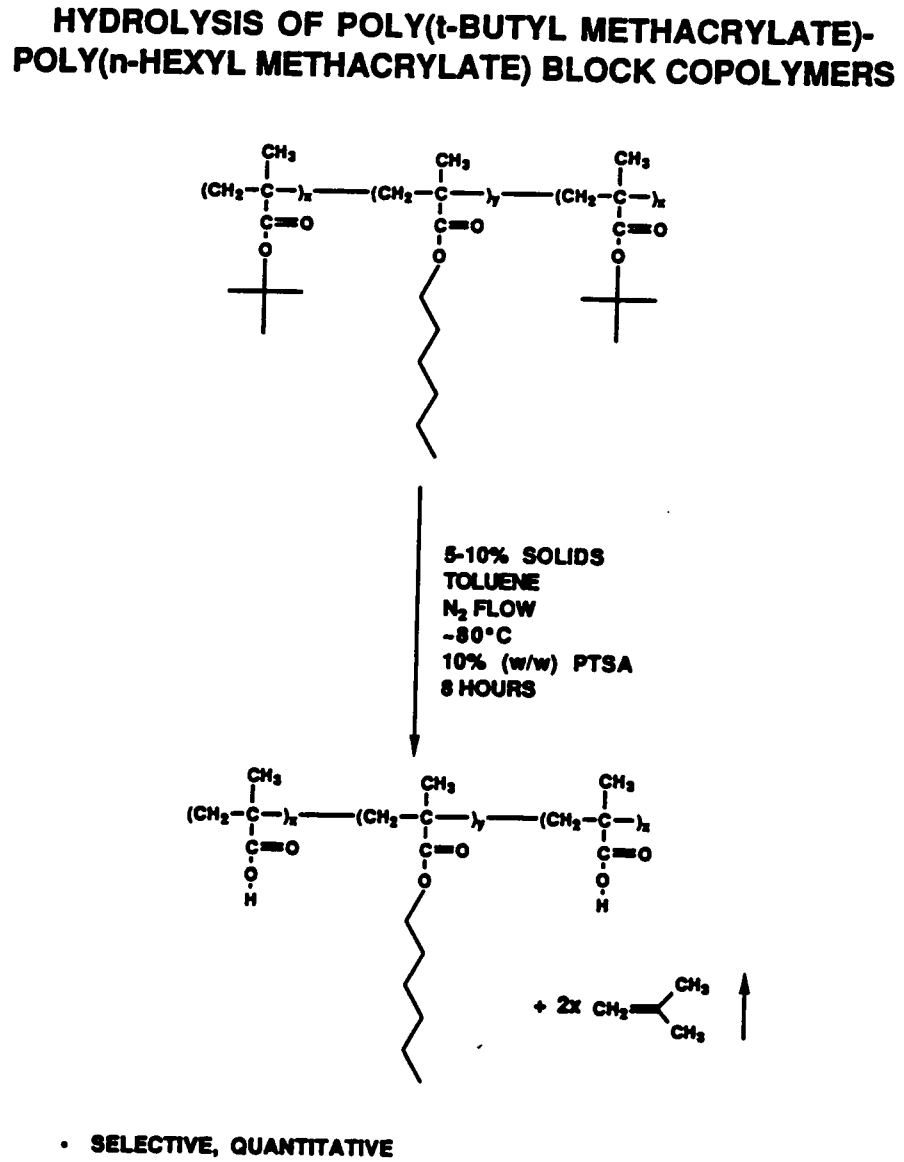

Figure 5.3. Reaction Scheme for the Hydrolysis Procedure to Obtain NHMA-TBMA Block Acid: From (206).

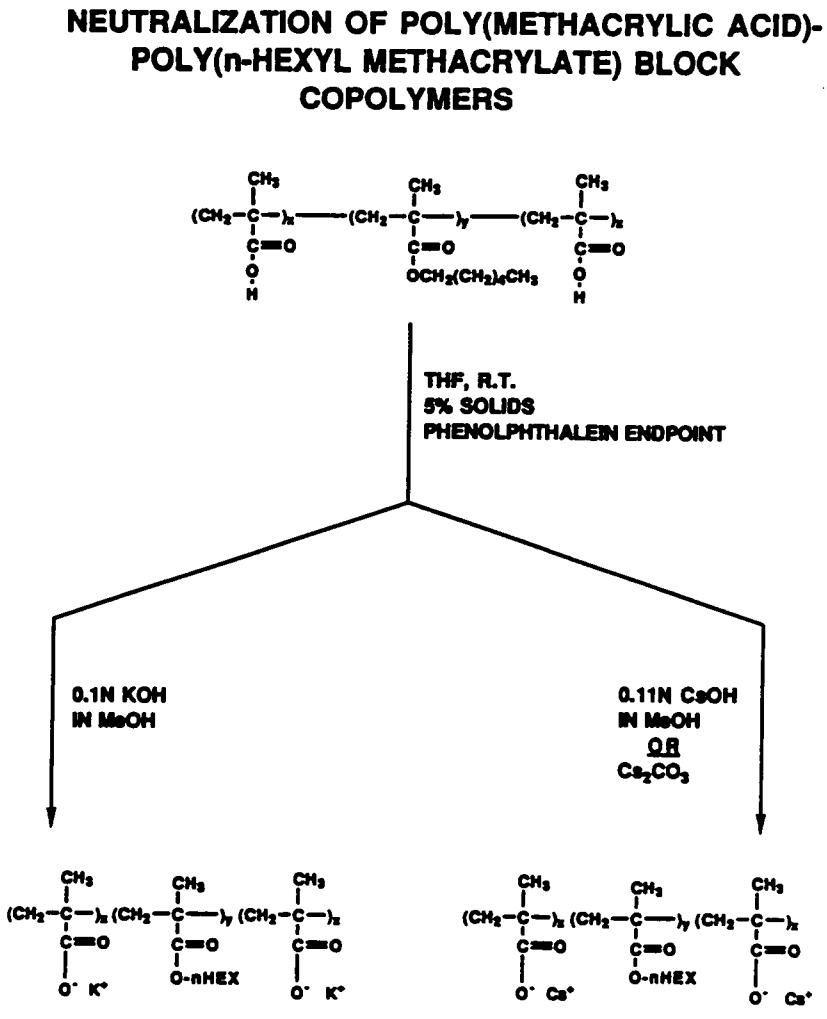

Figure 5.4. Reaction Scheme for the Neutralization Procedure to Obtain NHMA-TBMA Block Ionomer: From (206).

Table 5.1. Physical Characteristics of NHMA/TBMA Block Ionomers

SAMPLE	Total $\overline{Mn}$	Mw/Mn	NHMA Block mol. wt.	TBMA Block mol. wt.	# per TBMA Block
NT-98/2 (Cs)	52,900	1.16	51,842	1,058	8
NT-96/4 (Cs)	56,500	1.21	54,240	2,260	17
NT-94/6 (Cs)	53,600	1.20	50,384	3,216	25
NT-90/10 (Cs)	55,200	1.13	49,680	5,520	42
TNT-2/96/2 (Cs)	48,900	1.26	46,944	978	8
TNT-3/94/3 (Cs)	51,600	1.28	48,504	1,548	12
TNT-5/90/5 (Cs)	47,100	1.40	42,390	2,355	18

To study the processability of the ionene material, one of the samples (IB-NS-14) was compression molded at 180 °C for five minutes and quickly quenched to ambient conditions. Later, the samples was annealed at 70 °C in a vacuum oven. Samples at frequent intervals were removed to perform the tensile test.

5.2.2 Mechanical Properties

The tensile studies were conducted in an Instron Model 1122. Dog-bone samples measuring 10mm in length (gauge) and 2.8mm in width were tested at an initial strain rate of 20mm per minute for the telechelic and block ionomers and at 50 mm per minute for the ionene materials. The Young's modulus was calculated from the initial portion of the load-time profiles. The load-time profiles were digitized to obtain the stress-strain (or elongation) curves for the different materials.

Stress relaxation experiments were carried out on a Tensilon Model VTM-II (Toyo Measuring Co.) due to the excellent stability of this instrument over long periods of time. Samples were strained at 400% per minute to 25%, and the stress was monitored as function of time.

The creep experiments were conducted at room temperature by applying a specified load and monitoring the sample displacement as a function of time using a LVDT (linear voltage displacement transducer). The tensile creep compliance, D(t), was calculated from these data.

5.2.3 Dynamic Mechanical Analysis

For the dynamic mechanical analysis (DMA), the dynamic mechanical spectra were obtained using an autovibron viscoelastometer (Model DDV-II-C) (IMASS) which operates in a tensile mode. The dynamic storage modulus, E', the loss modulus, E'', and the loss tangent, tan δ, were obtained at a heating rate of 2 °C per minute. These parameters were determined as a function of temperature (-150 °C to 200 °C) at a frequency of 11 Hz.

5.2.4 *Thermal Analysis*

Thermomechanical analysis (TMA) was performed using a Perkin-Elmer TMS-2. The samples were scanned in the temperature range from -100 °C until softening (up to 200 °C) at a heating rate of 10 °C per minute, and the penetration of the probe under a 10g load was monitored. TMA experiments were performed under a nitrogen atmosphere.

Differential scanning calorimetry (DSC) was performed on a Perkin-Elmer DSC-4 over the range of 20 °C to 180°C at a scan rate of 10 °C per minute. The DSC experiments were performed under a nitrogen atmosphere.

5.2.5 *X-Ray Scattering*

The small angle x-ray scattering (SAXS) experiments were conducted on an automated Kratky slit collimated camera. The primary x-ray source was obtained from a Phillips PW1316/91 Cu tube operated at 40 kV and 20 mA by a Phillips generator PW1729. Cu K_{α} radiation with a wavelength of 1.542 Å was obtained from a copper target after nickel foil filtering. The scattered intensity was monitored by a one-dimensional position sensitive detector (M. Braun - Innovative Technology Inc.).

The wide angle experiments were conducted on a Phillips table-top x-ray generator model PW1170 equipped with a standard vacuum sealed Warhus photographic pinhole camera. The exposure times varied depending on the samples thickness, the sample composition and the placement of the photographic film cassette. To study the presence of strain induced crystallinity, the samples were strained to the required strain level and clamped in a rigid sample holder and mounted within the Warhus camera.

5.2.6 Electron Microscopy

5.2.6.1 Transmission Electron Microscopy

A Phillips EM-420 scanning transmission electron microscope (STEM) was operated in the transmission mode at 100 kV. Objective and condenser apertures of 30 and 50 μm, respectively, were used. Ultrathin sections of the block ionomer samples were microtomed at ca. -60 °C using a Reichert-Jung ULTRACUT System FC-4. Hexamethyl disiloxane was used as a liquid substrate to float the microtomed sections. The TEM micrographs were obtained by Mr. G. A. York in the Department of Materials Engineering at VPI&SU. His assistance is greatly appreciated.

5.2.6.2 Scanning Electron Microscopy

A Cambridge Instruments Stereoscan 200 scanning electron microscope (SEM) with a secondary electron detector was used to obtain micrographs of fractured surfaces. Fractured surfaces were prepared by breaking the samples that had been cooled in liquid nitrogen (-176 °C) for 15-25 minutes. Specimen surfaces were coated with a 150 Å layer of gold in a Surface Probe Inc. sputter-coater for contrast and painted with conducting silver paint to prevent charging. The assistance of Dr. L. Lopez is greatly appreciated in obtaining the SEM micrographs.

5.2.7 Rheological Measurements

The rheological measurements for the ionene polymers were conducted on a Rheometrics Mechanical Spectrometer (Model RMS-800) under a nitrogen atmosphere. All the measurements were conducted using the parallel plate (2.5 cm diameter) geometry. Frequency sweep measurements were conducted in the dynamic oscillatory mode at a constant strain of 7%. The non-isothermal cooling experiments were also conducted in the dynamic oscillatory mode at a frequency of 10 rad/s and at a strain of 7%. The jump strain experiments were conducted using an initial strain of 50%. The assistance of Ms. Alice Wilson and Dr. D. Done in Prof. D. G. Baird's laboratory is greatly appreciated.

6.0 STRUCTURE-PROPERTY STUDIES OF TELECHELIC IONOMERS

As discussed in Chapter IV, most of the morphological characterization of ionomers has been conducted on random ionomers. Since the location of the ionic groups is not well defined in these ionomers, relating the morphological observation from small angle x-ray scattering (SAXS) measurements to the observed properties has generally presented a problem. In the linear telechelic ionomers, however, the ionic groups are located at each of the chain ends. Hence, the telechelic ionomer can be considered as an ideal candidate to study the nature of ion aggregation in ionomers. However, only a few investigations have attempted to study the morphological features of these systems (5,29,82-84). Previous studies of the carboxy-telechelic ionomers by small angle x-ray scattering (SAXS) have indicated that they may form more layer-like or lamellar-type morphology rather than the spherical clusters postulated for random ionomers (39-42). In addition, in a prior dissertation from our laboratory, a distinct but broad SAXS peak or "ionic peak" which is indicative of the presence of a periodicity in the system,has sometimes been observed in the difunctional and trifunctional sulfonated polyisobutylene telechelic ionomers (187). Furthermore, an ionic peak was observed below a critical molecular weight for these materials, but not above. This molecular weight for the sulfonated telechelic polyisobutylene ionomers was ca. 10,000 $\overline{M}_n$.

Different models have been proposed in order to correlate the observed SAXS behavior to the morphology of ionomers. Most of these models have been system specific and have not yet been able to fit the observed SAXS data for all ionomers. Hence, there has been considerable controversy regarding the nature of ion aggregation in ionomers. In fact, all the morphological models to date have been formulated based on the information obtained from the observed features in random ionomers. The author believes that a part of the problem lies in the fact that the placement of the ions in random ionomers is not well defined. The telechelic ionomers, on the other hand, provides

an opportunity to study the nature of ion aggregation without the added uncertainty regarding the placement of the ions.

6.1 Chemical Structure and Nomenclature

As mentioned earlier, the carboxylated telechelic PIP ionomers were prepared anionically to obtain the required molecular weight of the non-ionic segment. The terminal acid groups were subsequently neutralized to form salts of different cations. For the present study on telechelic PIP ionomers two molecular weights of the non-ionic segments were considered (15,000 and 33,000 $\overline{M}_n$). The general bulk characterization of the PIP 15,000 $\overline{M}_n$ carboxylated ionomers have been previously studied by Tant et al. (187). The general bulk characterization of the 15,000 $\overline{M}_n$ sulfonated ionomers has been conducted in this study and compared to that of the corresponding carboxylated ionomers. Determining the overall properties and relating them to the morphological features obtained from small angle x-ray scattering has been conducted on both the PIP 33,000 and 15,000 $\overline{M}_n$ ionomers. The nomenclature used is best described by an example:

Sample	**PIP-33000-Al-1**
ITEM	DESCRIPTION
PIP	**Nature of the backbone polymer**
	PIP = polyisoprene; PBD = polybutadiene
33000	**$\overline{M}_n$ of the backbone polymer**
Al	**Type of the Cation**
	Na = sodium; Mg = magnesium; etc.
1	**Extent of Neutralization (%) x 10^{-2}**
	1 = 100% (0% excess or endpoint neutralized); 2 = 200% (100% excess) or X (in general)

6.2 The Effect of Molecular Weight of the Non-ionic Segment

The effect of the molecular weight of the non-ionic segment has been previously studied (83,187). The studies revealed that both the modulus and the stress at constant strain, increased with increasing molecular weight. This is not very surprising since it is anticipated that the number of entanglements per chain would increase as the molecular weight increases. It has been suggested that at lower molecular weight, the ionic interactions dominate, while chain entanglements dominate at higher molecular weight. Therefore, there exists a molecular weight where a cross over between the two modes of interaction takes place. Based on viscoelastic studies, Broze et al. (82) have determined that for magnesium-neutralized PIP linear ionomers, the transition in the observed behavior occurs at ca. $\overline{M}_n = 20{,}000$. It was also shown by Tant et al. (83) that the trend is reversed for the ionomer neutralized with higher valent cations such as titanium (Ti) and zirconium (Zr). At lower molecular weight these materials display a higher modulus and higher stress than what was observed for the divalent barium or magnesium ionomers. This is essentially due to differences in the nature of the interaction between the ions in these two systems. For the ionomers neutralized with K or Mg the interactions are mainly ionic while for the materials neutralized with the ions of transition metals (such as Ti or Zr) the interactions are more covalent in nature. Therefore, the higher valent cations form inorganic bridges (or crosslinks) which are likely polyfunctional (≥ 3) and would therefore display a more network-like character than the barium material. A lower molecular weight would then lead to a higher apparent crosslink density which would result in the observation of higher stresses.

To study the effect of the cation on the bulk properties, 33,000 $\overline{M}_n$ PIP ionomers, which have been neutralized with different cations and to different levels of neutralization, have been investigated. The different cations include Na (a monovalent cation), Mg (a divalent cation), Al (a trivalent cation), and Ti (a tetravalent cation).

6.3 Effect of the Type of the Cation and the Extent of Neutralization

6.3.1 Mechanical Properties

It is known from electrostatics that the force of attraction, F, between an anion of charge e_a and a cation of charge e_c is directly proportional to the product these charges and is inversely proportional with both the dielectric constant of the medium and the square of the distance of separation, "a", between them, i.e.

$$F = (\frac{1}{\varepsilon})(\frac{e_a e_c}{a^2}) \tag{6.1}$$

Assuming a primarily electrostatic or ionic interaction is present, it is apparent that the two variables of importance are the size (i.e., the radius of the cation which determines size) and the valence of the cation. The force of attraction should, therefore, increase with increasing valence and decreasing size of the cation.

Figure 6.1 shows the stress-strain behavior for the caboxy-telechelic polyisoprene ionomer of molecular weight 33,000 $\overline{M}_n$ and neutralized with Na, Mg, Al, and Ti to different levels of neutralization. For the endpoint neutralized ionomers, the stress-strain curves for the Na and Mg (curves A and C in Figure 6.1a) are quite similar up to a strain of ca. 200%, while at higher strains the Mg material exhibits a higher stress at a given strain. The ion content in these 33,000 $\overline{M}_n$ ionomers is ca. 0.4 ionic groups per 100 PIP repeat units. The initial response of the Na and Mg materials is not surprising since the initial viscoelastic response of the material is primarily from the PIP backbone chain. Only at higher extensions does the effect of the nature of cations play a role. At large strains, the Mg material exhibits a higher stress at a given strain than the Na material. This difference is believed due to the fact that the radius of a Mg ion (0.65 Å) is smaller than that of a Na ion (0.95 Å), resulting in a higher attractive force and, hence, a stiffer material. However, the trivalent Al material (curve A of Figure 6.1b) consistently exhibits a lower stress than either of the endpoint neutralized Na or Mg materials. Jerome et al. (82), from dynamic mechanical measurements, have suggested that the average number of Al ions per ionic aggregate is small, which indi-

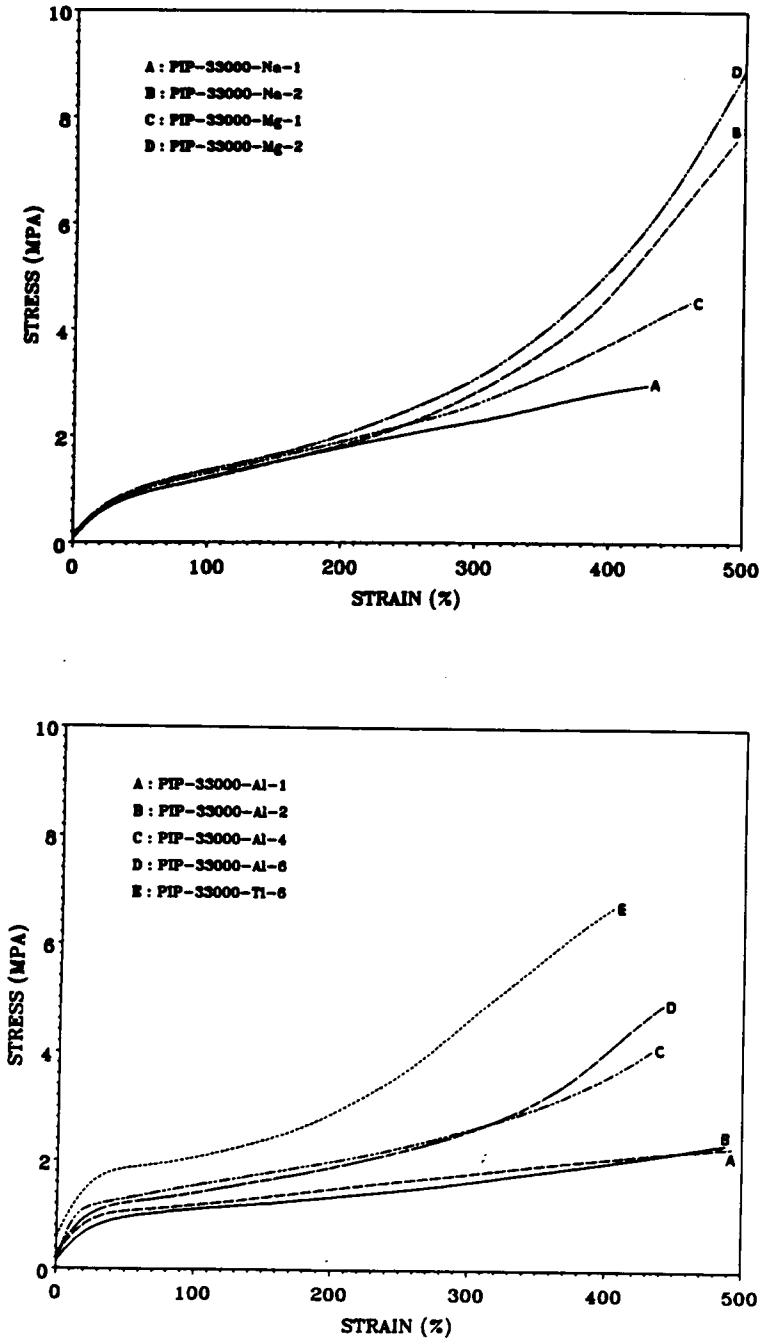

Figure 6.1. **Stress-Strain Behavior of the PIP-33000-M-X series:** (a) Na and Mg ionomers, (b) Al and Ti ionomers

cates that the Al ions are weakly associated in the ion aggregate. The association of the Al carboxylated end groups is strongly limited partly by the less metallic character of Al, which is responsible for the weaker ionic interactions of the Al carboxylates, and partly by the steric hindrance to a more compact packing of the Al ions (82).

With the addition of excess neutralizing agent (twice the stoichiometric amount), both Na and Mg materials exhibited a higher stress at a given strain (strain $\geq$ 250%). There are two possible reasons for the observed behavior. It should be remembered that with the addition of stoichiometric amounts of the neutralizing agent, often, not all the carboxylic acid groups are neutralized. Navratil and Eisenberg (57) have postulated that the un-neutralized acid groups usually plasticize the ionic domains. With the addition of excess neutralizing agent these un-neutralized acid groups are neutralized, resulting in a higher crosslink density in the system. The excess neutralizing agent is believed to preferentially surround the existing ionic domains, and they reinforce the ionic associations. Strengthening the associations within the ionic aggregates helps to reduce the ion hopping phenomenon which is believed to exist in ionomers (93).

There is apparently little difference in the stress-strain behavior of the Al materials with the addition of twice the stoichiometric amount of neutralizing agent. However, there is a considerable increase in the stress-strain behavior with the addition of four times the stoichiometric amount (curve C in Fig. 6.1b). Jerome et al. (82) have reported that neutralization of the transition metals, such as Ti and Zr, with stoichiometric amounts of alkoxides is often incomplete, due to the high steric hindrance of the four alkoxy groups which prevent complete neutralization of the acid groups in the telechelic polymer. A considerable excess of the alkoxide reagent is added to ensure complete neutralization (about one Ti [or Zr] alkoxide per chain end). Using a similar analogy as that used for the transition metals, one can assume that complete neutralization of the acid groups occurs when four times the stoichiometric amount of neutralizing agent is added. On complete neutralization not only the does the crosslink density or crosslink functionality increase, but also the free acid groups which could plasticize the ionic domains are removed.

Finally, the Ti ionomer displays a much higher stress at a given strain than the Al ionomer for the cases in which six times the stoichiometric amount of neutralizing agent was used in both the

systems (curves D and E in Figure 6.1b). With more than the recommended amount of neutralizing agent, it can safely be assumed that complete neutralization of the carboxylic acid groups must have taken place in both ionomers. The ion aggregates in the Ti ionomer are expected to be much larger than the aggregates in the Al ionomer, due to the presence of four alkoxide groups in the Ti aggregate, as compared to three alkoxide groups in the Al aggregate. The larger ion aggregates in Ti materials could also act as a reinforcing filler, which is then responsible for the higher stress at a given strain in these materials.

The tensile creep and the stress relaxation curves for the series of 33,000 $\overline{M}_n$ PIP telechelic ionomers is shown in Figures 6.2 and 6.3. Comparing the creep curves of endpoint neutralized materials for Na and Mg ionomers (curves A and C in Figure 6.2a), it is seen that the divalent Mg ion exhibits a greater network stability. Again, as in the stress-strain experiments, the smaller cation (Mg) provides a greater resistance to flow due to a higher attractive force (smaller "a") as well as due to its higher cation valence (see equation 6.1). However, the endpoint neutralized Al ionomer exhibits an onset of flow at an earlier time which is indicative of a weaker network stability. The nature of the interaction of Al ions is more covalent and less ionic in character which results in a poorer association of the Al ions in the aggregate. As mentioned earlier, more than the stoichiometric amount of aluminium alkoxide is required for complete neutralization of the acid groups. Therefore, the plasticization of the ionic groups by the un-neutralized acid groups may indeed be responsible for the weaker network stability that promotes an earlier onset of flow.

As expected, considerable increase in the network stability was observed with the addition of excess neutralizing agent for all the three cations studied (Na, Mg and Al). Comparing the network stability of Al and Ti ionomers neutralized with six times the stoichiometric amount of the neutralizing agent (curves D and E in Figure 6.2b), the Al ionomer exhibits a greater network stability than the Ti ionomer. Recall from the stress-strain measurements, the Ti ionomers maintained a higher stress at a given strain than the Al ionomer. As mentioned earlier, the Ti ions form larger ionic aggregates, but the strength of the interactions within the aggregates is weaker when compared to the Al aggregates. The interactions within the Ti domains are more covalent (less ionic) than that present within the Al domains. Therefore, at shorter time scales, the larger ionic domains of the

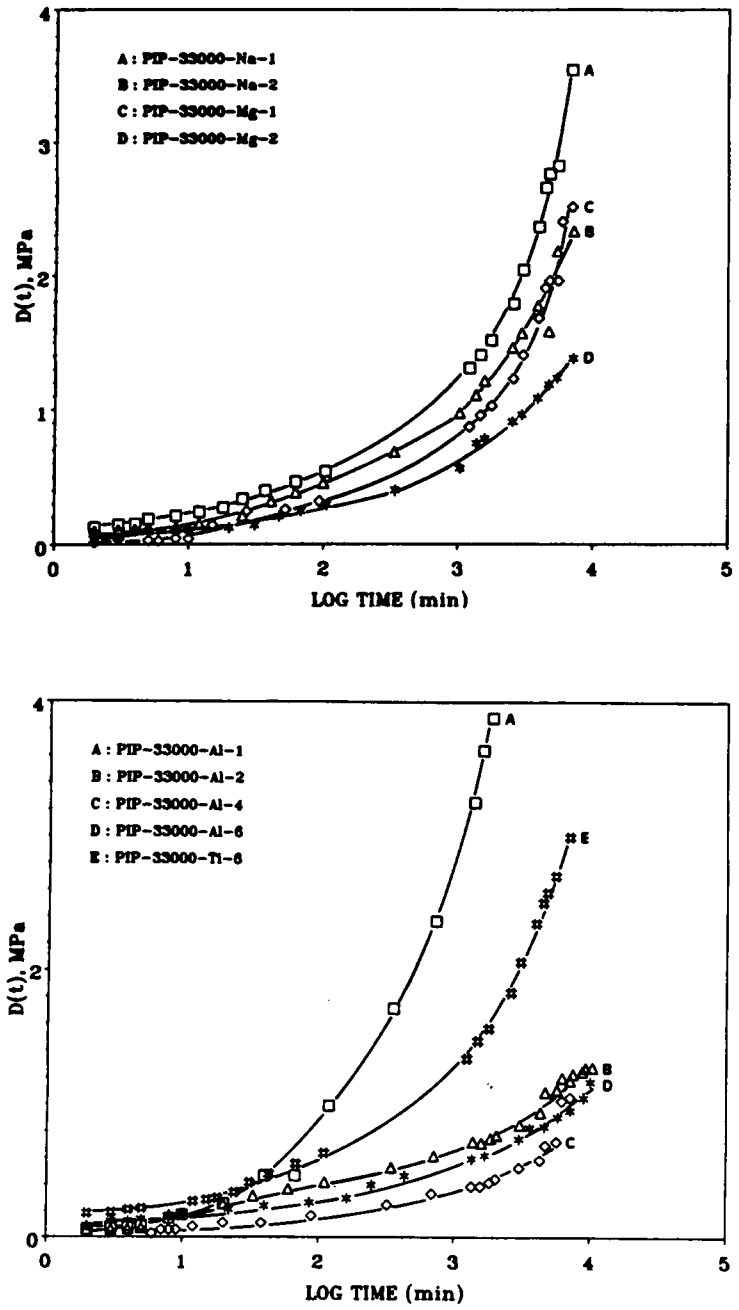

Figure 6.2. Tensile Creep Curves of PIP-33000-M-X Ionomers; σ_0 = 0.03-0.05 MPa: (a) Na and Mg ionomers, (b) Al and Ti ionomers

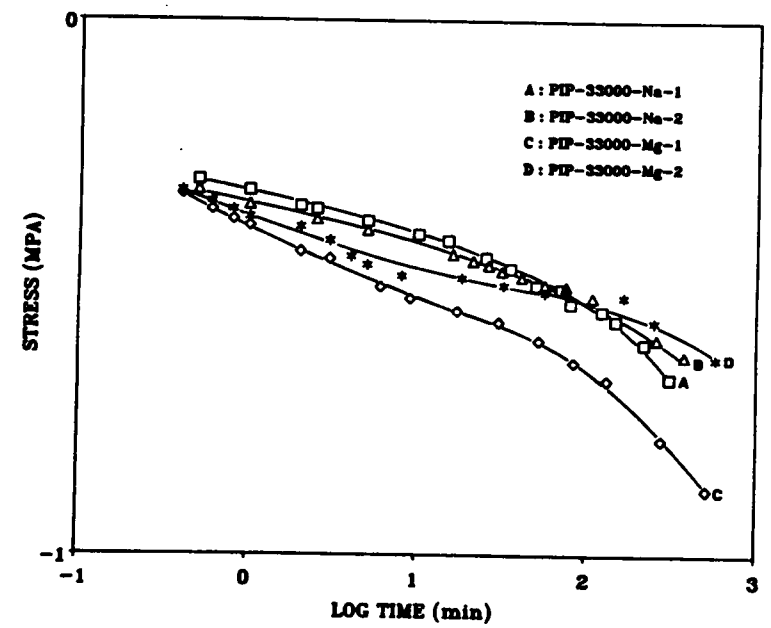

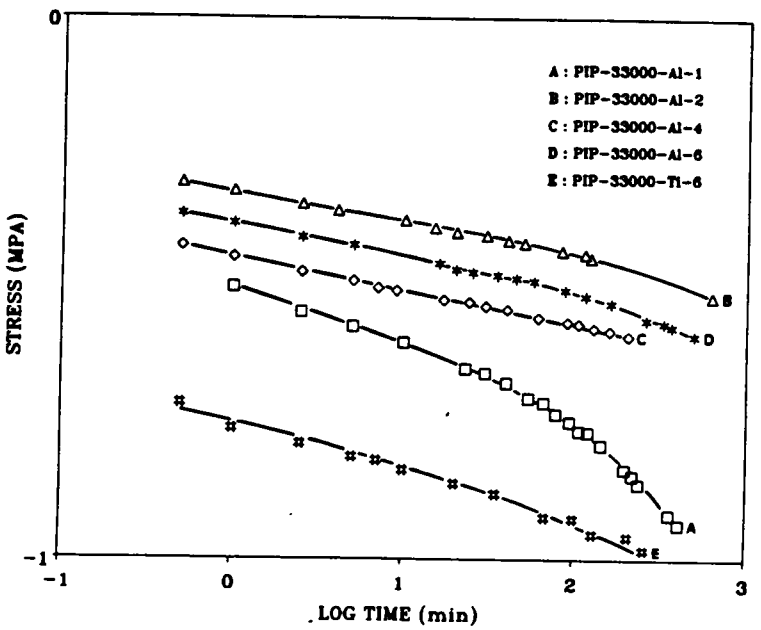

Figure 6.3. Stress-Relaxation Curves of PIP-33000-M-X Ionomers; $\lambda = 1.25$: (a) Na and Mg ionomers, (b) Al and Ti ionomers

Ti ionomer act as a reinforcing filler, which is responsible for the observed stress-strain behavior. At larger time scales, the aggregates in the Al ionomers are more stable due to the stronger association within the Al ions which is reflected in the observed tensile creep behavior.

Figure 6.3 shows the stress relaxation curves at an initial strain of 25% for all the 33,000 $\overline{M}_n$ telechelic ionomers. The reader should not take the stress values in this particular experiment as absolute because a drift was noticed for the full-scale load during the calibration procedure. Since the stability of the instrument was good over long periods of time, the data relating to the long term stability of the samples were of primary interest. Comparing the stress-relaxation curves of the endpoint neutralized Na and Mg ionomers (curves A and C in Figure 6.3a), the Mg material displays a rather rapid decrease in stress, suggesting a weaker network stability than the Na material, which is quite contrary to the observed behavior from the creep experiments. It is not apparent at this point as to why this should occur, especially when the tensile creep compliance (curve B in Fig. 6.2a), also indicative of the network stability, does not reflect a similar behavior. The endpoint neutralized Al material displays a weaker network character that is consistent with the observation from both stress-strain as well as from the tensile creep experiments. The remaining ionomers essentially maintain the stress over the entire time scale of the experiment (~ 1000 minutes). Tant et al. (187) have reported that the onset of flow for the 15,000 $\overline{M}_n$ endpoint neutralized Na and Mg PIP ionomers occur in the time interval between 10 and 100 minutes. The 33,000 $\overline{M}_n$ ionomers neutralized with the different cations maintain the applied stress for over 1000 minutes. The greater network stability of the 33,000 $\overline{M}_n$ ionomers is apparently due to the larger number of entanglements per chain which is anticipated due to its higher molecular weight.

6.4 Morphlogical Features of PIP Telechelic Ionomers

As mentioned earlier, the technique of small angle x-ray scattering (SAXS) provides information regarding the morphology of the system based on the differences in the local electron density. For a two phase system, the scattering theory has been well developed and has been discussed in detail in Chapter 3. It has been proposed that there are essentially two types of environments ex-

isting in ionomers, namely, ionic domains and the non-polar matrix, which provides the electron density contrast necessary for x-ray scattering. Indeed, SAXS has been routinely applied to obtain information regarding the periodic spacing between regions of similar electron density as well as the nature of phase separation of the dispersed phase (ionic domains in the present study).

6.4.1 Interdomain Spacings

The SAXS profiles of carboxy-telechelic PIP 33,000 $\overline{M}_n$ ionomers neutralized to different levels are shown in Figure 6.4. For the Na and Mg ionomers (curves A to D in Figure 6.4a), no evidence of a scattering or "ionic" peak is observed. The presence of an ionic peak has been considered evidence of ion aggregation since it was first reported (20). The absence of an ionic peak may be due to the absence of ion aggregation, the absence of periodicity between the ionic aggregates, or when the electron density difference between the ionic domains and the backbone matrix is too small to be detected. Recall that the ion content in the PIP 33,000 $\overline{M}_n$ ionomer is ca. 0.4 ionic groups per 100 PIP repeat units. Therefore, it is believed that the absence of the ionic peak is more likely to be due to the low concentration of ions coupled with the fact that both Na and Mg are poor scatterer of x-rays. This conclusion, which supports the presence of a network structure, is further supported from the observed mechanical properties As noted by others, a distinct upturn at low angles has been observed for all the ionomers with the upturn being more pronounced with increasing levels of neutralization. This is quite contrary to what was observed by Williams et al. for PBD ionomers (84). It has been proposed that the "zero-angle scattering" may either be due to very large domains or from isolated ion pairs being distributed throughout the system. Based on the physical evidence, the upturn is believed to be caused by the isolated ion pairs which are heterogeneously distributed in the system. This conclusion also supports the observation in this study that the zero angle scattering increases with increasing levels of neutralization. It should be emphasized that the origin of the upturn at low angles is still an unresolved problem.

For the endpoint neutralized Al ionomer (curve A in Figure 6.4b), again, no evidence of the ionic peak was observed. However, with increasing levels of neutralization, a distinct development of an ionic peak was observed for the Al materials (curves B to D in Figure 6B). A very broad ionic

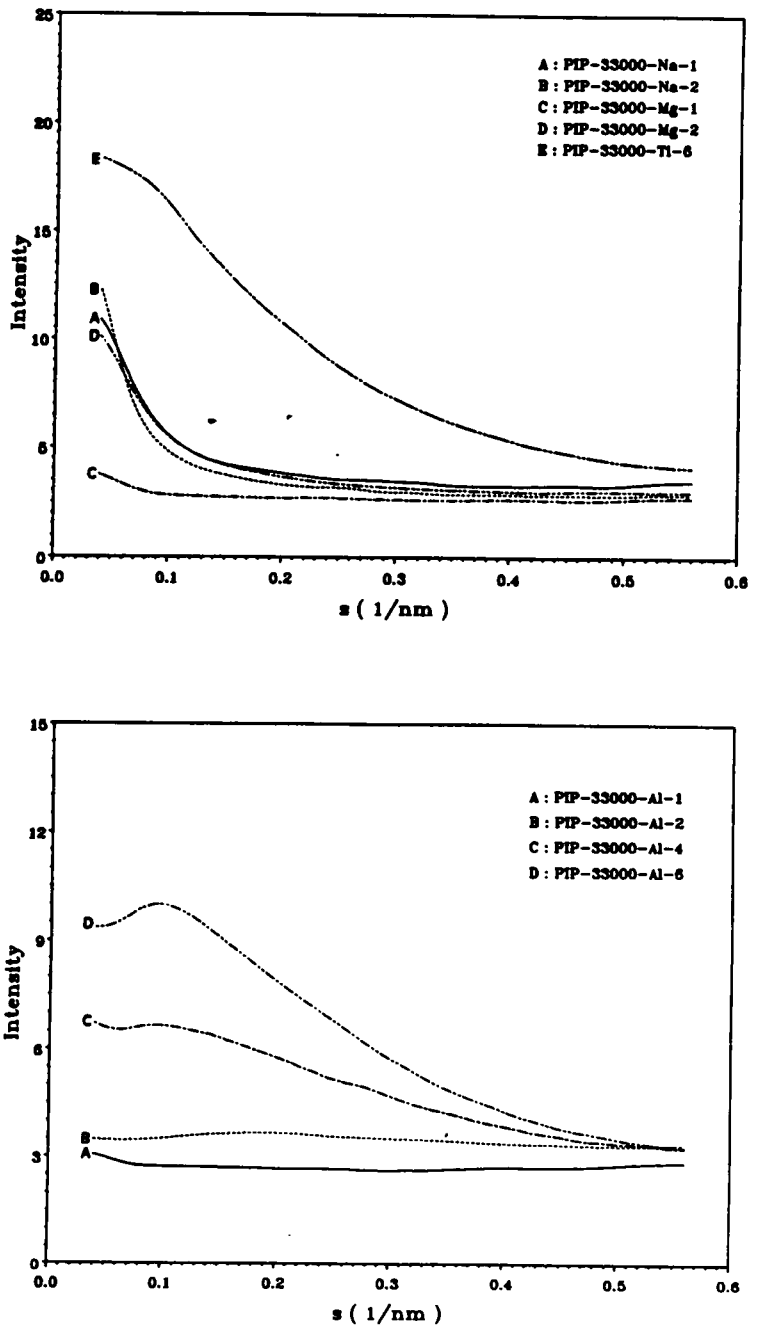

Figure 6.4. **Small Angle X-Ray Scattering Profiles of PIP-33000-M-X Ionomers:** (a) Na, Mg and Ti ionomers, (b) Al ionomers

Table 6.1. Periodic Spacing Between the Ionic Domains in 33000 $\overline{M}_n$ Carboxy-Telechelic PIP Ionomers as Determined by SAXS Analysis

Sample-id	Periodic Spacing between the Ionic Domains, (in nm)			
	$d_{smeared}$	$d_{desmeared}$	$\gamma_1(D)$	$\gamma_3(D)$
PIP-33000-Na-1	*	*	*	*
PIP-33000-Na-2	*	*	*	*
PIP-33000-Mg-1	*	*	*	*
PIP-33000-Mg-2	*	*	*	*
PIP-33000-Al-1	*	*	*	*
PIP-33000-Al-2	5.5	4.6	*	*
PIP-33000-Al-4	8.9	7.7	*	*
PIP-33000-Al-6	10.8	8.4	*	*
PIP-33000-Ti-6	16.2	*	*	

* - not available

peak is discernible for the Al ionomer neutralized to twice the stoichiometric amount (curve B in Figure 6.4b). From the position corresponding to the maximum in the scattering profile, a smeared spacing of 5.5 nm, which corresponds to a desmeared spacing of 4.6 nm, was observed. The desmearing procedure of the smeared scattering profile was carried out using Vonk's program (162). The desmearing procedure usually shifts the scattering profile to higher "s" values or lower "d" spacings. As discussed earlier, with the addition of twice the stoichiometric amount of neutralizing agent in the Al material, it is believed that not all the acid groups are completely neutralized. Hence, the weak scattering peak is due to a low concentration of the ionic groups in the system. With the addition of excess neutralization, a distinct development of an ionic peak is observed with the peak moving to lower scattering angles (from 7.8 nm for PIP-33000-Al-4 ionomer to 8.4 nm for the PIP-33000-Al-6 ionomer). Table 6.1 provides the periodic distances (or the "d" spacing) between the ionic domains for the 33,000 $\overline{M}_n$ carboxy-telechelic ionomers. The spacings have been obtained from the desmearing procedure and also from the analysis of the 1-D and 3-D correlation functions. The systematic increase in the interdomain spacing seems to favor the "interparticle interference" model rather than the "intraparticle interference" model. Other researchers who have studied telechelic ionomers have also arrived at this conclusion (84,99). As far as the author is aware, such a pronounced ionic peak has not been observed before in any other telechelic ionomers, especially at low levels of ion content. It is believed that the regular placement of the ions (at the chain ends) facilitates the aggregation process, which may be the reason for observing the ionic peak at such low ion concentrations. Most of the earlier investigations of telechelic ionomers with low ion content have been conducted on endpoint neutralized materials. Therefore, the ionic peak was not observed in those materials, whereas in the present study the ionic peak is observed in the Al materials containing more than one Al isopropoxide per chain end. The excess neutralizing agent essentially ensures complete neutralization of the acid groups. As stated earlier, it is speculated that the excess ions tend to surround the existing ionic aggregates, enhancing the scattering contrast of these ionic domains (188). This may be the reason why the ionic peak is observed only in the materials having excess neutralizing agent and not in endpoint neutralized materials. The ionic peak

has also been observed in the Ti ionomer which has been neutralized to six times the stoichiometric amount. This observation is consistent with the earlier explanation.

6.4.2 Diffuse Boundary Analysis

The analysis of the tail region provides information regarding the state of phase separation in these systems. For the ionomers in which the ionic peak was absent (curves A to D in Figure 6.4a and curves A and B in Figure 6.4b), it was estimated that the observed contribution to the tail region was essentially due to thermal background scattering. Hence, no further quantitative analysis could be made. Since the tail region was nearly flat for the all the ionomers, the thermal density fluctuations were estimated using Bonart's method. The estimated contribution due to thermal density fluctuations or background scattering was then removed from the observed scattering profile. Table 6.2 lists the interfacial or the diffuse boundary thickness values estimated from different methods. It can be seen that the interfacial thickness value is close to zero, irrespective of the method used for determination. This suggests that the interfacial region between the ionic and the organic phases are very sharp. A similar result was also obtained by Williams et al. (84) for both PBD and PIP ionomers. Figure 6.5 shows a schematic representation of a sharp boundary ($\sigma = 0$) and a diffuse boundary ($\sigma > 0$) for the caboxy-telechelic ionomers. This high degree of phase separation in these ionomers is responsible for their thermoplastic character. Ophir and Wilkes (189) have suggested that the interfacial thickness value can only serve as a relative parameter which is useful when comparing similar materials. Therefore, comparison of the interfacial thickness parameter in different systems has to be carried out with caution.

6.4.3 Degree of Phase Separation

As discussed in Chapter 3, the degree of phase separation can be estimated from the different ratios of the mean electron density fluctuations in the system. The ratios given in equations 3.55 to 3.57 provide information regarding the nature of aggregation of the ions in the system. The different ratios determined in this study are summarized in Table 6.3. To estimate the theoretical

Table 6.2. Diffuse Boundary Thickness Values Estimated from Different Methods for Carboxy-Telechelic 33,000 M_n PIP ionomers

Sample-id	Interfacial thickness values, σ (in nm)			
	Bonart	Exponential	Koberstein	Ruland
PIP-33000-Na-1	*	*	*	*
PIP-33000-Na-2	*	*	*	*
PIP-33000-Mg-1	*	*	*	*
PIP-33000-Mg-2	*	*	*	*
PIP-33000-Al-1	*	*	*	*
PIP-33000-Al-2	*	*	*	*
PIP-33000-Al-4	0.08	0.06	0.06	0.01
PIP-33000-Al-6	0.06	0.05	0.03	0.04
PIP-33000-Ti-6	0.02	*	*	0.04

* - not available (see text).

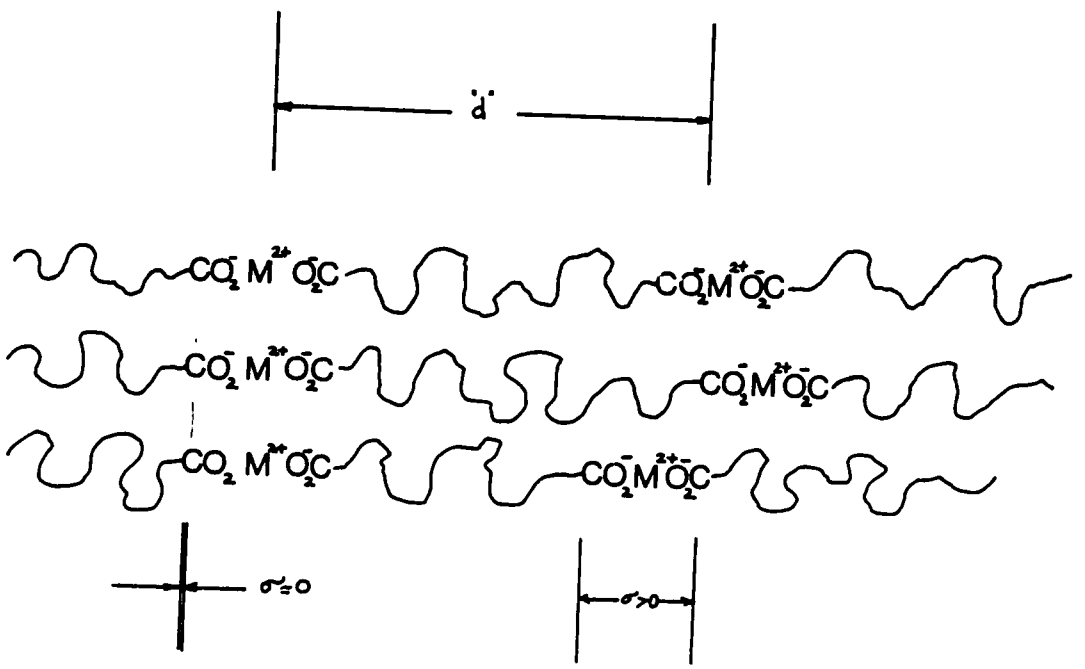

Figure 6.5. Schematic Representation of the Diffuse Boundary Region in a Carboxy-telechelic Ionomer:

Table 6.3. Mean Square Density Variances Determined for the 33,000 $\overline{M}_n$ Carboxy-Telechelic PIP ionomers

Sample-id	$\overline{\Delta\rho_e^2}$	$\Delta\rho^{2*}$	$\Delta\rho^{2*}$	$\Delta\rho^{2*}/\overline{\Delta\rho_e^2}$	$(\overline{\Delta\rho_e^2}/\Delta\rho^{2*}) - 1$	$(\Delta\rho^{2*}/\Delta\rho^{2*}) - 1$
PIP-33000-Na-1	*	*	*	*	*	*
PIP-33000-Na-2	*	*	*	*	*	*
PIP-33000-Mg-1	*	*	*	*	*	*
PIP-33000-Mg-2	*	*	*	*	*	*
PIP-33000-Al-1	*	*	*	*	*	*
PIP-33000-Al-2	*	*	*	*	*	*
PIP-33000-Al-4	0.383	0.79	0.81	2.07	- 0.53	0.03
PIP-33000-Al-6	0.383	1.40	1.41	3.66	- 0.73	0.01
PIP-33000-Ti-6	0.749	1.99	1.99	2.66	- 0.62	0.0

$\overline{\Delta\rho_e^2} = \Delta\rho^{2*} = \Delta\rho^{2*} = [mol\ e^-/cm^3]^2 \times 10^3$
* - not available.

electron density difference, $\overline{\Delta\rho_e^2}$, the density of the individual phases must be known. In ionomers, estimation of the density for the ionic phase is difficult since the position of the unassociated or the free ion is not known. The density of the ionic phase was approximated by using the density of the corresponding metal hydroxide. Also, the excess ions posed a potential problem in determining the different ratios mentioned above. In fact, the electron density variance determined experimentally, $\overline{\Delta\rho^2}^{exp}$, was found to be about 3 times more than $\overline{\Delta\rho_e^2}$ which was calculated from theoretical considerations, assuming complete phase separation between the ionic domains and the PIP backbone. Therefore, the analysis developed by Bonart (181,182) to determine the nature of ion aggregation could not be applied to these 33,000 $\overline{M}_n$ PIP ionomers. In fact, due to the presence of the excess neutralizing agent, the system was no longer a two phase system but was instead a three phase system (ionic domains, PIP backbone, and the isolated ion pairs). It is known that the theoretical electron density variance, $\overline{\Delta\rho_e^2}$, for a three phase system with sharp phase boundaries, can be calculated from the following expression;

$$\overline{\Delta\rho_e^2} = \phi_1\phi_2(\rho_1 - \rho_2)^2 + \phi_2\phi_3(\rho_2 - \rho_3)^2 + \phi_1\phi_3(\rho_1 - \rho_3)^2 \qquad (6.2)$$

where phase 1 represents the ionic domains, phase 2 represents the PIP backbone, and phase 3 represents the excess neutralizing agent. Detailed investigation of the ternary system was not within the scope of the present research and would in fact be an interesting problem to be looked at in detail at a latter time.

6.5 Effect of the Nature of the Functional Acid Groups

A series of 15,000 $\overline{M}_n$ sulfonated telechelic PIP ionomers provided by Professor Jerome, have been neutralized with different cations. It would be interesting to compare these materials to the 15,000 $\overline{M}_n$ carboxy-telechelic PIP ionomers that have been studied earlier by Tant et al. (83,187). Lundberg et al. (94) have shown that, in the random polystyrene ionomers, the ions in the sulfonated ionomers associate more strongly than the ions in the carboxylated ionomers. These

authors have suggested that the sulfonate ionomers possess a stronger (or tighter) network structure than the carboxylated ionomers.

The format of the discussion on the sulfonated telechelic PIP ionomers presented here consists of two parts. In the first part, the effect of the nature of the different cations studied (K, Mg, Zn and Zr) will be discussed; the second part will focus on comparing the behavior of these sulfonated ionomers to the corresponding carboxylated counterpart.

The stress-strain profiles of the telechelic 15,000 $\overline{M}_n$ sulfonated ionomers and that of the carboxylated ionomers studied by Tant et al. (187) have been neutralized with various cations, as shown in Figures 6.6a and 6.6b, respectively. All the ionomers shown in Figure 6.6 have been neutralized to the stoichiometric amount except for the Zr ionomer in which six times the stoichiometric amount was utilized. As discussed earlier, it is estimated that at least one Zr alkoxide per chain end is necessary for complete neutralization of the Zr ionomers (82). Comparing the effect of the various cations on the stress-strain behavior of the sulfonated ionomers, it is seen that the K ionomer exhibits the highest stress at a given strain followed by Mg, Zr and Zn ionomers, respectively. In the discussion on the PIP-33000-M-X ionomers, it was suggested that the coulombic forces predominate in the K and Mg ionomers. From equation 6.1 on page 123, it would be expected that the attractive forces within the Mg (0.65 Å) ionic domains would be larger than in the K (1.33 Å) ionic domains, due to both a higher valence and smaller ionic radius (hence smaller "a"). Therefore, the Mg ions aggregate to form smaller domains than the K ions. At shorter time scales (as in the stress-strain experiments) these larger ionic aggregates may act as reinforcing fillers which are then at least partially responsible for the higher stress at a given strain (at least in those systems where the chain entanglements do not dominate). At larger time scales of the experiment (such as in stress relaxation and creep tests) the smaller Mg ionic aggregates are more stable because of the greater mutual attractive forces existing within these aggregates. This greater network stability is reflected in the observed behavior of the Mg ionomers from both creep and stress relaxation experiments. The Zn ionomer exhibits the lowest stress at a given strain of all the four cations studied. It is believed, this is primarily due to the co-ordination tendency of Zn that is responsible for a weaker mutual association of the ions in the ionic domains. The Zr ionomer, however, exhibits a

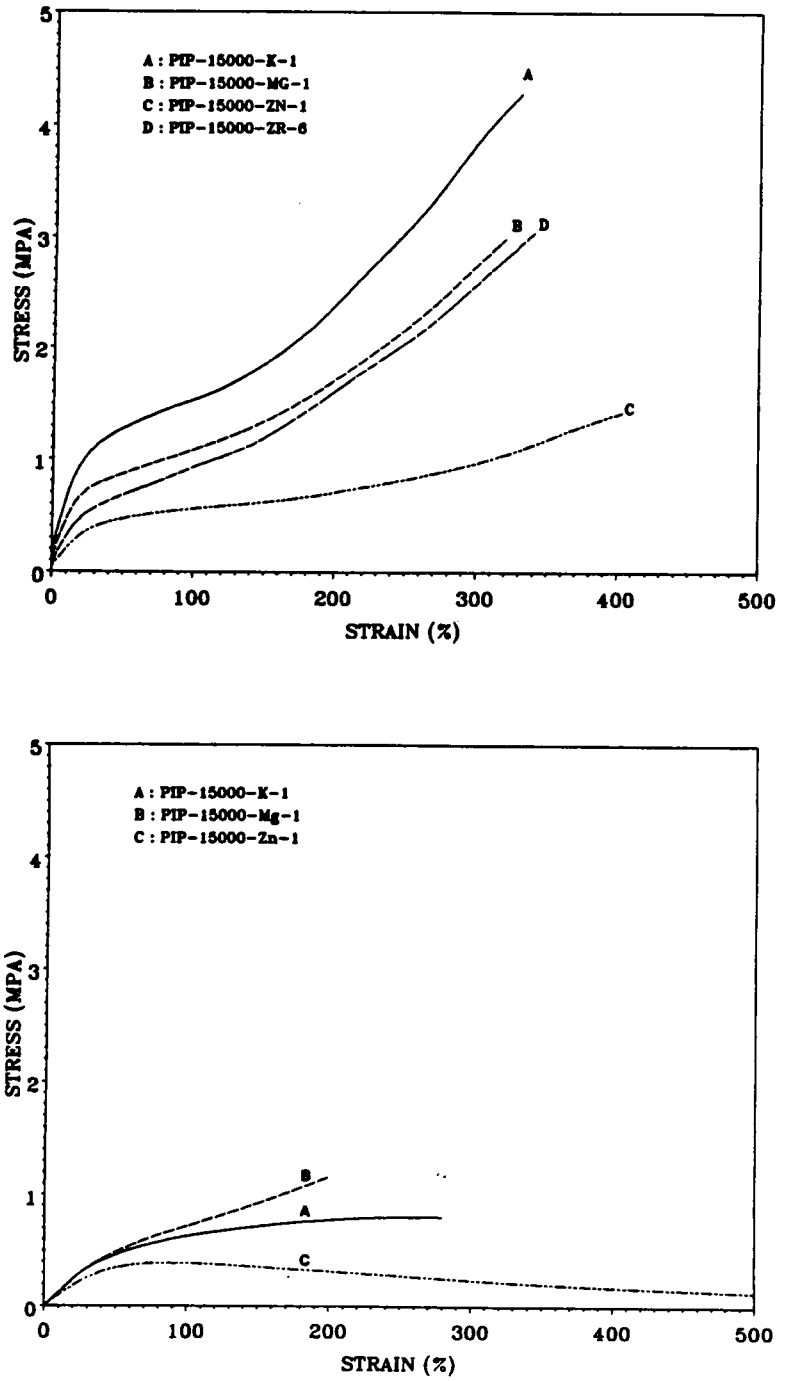

Figure 6.6. Stress Strain Curves for the 15,000 $\overline{M}_n$ PIP Telechelic Ionomers: (a) sulfonated ionomers and (b) carboxylated ionomers, from (187).

higher stress at a given strain than the Zn ionomer; the higher functionality of the Zr ionomer produces a more stable network structure than the Zn ionomer. As previously mentioned, the excess neutralizing agent not only ensures complete neutralization of the acid groups, but these excess ions also tend to aggregate near the ionic domains, enhancing the coulombic forces of attraction within the ionic domains.

To study the effect of the functionalized acid groups, a comparison is made between the performance between the sulfonated ionomers and the carboxylated ionomers that have been neutralized with the same cations (K, Mg, and Zn). All the carboxylated materials exhibit lower stress at a given strain than their sulfonated counterpart (refer to Figure 6.6b). The observed behavior indicates that the sulfonated ions tend to associate more strongly than the carboxylated ions. This observed behavior is in good agreement with the results obtained by Lundberg et al. (94) for the random polystyrene ionomers.

Figures 6.7 and 6.8 show the tensile creep and stress-relaxation response of both sulfonated and carboxylated ionomers, respectively. From the tensile creep response (Figures 6.7 a and b), the carboxylated ionomers displayed a tendency to flow in the time interval between 10 to 1000 minutes. However, in the sulfonated ionomers only the material neutralized with Zn displayed any indication to flow within this time interval. The greater network stability of the sulfonated ionomers was also evident from the stress-relaxation curves (Figure 6.8) where the sulfonated materials maintained the applied stresses over the entire time interval. The carboxylated ionomer, however, relaxed all the applied stress within this time interval. The results from both the tensile creep and the stress relaxation measurements further support the earlier conclusion that the sulfonated ionomers associate more strongly, providing a more stable network structure than the carboxylated ionomers.

As shown by Lundberg et al. (94), the softening temperatures for the sulfonated ionomers will be shifted to higher temperatures (see Figure 2.19 on page 58), due to the stronger association of the sulfonate groups. The thermo-mechanical behavior of both the sulfonated and carboxylated ionomers neutralized with K and Mg is shown in Figure 6.9. Complete penetration of the sulfonated ionomer neutralized with K (curve B in Figure 6.9) occurs nearly 60 °C higher than the

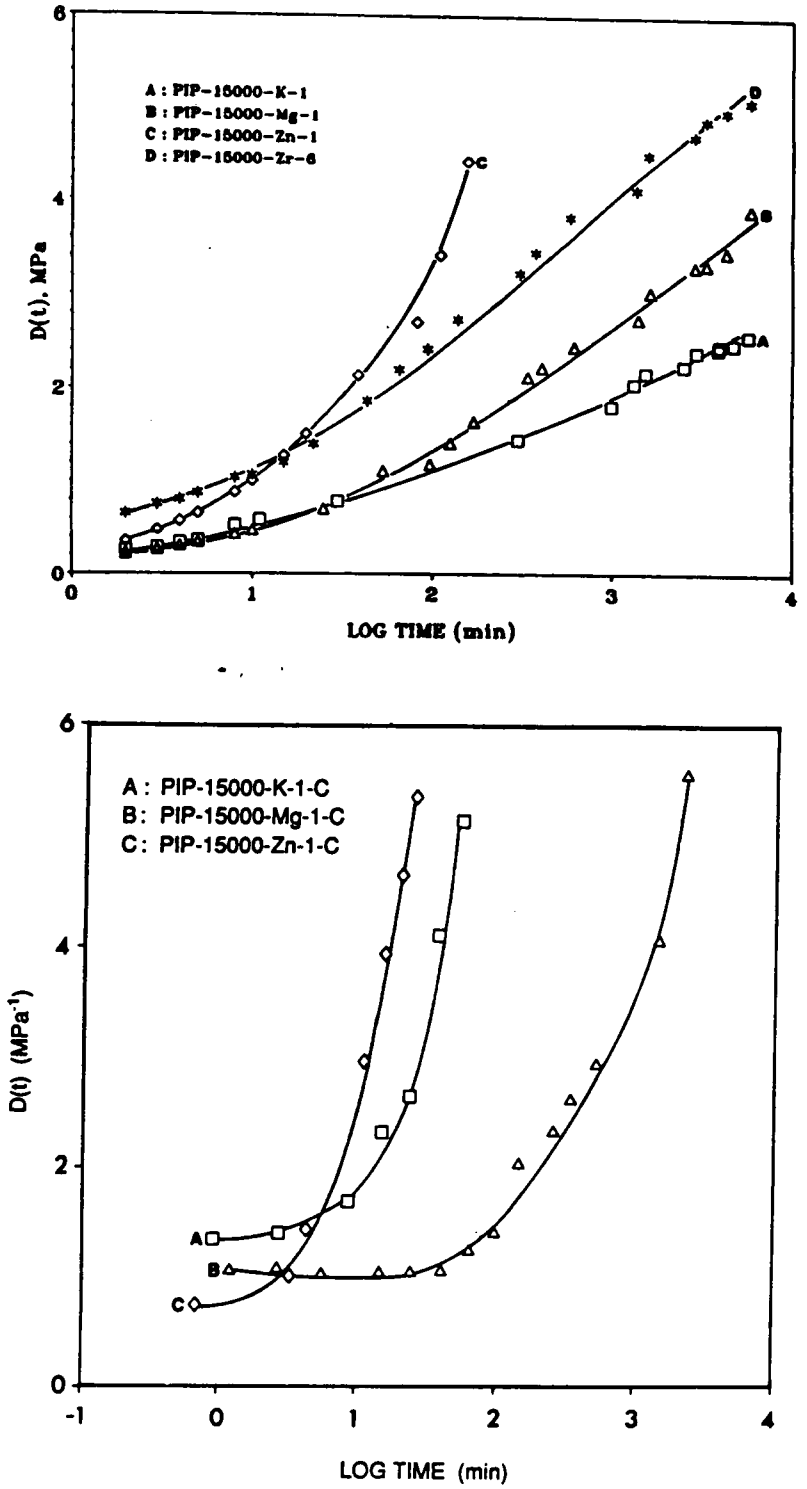

Figure 6.7. Tensile Creep Curves for the 15,000 $\overline{M}_n$ PIP Telechelic Ionomers: (a) sulfonated ionomers and (b) carboxylated ionomers,from (187). The experiment was conducted at 23 °C.

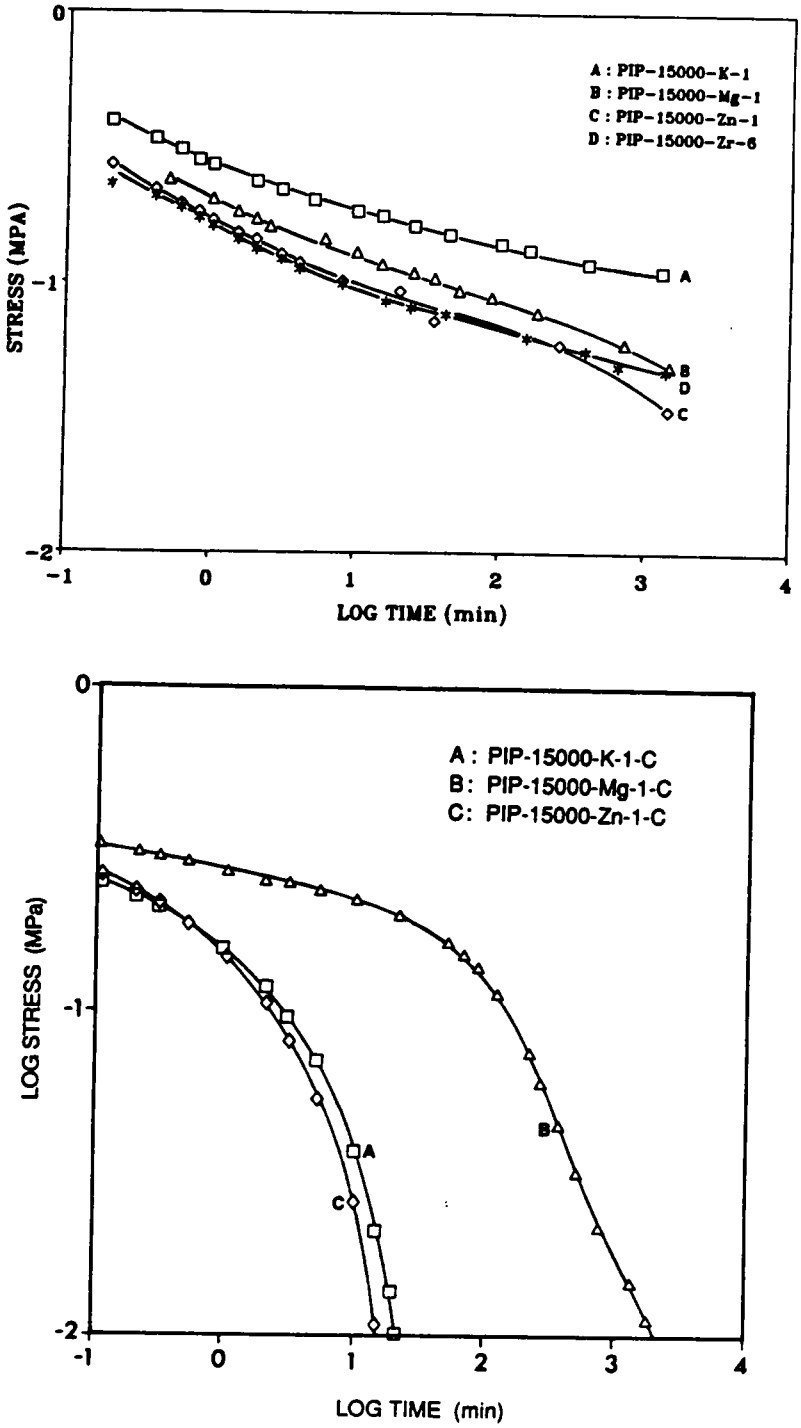

Figure 6.8. Stress-Relaxation Curves for the 15,000 $\overline{M}_n$ PIP Telechelic Ionomers: (a) sulfonated ionomers and (b) carboxylated ionomers, from (187). The experiment was conducted at 23 °C.

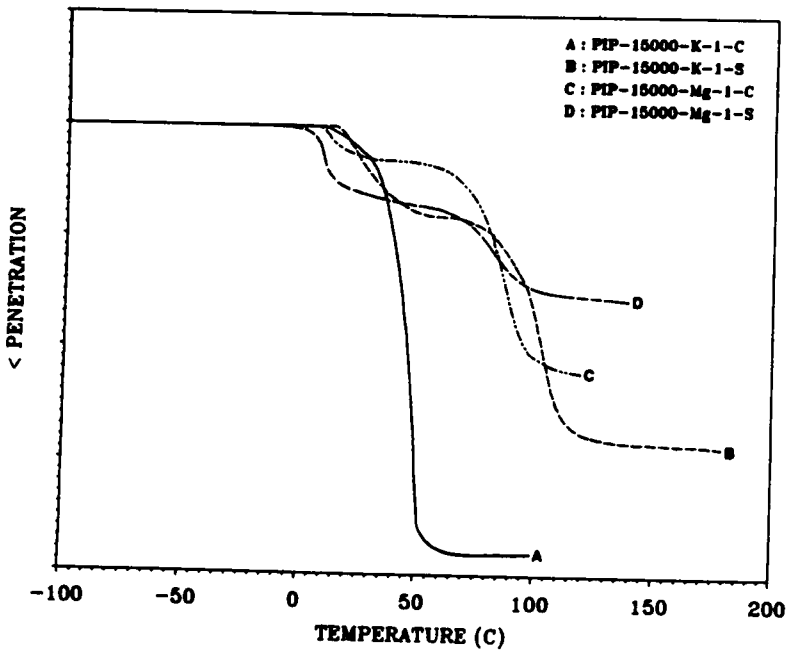

Figure 6.9. Thermo-mechanical Behavior of PIP-15000-M-X Ionomers: S - sulfonated ionomers; C - carboxylated ionomers; load = 10 g; scan rate = 10°/ min.

corresponding carboxylated ionomer. Also, a rubbery plateau extending for over 80 °C is observed for the sulfonated ionomer while it is absent in the carboxylated ionomer. A short rubbery plateau is observed for both the carboxylated and sulfonated ionomers neutralized with Mg, with the sulfonated ionomer having a higher rubbery modulus than the carboxylated ionomer. This behavior is again consistent with the earlier conclusion that sulfonate ionomers associate more strongly than the carboxylate ionomers.

6.5.1 Interdomain Spacings

The small angle x-ray scattering profiles of 15,000 $\overline{M}_n$ sulfonated and the carboxylated ionomers are shown in Figure 6.10. A distinct ionic peak is observed for all the ionomers irrespective of the nature of the acid groups. The nature of the cation has very little effect on the periodic (or the "d") spacing between the ionic domains in either the sulfonated or the carboxylated ionomers (ca. 7.2 to 8.7 nm for the sulfonate ionomers and between 6.9 to 7.6 nm for the carboxylated ionomers). Table 6.4 provides the periodic distances (or the "d" spacing) between the ionic domains for the 15,000 $\overline{M}_n$ carboxylated and the sulfonated telechelic ionomers. The spacings were obtained from the desmearing procedure and also from the analysis of the 1-D and the 3-D correlation functions. In the sulfonated ionomers, the K and the Zr ionomers have a slightly larger spacing. This may possibly be explained in terms of the larger ionic aggregates being present in these ionomers, which may account for the differences in the spacings. However, this is merely a speculation.

From Table 6.4, notice that the "d" spacings obtained for the sulfonated ionomers are consistently larger (ca. 11%) than the corresponding carboxylated ionomers when all other structural parameters are the same. Jerome et al. (190,191) have also observed a similar trend. This is surprising since it is expected that the carboxylate ion pairs, due to their weaker mutual interaction, would aggregate to form larger domains than the corresponding sulfonated ionomers. An inherent assumption in this speculation is that the number of aggregates in the ionic domains remains the same in both the systems. Also, the peak intensity of the sulfonate ionomers are, again, consistently larger than the carboxylate ionomers. This observation suggests that the ions in the sulfonate

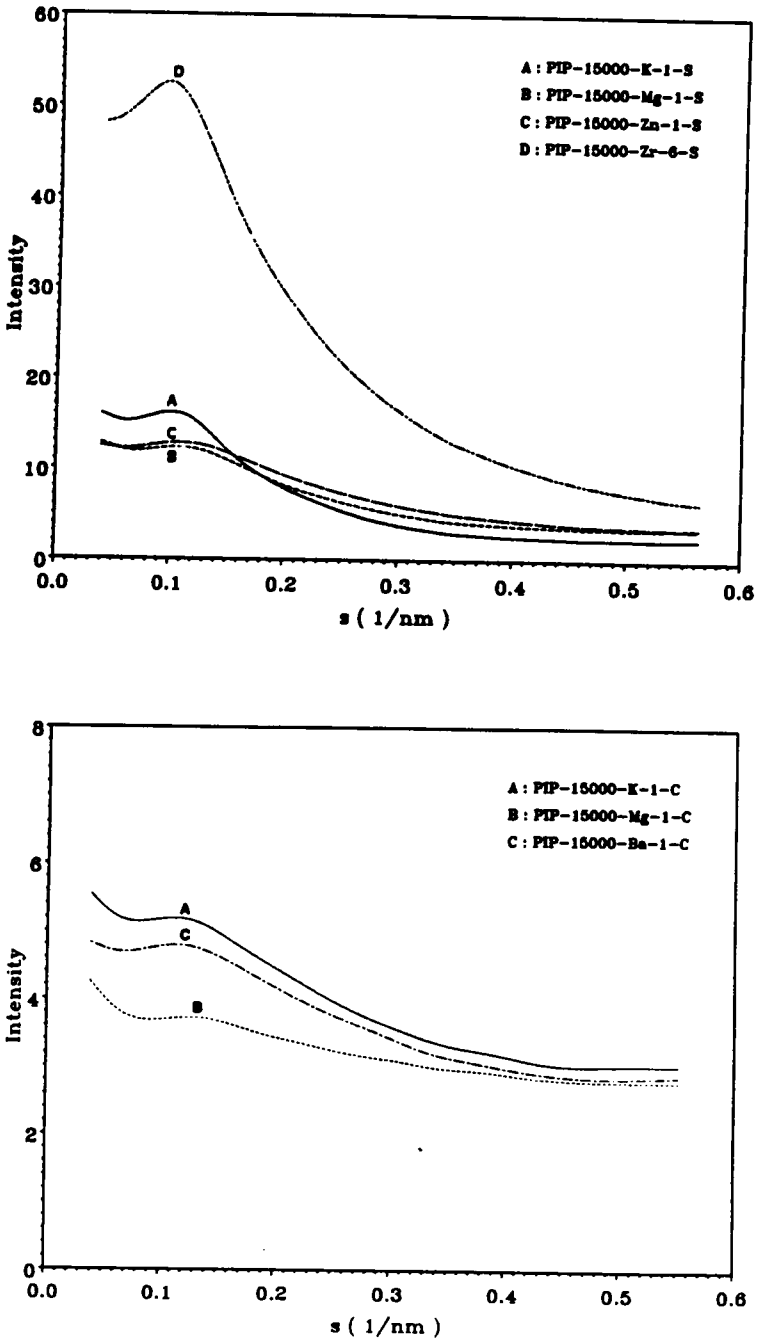

Figure 6.10. SAXS Profiles for the 15,000 $\overline{M}_n$ PIP Telechelic Ionomers: (a) sulfonated ionomers and (b) carboxylated ionomers

Table 6.4. Periodic Spacing Between the Ionic Domains in 15000 $\overline{M}_n$ PIP Carboxylated and Sulfonated Ionomers as Determined by SAXS Analysis

Sample-id	Periodic Spacing between the Ionic Domains, (in nm)			
	$d_{smeared}$	$d_{desmeared}$	$\gamma_1(D)$	$\gamma_3(D)$
PIP-15000-K-1-S	9.5	8.2	*	8.9
PIP-15000-Mg-1-S	8.8	7.6	*	8.8
PIP-15000-Zn-1-S	8.4	7.2	*	8.8
PIP-15000-Zr-1-S	10.4	8.7	*	8.9
PIP-15000-K-1-C	8.5	7.4	*	*
PIP-15000-Mg-1-C	7.1	6.9	*	*
PIP-15000-Ba-1-C	7.9	7.6	*	*

* - not available

ionomers are more tightly packed which would result in a higher electron density difference between the ionic domains and the non-ionic matrix. This may be responsible for the higher peak intensity in the sulfonate ionomers. Therefore, the differences in spacing cannot be accounted for by the differences in the sizes of the ionic domains. This suggests that the supermolecular morphology of the sulfonated ionomers may be inherently different from the carboxylated ionomers. This strange behavior may possibly be attributed to a phenomenon quite similar to the polyelectrolytic effect. More directly, if it is assumed that the pH of the medium, prior to the precipitation step, is the same for both the sulfonated and the carboxylated ionomers, the sulfonate groups are expected to be more completely ionized than the carboxylated groups. This is because the pK_a value of the sulfonate ions is ca. 2-3 while that for the carboxylate ion is ca. 4-5. For complete ionization, the difference between the pH value of the solution and the pK_a value of the ions should be greater than 3 (192). This can be calculated from the Henderson-Hasselbalch equation, i.e.,

$$pH = pK_a + \log \left[\frac{i}{(1-i)}\right] \tag{6.3}$$

where i = degree of ionization. Assuming a pH of 7 (for the sake of argument) for the medium prior to precipitation, one can envision that the sulfonate ions are almost completely ionized, while only partial ionization of the carboxylate ions take place. Assuming that the number of charges per ionic aggregate is nearly the same for both carboxylated and sulfonated systems, the separation distance in the sulfonated system would be greater than in the carboxylated system because of its higher degree of ionization. Since the ionomer is formed in solution, this could then have an effect on the supermolecular structure of the ionomers. Moreover, this argument assumes that the general structure in the solution is also carried over through the processing step into the final solid film form. This line of reasoning may explain why a larger spacing is obtained in the sulfonated ionomers. Another possible argument is based on the balance of forces in the system. It has been established that the sulfonate ions associate more strongly than the carboxylate ions. Hence, there is a greater driving force for the sulfonate ions to associate, due to the coulombic interactions between the ions. Therefore, it is speculated that during the melt processing step, these sulfonate ions

could then "stretch" or "extend" the PIP backbone in order to associate with the other sulfonate ions. However, the extension of the backbone is restricted by the entropic forces in the system which tend to prevent this extension. Due to these competing forces, the net effect on the amount of extension of the PIP backbone chain is based on the strength of the ionic interaction of the sulfonate ions.

6.5.2 Diffuse Boundary Analysis

Based on the Porod's analysis of the tail region, it was found that the interfacial or diffuse boundary thickness values for both the carboxylated and the sulfonated ionomers is <0.1 nm for all the materials studied. Notice that this value is less than the C-C bond (0.15 nm). This suggests that the interfacial region between the ionic and the organic phase is very sharp and that very few ionic moieties are dissolved in the non-ionic matrix, a result quite similar to that obtained for the PIP-33000-M-X ionomers. Table 6.5 lists the interfacial or the diffuse boundary thickness values estimated from different methods. It appears that the coulombic forces within the ionic domains prevent any potential mixing between the ionic domains, which are polar in nature, and the non-polar organic matrix.

6.5.3 Degree of Phase Separation

The mean square electron density variances determined for the sulfonated and carboxylated ionomers are reported in Table 6.6. Except for the Zr ionomer, the ratio $\overline{\Delta\rho^2}/\overline{\Delta\rho_c^2}$ indicates that the degree of phase separation in all other ionomers is not complete. This is contrary to what was observed from the diffuse boundary analysis. The author feels that the degree of phase separation analysis should not be applied in ionomeric systems since there will always be an uncertainty regarding the value of $\overline{\Delta\rho_c^2}$. Therefore, the observed values for the ratio $\overline{\Delta\rho^2}/\overline{\Delta\rho_c^2}$ are not very surprising because of the error already present in the estimation of $\overline{\Delta\rho_c^2}$. However, there are no such assumptions involved in the diffuse boundary analysis and is, therefore, more reliable than the degree of phase separation analysis.

Table 6.5. Diffuse Boundary Thickness Values Estimated from Different Methods for 15000 $\overline{M}_n$ Carboxylated and Sulfonated Ionomers

Sample-id	Interfacial thickness values, σ (in nm)			
	Bonart	Exponential	Koberstein	Ruland
PIP-15000-K-1-S	0.11	0.07	0.07	0.07
PIP-15000-Mg-1-S	0.03	0.02	0.02	0.02
PIP-15000-Zn-1-S	0.06	0.05	0.05	0.05
PIP-15000-Zr-6-S	0.08	0.05	0.06	0.05
PIP-15000-K-1-C	0.14	0.09	0.10	0.06
PIP-15000-Mg-1-C	0.17	0.10	0.11	0.0
PIP-15000-Ba-1-C	0.0	0.02	0.02	0.0

Table 6.6. Mean Square Density Variances Determined for the 15,000 $\overline{M}_n$ Telechelic PIP ionomers

Sample-id	$\overline{\Delta\rho_e^2}$	$\Delta\rho^{2r}$	$\Delta\rho^{2r}$	$\Delta\rho^{2r}/\overline{\Delta\rho_e^2}$	$(\overline{\Delta\rho_e^2}/\Delta\rho^{2r}) - 1$	$(\Delta\rho^{2r}/\Delta\rho^{2r}) - 1$
PIP-15000-K-1-S	5.21	1.44	1.47	0.28	2.54	0.02
PIP-15000-Mg-1-S	1.88	1.33	1.34	0.71	0.40	0.01
PIP-15000-Zn-1-S	4.16	1.68	1.70	0.40	1.44	0.01
PIP-15000-Zr-6-S	3.38	5.44	5.55	1.61	- 0.39	0.02
PIP-15000-K-1-C	0.85	0.43	0.45	0.51	0.88	0.05
PIP-15000-Mg-1-C	0.66	0.27	0.30	0.41	1.21	0.11
PIP-15000-Ba-1-C	1.85	0.52	0.52	0.28	2.55	0.0

$\overline{\Delta\rho_e^2} = \Delta\rho^{2r} = \Delta\rho^{2r} = [mol\ e^-/cm^3]^2 \times 10^3$

6.6 Morphlogy of PBD Carboxy-telechelic Ionomers

Apart from the PIP carboxy-telechelic ionomers, PBD based ionomers are the other carboxy-telechelic ionomers that have been widely studied. It would be interesting to compare the degree of phase separation in these systems with the observed behavior of the carboxy-telechelic PIP ionomers discussed earlier. Hence, carboxy-telechelic PBD ionomers neutralized with barium to different levels of neutralization were considered for the study. The most widely studied PBD ionomers have been the 4600 $\overline{M}_n$ material (82,84,85). This material is readily available in the acid form commercially from BF Goodrich. A variation on the molecular weight, 2000 vs. 4600 $\overline{M}_n$, was also considered to study the effect of the ion content.

6.7 Extent of Neutralization

One of the critical parameters affecting the morphology of ionomers is their ion content. There are essentially two ways by which the ion content in the polymer can be varied. It can be varied by changing the molecular weight of the non-ionic segment, or by partial neutralization of the ionic groups, or both the routes can be utilized simultaneously. The literature suggests that increasing the intervening molecular weight, only increases the spacing between the ionic domains (84). However, with partial neutralization of the acid groups, the resulting morphology is more complex in nature. Depending on the degree of neutralization, the linear telechelic chain can then be terminated with zero, one or two salt groups. This would have a significant effect on the morphology of the ionomers because the un-neutralized acid groups can now not only plasticize the ionic domains but may also interfere with the the ion aggregation process.

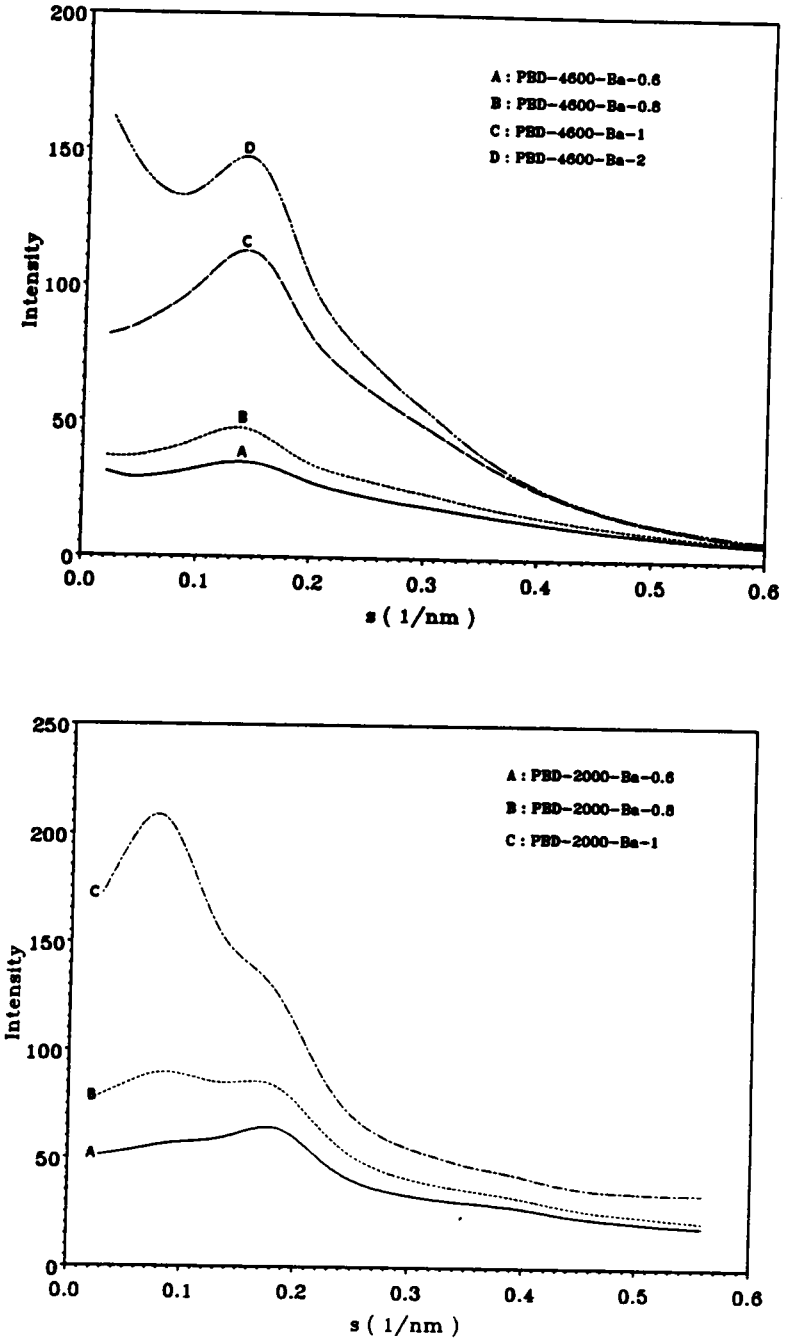

Figure 6.11. **Small Angle X-Ray Scattering Profiles of PBD Ionomers:** (a) 4600 $\overline{M}_n$ ionomers, and (b) 2000 $\overline{M}_n$ ionomers

6.7.1 Interdomain Spacings

The small angle x-ray scattering profiles for the PBD 4600 $\overline{M}_n$ and 2000 $\overline{M}_n$ series are shown in Figure 6.11. A discernible ionic peak is observed even for the ionomer which has been neutralized to only 60% ! (see Figure 6.11a). The intensity of the ionic peak increases with increasing extent of neutralization. With increasing neutralization, the number density of un-neutralized acid groups decreases, and the increasing number of scattering entities are responsible for the higher scattered intensity. In addition, once all the acid groups are neutralized, the excess neutralizing agent tends to aggregate around the existing ionic domains, enhancing the scattering contrast in the medium which again results in a higher scattered intensity. The ionic peak becomes more pronounced and sharpens with increasing levels of neutralization (i.e. from 60% to 200% - curves A to D in Figure 6.11a). Table 6.7 provides the periodic distances (or the "d" spacing) between the ionic domains for the carboxy-telechelic PBD ionomers. The spacings were obtained from the desmearing procedure and also from the analysis of the 1-D and the 3-D correlation functions. It was found that the degree of neutralization of the acid end-groups had very little effect on the spacing between the ionic domains in the range 60 to 200%. Earlier, Williams et al. (84) observed that the Bragg spacing increases with neutralization following an S-shaped curve similar to that of the titration curve. Figure 6.12 shows the plot of the ratio of the spacing corresponding to the primary peak position (denoted as "d") to that of the endpoint neutralized ionomer (denoted as "d_{100}") as a function of the extent of neutralization. With increasing levels of neutralization, the spacings corresponding to the primary peak for the 4600 $\overline{M}_n$ PBD ionomers neutralized with barium scale in a similar fashion to that earlier observed in magnesium (84). It was also noticed that with the addition of twice the stoichiometric amount of the neutralization agent, a considerable increase in the zero angle scattering was observed. This observation supports the earlier speculation that the origin of the upturn in the intensity near the zero angle region may be due to the excess cations that are heterogeneously distributed in the non-ionic matrix.

Figure 6.11b shows the SAXS profiles of the 2000 $\overline{M}_n$ PBD ionomers neutralized with barium to different levels of neutralization. For the first time, more than one distinct scattering or ionic peak

Table 6.7. Periodic Spacing Between the Ionic Domains in Carboxy-Telechelic PBD Ionomers as Determined by SAXS Analysis

Sample-id	Periodic Spacing between the Ionic Domains, (in nm)					
	$d_{smeared}$		$d_{desmeared}$		$\gamma_1(D)$	$\gamma_3(D)$
	I	II	I	II		
PBD-4600-Ba-0.6	7.2		6.5			6.9
PBD-4600-Ba-0.8	7.5		6.7			7.0
PBD-4600-Ba-1.0	7.5		6.7			7.0
PBD-4600-Ba-2.0	7.5		6.8			7.0
PBD-2000-Ba-0.6	10.7	5.5	9.7	5.1		5.2
PBD-2000-Ba-0.8	11.3	5.5	9.9	5.2		5.2
PBD-2000-Ba-1.0	12.5	5.7	10.9	5.4	4.8	11.5

I = spacing corresponding to the position of the primary SAXS peak
II = spacing corresponding to the position of the secondary SAXS peak

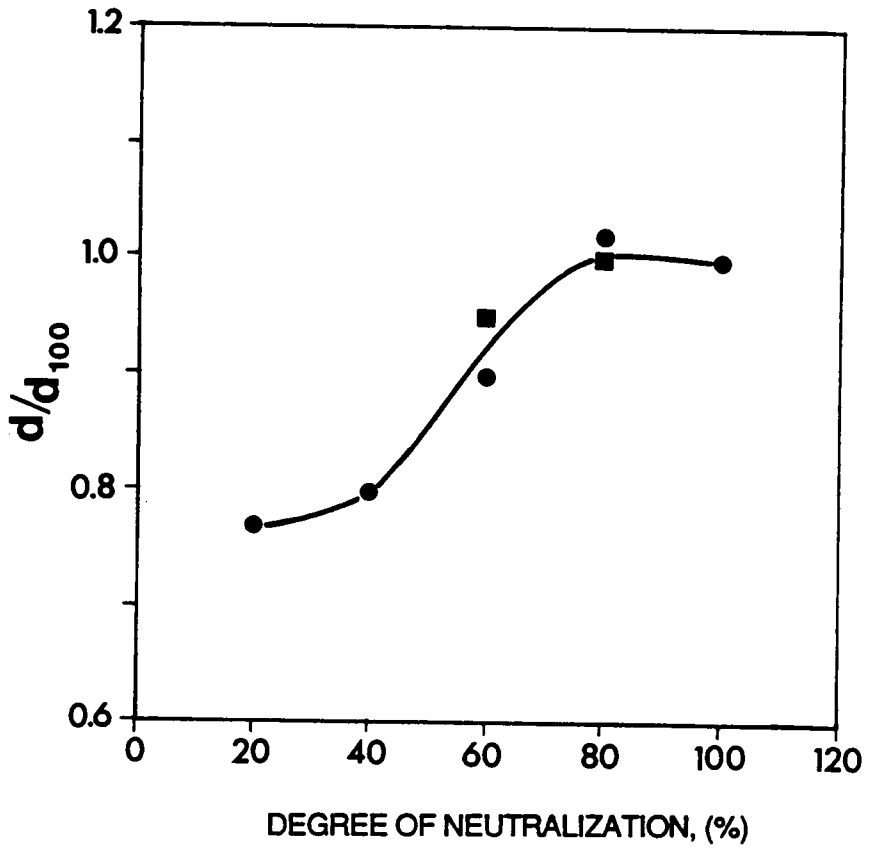

Figure 6.12. Bragg Spacing Corresponding to the Position of the SAXS Maxima vs. Extent of Neutralization: ■ - PBD-4600-Ba-X; ● - PBD-4600-Mg-X, from (84).

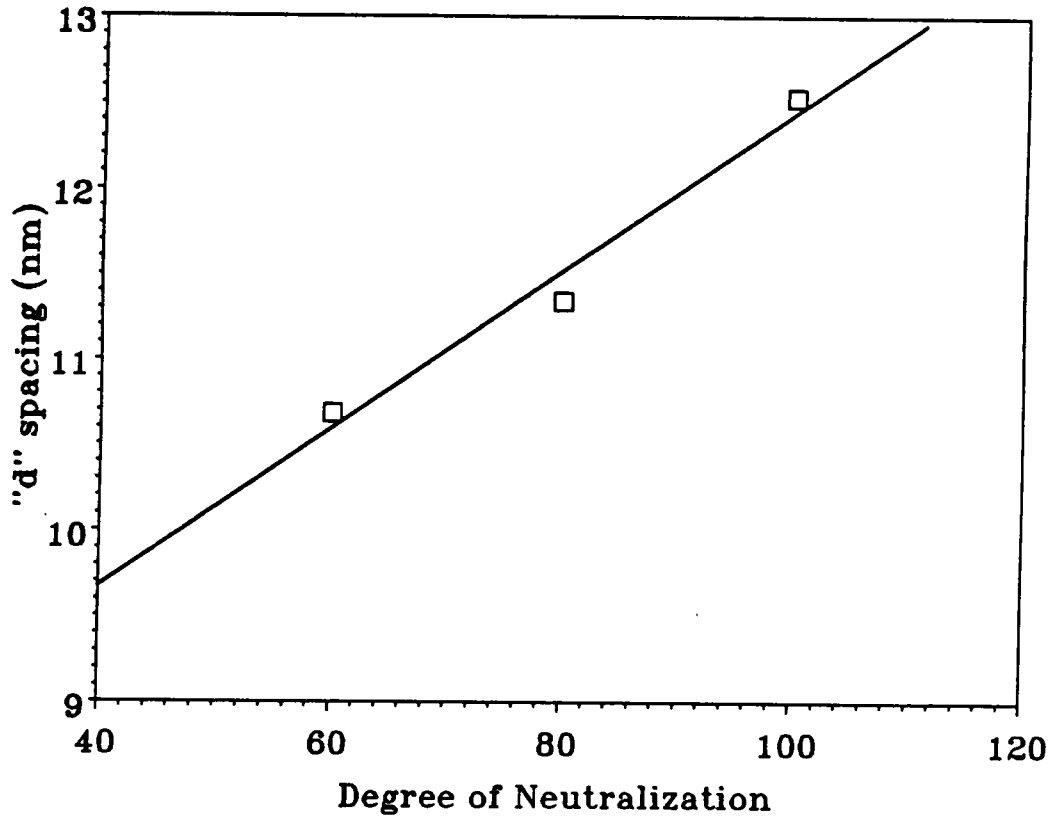

Figure 6.13. Plot "d" Spacing Corresponding to the Primary Peak vs. Extent of Neutralization for PBD-2000-Ba-X Ionomers:

is observed in telechelic ionomers. In fact a bimodal type of scattering behavior is observed for the 2000 $\overline{M}_n$ PBD ionomer. The relation between the extent of neutralization and the periodic or "d" spacing corresponding to the position of the primary peak (near s = 0.7-0.8 nm^{-1}) for PBD-2000-Ba-X ionomers is shown in Figure 6.13. The "d" spacing corresponding to the primary peak increases linearly with increasing levels of neutralization. But, the position of the secondary peak remains nearly constant, similar to the behavior observed observed for the 4600 $\overline{M}_n$ PBD ionomer. However, the intensity of both the peaks increases with increasing levels of neutralization. Notice that the increase in intensity of the primary peak with the extent of neutralization is much greater than that observed for the secondary peak. It is speculated that the origin of the two scattering peaks may be due to two competing structures with the one corresponding to the primary peak being more dominant. Since the position of the secondary peak in the 2000 $\overline{M}_n$ PBD ionomer remains nearly unchanged with degree of neutralization (a behavior similar to that observed for the 4600 $\overline{M}_n$ ionomer), it is believed that the secondary peak in the 2000 $\overline{M}_n$ ionomer may be related to the primary ionic peak of the 4600 $\overline{M}_n$ ionomer. Ledent et al. (191) suggested that a lamellar type of morphology may exist in the 4600 $\overline{M}_n$ PBD ionomers. It is speculated that a dual type of morphology, both spherical as well as a lamellar or sheet-like structure, may be present in the system. The origin of the secondary peak may be due to spherical ionic domains, while that of the primary peak may be due to the presence of a lamellar or sheet-like structure. Any higher order scattering from such a structure may be dominated by the presence of the secondary peak due to the spherical morphology. It is speculated that there might be a critical number of ion pairs that can be accommodated in a spherical aggregate. The size of spherical aggregate will depend on the dielectric constant of the backbone medium. It is self evident that the critical number of ion pairs will depend on the size of the aggregate. In the 2000 $\overline{M}_n$ ionomer, it is believed that the critical number of ion pairs for the spherical aggregates are soon reached even at low levels of neutralization. With increasing levels of neutralization the additional ionic pairs are accommodated in a higher order morphology such as the lamellar or the sheet like structures. Hence, the intensity of the primary peak increases more rapidly than that for the secondary peak because above 60% most of the additional neutralized salts are accommodated in the higher order structures. There are

also some indication from the TMA measurements that supports the dual morphology speculation in the 2000 $\overline{M}_n$ ionomer. Details regarding the TMA measurements will be discussed later.

Furthermore, notice that the spacing corresponding to the secondary peak in the 2000 $\overline{M}_n$ material is lower than the spacing observed for the primary peak in the 4600 $\overline{M}_n$ material. This lower spacing is expected since the number of PBD repeat units is lower for the 2000 $\overline{M}_n$ material. Taking the ratio of the primary to the secondary peak provides information regarding the nature of packing of the ionic domains if indeed they pack into a pseudo-lattice. For lamellar systems, the ratio should scale as 1:2:3 while for a hexagonally packed system the ratio scales as 1:$\sqrt{3}$:2, etc. From Table 6.7, for the endpoint neutralized 2000 $\overline{M}_n$ PBD ionomer, the ratio is nearly 2.0 for the endpoint neutralized material, a ratio which is indicative of the presence of a lamellar morphology. At lower levels of neutralization, a value of 1.90 is obtained which is between 1.732 and 2.0 which is again indicative of the presence of a dual morphology.

6.7.2 Diffuse Boundary Analysis and Degree of Phase Separation

Table 6.8 lists the interfacial or the diffuse boundary thickness values estimated from different methods. Different plots for a representative sample, PBD-4600-Ba-100 ionomer, is shown in Figure 6.14. From all the different methods the behavior of the tail region is nearly ideal in nature (i.e. zero slope) which indicates that the interfacial regions in these materials is in fact very sharp. The interfacial thickness values obtained for the 4600 $\overline{M}_n$ ionomers are very small (<0.1 nm), which is indicative of a sharp phase boundary existing between the ionic domains and the non-ionic matrix. However, the diffuse boundary thickness values for the 2000 $\overline{M}_n$ PBD ionomers are somewhat higher. The higher values are observed because of the presence of the interference peak near the region where the interfacial thickness values are determined. Hence, the estimation of a realistic value for σ becomes difficult. The mean square electron density variances for the carboxy-telechelic PBD ionomers are summarized in Table 6.9. As mentioned earlier, no reliable inferences can be made from ratio of the different variances since there is a considerable amount of uncertainity involved in the determination of the $\overline{\Delta\rho_e^2}$ values. From Table 6.9, the values obtained for the different

Table 6.8. Diffuse Boundary Thickness Values Estimated from Different Methods for Carboxy-Telechelic PBD Ionomers

Sample-id	Interfacial thickness values, σ (in nm)			
	Bonart	Exponential	Koberstein	Ruland
PBD-4600-Ba-0.6	0.03	0.0	0.0	0.05
PBD-4600-Ba-0.8	0.04	0.03	0.03	0.05
PBD-4600-Ba-1.0	0.01	0.01	0.01	0.01
PBD-4600-Ba-2.0	0.0	0.0	0.0	0.01
PBD-2000-Ba-0.6	0.05	0.04	0.04	0.0
PBD-2000-Ba-0.8	0.06	0.06	0.05	0.06
PBD-2000-Ba-1.0	0.29	0.20	0.25	0.15

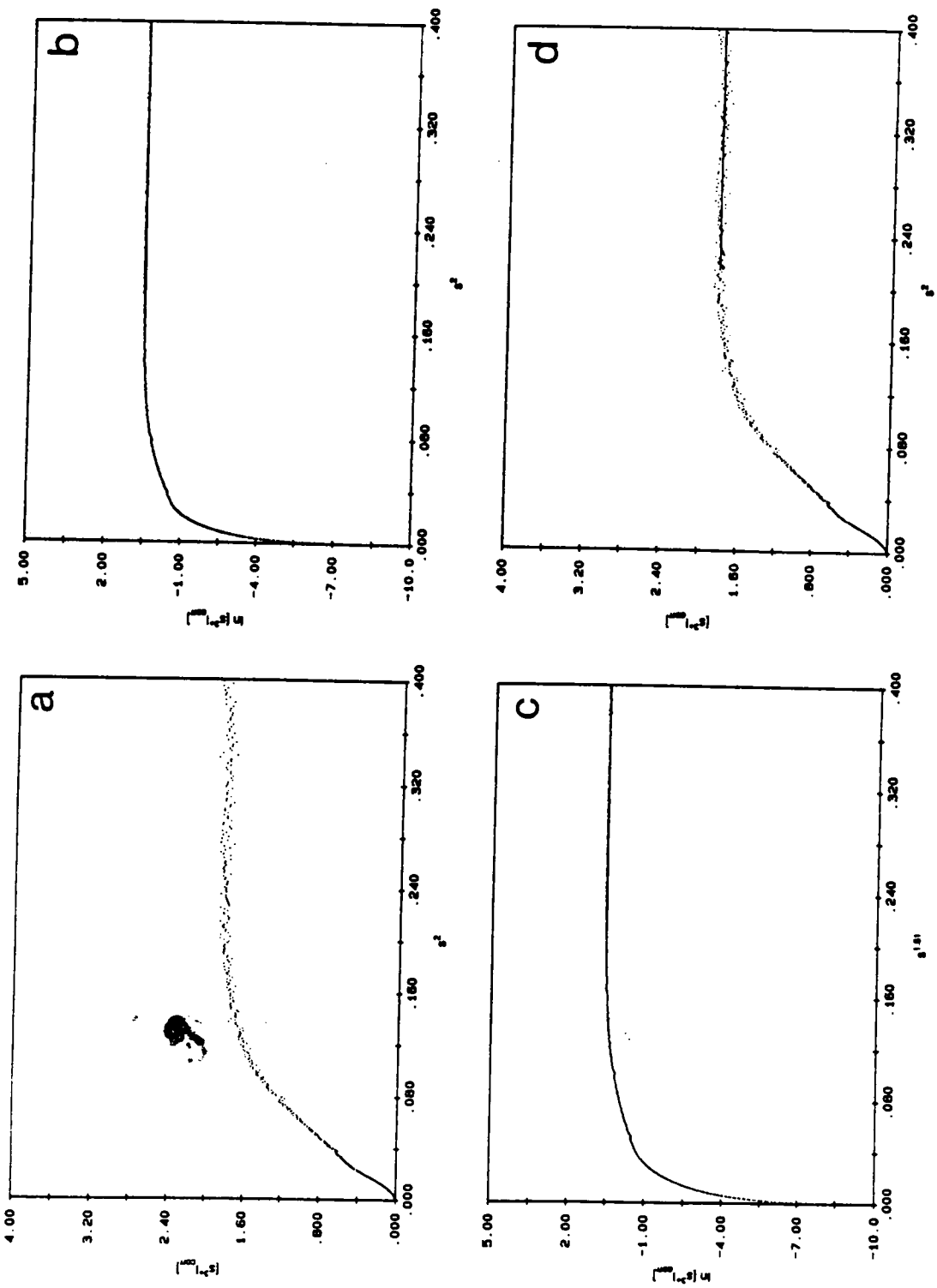

Figure 6.14. Different Methods Utilized to Determine the Diffuse Boundary Thickness for PBD-4600-Ba-100 Ionomer: (a) Porod' plot, (b) Bonart' plot, (c) Koberstein's plot, and (d) Ruland's plot

Table 6.9. Mean Square Density Variances Estimated for Carboxy-Telechelic PBD ionomers

Sample-id	$\overline{\Delta\rho_c^2}$	$\Delta\rho^{2'}$	$\Delta\rho^{2}$	$\Delta\rho^{2}/\overline{\Delta\rho_c^2}$	$(\overline{\Delta\rho_c^2}/\Delta\rho^{2'}) - 1$	$(\Delta\rho^{2}/\Delta\rho^{2'}) - 1$
PBD-4600-Ba-0.6	5.51	8.47	8.47	1.54	-	*
PBD-4600-Ba-0.8	5.51	10.74	10.83	1.95	-	0.01
PBD-4600-Ba-1.0	5.51	24.36	24.37	4.42	-	*
PBD-4600-Ba-2.0	5.51	27.37	27.37	4.97	-	*
PBD-2000-Ba-0.6	11.77	10.09	10.22	0.86	0.15	0.01
PBD-2000-Ba-0.8	11.77	13.47	13.71	1.14	-	0.02
PBD-2000-Ba-1.0	11.77	16.33	20.99	1.39	-	0.29

$\overline{\Delta\rho_c^2} = \Delta\rho^{2'} = \Delta\rho^{2} = [mol\ e^{-}/cm^3]^2 \times 10^3$

- = values are less than zero

* = not available (due to positive deviation from Porod's law).

ratios seem to indicate the failure of the degree of phase separation analysis for the carboxy-telechelic PBD ionomers.

6.7.3 Thermal Analysis

The thermo-mechanical behavior of the 2000 $\overline{M}_n$ and 4600 $\overline{M}_n$ PBD ionomers neutralized to the stoichiometric end-point is shown in Figure 6.15. For the 4600 $\overline{M}_n$ material, the onset of the penetration of the probe occurs at ca. 46 °C while for the 2000 $\overline{M}_n$ ionomer a double penetration behavior is observed. The onset of the initial penetration is ca. 80 °C, and that of the final penetration occurs ca. 113 °C. Clearly, this observation is consistent with the earlier speculation that a dual type of morphology exists in the 2000 $\overline{M}_n$ PBD ionomer. If indeed a dual morphology were present, the resistance to penetration for the lamellar structures would be greater than the spherical structures due to the inherent geometric anisotropy. Therefore, the lower transition at ca. 80 °C might correspond to the spherical structure, while that at ca. 113 °C might be due to lamellar structures, though this is clearly a speculation.

6.8 Summary

Based on the SAXS analysis, it has been shown that the phase boundary between the ionic phase and the non-ionic matrix is very sharp in all the materials investigated. The sharp interface present may also be responsible for the observed bulk behavior. It has been suggested that the coulombic forces of interaction in the system might prevent any potential mixing between the ionic domains and the non-ionic matrix in the interfacial region. The upturn in the intensity near the zero angle region increased with increasing levels of neutralization, suggesting that the upturn may be caused by the isolated ion pairs in the system.

The observed mechanical properties were highly dependent on the nature of the cation, its valency, and its ionic radius. The size of the cation not only determined the magnitude of the force of association within the ionic domains, but also its cohesiveness from steric considerations. When the experimental time scale was small (such as in stress-strain measurements), the size of the ionic

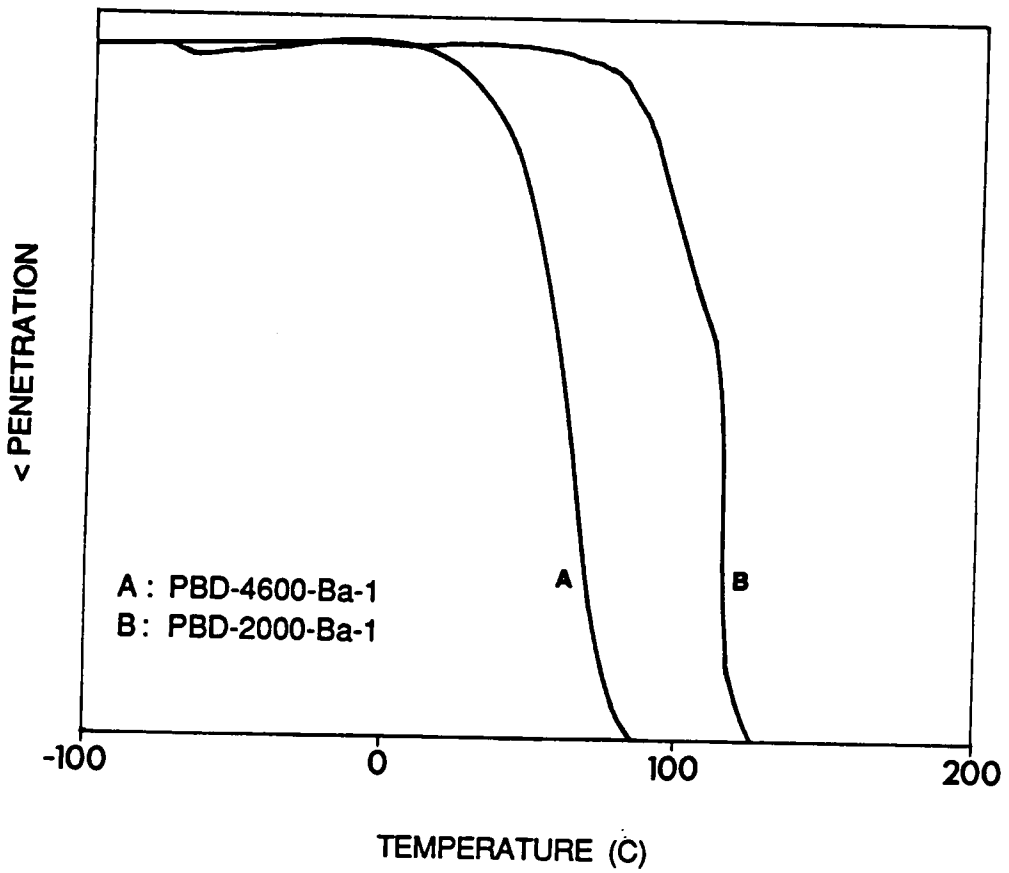

Figure 6.15. TMA curves for the endpoint neutralized of 2000 and 4600 $\overline{M}_n$ PBD Ionomers:

aggregates might play a dominant role - a filler effect. But, when the experimental time scale was large (such as in creep and stress relaxation tests), the nature of interaction within the ionic domains seemed to play the dominant role.

Significant morphological changes were observed on complete neutralization of the acid groups in all the PIP and PBD materials. It was observed that the ratio of the acid groups to the neutralizing agent should be at least 1:1 for complete neutralization of the higher valent ions that exhibit less metallic character. In the PIP-33000-M-X ionomers, the ionic peak was observed only for the higher valent cations (Al or Ti) where there was sufficient electron density contrast for detection. The ionic peak was observed only in those systems in which complete neutralization seemed to have taken place. The invariant or the degree of phase separation analysis, in ionomers, was observed to break down (or was inapplicable) because of the uncertainty involved in the determination of $\overline{\Delta\rho_e^2}$ values.

The nature of the association of the ions in the sulfonate ionomers was found to be much stronger than in the carboxylated ionomers based on the observed bulk properties. This observation is in good agreement with the earlier work of Lundberg et al. (94). A distinct SAXS or ionic peak was observed for both the sulfonated and carboxylated ionomers for the 15,000 $\overline{M}_n$ PIP ionomers, but surprisingly the periodic spacings obtained for the sulfonate ionomers were consistently higher than the carboxylate ionomers.

For the first time, more than one distinct ionic peak was observed in telechelic ionomers. In the 2000 $\overline{M}_n$ PBD ionomer, a bimodal type of scattering behavior was observed. It is speculated that a dual morphology with both a spherical as well as a lamellar structure may co-exist in the PBD 2000 $\overline{M}_n$ ionomer. This, however, is a speculation which has not yet been confirmed.

Based on the SAXS analysis of the experimental data of the telechelic ionomers investigated in this study, it is believed that the nature of ion aggregation seems to favor the "interparticle interference" model. In addition, it has been shown that the degree of neutralization plays a significant role in determining the final morphology of the ionomers. Due to the observation of more than one scattering peak, it is expected that the determination of the arrangement of the ionic domains in these model ionomers will be facilitated. The ratio between the spacings corresponding to the

respective peak, may provide a clue as to the type of morphological structure in the system. With the utilization of the proper modeling tools, one can even confirm the speculated morphologies.

7.0 SMALL ANGLE X-RAY INVESTIGATIONS OF NOVEL IONENE POLYMERS

As mentioned in the literature review section, most of the earlier studies on ionene polymers have focused on studying their dilute viscosity behavior and no detailed investigation has been made relating the morphological features to the observed solid state properties. A systematic series of well defined ionene polymers with poly(tetramethylene oxide) (PTMO) as the soft segment was kindly provided by Dr. C. M. Leir's group at the Specialty Chemicals Division at 3M, St. Paul, Minnesota. One of the attractive features in studying these segmented ionene materials is that the ionic groups are located at well defined positions along the polymer backbone. This particular study is a part of a joint investigation where the details relating to the mechanical, dynamic mechanical and electron microscopy have been reported by Feng (194) while those relating to the small angle x-ray scattering will be discussed in this section.

The nomenclature adopted in identifying the different samples is best described by an example ;

Sample **IB-NS-18**

ITEM	DESCRIPTION
I	**Ionene**
B	**Type of Counterion**
	B = bromide; C = chloride; and I = iodide
NS	**Type of Ionene Hard Segment**
	NS (no spacer) = dihalide xylene; S (spacer) = benzyl dihalide butane
18	**PTMO segment $\overline{M}_n$ x 10^{-2}**

The chemical structure of these ionene materials are shown in Figure 7.1 and their physical characteristics are provided in Table 7.1.

7.1 Bulk Properties of the Ionene Materials

Detailed investigation of the bulk properties of these ionene materials have been reported earlier by Feng (194). Some of the important characteristics of these materials are provided here so that the morphological results that are obtained in this study can then be related to the observed bulk properties. Typical stress-strain behavior of the IB-NS series is shown in Figure 7.2. These materials exhibit excellent elastomeric properties with low initial modulus, significant elongation at break (ca. 1000%) and tensile strength reaching up to 40 MPa for some materials. A distinct upturn in the stress was observed when elongations of the order of 400% are exceeded. This behavior is primarily due to the strain induced crystallization of the PTMO soft segments which has been confirmed using wide angle x-ray scattering (WAXS). These materials also display excellent network stability at ambient conditions as evidenced from creep and stress relaxation experiments (194). This distinct elastomeric character of these materials indicates that sufficient microphase separation must have occurred which is an expected event in view of the ionene chemistry (195). It was also shown that there was a tendency for the PTMO segments to crystallize at ambient conditions when PTMO segment molecular weight exceeds 3400 $\overline{M}_n$. Hence, all the materials were initially heated to 60 °C for 1-2 hours prior to testing for purposes of completely melting out any possible PTMO crystallinity. It has been shown that any signs of PTMO crystallinity are removed beyond ca. 40 °C (194).

The objectives of the present investigation is to study the nature of phase separation in the ionene materials as a function of :

- PTMO soft segment molecular weight,
- counterion of the ionene segment, and
- architecture of the ionene segment

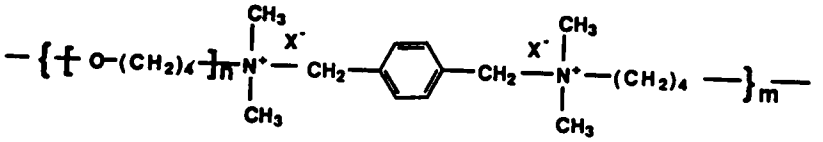

X = Cl, Br, I

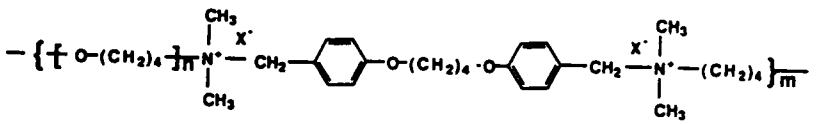

X = Cl, Br, I

Figure 7.1. Chemical Structures of the Ionene Polymers Addressed in this Study: (a) dihalide xylene based ionenes; (b) benzyl dihalide butane based ionenes

Table 7.1. Physical Characteristics of the Ionene Polymers Addressed in this Study

Sample	PTMO segment $\overline{M}_n$	I.V. 0.4 dL/gm	Ion Content, % #ion/PTMO unit	Hard Segm. (vol%)	Hard Segm. (mol%)
IB-NS-14	1400	0.43	10.0	7.9@	5.0
IB-NS-18	1800	0.75	8.0	6.4	4.0
IB-NS-26	2600	1.17	5.6	4.5	2.8
IB-NS-34	3400	1.31	4.3	3.6	2.1
IB-NS-38	3800	1.37	3.8	3.2	1.9
IB-NS-66	6600	2.13	2.2	1.9	1.1
IB-NS-100	10000	2.23	1.4	1.3	0.7
IB-S-34	3400	1.57	4.3	7.5#	2.1
IB-S-66	6600	2.77	2.2	4.0	1.1
IB-S-100	10000	2.62	1.4	2.7	0.7
IC-NS-16	1600	0.35	9.2	7.1*	4.6
IC-NS-21	2100	0.69	6.9	5.5	3.5
IC-NS-38	3800	1.32	3.8	3.1	1.9
IC-NS-66	6600	2.52	2.2	1.8	1.1
IC-NS-100	10000	3.20	1.4	1.2	0.7
IC-S-66	6600	2.35	2.2	4.9†	1.1
IC-S-100	10000	2.48	1.4	3.3	0.7
II-NS-15	1500	0.70	9.6	8.8‡	4.8
II-NS-72	7200	1.00	2.0	2.0	1.0

@ = Estimated from assuming $\rho_{Br-NS} = 2.1$ gm/cc
\# = Estimated from assuming $\rho_{Br-S} = 1.4$ gm/cc (approx.)
* = Estimated from assuming $\rho_{Cl-NS} = 1.5$ gm/cc
† = Estimated from assuming $\rho_{Cl-S} = 1.0$ gm/cc (approx.)
‡ = Estimated from assuming $\rho_{I-NS} = 3.0$ gm/cc (approx.)

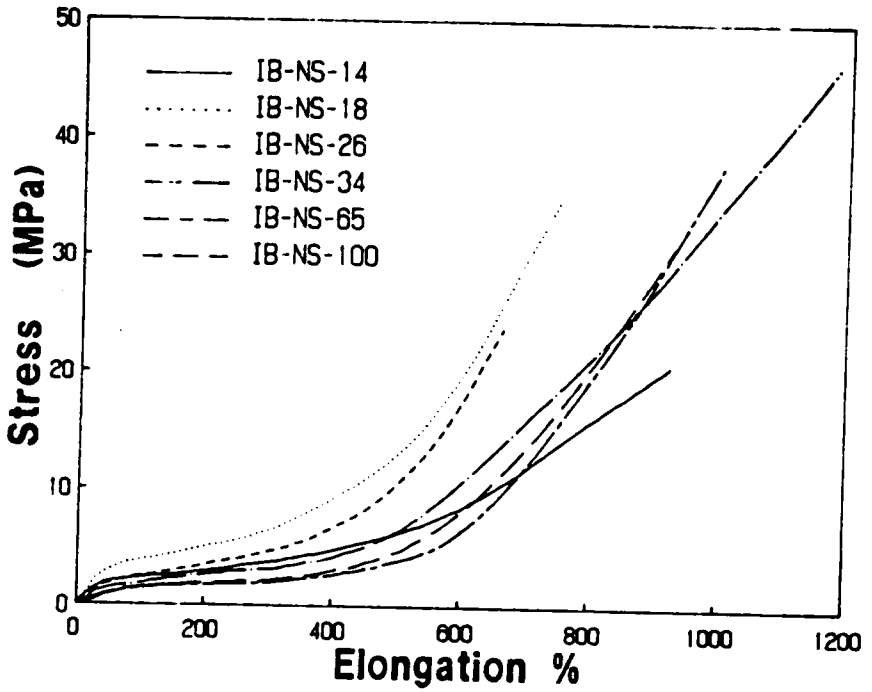

Figure 7.2. Stress-Strain Behavior of the IB-NS-Series: From Feng (194).

The technique of small angle x-ray scattering has been widely used to study the degree of phase separation in polymers (151,152,154). Information relating to the nature of phase separation can be obtained from the analysis of the small angle x-ray scattering (SAXS) profile. Prior to discussing the results obtained from the study, details regarding processing of the experimental data will be initially discussed.

7.2 Thermal Density Fluctuation Corrections

The SAXS data were collected from a Kratky camera with an entrance slit height of 100μ (microns). Parasitic scattering was determined for all samples over the identical angular ranges utilized in the scattering runs. The parasitic scattering represents the scattering emanating from the instrument and also that of the surroundings. The parasitic scattering was subtracted from the overall scattering profile and the resulting profile now represents the scattering from the sample. It should be noted that the scattered intensity profile is a slit smeared intensity profile.

The next step in the analysis is the removal from the scattering profile, the contribution due to thermal density fluctuations in the system. Details regarding the different methods and the associated limitations can be found in section 3.3.5 of this dissertation. This step has been routinely applied in block and segmented polymers, but for the materials under investigation this step represents an important procedure since sharp interfacial regions are expected in these systems in view of the ionene chemistry. Since the tail of the scattering profile was essentially flat (almost parallel to the x-axis) for all the samples studied, Bonart's method was utilized to determine the contribution due to thermal density fluctuations, I_B, in the system. Bonart's method assumes a constant thermal or background scattering. The estimated I_B value were subsequently subtracted from the scattered intensity profile over the whole angular range. The resulting intensity profile, I_{corr}, represents the actual contribution from the electron density fluctuations present in the sample. Since many of the analysis have been modified to incorporate smeared intensities, the slit smeared I_{corr} data was directly utilized for subsequent analysis. However, the I_{corr} data was desmeared using the program developed by Vonk (162), to obtain the actual periodic distances in the system and this

spacing is referred to as the desmeared spacing in subsequent discussions. The 1-D and the 3-D correlation functions were also obtained from Vonk's program. However, the interfacial thickness values and the mean square electron density fluctuation values were obtained from a program developed by Tyagi using the ASYST® data acquisition package and is based on the program developed by Vonk.

7.3 Interdomain Spacings

Figures 7.3-7.5 depict the effect of changing the PTMO segment molecular weight on the small angle x-ray scattering profiles of dihalide xylene based ionene polymers. Both the slit smeared and the desmeared intensity profiles are provided. The scattered intensity is plotted against the angular variable, s, which has already been defined earlier (equation 3.6 on page 67). By varying the PTMO segment length, the ion content in the system is altered. For example, increasing the PTMO segment length increases the distance between the ionene segments but results in a decrease in the overall ion content in the system (see Table 7.1). There are essentially two general characteristics that are observed in Figures 7.3-7.5. With increasing PTMO segment molecular weight, the scattering peak intensity decreases and moves to lower s values or larger spacings. The lowering of the peak intensity can be related to the decrease in the ion content (due to a decrease in the number of scattering centers per unit volume) with increasing PTMO segment molecular weight. Also, the distance of separation between the ionene segments increases with increasing PTMO segment molecular weight which results in larger interdomain spacing, as expected.

An interesting feature of the ionene polymers studied are the multiple scattering peaks that are observed when the PTMO segment molecular weight is less than 3400 $\overline{M}_n$. Since the position of the successive peaks scales in a regular fashion, it is believed that the scattering peaks are a higher order reflections of the primary peak. The multiple peaks are observed in all the three dihalide xylene based materials irrespective of the nature of the counterion. Such distinct higher order scattering has never been observed before in ionomeric materials prior to this work. However, multiple scattering peaks have been observed before in telechelic ionomers (see Chapter 6) but they are not be-

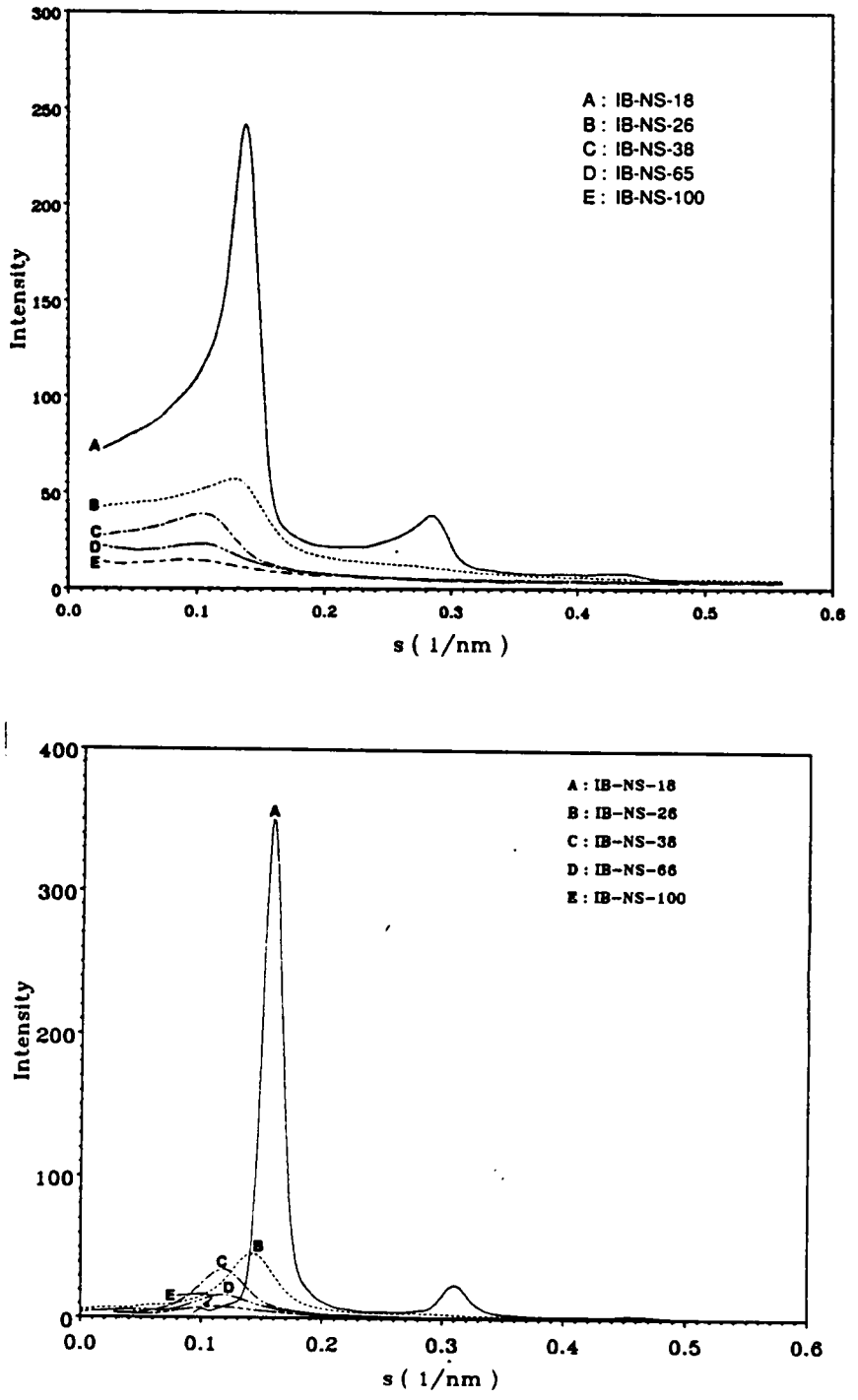

Figure 7.3. **Small Angle X-Ray Scattering Profiles of the IB-NS-series:** (a) slit smeared profiles, and (b) desmeared profiles

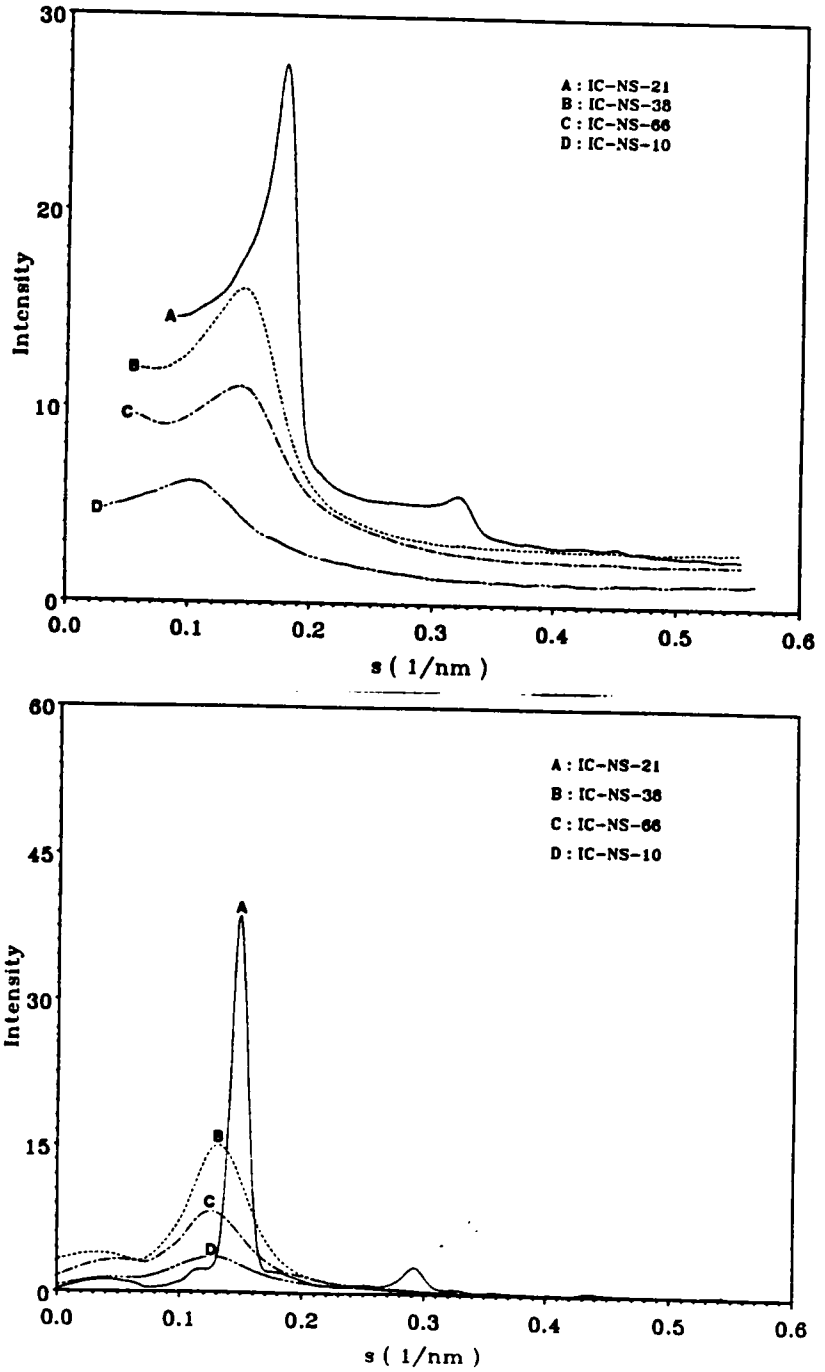

Figure 7.4. **Small Angle X-Ray Scattering profiles of IC-NS-series:** (a) slit smeared profiles, and (b) desmeared profiles

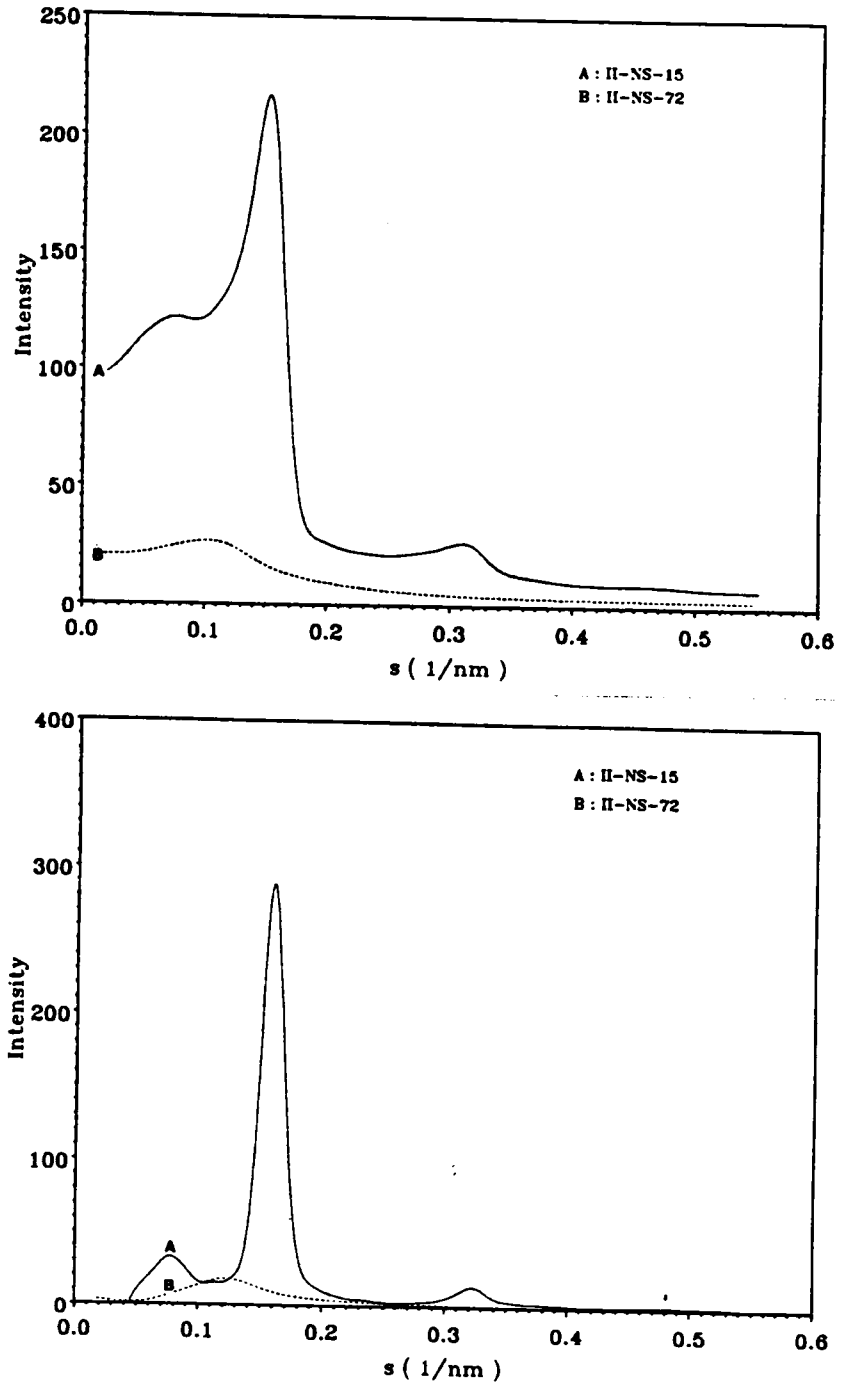

Figure 7.5. **Small Angle X-Ray Scattering profiles of II-NS-series:** (a) slit smeared profiles, and (b) desmeared profiles

lieved to be higher order reflections of the primary scattering peak. In fact, the IB-NS-18 material even exhibits the presence of a third peak. Also, from the desmeared scattering profiles it is evident that the line width of the primary scattering peaks are very sharp which are quite unique especially for ionomeric materials. It should be noted that the ion content in these systems is typically less than 10 volume percent. Based on the general observations from the line width measurements, it is not surprising that higher order peaks are observed in these systems. The multiple order scattering peaks gradually disappears as the PTMO molecular weight increases which suggests that the long range ordering is no longer maintained due to a decrease in the volume fraction of the ionene segments (see Table 7.1). Figure 7.6 shows the dependence of the interdomain or the "d" spacing with the PTMO segment molecular weight. For both bromine and chlorine ionene polymers, a distinct change in the slope is observed when the PTMO segment molecular weight exceeds 3400 $\overline{M}_n$. It is believed that the change in the slope may be related to a change in morphology occurring when the PTMO segment molecular weight of 3400 $\overline{M}_n$ is exceeded. In Tables 7.2 and 7.3, the RMS values present the unperturbed dimensions for the PTMO segments calculated from the relation $< r_0 > / M^{0.5} = 0.093$. From these tables, it can be seen that the PTMO segments below 3400 $\overline{M}_n$ are in a more perturbed conformation than above that value. In these ionenes, the PTMO segments are connected to the hard segments which are ionic in nature. There appears to be a critical ion concentration (or PTMO segment molecular weight) above which the forces of repulsion between adjacent ionic domains become significant and which is responsible for the extension of the intervening PTMO soft segments. Feng utilizing TEM (194) has observed highly ordered regions which are cylindrical or lamellar in texture for the IB-NS-18 ionene polymer. But, on increasing the segment molecular weight to 3400 $\overline{M}_n$, the texture observed tended to appear more spherical in nature. Since the morphological texture was quite similar to the salt and pepper pattern often associated with phase contrast, a definitive morphology was not provided. He has suggested that spherical textures are difficult to interpret using the TEM analysis. In these systems, ionic domains are expected to be small due to the low concentration of the ions. One of the main limitation in using TEM is that the small ionic aggregates appear to be similar in texture to that of the phase contrast. Therefore, differentiation between the two types of observed texture is often a difficult problem.

Feng has, therefore, hesitated in concluding that a spherical morphology is definitely present in the 3400 $\overline{M}_n$ ionene material (194).

The interdomain spacing can also be obtained from the 1-D and the 3-D correlation functions using equation 3.26 and 3.25, respectively. Figure 7.7 depicts both the 1-D and the 3-D correlation function for sample IB-NS-18. The periodic spacing is obtained from the position of the first maxima from either of these functions. The 3-D correlation function does not decay exponentially, indicating that the structure in the material is not totally random as required by equation 3.25. The periodic spacings obtained from both the 1-D and the 3-D correlation functions is provided in Tables 7.2 and 7.3 for the bromide and the chloride ionene materials, respectively. Since multiple order scattering peaks were observed in the IB-NS-18 scattering profile, the spacings corresponding to the position of successive maxima in the correlation function was also considered. The ratio of the spacings corresponding to the successive peaks provide information regarding the morphological state of the system. According to the predictions from the block copolymer theory, the ratio of the successive peak positions scale as 1:2:3 for lamellar morphology and as 1:1.732:2 for hexagonally packed cylindrical morphology (193,196,197). However, no prior work has been conducted in which the spacings corresponding to the successive maxima in the correlation functions were considered. Since the correlation function is closely related to the periodicity in the system, the author strongly feels that the spacing corresponding to the position of the successive maxima should closely reflect the spacing corresponding to that observed from the intensity profiles. It can be seen from Table 7.2 and 7.3 that the spacings obtained from the 1-D correlation function are in good agreement to that obtained from the desmeared data for materials having PTMO segment molecular weight <3400 $\overline{M}_n$. Also, the ratio of successive peak positions scale, from both the desmeared data as well as from the 1-D correlation data scale, as 1:2:3. This clearly suggests that the morphology of the ionene domains is geometrically anisotropic in nature. Another noteworthy feature observed from Figure 7.7 for the IB-NS-18 material is that the periodic oscillation in the 1-D correlation function is a much more pronounced than in the 3-D correlation function. This again strongly suggests that considerable anisotropy might be present in the system. Based on the observed ratio of the successive peak positions, one may be tempted to conclude that a lamellar type of

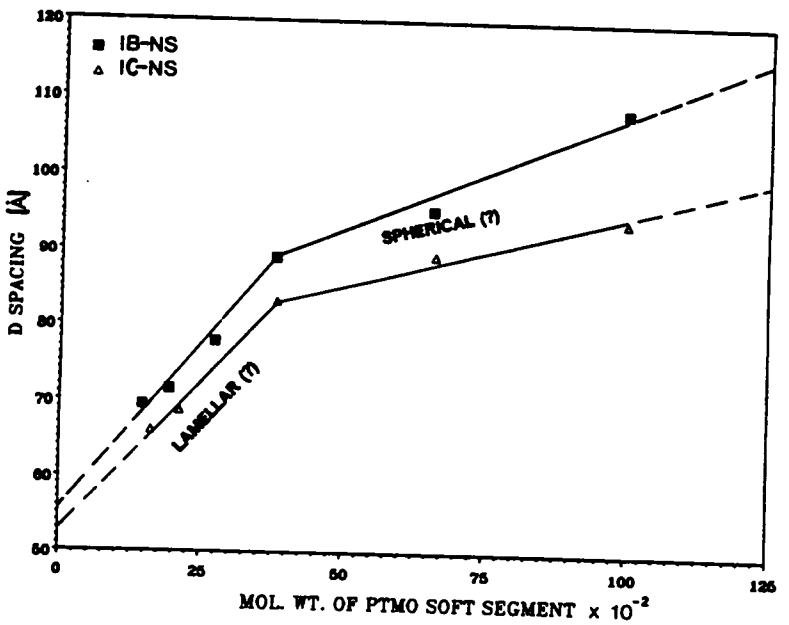

Figure 7.6. Dependence of the "d" Spacing on the PTMO Segment Molecular Weight of IB-NS and IC-NS Series: The morphologies indicated (lamellar or spherical) are purely speculative in nature

Table 7.2. Periodic Spacing Between the Ionic Domains in Dibenzyl Halide based Ionene Polymers (in nm) as Determined by SAXS Analysis

Sample	$d_{smeared}$	$d_{desmeared}$	$\gamma_1(D)$	$\gamma_3(D)$	RMS
IB-NS-14					
d1	6.9	6.8	6.7	7.9	3.5
d2	3.5	3.4	13.5	14.7	
d3			20.2	21.5	
d4			26.9	28.3	
IB-NS-18					
d1	6.6	6.3	6.4	7.5	4.0
d2	3.3	3.3	12.6	14.0	
d3			19.0	20.4	
d4			25.4	26.8	
IB-NS-26					
d1	7.4	7.1	7.0	8.2	4.7
d2			14.0	15.0	
d3			21.1	22.0	
d4			28.0	28.8	
IB-NS-34					
d1	8.0	7.4	6.9	8.9	5.4
d2	4.1	4.1	14.8	16.2	
IB-NS-38					
d1	9.4	8.3	7.4	9.9	5.7
d2			15.8	18.5	
d3			25.1	26.2	
IB-NS-66					
d1	9.0	8.3	7.9	9.9	7.6
d2			15.7	16.5	
IB-NS-100					
d1	9.9	8.7	10.8	6.7	9.3

RMS = unperturbed root mean square end-to-end distance of the PTMO segments

Table 7.3. Periodic Spacing Between the Ionic Domains in Benzyl Dihalide based Ionene Polymers (in nm) as Determined by SAXS Analysis

Sample	$d_{smeared}$	$d_{desmeared}$	$\gamma_1(D)$	$\gamma_3(D)$	RMS
IC-NS-16					
d1	7.2	7.0	7.1	8.3	3.7
d2	3.6	3.6	14.2	15.4	
d3			21.3	22.6	
d4					
IC-NS-21					
d1	6.9	6.7	6.8	8.0	4.3
d2	3.5	3.4	13.7	14.9	
d3			20.5	21.7	
d4			27.3	28.5	
IC-NS-38					
d1	8.1	7.9	7.0	8.8	5.7
d2			14.1	16.7	
d3					
IC-NS-66					
d1	8.9	7.8	7.1	9.0	7.6
d2			15.5	16.4	
IC-NS-100					
d1	10.8	7.4	7.1	9.4	9.3
d2			16.8	14.6	
II-NS-15					
d1	13.2	13.1	6.3	7.4	3.6
d2	6.6	6.3	12.6	13.8	
d3	3.2	3.1			
II-NS-72					
d1	9.5	8.2	6.7	9.3	7.9

RMS = unperturbed root mean square end-to-end distance of the PTMO segments

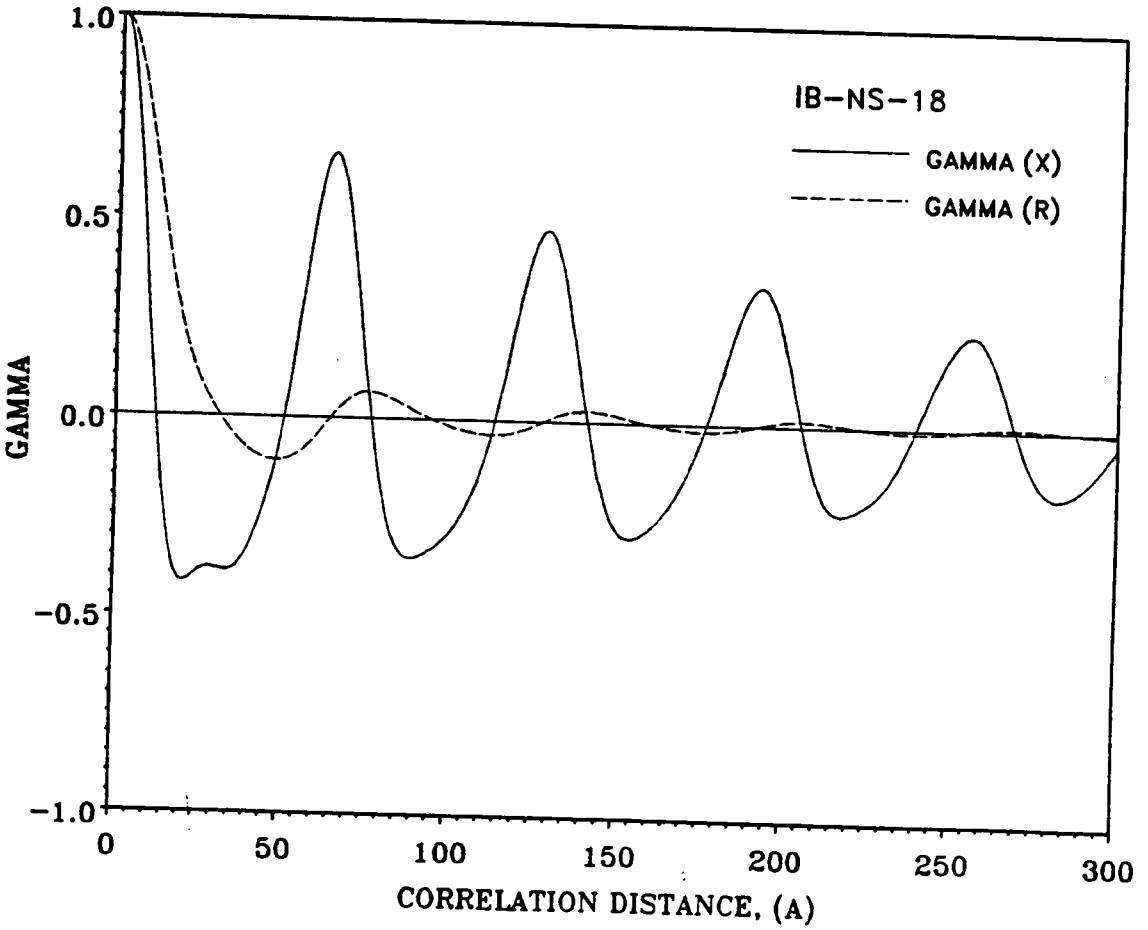

Figure 7.7. The 1-D and the 3-D Correlation Functions for Sample IB-NS-18:

morphology may exist in these ionene systems. However, Feng in his study of IB-NS-18 materials using a pin-hole collimated system (Warhus camera) had observed a strong azimuthal dependence when the x-ray beam was passed parallel to the plane of the film (edge shot) and no orientation effects were observed when the x-ray beam was passed perpendicular to the plane of the film. Clearly, no definitive conclusions can be made from these observations. Based on some first approximation numerical estimations, Feng (194) showed that the IB-NS-18 material is unlikely to form a lamellar type of morphology and that a cylindrical morphology is a more realistic possibility. Though the evidence for a cylindrical morphology is particularly strong, the ratio of the successive peak positions (i.e. 1:2:3) seem to favor a lamellar morphology. If a suitable arrangement of the cylinders in a pseudo-lattice can be identified such that the position of the scattering peaks obtained from the long range periodicity in the system scale as 1:2:3, then it would provide a strong support for the cylindrical morphology argument, at least for the IB-NS-18 material.

Sasisekharan and Ramachandran (198,199) in their study of collagen systems had encountered a similar situation. They had proposed a roll structure or a spiral lattice model where there is a correlation between lattice points only along the radial and the circumferential direction. Under certain conditions, only a certain set of reflections occur and the positions of these reflections scale in the ratio of 1:2:3. Based on this study, a similar spiral lattice model is proposed for the arrangement of the ionene domains in IB-NS-18 material. The schematic representation of the model is shown in Figure 7.8. Each solid circle in the figure represents an end on view of the cylindrical arrangement of the ionene domains. If one lets the distance between successive cylinders in the radial direction be "a" and the distance between cylinders along the circumference be "b", then the relation given below can be used to construct the spiral lattice;

$$\Delta n = n_j - n_{j-1} = 2\pi \frac{a}{b} \tag{7.1}$$

where n_j is the number of cylindrical domains on the j-th cylindrical surface. By a proper choice of the parameters a and b, one might be able to mathematically model the scattering behavior for

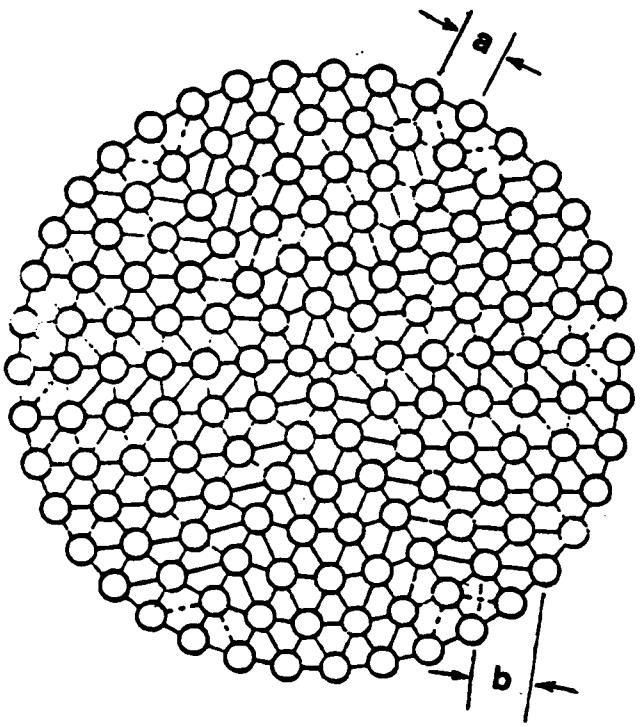

Figure 7.8. Roll Structure or the Spiral Lattice Model Proposed for Sample IB-NS-18:

the IB-NS-18 material. Since, the mathematics of the problem is quite involved, the modelling portion of the problem was not included as a part of this study.

The effect of changing the counterion of the ionene segment from Cl to Br to I is shown in Figure 7.9. A significant increase in the intensity of the scattering peaks is observed with increasing atomic number of the cation (Cl<Br<I). With increasing atomic number both the number of electrons and the size of the atom increase. But the increase in the size of the atom is not proportional to the increase in the atomic number (at least for the halogen series). Therefore, a net increase in the electron density of the atom is realized which contributes to an increase in the electron density of the domains containing the cation. In fact, a considerable increase in the electron density of the ionene domains is realized in going from Cl to Br to I (for estimation of the electron density - see Appendix I). Thus the increase in the scattered intensity results from an increase in the scattering contrast (electron density difference) in the system. An additional scattering peak occurring at ca. 0.075 nm^{-1} corresponding to a desmeared spacing of 13.2 nm is observed for sample II-NS-15. However, the spacing corresponding to this peak is almost twice that of the main peak. Therefore, it is believed that the origin of this peak may be related to the main peak scattering peak which has already been discussed earlier.

The small angle x-ray scattering profiles of materials containing a spacer group in the ionene segment is shown in Figure 7.10 and the spacings obtained from the SAXS analysis is given in Table 7.4. It was believed that the incorporation of the aliphatic group may promote some degree of phase mixing between the ionene segment and the PTMO backbone. Based on mechanical and dynamical studies, Feng (194) had observed that the spacer containing materials exhibited weaker association and therefore suggested poorer phase separation than the dihalide xylene based materials. From the SAXS measurements, it was observed that there was little difference in the scattering intensity which suggests that the phase boundaries in these materials is still relatively sharp. As suggested by Feng (194), it is believed that the lowering of the softening temperature and somewhat poorer tensile properties observed for these materials are primarily due to weaker association of the ionic groups within the ionene domains possibly caused by packing hindrances with the presence of the aliphatic group - however, this is merely a speculation. Hence, it is believed that the some-

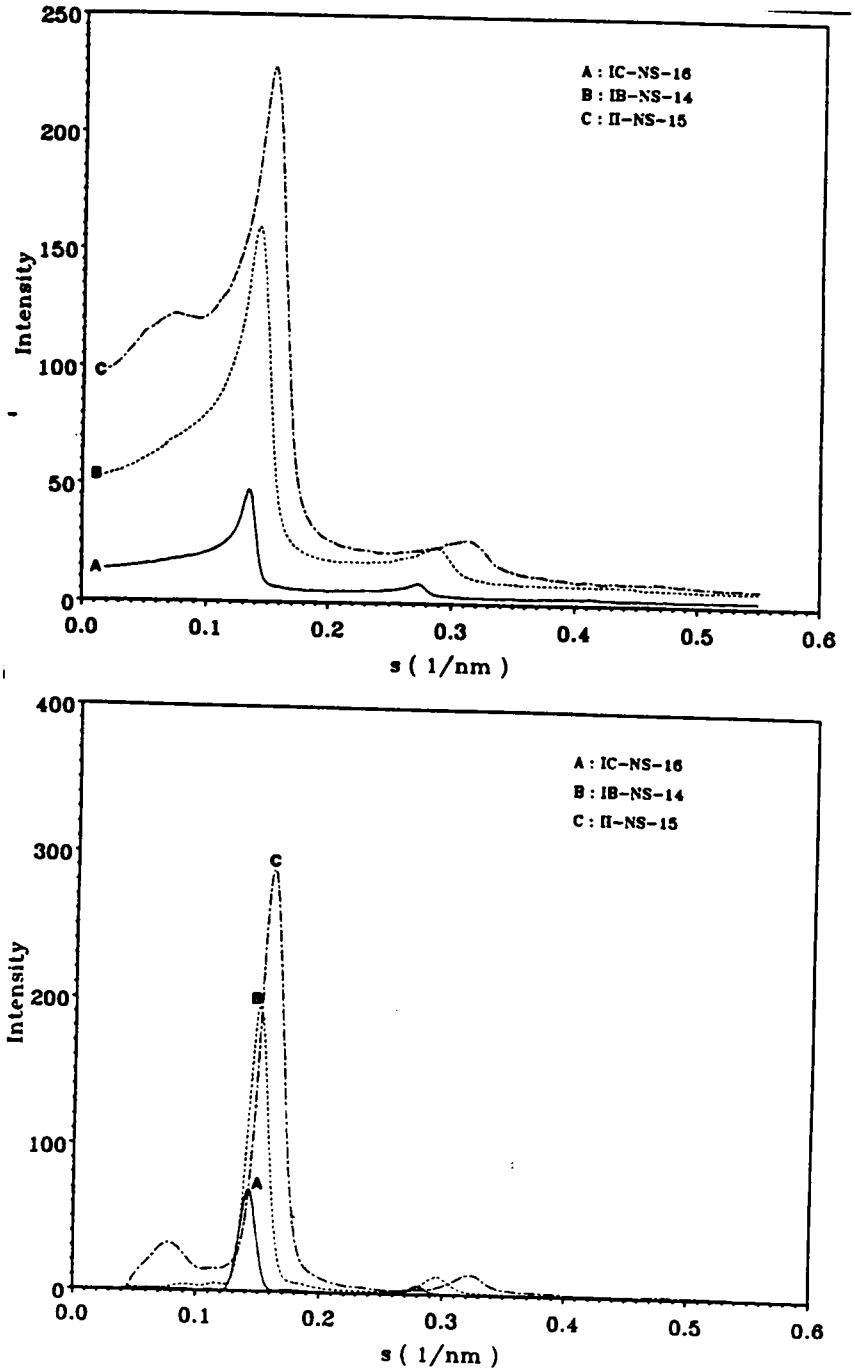

Figure 7.9. Effect of the Varying the Counterion of the Ionene Segment:

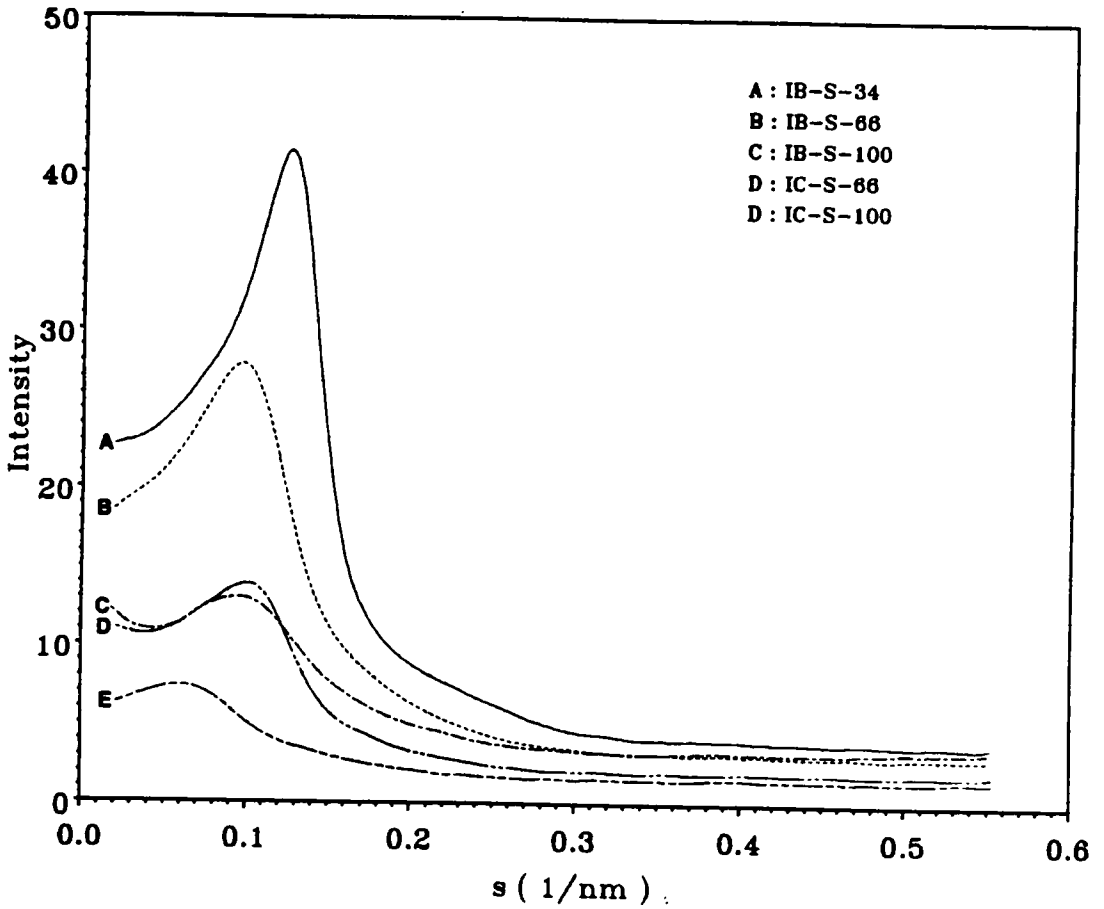

Figure 7.10. Small Angle X-Ray Scattering Profiles of IX-S Series:

Table 7.4. Periodic Spacing between the Ionene Domains based on dibenzyl halide butane (in nm) as Determined from SAXS Analysis

Sample	$d_{smeared}$	$d_{desmeared}$	$\gamma_1(D)$	$\gamma_3(D)$	RMS
IB-S-34 d1	7.9	7.4	6.9	8.9	5.4
IB-S-66 d1	10.2	9.0	8.6	10.5	7.7
IB-S-100 d1	10.1	8.8	7.3	10.3	9.3
IC-S-66 d1	9.9	8.7	8.0	10.2	7.7
IC-S-100 d1					9.3

RMS = unperturbed root mean square end-to-end distance of the PTMO segments

what poorer tensile properties exhibited by the ionene materials with a spacer in the hard segment is primarily due to the poorer associations present with the ionene segments.

7.4 Diffuse Boundary Analysis

The estimation of the diffuse boundary thickness was determined in terms of the Porod's law behavior. Slit smeared intensity was directly used in the diffuse boundary analysis. The tail region of the Porod's plot ($\tilde{I}(s)*s^3$ vs. s^3) provides information regarding the nature of the phase boundary. A negative slope is indicative of the presence of a diffuse phase boundary while a positive slope indicates the presence of isolated mixing of hard/soft segments in the domains. A zero slope is indicative of a sharp phase boundary. Figure 7.11 shows a schematic representation of a sharp phase boundary ($\sigma = 0$) and a diffuse phase boundary ($\sigma > 0$) for the case of dibromo-xylene based ionene polymers. As mentioned earlier, the slit-smeared intensity data has been carefully treated for the thermal density fluctuations in the system. Different methods were utilized to estimate the diffuse boundary thickness (or the interfacial thickness) between the two phases in the system (see Table 3.4).

Based on the chemistry of these ionene polymers, it is anticipated that the interfacial region should be small. Different plots for IB-NS-18 is shown in Figure 7.12 and that for IB-NS-66 is shown in Figure 7.13. Sample IB-NS-18 was chosen to represent the materials that exhibit multiple scattering peaks while IB-NS-66 was chosen to represent those materials which exhibit essentially one scattering peak. From the Porod plot (Figure 7.12a), it can be seen that the tail region for IB-NS-18 is severely limited due to the presence of the higher order scattering peaks in this region. However, even in such a small region, a distinct linear region is observed from which the slope can be determined in order to calculate the diffuse boundary thickness. Though the tail region is small, it is observed that there is only a very small negative deviation observed which indirectly suggests that the interfacial region is relatively sharp. It will be shown later that the phase separation in this system is almost complete and therefore the near "ideal" or Porod type of behavior is not surprising. The ionene materials that is speculated to have a spherical morphology (refer to Figure 7.6) also

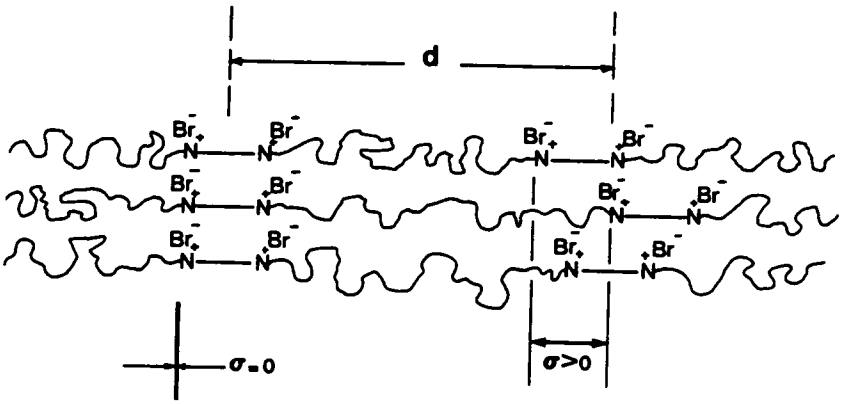

Figure 7.11. Schematic Representation of the Diffuse Boundary Region in a Dihalide-xylene based Ionene Polymer:

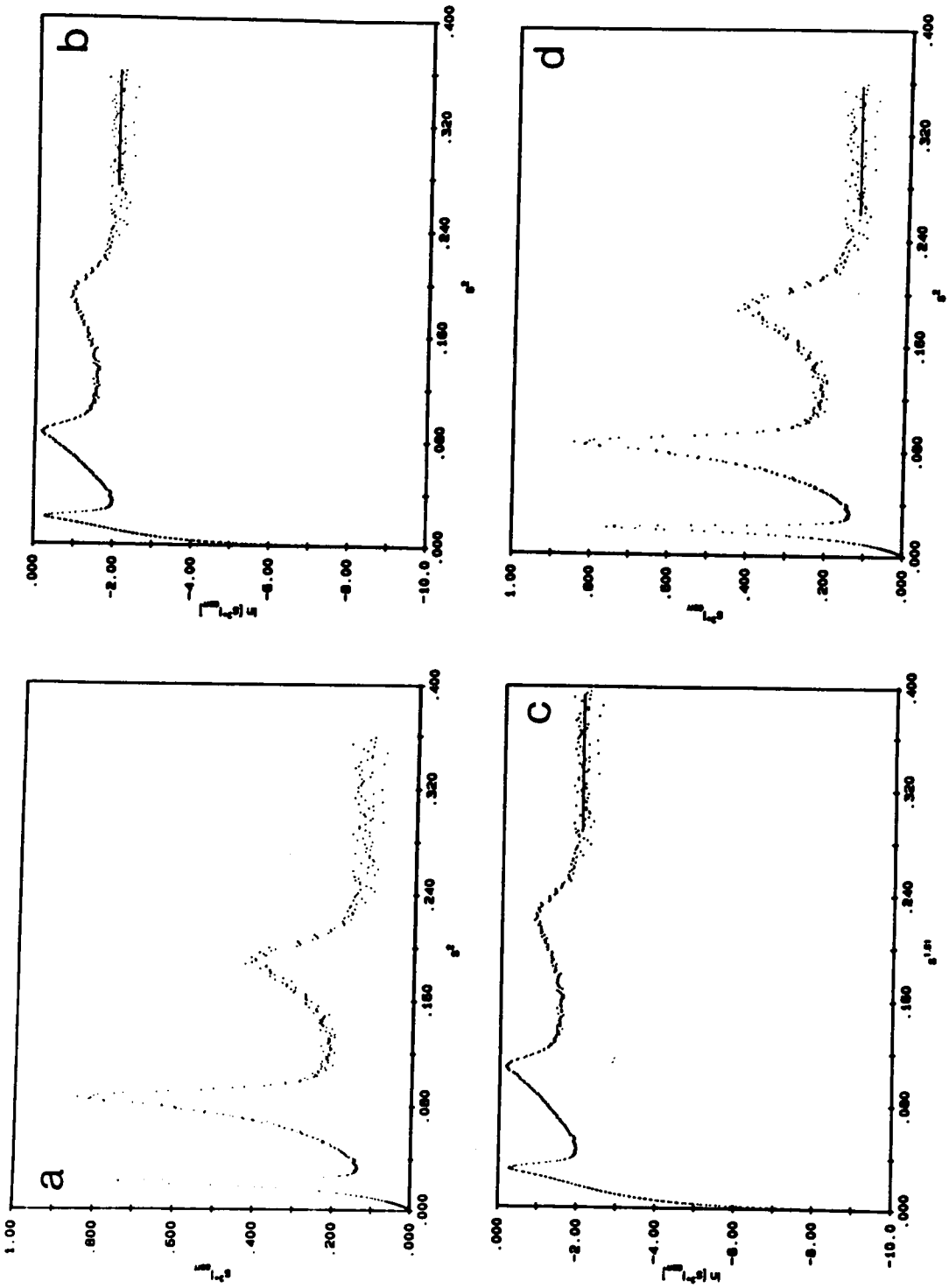

Figure 7.12. Different Methods Utilized to Determine the Diffuse Boundary Thickness for Sample IB-NS-18: (a) Porod' plot, (b) Bonart' plot, (c) Koberstein's plot, and (d) Ruland's plot

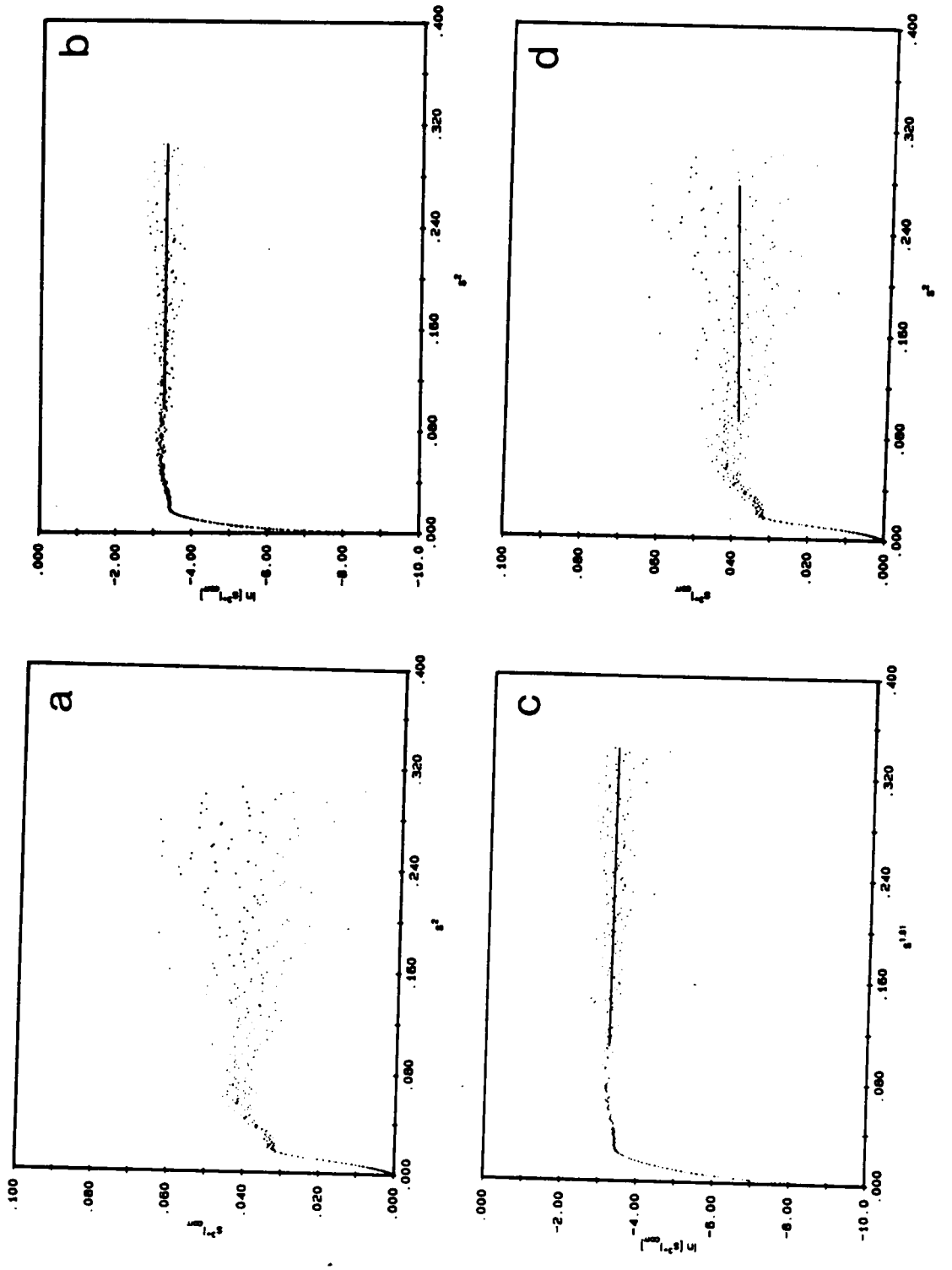

Figure 7.13. Different Methods Utilized to Determine the Diffuse Boundary Thickness for Sample IB-NS-66: (a) Porod' plot, (b) Bonart' plot, (c) Koberstein's plot, and (d) Ruland's plot

Table 7.5. Diffuse Boundary Thickness Values Obtained from Different Methods for Ionene Polymers with Bromide as the Counterion

Sample-id	Interfacial thickness values, σ (in nm)			
	Bonart	Exponential	Koberstein	Ruland
IB-NS-14	*	*	*	*
IB-NS-18	0.089	0.059	0.0	*
IB-NS-26	0.136	0.093	0.102	0.069
IB-NS-34	0.193	0.116	0.134	0.118
IB-NS-38	0.212	0.149	0.187	0.063
IB-NS-66	0.052	0.050	0.053	*
IB-NS-100	0.051	0.028	0.028	*
IB-S-34	0.123	0.089	0.101	0.086
IB-S-66	*	*	*	*
IB-S-100	*	*	*	*

* = not available (due to positive deviation from Porod's law)

Table 7.6. Diffuse Boundary Thickness Values Obtained from Different Methods for Ionene Polymers with Chloride as the Counterion

Sample-id	Interfacial thickness values, σ (in nm)			
	Bonart	Exponential	Koberstein	Ruland
IC-NS-16	*	*	*	*
IC-NS-21	0.163	0.115	0.096	0.043
IC-NS-38	0.157	0.125	0.123	0.051
IC-NS-66	0.183	0.135	0.157	0.078
IC-NS-100	*	*	*	*
IC-S-66	*	*	*	*
IC-S-100	*	*	*	*
II-NS-15	0.166	0.036	0.076	0.108
II-NS-72	0.046	0.039	0.038	*

* = not available (due to positive deviation from Porod's law)

exhibit a near "ideal" or a Porod type behavior. The various plots obtained for IB-NS-66 exhibit a near zero slope which is again indicative of a sharp interface boundary. The interfacial thickness values estimated from the methods discussed earlier in Chapter 3 are given in Tables 7.5 and 7.6. To determine the diffuse boundary thickness, the interfacial thickness boundary can be assumed to be either linear or sigmoidal in shape as shown in Figure 3.6. It has been shown that the sigmoidal gradient is most likely to occur in a phase separated system (164,167). Therefore, a sigmoidal gradient was assumed to represent the diffuse boundary region in the ionene systems. For IB-NS-18, the interfacial thickness value obtained was less than the bond length of the C-C bond (ca. < 0.1 nm). This observation clearly suggests that the interfacial region is, indeed, very sharp !. For nearly all the dihalide xylene (-NS-) based ionene materials, very small interfacial thickness values were obtained. Such sharp phase boundary has also been observed earlier by Williams et al. in carboxy-telechelic PBD ionomers (84). Similar observation was also observed in our study of telechelic ionomers based on PIP as well as PBD ionomers (discussed Chapter 6). In view of the very good ionic network behavior observed indirectly via mechanical measurements, it is not surprising to observe a very sharp phase boundary in these dihalide xylene based ionene polymers. Also, the ionic or electrostatic nature of the ionene segments (with counterion) provide the necessary driving force for phase separation. In some cases, a small positive deviation from the Porod's law was observed and therefore diffuse boundary thickness values could not be estimated for such systems. This behavior is indicative of isolated mixing of one segment in that of the other component. It is observed that the interfacial thickness values determined from Bonart's method is consistently larger while that determined from Ruland's method is consistently smaller than that obtained from other methods. This observation is consistent with the earlier work of Koberstein et al. (154,177,183). They had earlier concluded that Bonart's method essentially over estimates the value of σ while Ruland's method under estimates the true interfacial thickness value. This arises primarily from the type of approximations utilized for the smoothing function term (see Chapter 3). In earlier work, it was shown that the method of Koberstein which is also referred to as the empirical method provides a σ value closest to the true σ (177,183). Moreover, it should be realized that the deter-

mination of the true value of the diffuse boundary thickness is not feasible and that only estimations to the true value can be obtained.

From Tables 7.5 and 7.6, it can be seen that there is no appreciable difference in the diffuse boundary thickness values in varying the nature of the counterion of the system. It will be shown shortly that the primary driving force for phase separation is the ionic nature of the ionene segments. The inherent nature of these ionene segments are not significantly altered by changing the nature of the counterion. Hence, very little differences in the diffuse boundary thickness is observed when varying the nature of the counterion of the ionene segment. Most of the materials containing the spacer unit in the ionene segment exhibited a positive deviation and hence the diffuse boundary thickness could not be evaluated. Only one material, IB-S-34, exhibited negative deviation from Porod's law from which a diffuse boundary thickness of 0.1 nm was obtained using Koberstein's method whereas a value of 0.13 nm was obtained for IB-NS-34. But, even the value obtained for IB-NS-34 is lower than the C-C bond length. Below this value, the numerical value of the diffuse boundary thickness is of little significance. Thus it is seen that the diffuse boundary region is very sharp in all the ionene materials irrespective of the ion concentration in the system, the nature of the counterion or architecture of the ionene segment.

Based on their work on segmented urethane systems, Ophir and Wilkes (189) have stated that the diffuse boundary thickness values that are obtained can only serve as a relative parameter when comparing similar materials. The results that are obtained also support such a viewpoint. The diffuse boundary thickness parameter was found to be a very sensitive to the thermal density fluctuation estimation procedure. Hence, the "goodness" of the fit becomes crucial in the estimation of thermal density fluctuation in the system. However, there is no preference of any particular method in the diffuse boundary estimation procedure.

7.5 Degree of Phase Separation

It was discussed earlier that the mean square electron density fluctuation is related to the scattering invariant in the system (equation 3.24). Comparison of the different variances $\overline{\Delta\rho_e^2}$,

$\overline{\Delta\rho^2}$, and $\overline{\Delta\rho^{2''}}$ (as were defined in Chapter 3) provide valuable insight into the state and degree of phase separation in these systems. The different variances have been defined earlier in equations 3.51, 3.53 and 3.54, respectively. To obtain the value of $\overline{\Delta\rho^{2''}}$, the diffuse boundary thickness obtained from Koberstein's method was utilized to determine the smoothing function, $H^2(s)$, since it is believed that the σ value obtained from Koberstein's method more closely represents the true σ value. The overall degree of phase separation can be obtained from the ratio of $\overline{\Delta\rho^2}/\overline{\Delta\rho^{2''}}$. This ratio approaches unity for a completely phase separated system while it approaches zero for a completely phase mixed system. The amount of phase mixing within the domains irrespective of any boundary diffuseness is obtained from the ratio $(\overline{\Delta\rho_e^2}/\overline{\Delta\rho^{2''}}\text{-}1)$. This ratio is zero in the absence of any intradomain segmental mixing. Finally, a third ratio $(\overline{\Delta\rho^{2''}}/\overline{\Delta\rho^2}\text{-}1)$ provides a measure of the boundary diffuseness, irrespective of intradomain mixing. For sharp phase boundaries this ratio is zero. One of the main limitations of this analysis is the determination of the variance $\overline{\Delta\rho_e^2}$. The procedure for the estimation of this quantity is given in Appendix I and it requires that the density of the individual phases be known. This problem is accented in ionomers since the position of the unassociated or free cation or the anion is not known. Often the density of the precursors are utilized instead of the true density since the true density cannot be determined. Moreover, if impurities were to be present, they would also contribute to the overall scattering. Hence, quantification of the degree of phase separation analysis should be done with caution.

The different mean square electron density variances along with the different ratios is given in Tables 7.7 and 7.8. Considering the IB-NS series, it is observed that an almost complete phase separation is seen for the IB-NS-18 material. The high degree of ordering (especially the observance of a third peak - not seen in other materials) in this material is related to the high degree of phase separation in the system. Moreover, it was observed that the peak intensity of the IB-NS-14 was lower than that of the IB-NS-18 material. Though it was a surprising observation at first, the degree of phase separation in the IB-NS-14 material is only ca. 48% while it was ca. 91% for the IB-NS-18 material. Phase mixing in effect reduces the scattering contrast in the medium which results in lowering of the scattered intensity. There is no particular trend observed in the degree of phase separation with increasing PTMO segment molecular weight. The chloride ionene in general seem

Table 7.7. Mean Square Density Variances Obtained for the Ionene Polymers with Bromide as the Counterion

Sample-id	$\overline{\Delta\rho_e^2}$	$\Delta\rho^{2'}$	$\Delta\rho^{2}$	$\Delta\rho^{2}/\overline{\Delta\rho_e^2}$	$(\overline{\Delta\rho_e^2}/\Delta\rho^{2'}) - 1$	$(\Delta\rho^{2}/\Delta\rho^{2'}) - 1$
IB-NS-14	13.81	6.57	*	0.48	*	*
IB-NS-18	11.43	10.45	10.45	0.91	0.09	0.0
IB-NS-26	8.33	4.36	4.54	0.52	0.83	0.04
IB-NS-34	6.41	2.99	3.20	0.47	1.00	0.07
IB-NS-38	5.82	1.73	1.89	0.30	2.08	0.09
IB-NS-66	3.38	1.26	1.28	0.37	1.64	0.02
IB-NS-100	2.33	0.98	0.99	0.42	0.34	0.01
IB-S-34	2.34@	1.86	1.91	0.79	0.22	0.03
IB-S-66	1.29@	1.15	*	*	*	*
IB-S-100	0.89@	0.72	*	*	*	*

$\overline{\Delta\rho_e^2} = \Delta\rho^{2'} = \Delta\rho^{2} = [mol\ e^-/cm^3]^2 \times 10^3$

* = not available (due to positive deviation from Porod's law)

@ = Estimated from assuming $\rho_{Br^-S} = 1.5$ gm/cc

Table 7.8. Mean Square Density Variances Obtained for the Ionene Polymers with Chloride as the Counterion

Sample-id	$\overline{\Delta\rho_c^2}$	$\overline{\Delta\rho^2}$	$\overline{\Delta\rho^{2''}}$	$\overline{\Delta\rho^2}/\overline{\Delta\rho_c^2}$	$(\overline{\Delta\rho_c^2}/\overline{\Delta\rho^{2''}}) - 1$	$(\overline{\Delta\rho^{2''}}/\overline{\Delta\rho^2}) - 1$
IC-NS-16	1.56	1.39	*	0.89	*	*
IC-NS-21	1.24	1.17	1.21	0.94	0.02	0.04
IC-NS-38	0.72	0.94	0.99	1.31	- 0.27	0.05
IC-NS-66	0.43	0.83	0.90	1.93	- 0.52	0.08
IC-NS-100	0.28	0.69	*	2.46	*	*
IC-S-66	0.15#	0.56	*	3.73	*	*
IC-S-100	0.22#	0.10	*	2.20	*	*
II-NS-15	42.70@	12.50	12.81	0.29	2.33	0.03
II-NS-72	10.16@	1.85	1.87	0.18	4.43	0.01

$\overline{\Delta\rho_c^2} = \overline{\Delta\rho^2} = \overline{\Delta\rho^{2''}} = [mol\ e^-/cm^3]^2 \times 10^3$

* = not available (due to positive deviation from Porod's law)

= Estimated from assuming $\rho_{Cl-S} = 1.0$ gm/cc

@ = Estimated from assuming $\rho_{I-NS} = 3.0$ gm/cc

to exhibit a higher degree of phase separation (column 5 in Tables 7.7 and 7.8) than either bromide or the iodide ionenes. In the chloride materials, phase mixing within the domains (column 6) was almost absent while the bromide and the iodide materials provided indications of intradomain mixing. Surprisingly, only a faint secondary peak was observed for the IB-NS-26 material. From Table 7.7, it is evident that the degree of phase separation in this material is low (ca. 52%) and there was considerable amount of phase mixing within domains (intradomain mixing) which essentially reduces the scattering contrast of the ionene domains. However, isolated segmental mixing of one phase in the other would also decrease the electron density contrast in the system. Both, intradomain mixing and isolated segmental mixing would lower the value for value for the experimentally observed electron density variance, $\overline{\Delta\rho^2}$. Based on the chemical structure of the ionene segment, it is believed that the isolated mixing of the ionene segments in the PTMO matrix may be responsible for lowering the $\overline{\Delta\rho^2}$ value. The absence of long range order and the observance of lower than expected intensity in the IB-NS-26 material can be attributed to both diffuse phase boundary and also due to isolated segmental mixing in the system. A considerable amount of phase mixing is also observed in the iodide ionene polymers. As mentioned earlier, the ratio in column 7 of Table 7.7 and 7.8 provide information regarding the nature of boundary diffuseness irrespective of domain mixing. The value of this ratio for all the materials studied is essentially zero which indicates that the interfacial boundary region is considerably sharp, a result consistent with the observed values for the diffuse boundary thickness.

7.6 Origin of Microphase Separation in the Ionene Polymers

In block copolymers, microphase separation is primarily driven by segmental incompatibility or the solubility parameter differences between the different segments or domains. In materials that contain ions, there is an additional factor in the system (coulombic forces) which can also provide the necessary driving force for phase separation. It has been demonstrated that a high degree of microphase separation exists in these ionene polymers. However, it is not known at this point whether microphase separation is promoted by segmental incompatibility or due to the charge ef-

fects in the system. In order to determine the primary cause for phase separation in the ionene polymers, an charged segmented polymer with PTMO as the soft segment and brominated hard segment quite similar to dibromo-p-xylene but with an higher electron density contrast was synthesized by Dr. Leir's group so that the behavior of the non-ionene (or uncharged) material could be directly compared to that of the ionenes. The non-ionene segment was based on tetrabromobisphenol so that the potential for hard segment crystallization could be is eliminated. The chemical structure of the non-ionene material is given on page 110 and henceforth this material will be designated as IB-NSC-20. If the phase separation process were to be primarily driven by segmental incompatibility, then the IB-NSC-20 material should exhibit elastomeric behavior similar to that observed in the ionene polymers since the solubility parameter of the two hard segments are similar.

From dynamic mechanical analysis, Feng (194) has observed that the IB-NSC-20 essentially flows above the melting point of the PTMO (~ 30 °C) and the material does not display good elastomeric behavior at ambient conditions. This observation clearly suggests the absence of microphase separation in the IB-NSC-20. To illustrate that microphase separation does not exist in the IB-NSC-20 material, the more direct method of SAXS was utilized. It should be noted that electron density contrast for the IB-NSC-20 material is higher than the IB-NS-18 ionene material since four bromine atoms are present in its hard segment as compared to two for the ionene polymer. Figure 7.14 shows the SAXS profile of both IB-NSC-20 material and the IB-NS-18 ionene polymer. It can be clearly observed that no indication whatsoever of the inducement of microphase separation is seen in the uncharged IB-NSC-20 material whose chemical structure is relatively similar to the ionene segment. Clearly, the low and monotonically decreasing intensity is indicative of a rather homogeneous system at least at the dimensional scale probed by SAXS. Hence, the observed behavior strongly suggests that it is the charged quaternary ammonium groups that is the primary driving force for microphase separation in the ionene polymers.

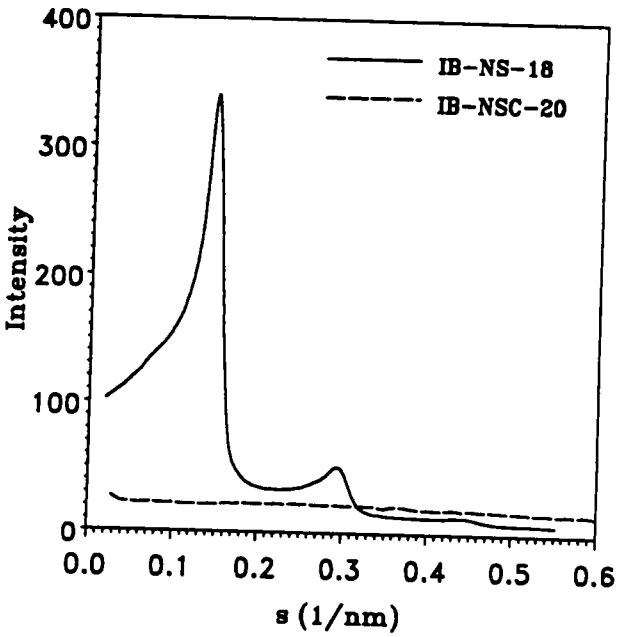

Figure 7.14. Small Angle X-Ray Scattering Profiles: (a) IB-NS-18, and (b) IB-NSC-20

7.7 Summary

The segmented ionene materials display very interesting behavior. Microphase separation is these materials is primarily promoted due to charge effects in the system. Almost all the materials investigated exhibit a near "ideal" or a Porod law type of behavior. This is evidenced by the presence of a sharp phase boundary that was observed in almost all the materials investigated. The degree of phase separation plays an important role in the observed SAXS behavior. While the chloride materials exhibited no intradomain segmental mixing, the systems with bromide and iodide as the counterion indicated that there may a small degree of intradomain mixing. However, based on the structure of ionene segment, it is believed that the lowering of the $\overline{\Delta\rho^2}$ value is primarily due to isolated segmental mixing in the system and not due intradomain mixing. The Br and the I ions, due to their larger size may pull out of the ionene domains, contributing to the isolated segmental mixing phenomenon.

The periodic spacing systematically increases with PTMO segment molecular. A change in the morphology is indicated when the PTMO segment molecular exceeds 3400 $\overline{M}_n$. Some of the materials displayed multiple scattering peaks which has not been observed before in ionomeric systems. In a concurrent study, Feng was able to observe long range ordering in these systems especially when the volume percent of the ionic moieties was ca. 6.4%. This high degree of ordering in the IB-NS-18 material is primarily believed to be due to a high degree of phase separation in the system along with the absence of other effects such as intradomain mixing, etc. Though there is a strong indication that the ionene domains in the IB-NS-18 material may exist in a cylindrical morphology, there is not any definitive indication to that effect. Future studies will attempt to resolve this issue.

8.0 SELECTIVE PLASTICIZATION OF SEGMENTED IONENE POLYMER

In a concurrent study by Feng, it was shown that the segmented ionene polymers at ambient conditions displayed good elastomeric properties with excellent tensile strength (upto 30-40 MPa), significant elongations at break (>1000%) and quite high recoverability (195). These materials, therefore, have a good potential to be thermoplastic elastomers. The softening temperatures of these ionene materials are ca. 150-180 °C depending on the counterion and the architecture of the ionene segment. However, when they are processed at elevated temperatures, irreversible breakdown of properties occur which necessitates the need to identify a procedure to lower the softening temperature, thus enabling thermal processing.

To put the present study in a proper perspective, the need for lowering the softening temperature of the ionene polymer will first be established. Later, the identification of a suitable additive to lower the softening temperature will be discussed. Finally, the effects of the chosen additive on the structure-property behavior of the resulting additive-ionene polymer will be presented. The ionene polymer chosen for the present study is IB-NS-14 which has a PTMO molecular weight of 1400 $\overline{M}_n$ and the ionene segment of this material is based on a α, α' dibromo-p-xylene.

The main advantage anticipated from thermoplastic materials which depolymerize to the initial reactants at elevated temperatures is that the melt viscosity would be significantly lower than the conventional thermoplastic materials (116). Ideally, in the case of the ionene polymer, it was anticipated that at elevated temperatures the ionene polymer would dequaternize rapidly and without any side reactions yielding a readily processable syrup of lower molecular weight amines and dihalides. On cooling, it would hopefully requaternize sufficiently fast and completely to its original molecular weight. However, it has been reported by Leir and Stark (116) that extensive irreversible degradation occurs in these ionene polymers when heated to elevated temperatures.

8.1 Preliminary Investigation

Figure 8.1 shows the stress-strain behavior of the IB-NS-14 ionene polymer as a function of the annealing time after the material was given a thermal treatment. The material was compression molded at 180 °C for ca. 5 minutes, quickly quenched to ambient conditions and annealed in a vacuum oven until the time of the experiment. The time interval shown in Figure 8.1 represents the annealing time in the vacuum oven. The figure shows only a part of the stress-strain profile of the sample that has not been compression molded (notice the arrow in curve E), and that sample serves as a reference material. Details regarding the complete stress-strain profile of this material will be discussed later. All the materials that underwent this thermal treatment exhibit very poor mechanical properties (i.e. low modulus, low ultimate tensile strength, and ultimate elongation). In fact, immediately after the thermal treatment, the material was tacky in nature. The ultimate tensile strength and ultimate elongation of the reference material that has not undergone thermal treatment is ca. 14 MPa. and 1300%, respectively. The tensile strength recovers from ca. 0.4 MPa after 10 minutes annealing (curve A) to ca. 1.6 MPa in 29 hours (curve D); however, no significant improvement in the ultimate elongation is observed (ca. 750% for curves A-D). Based on the earlier work of Leir & Stark (116), it is speculated that extensive degradation must have occurred. In order to substantiate this speculation, inherent viscosity (I.V.) measurements (which are indicative of the overall molecular weight) were conducted. Table 8.1 shows the inherent viscosity values obtained from IB-NS-14 samples that had been heated to 180 °C for different lengths of time. A considerable decrease in the I.V. of the IB-NS-14 samples was observed with time (from 0.43 to 0.17, a 60% decrease in 22 minutes). This suggests that significant lowering of the overall molecular weight occurs in these ionene materials at elevated temperatures. The origin of this degradation is not yet known. Since these ionene polymers cannot be thermally processed without loss of material properties, they clearly cannot function as thermoplastic elastomers.

Figure 8.1b shows the modulus of the material that underwent thermal treatment with annealing time. Notice that the modulus of the untreated sample is ca. 9.2 MPa. For the thermally treated samples, the modulus of the material significantly recovers with time (ca. 8.2 MPa in 29

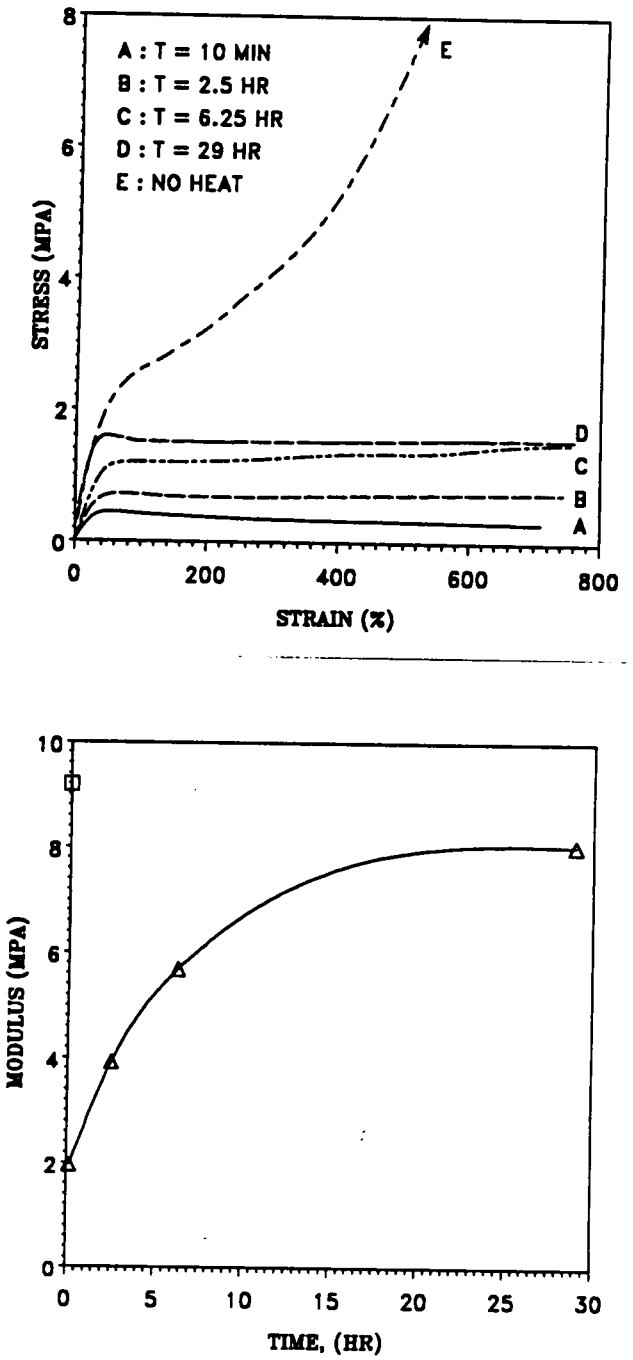

Figure 8.1. Effect of thermal cycling at 180 °C for IB-NS-14: (a) Stress-strain behavior, (b) Modulus Recovery (□ = untreated; △ = thermally treated)

Table 8.1. I. V. Measurements of Sample IB-NS-14 as a Function of Time Following Thermal Treatment

Time (minutes)	I.V.@ (dL/0.4 g in $CHCl_3$)
0#	0.43
14	0.23
22	0.17

@ - at room temperature
# - material was not compression molded

hours). The recovery that is observed for the modulus is primarily due to the aggregation of the ionene segments to form domains.

Based on ionene chemistry, it is expected that the ionene polymer will revert to the initial reactants near the softening point of the ionene segments. Leir and Stark (116) have speculated that the requaternization reaction in the solid state may be slow. In addition, Dreyfus (200) has showed that the hydroxy terminated PTMO segments tend to degrade (even in vacuum) above 150 °C. Therefore, the end group plays a significant role in the stability of the PTMO segments. If degreadation of the PTMO segments were to occur, the overall functionality for Menshutkin reaction of the dimethyl amino terminated PTMO would become less than two. In step growth polymerization, a functionality close to two is required for obtaining high molecular weight polymer. Both the above mechanisms can significantly lower the overall molecular weight of the resulting polymer which might be the reason for the poor properties exhibited by these materials. Also, the modulus of the material recovers significantly on annealing which is believed to be primarily due to the association of the ionene segments. This again supports the speculation that the PTMO segments in the material may have indeed degraded when heated to elevated temperature. It is anticipated that by lowering the softening temperature of the ionene polymer, the degradation of the PTMO soft segments can be averted. The objective of the present study is to identify a suitable additive that would lower the softening temperature so that the ionene materials could be thermally processed without significant loss of the bulk properties.

It has been shown earlier that the ionic moieties in the ionene segments are responsible for the excellent network character of these ionene polymers (195). Therefore, it is probable that if an additive were to shield the ionic interactions of the ionene polymer at the use temperature, the material properties would deteriorate to that of the backbone chain (i.e. PTMO segments with no ionic interactions). It has been suggested by Duvdevani et al. (134) that some polar additives could weaken or destroy the ionic interactions (responsible for network formation) at melt processing temperatures but would allow re-establishment of the ionic interactions at the use temperatures. One convenient way of shielding the ionic interactions is by using using a polar additive which is highly crystalline in nature, such as zinc stearate. Upon melting (T_m of zinc stearate = 124 °C), zinc

stearate shields the ionic interactions, resulting in a significant reduction in the melt viscosity in ionomers. Upon cooling, due to the strong tendency for zinc stearate to recrystallize below the melting point, there is a tendency for the zinc stearate to migrate out of the ionic domains. This enables re-formation of the ionic interactions which results in the re-establishment of the ionic network (134). Thus, it is clearly seen that zinc stearate is an ideal candidate for the plasticization of the ionic domains in order to lower the softening temperature in segmented ionene polymers. However, the question still remained as to the usage of zinc stearate as a ionic plasticizer in an entirely different system, such as in the ionene polymer.

8.2 Effect of Zinc Stearate Incorporation on Polymer Properties

8.2.1 Dynamic Mechanical Properties

Figure 8.2 provides the dynamic mechanical spectra of the ionene polymer as a function of the zinc stearate loading level (from 0 phr to 60 phr). Recall the 0 phr material was solution cast and did not have any prior heat treatment. However, all the plasticized samples were compression molded at 120 °C. From these data, there are essentially four main transitions. The tan δ data was plotted on a logarithmic scale so that subtle changes in the transitions could be clearly distinguished. The transition occurring at -120 °C, which is conventionally designated as γ, is seen in all the samples and is believed to arise from rotation of the methylene sequences in the PTMO backbone. The temperature at which the γ transition occurs is in excellent agreement with the reported values for this same transition observed in other polymers possessing methylene sequences in the backbone (201). The intensity of this transition decreases with increasing zinc stearate loading level because of the restrictions placed on the relaxation process of the methylene sequences by the zinc stearate crystallites present within the polymer matrix.

A second transition, attributed to the glass transition of the PTMO segments and designated as α_g, occurs around -70 °C. As the data illustrates, the location of the glass transition peak is nearly the same for all samples. This is a characteristic feature of ionic plasticizers where the T_g of the

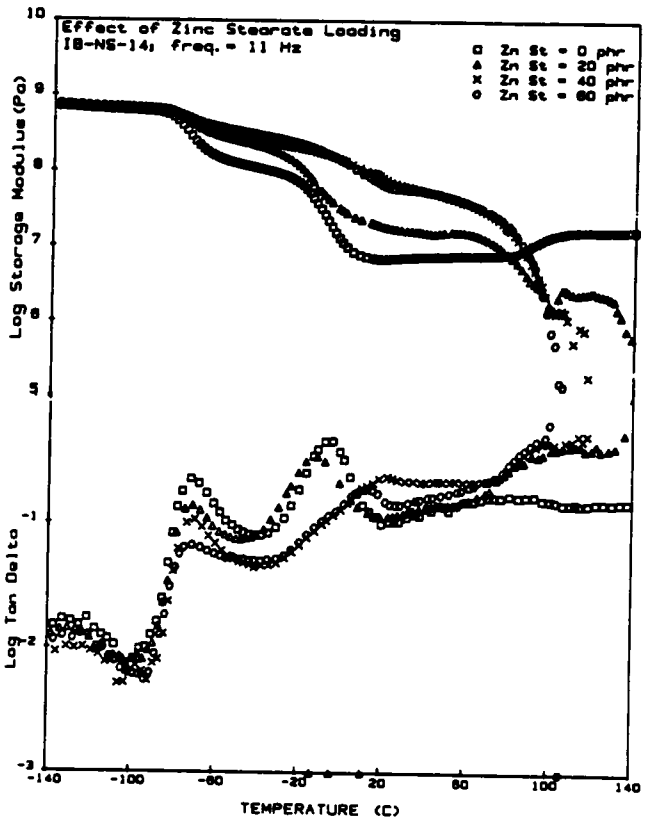

Figure 8.2. Dynamic Mechanical Analysis of IB-NS-14 Samples: (a) E′ curves, and (b) tan δ curves

backbone material is not significantly affected. From the tan δ curve, as in the γ transition, the intensity of the α_g peak decreases with increasing zinc stearate loading. The reason for this occurrence is similar to that observed for the γ transition. Beyond the glass transition temperature, the modulus of the plasticized materials is greater than the unplasticized ionene polymer due to the presence of zinc stearate which is crystalline in form at these temperatures and acts as a reinforcing filler.

A third transition, designated as α_c, is related to the general crystallization and melting behavior of the PTMO soft segment and occurs ca. 0 °C. The reason for the decreasing modulus extending from nearly -70 °C to 25 °C is undoubtedly due to the initial softening of the amorphous PTMO in conjunction with the melting of PTMO crystallites. However, in the plasticized samples, two types of crystallites are expected to be present, PTMO and zinc stearate. Among the plasticized samples, a distinct α_c transition is only observed in the 20 phr sample, while the high concentration of the zinc stearate crystallites masks the effect of the melting of PTMO crystallites in the 40 phr and the 60 phr samples.

In the temperature range between 0-70 °C, the modulus of the material increases with increasing zinc stearate loading levels. This is is not very surprising since it has been reported in the literature that zinc stearate acts as a reinforcing filler below its melting point (T_m = 124 °C) (202). However, in the unplasticized material above 70 °C, the storage modulus surprisingly increases with temperature. The reason for this occurrence is not known at this time, but, in a concurrent study in our laboratory, it has been speculated that the increase in the modulus may be due to an ordering mechanism of the ionene segments above 70°C (194).

The fourth transition occurs ca. 180 °C (not shown in the Figure 8.2) at which point the unplasticized material displays significant softening, due to the loss of association of the ionic moieties. This softening temperature reduces to ca. 120°C for the 60 phr sample, due to the plasticization effect of the zinc stearate. It is clearly seen that on incorporation of zinc stearate, the softening temperature of the ionene polymer is significantly reduced which is the main objective in this study. In the discussion following, the effect of the incorporation of zinc stearate on the physical and morphological properties will be discussed.

8.2.2 Mechanical Properties

Figure 8.3 shows the effect of zinc stearate loading on the stress-strain behavior of IB-NS-14 ionene polymer. All the plasticized material were compression molded at 120 °C for a period of 5 minutes. The unplasticized sample was not thermally treated because, as it was shown earlier, this material undergoes irreversible structural damage near its softening temperature. At ambient conditions, from Figure 8.3a, it is observed that only a small reduction in the ultimate tensile strength is observed with increasing levels of zinc stearate loading (from 15 MPa to 12 MPa with the addition of 60 phr zinc stearate). At strains greater than 500 %, the tensile strength is particularly enhanced by the strain induced crystallization of the PTMO segments (195). This effect is seen in the 0 phr and the 20 phr materials in Figure 8.3a. The ultimate elongation decreases slightly, from 1300% to 1000%, due to zinc stearate incorporation. It is speculated that the ion hopping mechanism, which tends to provide higher elongations in ionomers (but usually accents permanent set or hysteresis), is severely restricted with zinc stearate incorporation. This may be the cause for the reduction in the ultimate elongation. In addition, a distinct yielding behavior is observed in the 40 phr and the 60 phr materials but is absent in the 0 phr and the 20 phr materials. The yielding behavior is typical of filled systems. The modulus of the material is indicative of the initial response of the material. In Figure 8.3b, the modulus of the material is plotted as a function of zinc stearate loading. As expected, the modulus increases with increasing levels of zinc stearate.

The addition of zinc stearate does not greatly alter the mechanical properties of the parent ionene polymer. The ultimate tensile strength and the ultimate elongation decrease slightly, but an improvement in the modulus of the material is observed with increasing loading levels, as expected.

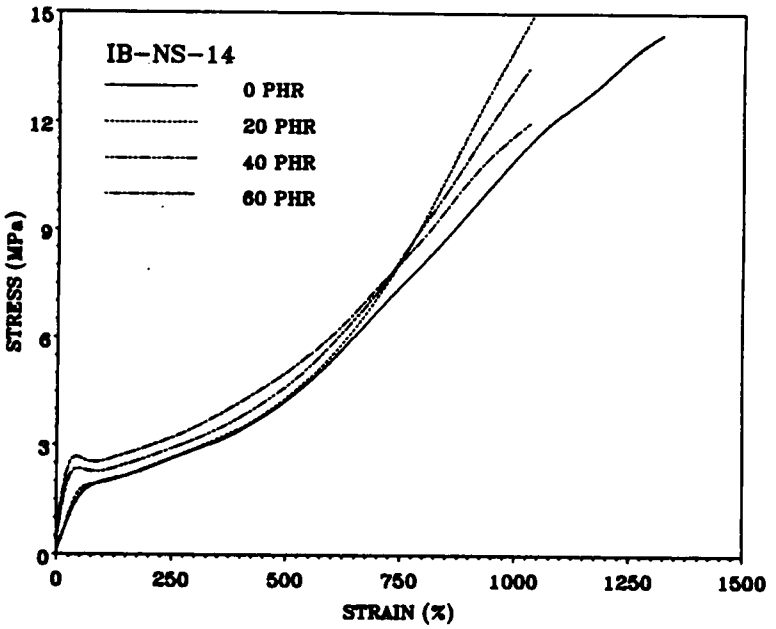

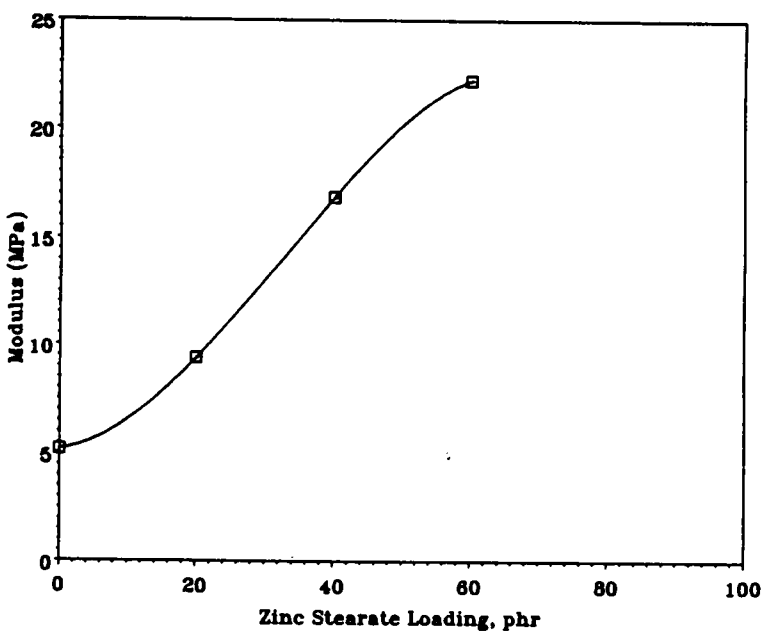

Figure 8.3. Effect of Zinc Stearate Loading on the Mechanical Properties of IB-NS-14 Samples: (a) Stress-strain behavior, and (b) modulus of the material

8.2.3 Structure and Morphology

8.2.3.1 Wide Angle X-Ray Scattering (WAXS)

It is well known from the literature that zinc stearate is a polar crystalline material. Figure 8.4 depicts the wide angle x-ray scattering pattern for the industrial grade zinc stearate which had been pressed into a film form at 130 °C. The diffraction rings seen in the pattern are very sharp resulting from zinc stearate crystallites. Figure 8.5 depicts the wide angle x-ray scattering patterns of the unplasticized sample along with the plasticized sample with 40 phr zinc stearate. The 20 phr and the 60 phr samples also show a similar behavior. The absence of crystalline rings in the unplasticized sample (Figure 8.5a) is indicative of the material being amorphous in nature. Though it has been reported that PTMO segments crystallize at ambient conditions, Feng (194) has shown that PTMO segments in these ionene materials can crystallize at ambient conditions only when the PTMO segment molecular weight exceeds 3400 $\overline{M}_n$. Therefore, the PTMO segments being amorphous in the 1400 $\overline{M}_n$ ionene polymer is not surprising. Distinct diffraction rings, similar to those of the zinc stearate powder, are seen in all the plasticized samples (Figure 8.5b). A similar observation was also made in zinc stearate plasticized sulfonated EDPM systems studied earlier in this laboratory (202). This suggests that the zinc stearate in the ionene polymer is crystalline at ambient conditions. In addition, no azimuthal dependence in the WAXS pattern is observed in Figure 8.5b which indicates that these crystallites are randomly oriented in the polymer matrix. On stretching the samples, however, considerable orientation of the zinc crystallites occur. The orientation of the zinc stearate crystallites can be inferred from the presence of a high degree of azimuthal dependence in the WAXS patterns, seen in Figure 8.5c. On the release of the applied stress, some degree of azimuthal dependence is still observed (Figure 8.5d), indicating that the orientation instilled by the applied stress is not completely dissipated. With increasing zinc stearate loading, the number and/or the size of the crystallites increases. This may be responsible for the observed increase in the modulus with increasing zinc stearate loading. Based on the WAXS results, no conclusion can be made regarding the size and the distribution of the crystallites in the plasticized materials.

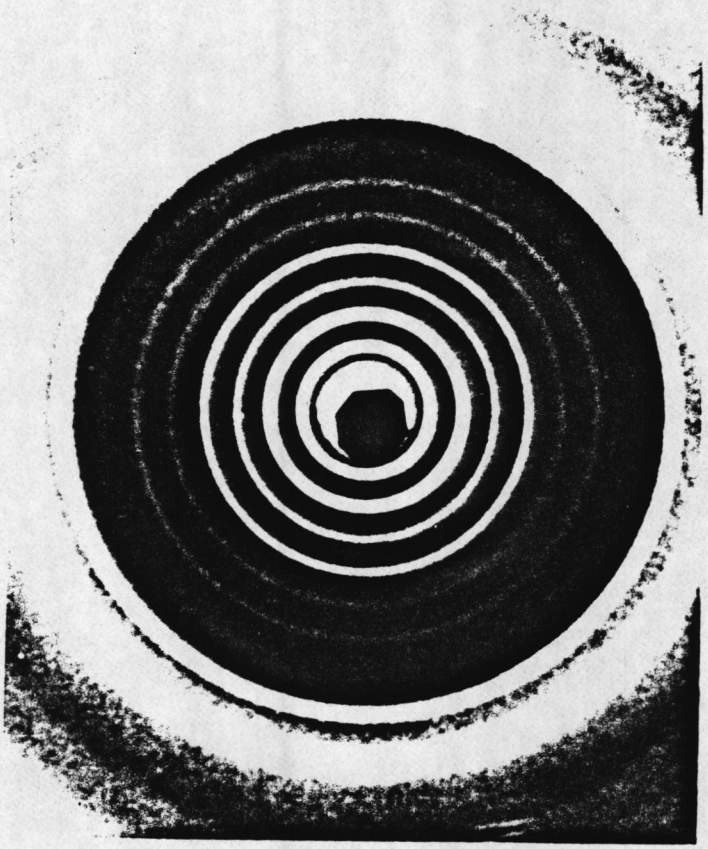

Figure 8.4. WAXS Pattern of Industrial Grade Zinc Stearate: pressed at 130 °C.

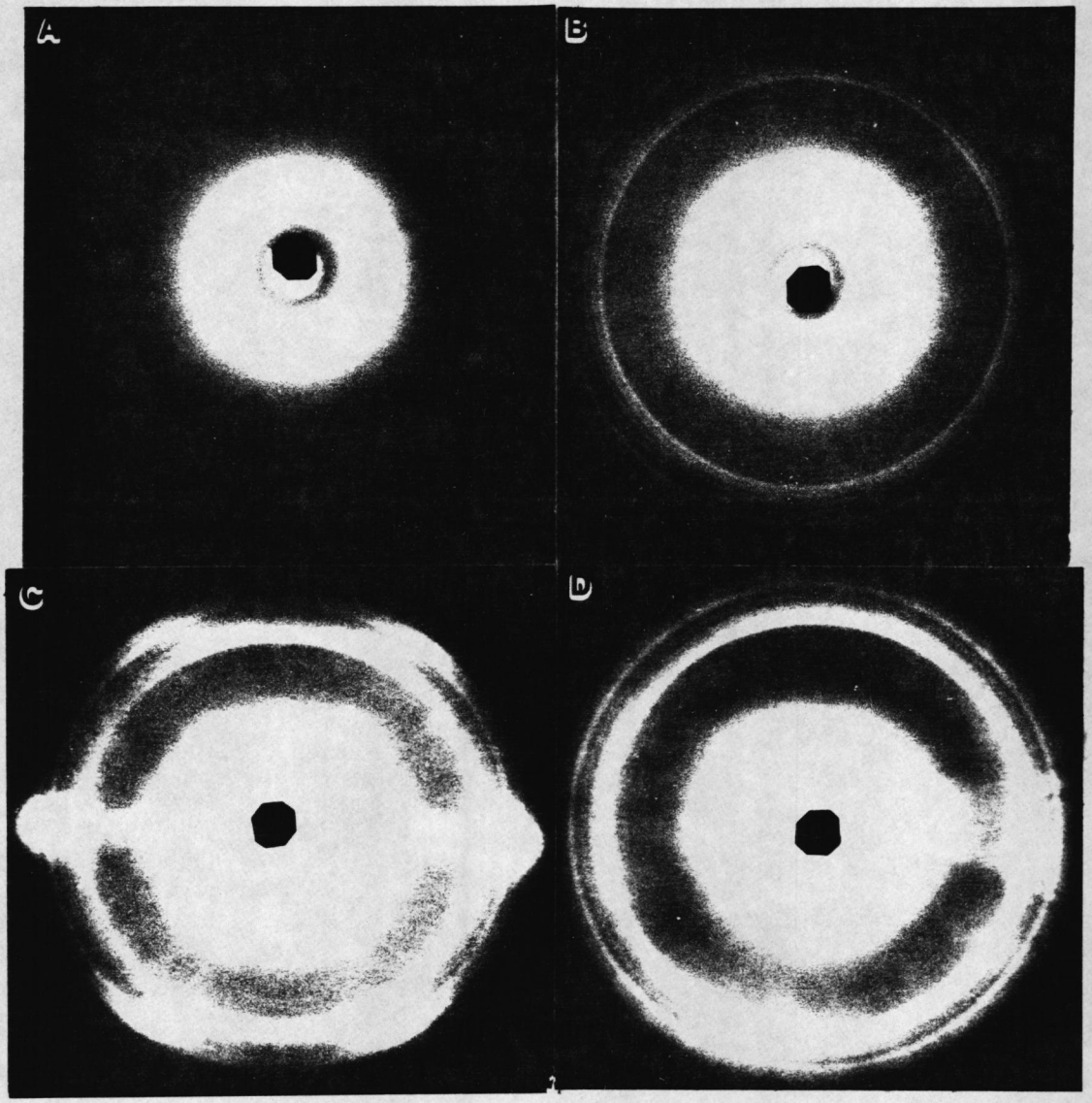

Figure 8.5. WAXS Patterns of the IB-NS-14 Samples: (a) 0 phr, (b) 40 phr - ambient, (c) 40 phr - stretched ($\lambda = 7$), and (d) 40 phr - after release of the applied stress

8.2.3.2 Scanning Electron Microscopy (SEM)

Scanning electron microscopy (SEM) was used in an attempt to determine the uniformity of the distribution of the zinc stearate crystallites. In Figure 8.6, SEM micrographs of the fractured surfaces of both unplasticized and plasticized samples are shown at nearly the same magnification of ca. 1100X. The morphology of the unplasticized polymer is very different than those that contain zinc stearate, but no distinct crystallites can be seen. The edges of the fractured surface of the unplasticized sample (Figure 8.6a) are rather smooth which is indicative of a ductile mode of failure. In Figures 8.6b and 8.6c, where the zinc stearate loading level is 20 and 40 phr, respectively, zinc stearate is uniformly distributed, and no regions of zinc stearate aggregation were noticed in the entire viewing region of either of these samples. However, in the 60 phr sample (Figure 8.6d), some small aggregates with an average aggregate size of 2 μm (microns) were observed. These aggregates were highly crystalline in nature and were believed to be zinc stearate crystallites based on the similarity between their structure and that present in the industrial grade zinc stearate powder. Figure 8.7a shows a higher magnification (18.8KX) of one of these aggregates. For comparison, an SEM micrograph of the zinc stearate powder of similar magnification is shown in Figure 8.7b. The morphological features of the aggregate in the 60 phr material appears to be similar in structure to the aggregate from zinc stearate powder with an average size of ca. 4 μm. Figure 8.8 shows a higher magnification of a representative region for samples 20 phr and 40 phr samples. The micrograph to the right represents a 4X magnification of the highlighted region on the left. Even at such high magnification, no aggregation is observed which indicates that zinc stearate is very compatible with the ionene polymer up to a loading level of 40 phr. The term "compatible" has been used here to imply that zinc stearate does not migrate (or bloom) to the surface. Due to its polar nature, zinc stearate is expected to be distributed preferentially near the ionic domains. From the micrographs in Figure 8.6, it can be seen that the fractured surface area of the plasticized samples is very much higher than in the unplasticized sample. This indicates that a higher surface energy is required to create the additional surface area. Based on this information, it is speculated that the fractured toughness of the plasticized materials might be higher than the parent ionene polymer. Of course,

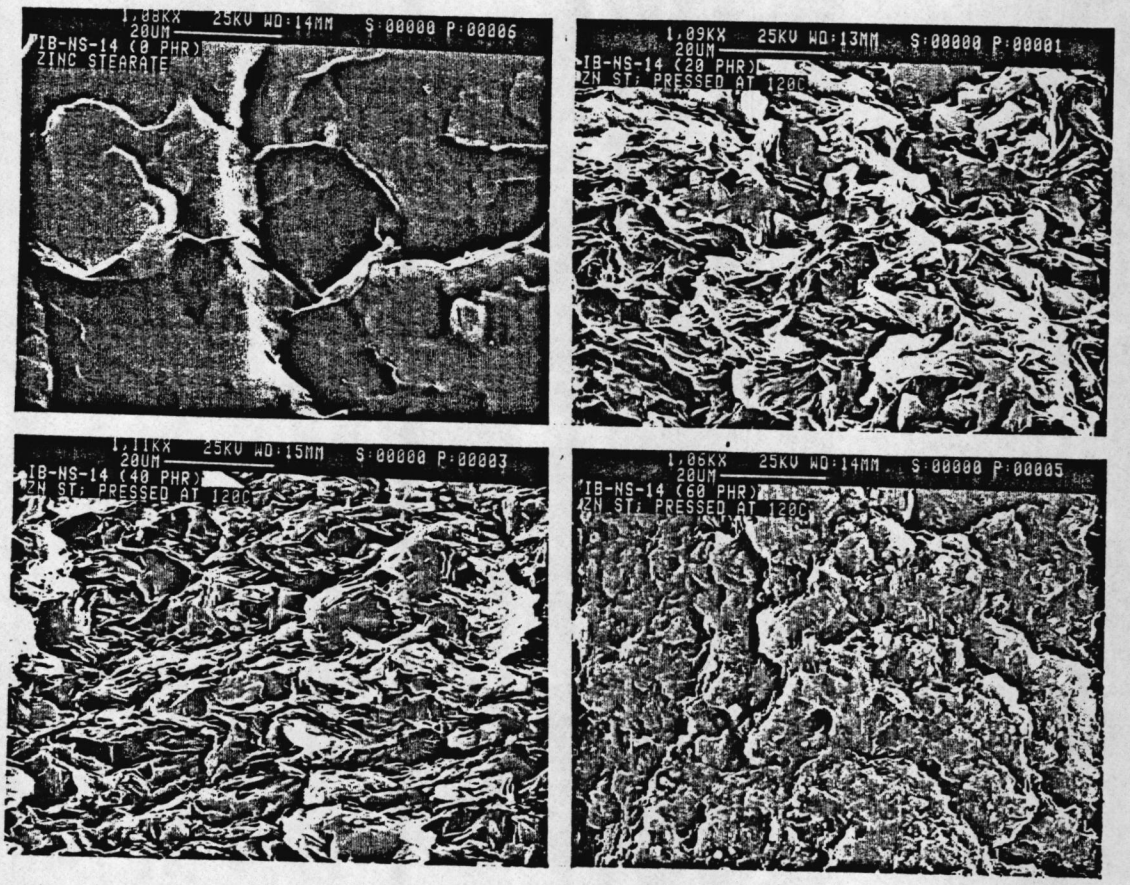

Figure 8.6. SEM Micrographs of Fractured Surfaces of IB-NS-14 Samples:

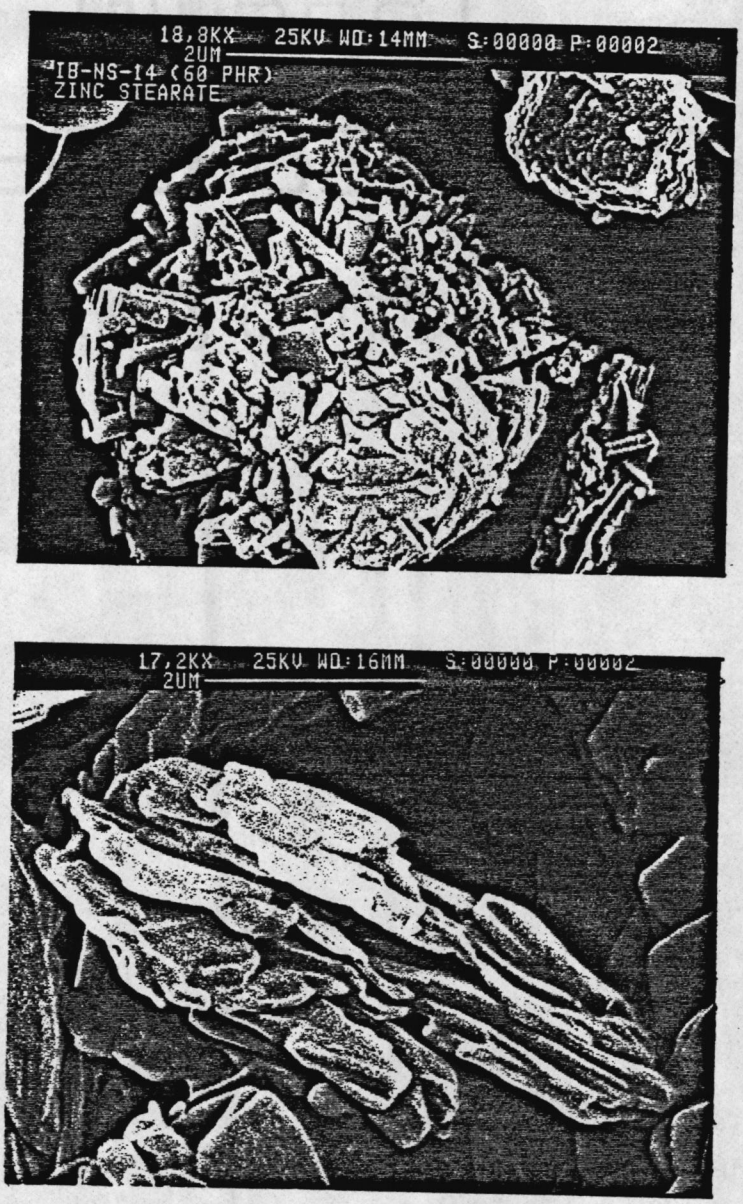

Figure 8.7. **SEM Micrographs of Zinc Stearate Aggregates:** (a) plasticized sample (60 phr) and (b) zinc stearate powder

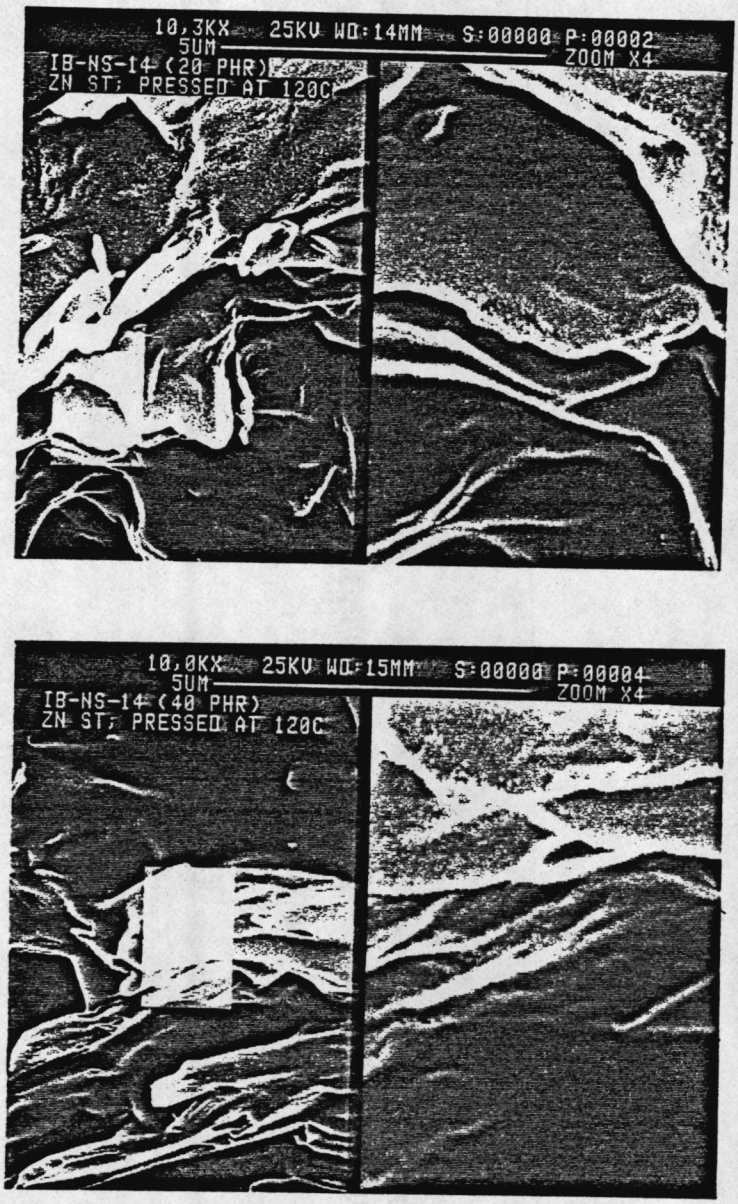

Figure 8.8. **Fractures Surfaces of Zinc Stearate Plasticized Samples:** (a) 20 phr, and (b) 40 phr; Magnification = 18KX

the fracture path in the filled samples is greatly enhanced on account of zinc stearate incorporation. This would also create additional surface area. However, no further studies have been conducted to quantify the increase in the fracture toughness due to zinc stearate incorporation.

8.2.4 Thermal Properties

Figure 8.9 shows a differential scanning calorimetry (DSC) scan of an industrial grade zinc stearate and the unplasticized ionene polymer. A sharp endothermic peak is observed in Figure 8.9a at ca. 124 °C which is attributed to the melting of the zinc stearate crystallites. This melting point is in good agreement with the reported values of zinc stearate in the literature (203). Figure 8.9b shows the DSC scan of the unplasticized ionene polymer. An endothermic peak is observed at ca. 173 °C. From TGA measurements, the onset of the weight loss also occurs near this temperature. Hence, the endothermic peak may be due to the weakening of the ionic interactions in the polymer or to the onset of degradation in the ionene segments. The origin of this endothermic peak will be determined in the ongoing study.

Figure 8.10 shows the effect of zinc stearate incorporation on the melting transitions in the plasticized sample with 60 phr zinc stearate. The sample was scanned in the temperature range between 50 to 130 °C at a scanning rate of 20 °C per minute. Curve 1 represents the initial scan of the solution cast material without any thermal treatment. The sample was then cooled slowly at 1.5 °C per minute (which is the cooling rate utilized in the non-isothermal cooling experiment in the dynamic melt studies). The sample was cooled to ambient conditions and later rescanned at 20 °C per minute (Curve 2). In curve 1, an endothermic peak is observed at ca. 106 °C, resulting from the melting of the zinc stearate crystallites. Recall that the endothermic peak for the zinc stearate powder occurs at ca. 124 °C. A considerable depression (about 18 °C) in the melting point of zinc stearate is observed when incorporated in the ionene polymer. The depression in the melting point was also observed in the plasticized EPDM systems studied earlier by Duvdevani et al. (134). It is speculated that some of the ionene segments may form nucleation sites for the crystallization of zinc stearate. If this were to occur, a depression in the melting point is expected due to the presence of impurities in the crystallites. On visual examination, it was observed that the zinc stearate even with

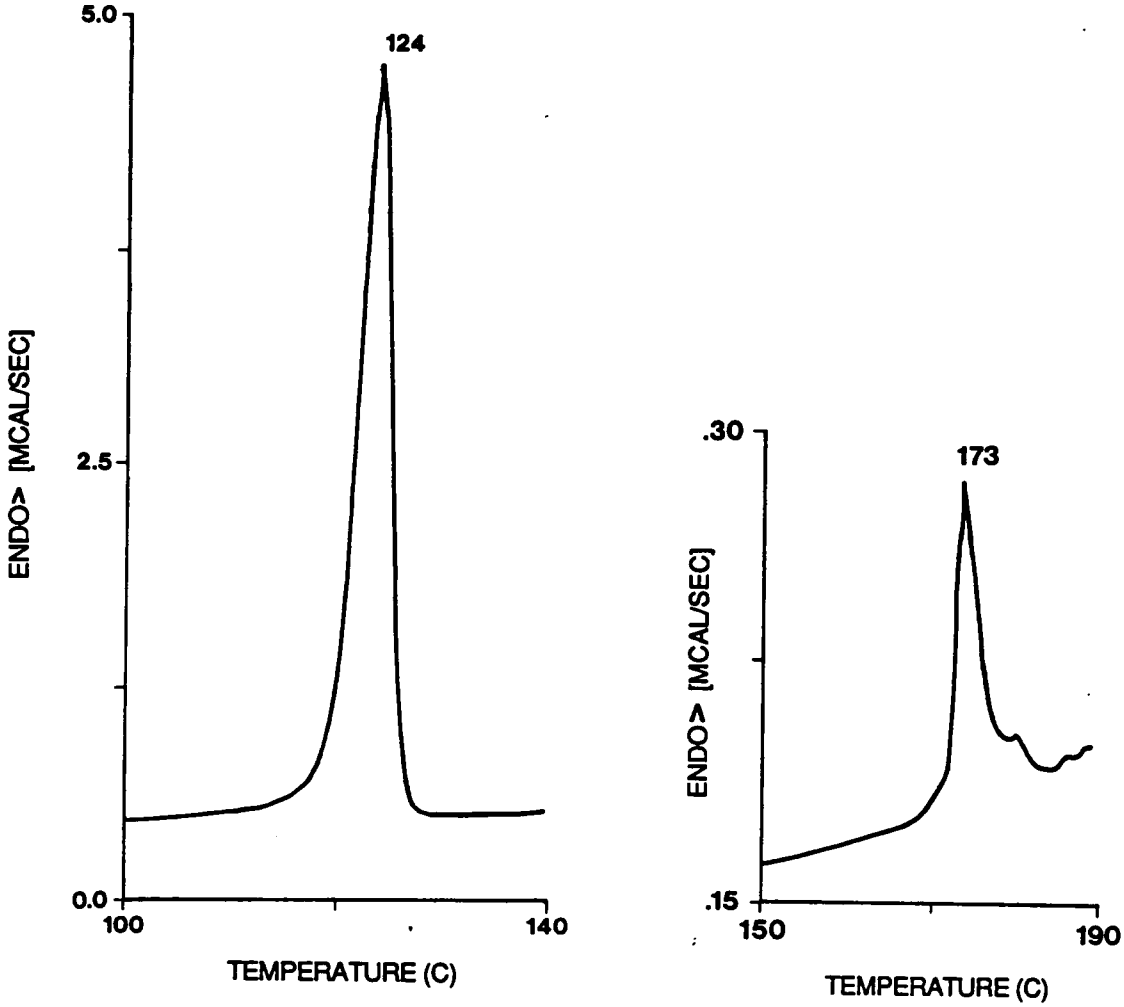

Figure 8.9. DSC Scan of (a) Industrial Grade Zinc Stearate and (b) Unplasticized IB-NS-14: scan rate = 20 °C per minute

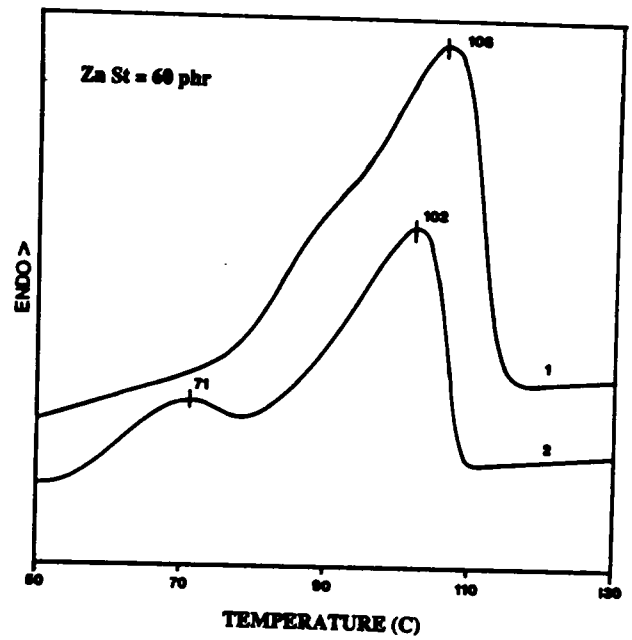

Figure 8.10. Effect of Zinc Stearate Incorporation on Thermal Transitions for 60 phr Sample: Curve 1 represents the initial scan of the solvent cast sample, and Curve 2 represents a rescan of the same sample after cooling it at 1.5° C per minute to room temperature (23 °C).

a loading of 60 phr, was completely compatible with the ionene polymer and exhibited no signs of "blooming" occurring to the surface. The melting peak of zinc stearate crystallites broadens considerably when the plasticizer is incorporated in the ionene polymer. This can be attributed to the presence of impurities in the zinc stearate crystallites and also to a distribution in their sizes. A distinct shoulder is also observed in curve 1 around 80-85°C. In the industrial grade zinc stearate, stearic acid is a main contaminant. During the slow solvent casting process, both zinc stearate and stearic acid may have co-crystallized together at ambient conditions. The literature suggests that the melting point of stearic acid is ca. 70 °C (203). It is speculated that due to the co-crystallization process, the melting point of stearic acid may have probably shifted to somewhat higher temperatures, possibly causing the observance of the shoulder at ca. 80-85°C. The slow cooling process provides ample time for both zinc stearate and stearic acid molecules to find their own kind in order to crystallize. Therefore, on rescanning, a distinct endothermic peak is observed at ca. 71°C which is in good agreement with the reported values for the melting point of stearic acid crystallites. This strongly supports the earlier speculation that the presence of stearic acid is responsible for the shoulder near 80-85 °C.

8.2.5 Rheological Properties

One of the main purposes in incorporating zinc stearate was to lower the softening temperatures of the ionene polymer so that the material could be thermally processed. It was discussed earlier that above its melting point, zinc stearate shields the ionic interactions lowering not only the softening temperature but also the melt viscosity. Dynamic mechanical measurements in the melt were conducted on a Rheometrics Mechanical Spectrometer (RMS) to determine the effect of zinc stearate incorporation on the melt properties of the ionene polymer. From dynamic mechanical analysis (recall Figure 8.2), it was observed that the plasticized samples essentially soften ca. 120 °C. Therefore, the melt studies for the plasticized samples were conducted at 120 °C. In addition, the unplasticized polymer softens ca. 180 °C. For purposes of comparison with the plasticized samples, the unplasticized samples could not be tested at 120 °C because it was still a solid at that temper-

ature. Hence, the unplasticized sample was tested at 180 °C although it was realized that during the test degradation would occur as will be pointed out shortly.

The frequency sweep measurements of the plasticized samples and the unplasticized samples are shown in Figure 8.11. Notice that the shape of the 0 phr sample (curve A) is very different from the general shape of the plasticized samples (curves B-D). It is speculated that considerable degradation of the ionene polymer occurs during the duration of the experiment (~ 15 minutes) and which is responsible for the observed behavior. Specifically, from the time sweep measurements conducted initially on this sample, η^* decreases by almost an order of magnitude for the 0 phr sample in ca. 15 minutes. This clearly supports the speculation that considerable degradation must have occurred in the unplasticized material at 180 °C. Though the data on the plasticized material is of no considerable significance due to the potential problem of degradation, it nevertheless serves somewhat as a reference material for comparison with the plasticized samples.

The dynamic melt viscosity of the plasticized samples decreases with increasing levels of zinc stearate loading. It is expected that with increasing zinc stearate loading, more of the ionic domains are shielded which would in effect reduce the ionic crosslink density in the system and lower the melt viscosity of the medium. In addition, zinc stearate being an ionic plasticizer, also plasticizes the ionic domains. All the plasticized samples show typical shear thinning behavior which is a characteristic feature of all thermoplastic materials.

Figure 8.12 depicts the location of the cross-over frequency as a function of zinc stearate loading. The cross-over frequency corresponds to that frequency where the ratio $G''/G' = 1$ (or tan $\delta = 1$). The cross-over frequency for the unplasticized material does not appear within the frequency range studied. It should be remembered that the data from the 0 phr material is of little significance because of the occurrence of degradation in this material. For the plasticized samples, the cross-over frequency shifts to higher frequencies with increasing zinc stearate loading. The shift to the higher frequencies is indicative of shorter relaxation times in the material which may be due to a reduction in the apparent ionic crosslink density and also due to the plasticization of the ionic domains by zinc stearate. This further confirms the earlier speculation that more of the ionic domains are plasticized with increasing zinc stearate loading.

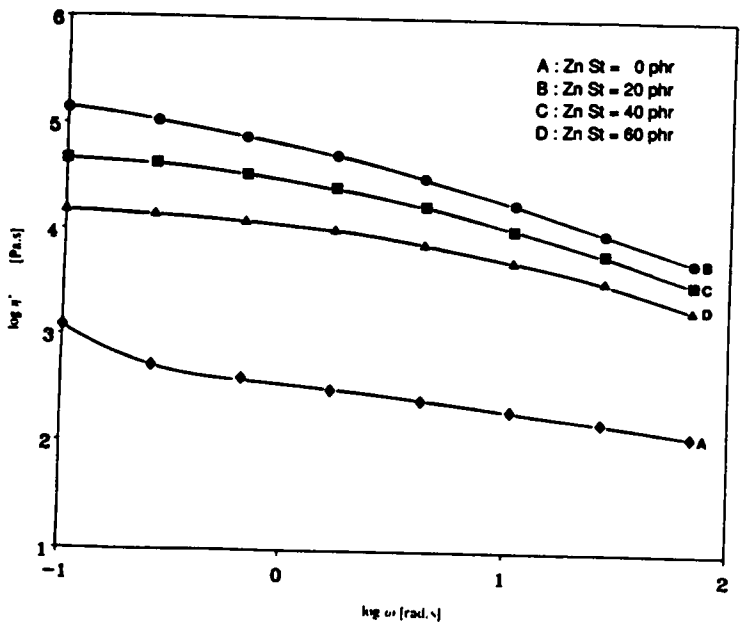

Figure 8.11. Effect of Zinc Stearate Incorporation on the Melt Viscoity of IB-NS-14 Ionene Polymer:

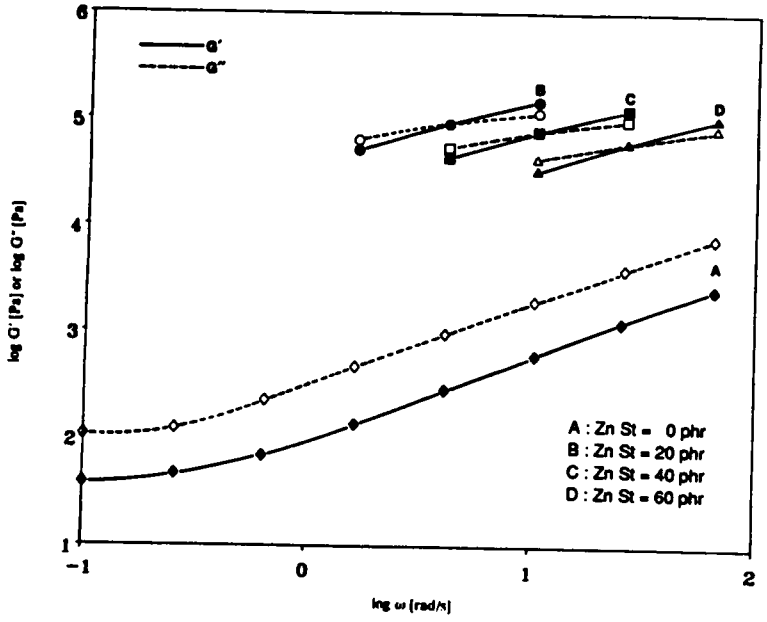

Figure 8.12. Location of the Crossover Frequency for the IB-NS-14 Plasticized Samples:

To understand the relaxation behavior of the ionene polymer as a function of zinc stearate loading levels, the well-known jump strain experiment in the melt was attempted. In this experiment, the material is strained quickly to a given level and the torque is monitored as a function of time. The relaxation stress, $\sigma(t)$, and the relaxation modulus, G(t), can then be obtained from the observed torque values. The initial strain utilized in the experiment was 50% (or 0.5 strain units). While all the plasticized samples were tested at 120 °C, the unplasticized sample (0 phr) was tested at 180 °C. Figure 8.13 provides the results of the jump strain test. The relaxation modulus data, G(t), is plotted on a semi-log scale in Figure 8.13a and on a log-log plot in Figure 8.13b. In Figure 8.13a, it is seen that the material relaxes faster with increasing zinc stearate loading. At low zinc stearate loading, it is speculated that small amounts are incorporated in each of the ionic domains which would in effect plasticize the ionic domains to a certain extent. With the increasing zinc stearate loading, the ionic domains are further plasticized and therefore the material relaxes faster or in a shorter time scale with increasing plasticizer content. It is expected that zinc stearate will not only shield the ionic interactions in the system but will also plasticize the ionic domains and, hence, functions in dual roles. All the applied stresses are essentially relaxed in the unplasticized material (curve A) since after the degradation process, the material may contain lower molecular weight segments of the original polymer. Also, the relaxation time decreases considerably with temperature (recall that the 0 phr material was tested at 180 °C). The log-log scale in Figure 8.13b serves to expand the time scales at shorter time intervals. The response time of the RMS instrument is ca. 0.03 seconds, and therefore any data below this time is not expected to be of any significance. It is clearly seen that the relaxation process is accelerated with increasing zinc stearate loading. However, an apparent residual stress is observed even after 70 seconds in all the plasticized samples except the 60 phr material. This is an interesting observation. Based on the SEM analysis it was expected that all the ionic domains would have been plasticized at least at a loading level of level of 40 phr. At present no explanation is provided for the observed behavior.

Non-isothermal cooling experiments were conducted to determine the temperature at which the structure of the material is regained as a result of zinc stearate crystallization. It was expected that there would be considerable increase in the viscosity of the material when the zinc stearate

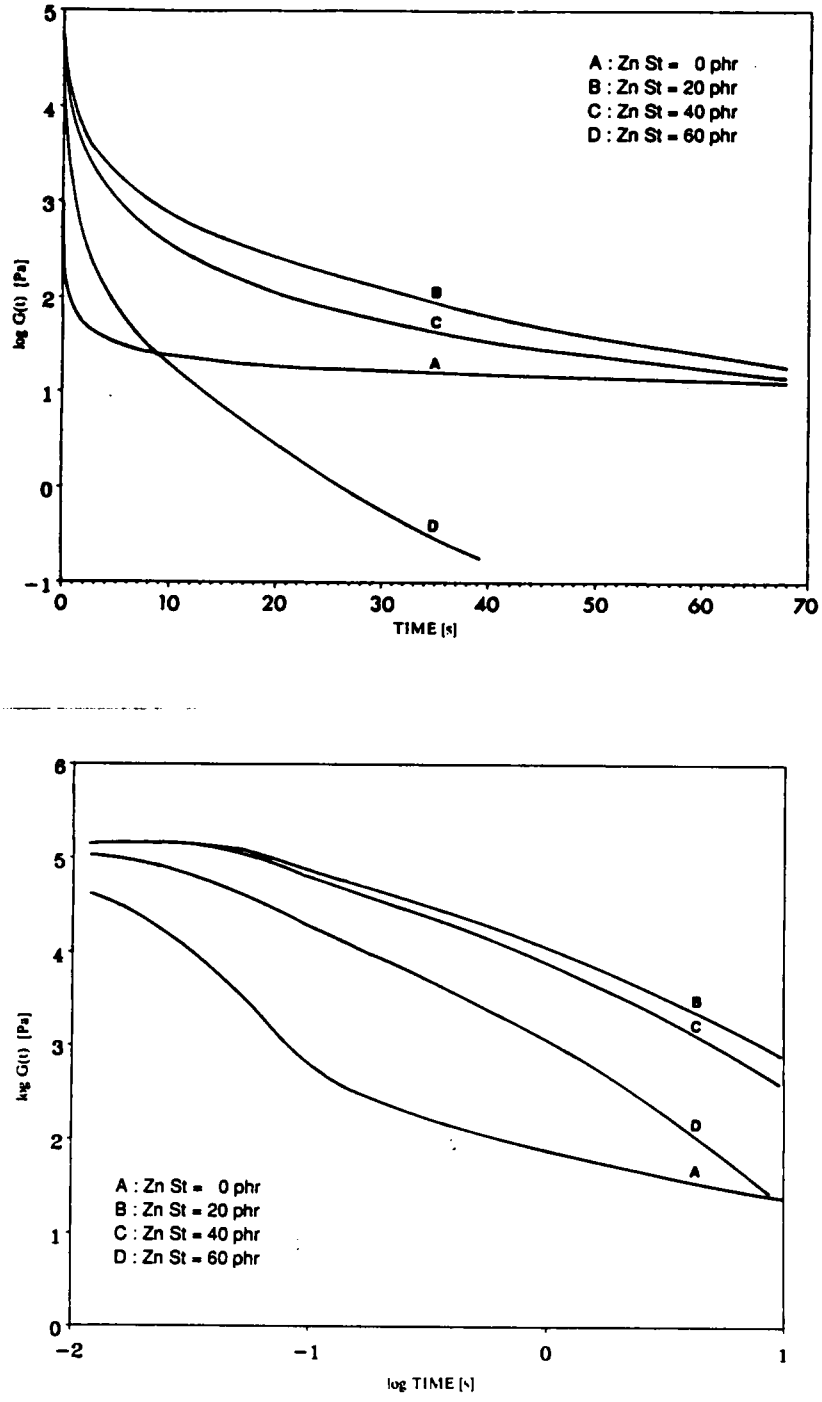

Figure 8.13. Results of the Jump Strain Experiment; Initial Strain = 50%: (a) semi-log scale, and (b) log-log scale

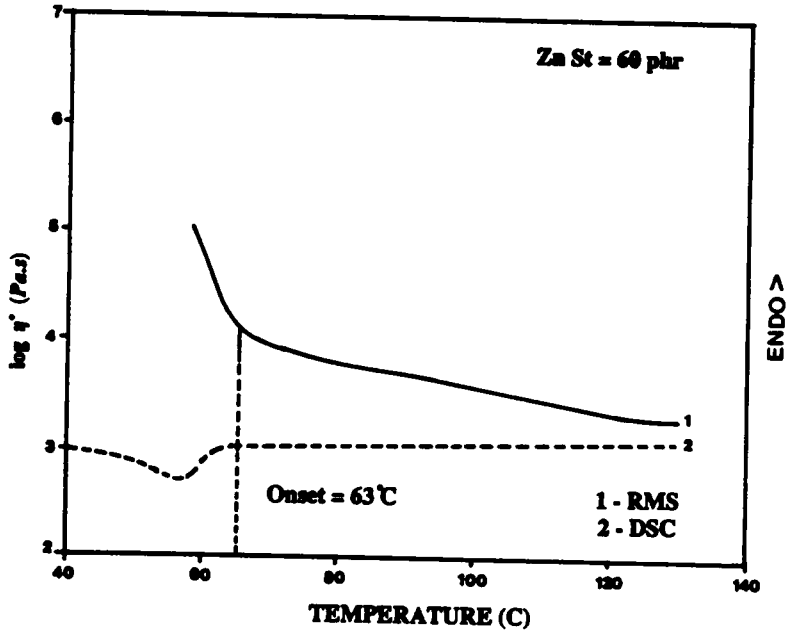

Figure 8.14. Non-Isothermal Cooling Profiles of IB-NS-14 with 60 phr Zinc Stearate:

begins to crystallize. Therefore, the melt viscosity was monitored as a function of cooling temperature (Figure 8.14). The 60 phr sample was heated to 130 °C, and the material was cooled at 1.5 °C/min. till the torque values exceeded the acceptable range. While cooling from 130 °C, a gradual increase in the viscosity was observed which is essentially caused by the decreasing temperature. On further cooling, a considerable increase in the melt viscosity was observed with the onset being at ca. 63 °C. This is apparently due to the crystallization of zinc stearate, which is expected, since there is a 40 °C supercooling present. An entirely unrelated technique such as the differential scanning calorimetry (DSC), was used to confirm that zinc stearate was responsible for the observed behavior. In the DSC, the sample was heated to 130 °C and then cooled at a controlled rate of 1.5 °C/min (the same as in the RMS). As expected, the onset for an exotherm was observed at ca. 63 °C with the peak located at ca. 56 °C. This observation supports the earlier speculation that the structure being formed at ca. 63 °C is due to zinc stearate crystallization. Based on this information, it is believed that a lower cycle time would result if these materials were to be injection molded at 120 °C and with a mold temperature of 55-60 °C.

8.3 Summary

This study has shown that the strong ionic crosslinks, which are responsible for the excellent mechanical properties at ambient conditions in segmented ionene polymers, can be controlled with the use of a suitable polar additive, such as zinc stearate. The mechanical properties of the host ionene polymer are not adversely affected with the zinc stearate addition. The additive is very "compatible" with the ionene polymer even up to the loading level of 60 phr. In addition, the softening temperature and the melt viscosity are significantly reduced with the zinc stearate addition. By appropriate selection of the zinc stearate loading, the segmented ionene polymers can now be thermally processed without any problems of degradation and hence loss of properties.

9.0 STRUCTURE-PROPERTY STUDIES OF BLOCK IONOMERS

The block ionomers are a natural extension of the telechelic ionomers where instead of a single ionic group at each chain end, a sequence of groups which are ionic in nature is present at the chain ends. According to Gallot (204), these materials can be considered amphiphiles in the sense that they combine the properties of classical block copolymers with those of the ionomers. It was earlier discussed in Chapter 6 that the sulfonate ionomers provide much tighter or more strongly associating network than the equivalent carboxylate ionomers. However, one potential limitation of the sulfonic acid based ionomers is if these groups are not neutralized, they can undergo thermal degradation at higher temperatures. By using a sequence of carboxylate groups, the network properties similar to that of the sulfonate ionomers might be mimicked provided that the higher ion content does not pose any other potential problems (such as a shift to a more hydrophylic nature). As a consequence, one can then determine the number of carboxylate groups needed to match the performance of a single sulfonate unit. This knowledge would be useful in the design of carboxylate ionomers. The author is aware of only one other investigation of somewhat similar objectives which is currently in progress aimed at studying the morphological features of styrene-4-vinylpyridium based ABA block ionomers (99). In the present investigation the structure-property of methacrylic based block ionomers will be reported.

9.1 Chemical Structure and Nomenclature

9.1.1 Stress-Strain Behavior

The carboxylated telechelic block ionomers have been synthesized in Prof. McGrath's laboratory in the Department of Chemistry at Virginia Polytechnic Institute & State University by Mr. C. D. DePorter. Details regarding the synthesis procedures is available elsewhere (97,205,206). For

the present study, the elastomeric segment was based on both 2-ethyl hexyl methacrylate (EHMA, T_g = -27 °C) and n-hexyl methacrylate (NHMA, T_g = -10 °C) while the ion containing blocks were based on t-butyl methacrylate (TBMA, T_g = 118 °C). The targeted overall molecular weight was 50,000 $\overline{M}_n$ for the precursors (ester derivative) for both the di- and tri- block ionomers. Both KOH and CsOH (or Cs_2CO_3) have been used to neutralize the hydrolyzed blocks. Either would alter the inherent electron density contrast of the ionic domains relative to the NHMA block. This would help to elucidate the morphological features of the ionic domains as determined by small angle x-ray scattering (SAXS) and transmission electron microscopy (TEM). Thin films of the diblock ionomers were cast from THF whereas small amounts of MeOH was added as a co-solvent for the triblock ionomers. The nomenclature used to designate the samples can be best explained using an example. The designation TNT-5/90/5 (K) refers to a triblock ionomer with NHMA as the elastomeric block, with the composition of the precursor (ester) being 5% (TBMA) - 90% (NHMA) - 5% (TBMA) by weight and neutralized with a KOH. Similarly, NT-90/10 (Cs) would correspond to a diblock ionomer with NHMA as the elastomeric segment, with the composition of the precursor (ester) being 90% (NHMA) - 10% (TBMA) by weight and neutralized with CsOH. In the text, the hydrolysed form of the TBMA segments would be referred to as h-TBMA and the neutralized form would be referred to as nh-TBMA. The notation "N" will be replaced by "E" for the EHMA based material. All the ionomers were neutralized to the stoichiometric endpoint.

9.2 Effect of Ion Incorporation

The effect of increasing the block length of the precursor (TBMA-EHMA-TBMA block copolymer) on the observed stress-strain properties is shown in Figure 9.1. As expected, both the modulus and the tensile stress of the material increases with increasing TBMA block length. Since the solubility parameter of the TBMA [δ = 8.94 $(cal/cc)^{1/2}$] and EHMA [δ = 8.46 $(cal/cc)^{1/2}$] are very similar, considerable mixing between the two segments is expected. Therefore, the resulting copolymer would exhibit a more glassy behavior since the T_g would now be shifted to a higher

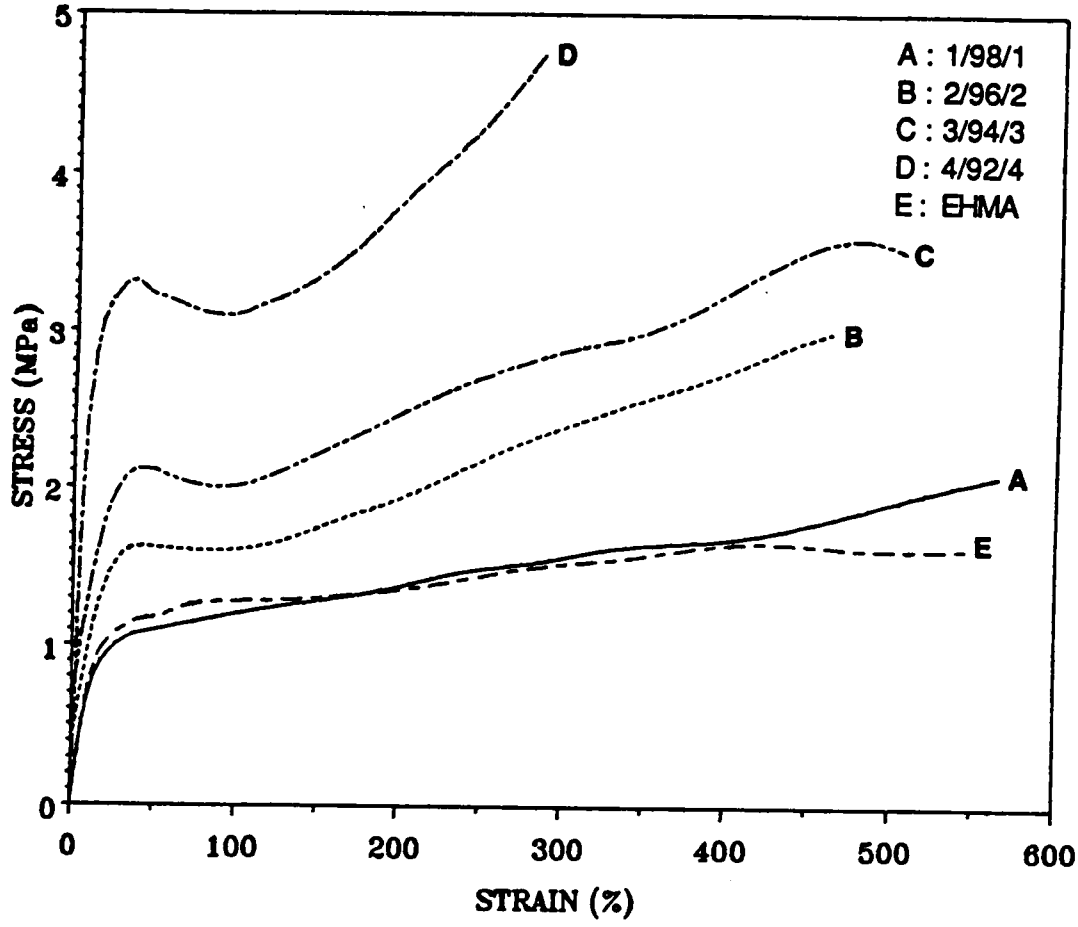

Figure 9.1. Stress-Strain Behavior of the EHMA and EHMA/TBMA Copolymers: (a) EHMA, (b) TET-1/98/1 (K), (c) TET-2/96/2 (K), (d) TET-3/94/3 (K), and (e) TET-4/92/4 (K).

temperature. Notice that above 4% TBMA, all the block copolymers exhibit a distinct yielding behavior. Initially some resistance is offered by the the glassy domains on deformation by thay are soon overcome by the applied forces. Yielding behavior is observed when the resistance to deformation is overcome by the applied forces.

Changing the polarity of the medium significantly alters the morphological features in these TET ionomers. Figure 9.2 shows the stress-strain and the stress-relaxation behavior of the TET 4/92/4 (K) block material. Curve D (EHMA homopolymer) in Figure 9.2a serves as a reference material for comparison purposes. Notice that on incorporation of 8% of the TBMA block to the EHMA backbone (curve A in Figure 9.2a), a substantial increase in both the modulus and the tensile stress of the material is observed which is primarily believed to be due to a high degree of mixing between the TBMA and EHMA segments. On hydrolysis of the TBMA segments, some degree of phase separation takes place due to the more polar nature of the h-TBMA acid blocks which are formed on hydrolysis. This promotes considerable "demixing" of the h-TBMA and EHMA segments. The demixing process substantially decreases both the modulus and tensile stress of the material since there will be two T_g's associated with the system, one for the backbone matrix and the other for the h-TBMA segments. Since the continuous phase will now have a lower T_g, the intial response on deformation will be more rubbery in nature. Hence, the observation of lower modulus and tensile stress (see curve B in Figure 9.2a). Neutralization of the acid blocks promotes further demixing to occur between the nh-TBMA and the EHMA segments, resulting in further lowering both the modulus and the tensile stress of the material (curve C in Figure 9.2a). The phase separated nh-TBMA segments is believed to form more cohesive domains due to the stronger associations between the ionic groups within the domains, resulting in a greater network stability.

Figure 9.2b shows the stress-relaxation behavior of the acid and the ionomer of the TET-4/92/4 material. The ionomer (curve B in Figure 9.2b) maintains the applied stress over a longer period (ca. 1000 minutes) than the acid (curve A in Figure 9.2b). Recall that from stress-strain measurements both the precursor and the acid exhibited a higher modulus and tensile stress (at a given elongation) than the ionomers. As explained earlier, the higher stress is due to the occurrence of phase mixing between the TBMA and the EHMA segments. These associations are

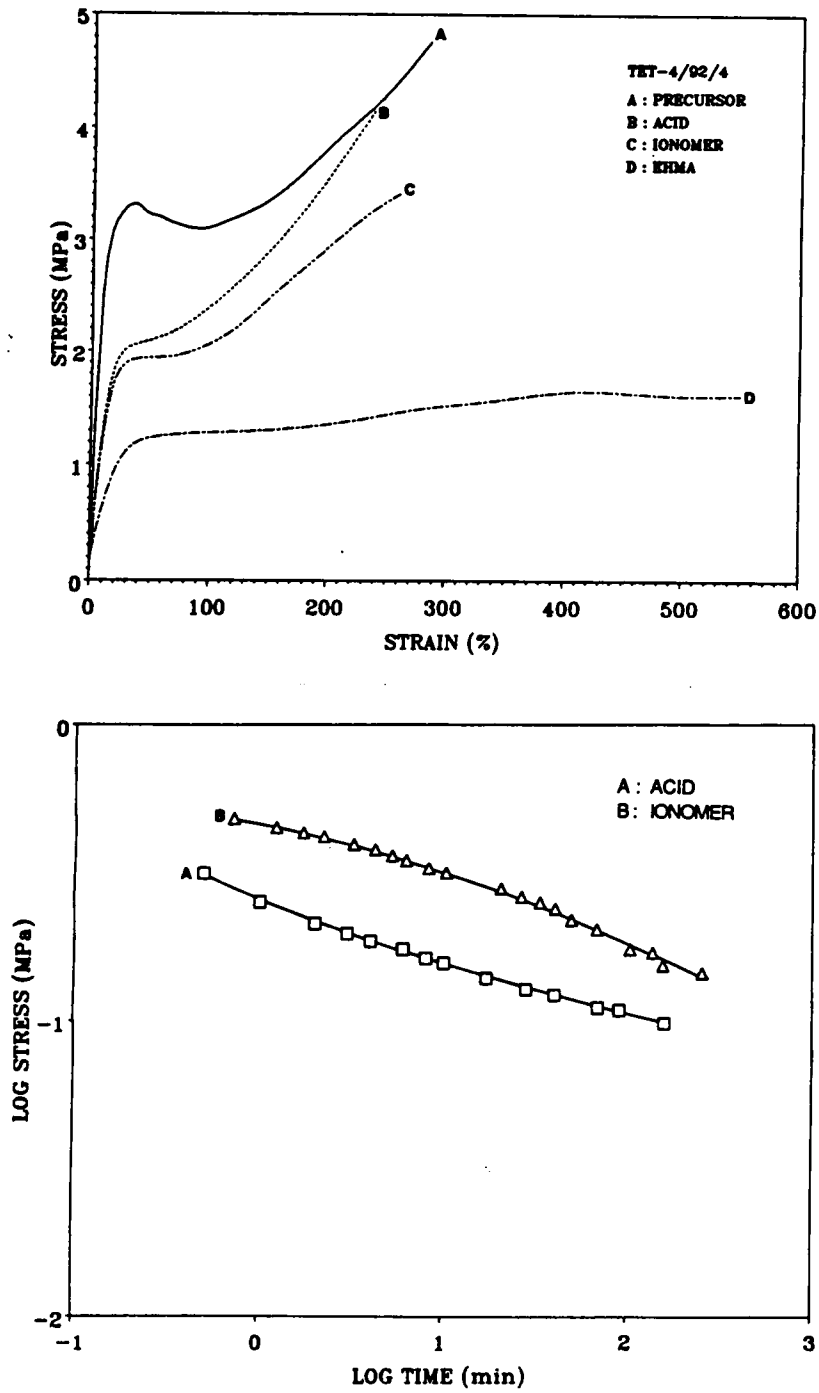

Figure 9.2. Effect of Ion Incorporation on the Bulk Properties of TET Ionomers: (a) Stress-strain behavior, and (b) Stress-relaxation behavior

temporal in nature unlike the associations within the ionic domains. Therefore, the applied stresses are quickly relaxed during the stress-relaxation experiment. The greater network stability in the ionomer is primarily due to its more electrostatic nature which is responsible for the cohesive network formed as a result of the stronger mutual associations within the ionic domains.

9.2.1 SAXS Analysis

The small angle x-ray scattering profiles (SAXS) of the precursor, acid and the ionomer for the TET-4/92/4 material is given in Figure 9.3. No scattering peak was observed for the precursor material which is indicative of a lack of periodicity in the system. The lack of observation of the scattering peak may be due to both TBMA and the NHMA segments being phase mixed or that the electron density difference between the two segments is too small to be detected. However, the stress-strain measurements seems to imply that the TBMA and the NHMA segments are well mixed. Also, from DSC measurements, only a single but a broad T_g was observed which again indicates that the two segments are phase mixed (207). On hydrolysis of the TBMA segments, a distinct scattering peak was observed. Considerable reorganization due to the association of the polar acid groups is believed to take place which is responsible for the scattering peak in the acid. The smeared spacing obtained from the position of the scattering peak is ca. 14.8 nm. As mentioned earlier, the reorganization of the segments is essentially promoted by the demixing process which arises due to segment incompatibility between the more polar h-TBMA segments and the non-polar EHMA block segments. On neutralization of the acid groups, there is a significant increase in the scattering intensity but the SAXS peak shifts to a larger value of "s" or lower spacing (11.9 nm). The increase in the scattering intensity can be attributed to the enhancement of the scattering contrast on account of neutralization. In addition, the polarity of the nh-TBMA segments increases substantially due to the neutralization procedure which provides a greater driving force for demixing (or phase separation) between the nh-TBMA and the EHMA segments. It is, therefore, speculated that most of the nh-TBMA segments phase separate from the EHMA matrix, resulting in lowering the T_g of the EHMA backbone. With very few nh-TBMA segments in the EHMA matrix, the EHMA segments can now obtain its coiled formation which results in shifting the scattering peak

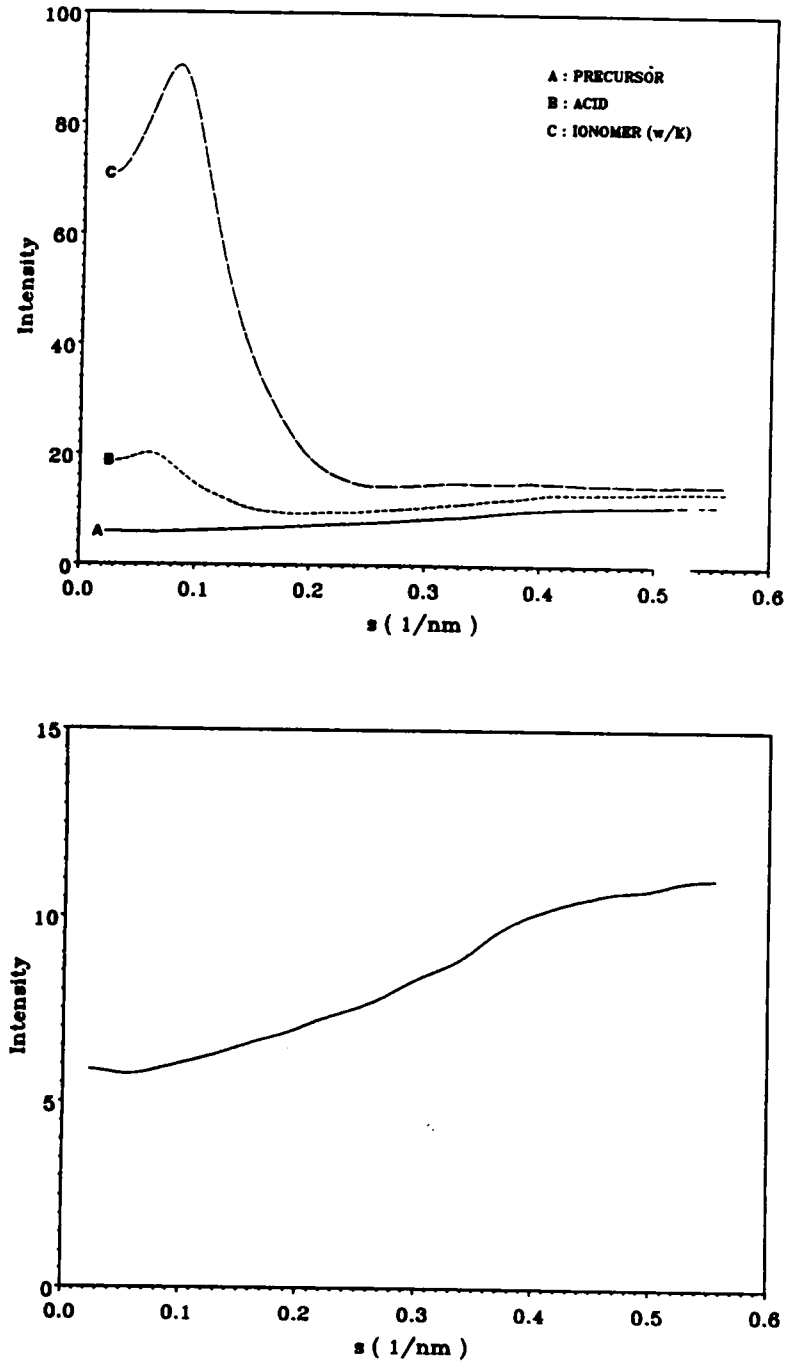

Figure 9.3. SAXS Profiles of the TET-4/92/4 Material: (a) composite plot (b) precursor (ester form)-note the expanded scale relative to (a).

to higher "s" values or lower spacings. It can be seen from Figure 9.3b, that the high angle region of the precursor exhibits an unusual increase (almost "steplike") in the scattered intensity which the author believes may be due to contributions other than the onset of wide angle x-ray scattering. Background subtraction using any of the methods discussed earlier resulted in negative intensity values being obtained near "s" values ca. 0.2 - 0.25 nm^{-1}. The origin of the excess scattering at the high angle region is not known at this time but is believed to be a characteristic feature of the precursor. Hence, no further quantitative analysis such as the invariant or the diffuse boundary analysis could be performed for the TET block ionomers.

9.3 Effect of Ionic Segment Architecture

In ionomers, the architectural factors greatly influence the nature of ion aggregation in the system. As discussed in the literature review, multiplet or cluster formation have been observed in a number of systems in random ionomers where the ion groups are randomly placed along the polymeric backbone. In the telechelic systems, however, where the ionic groups are placed only at the chain ends, the multiplets aggregate in an ordered fashion to form supermultiplets and therefore the formation of clusters is unlikely (208). Hence, the morphology of the ionomers are significantly affected depending on the architectural features of the ionomers. To determine the nature of ion aggregation of block ionomers, two variations in the architecture have been considered in this study, diblock and triblock ionomers. In these systems, the ionic segment was again based on t-butyl methacrylate and the elastomeric or non-ionic segment was based this time on n-hexyl methacrylate (NHMA, T_g = -10 °C).

9.3.1 Stress-Strain Behavior

The stress-strain behavior of the diblock ionomers neutralized with K and Cs is shown in Figure 9.4. As expected, these materials essentially flow at ambient conditions and indeed on physical examination, these materials were tacky in nature. This is not surprising since these diblock ionomers form micellar type of structures with the ionic aggregates located at the core surrounded

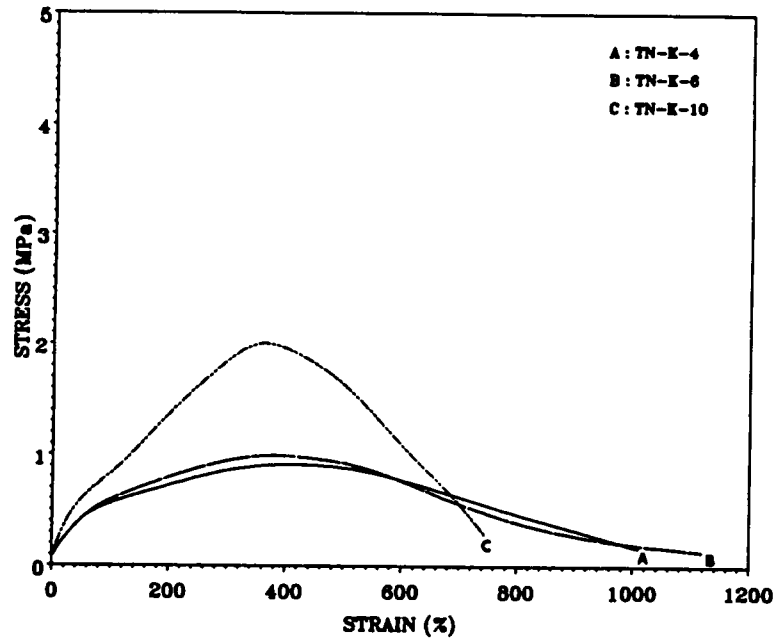

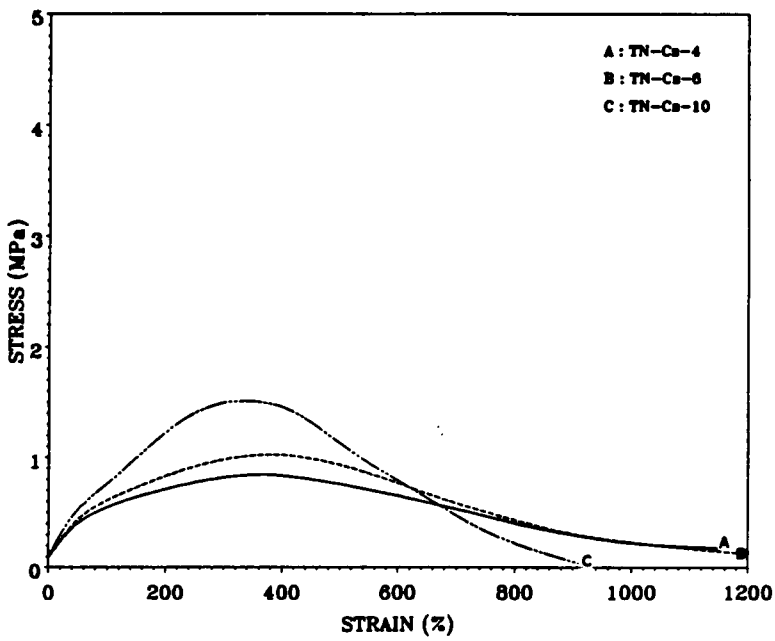

Figure 9.4. Stress-Strain Behavior of NHMA/TBMA Diblock Ionomers: (a) K ionomers, and (b) Cs ionomers.

by the elastomeric NHMA chains. The ionic domains which are glassy at room temperature act as a reinforcing filler and provides some resistance to the applied stress which is observed in the stress-strain behavior up to ca. 400% elongation. With only one end of the chains anchored, the applied stresses are quickly relaxed by the NHMA segments. In both K and Cs diblock ionomers, the modulus and the tensile stress at a given strain increases with increasing nh-TBMA block length. With increasing nh-TBMA block length, the ion content in the material increases, resulting in either larger ionic domains and/or an increase in the number of ionic domains in the material, both of which can be responsible for the observed stress-strain behavior. It is observed that the K ionomers display both a higher modulus and a higher tensile stress than the corresponding Cs ionomer. Since the ionic radius of K (1.33 Å) is smaller than that of Cs (1.69 Å), the reason for the observed behavior is clear - from equation 6.1 on page 123, it can be seen that the smaller ionic radius results in higher attractive forces within the ionic domains resulting in a stiffer material.

A significant improvement in the mechanical properties is expected in going from a diblock to a triblock ionomer. The stress-strain behavior of the K and Cs triblock ionomers is shown in Figure 9.5. The tensile stress is considerable improved reaching up to ca. 4-4.5 MPa for the material with 10% ion content. Since both ends of the chain can now be potentially anchored in the ionic domains, a higher tensile stress is therefore anticipated. These triblock carboxylated ionomers display very poor stress-strain behavior when compared to linear sulfonated telechelic PIB ionomers studied earlier in this laboratory (93). Again, as in the diblock ionomers, both the modulus as well as the tensile stress of the triblock ionomers increases with increasing nh-TBMA block length. The reason for the observed behavior is exactly the same as that for the diblock ionomers. Also, as in the diblock ionomers, the K ionomers exhibit a higher modulus and tensile strength than the Cs ionomers.

9.3.2 SAXS Analysis of the Diblock Ionomers

The slit smeared and the desmeared small angle x-ray scattering profiles of K and Cs neutralized diblock ionomers are shown in Figures 9.6 and 9.7, respectively. Except for the NT-98/2 ionomer, all other ionomers exhibit at least one very distinct SAXS peak and a strong evidence of

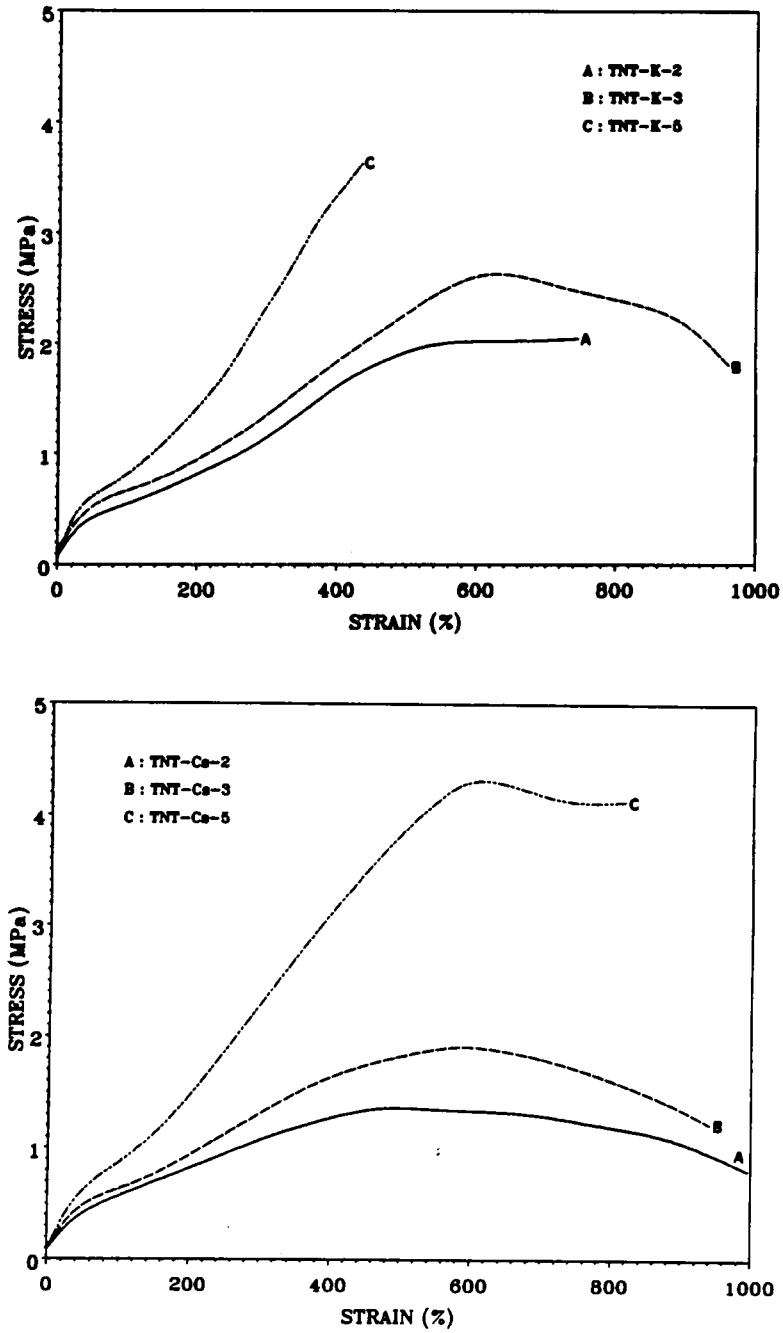

Figure 9.5. Stress-Strain Behavior of TBMA/NHMA/TBMA Triblock Ionomers: (a) K ionomers, and (b) Cs ionomers.

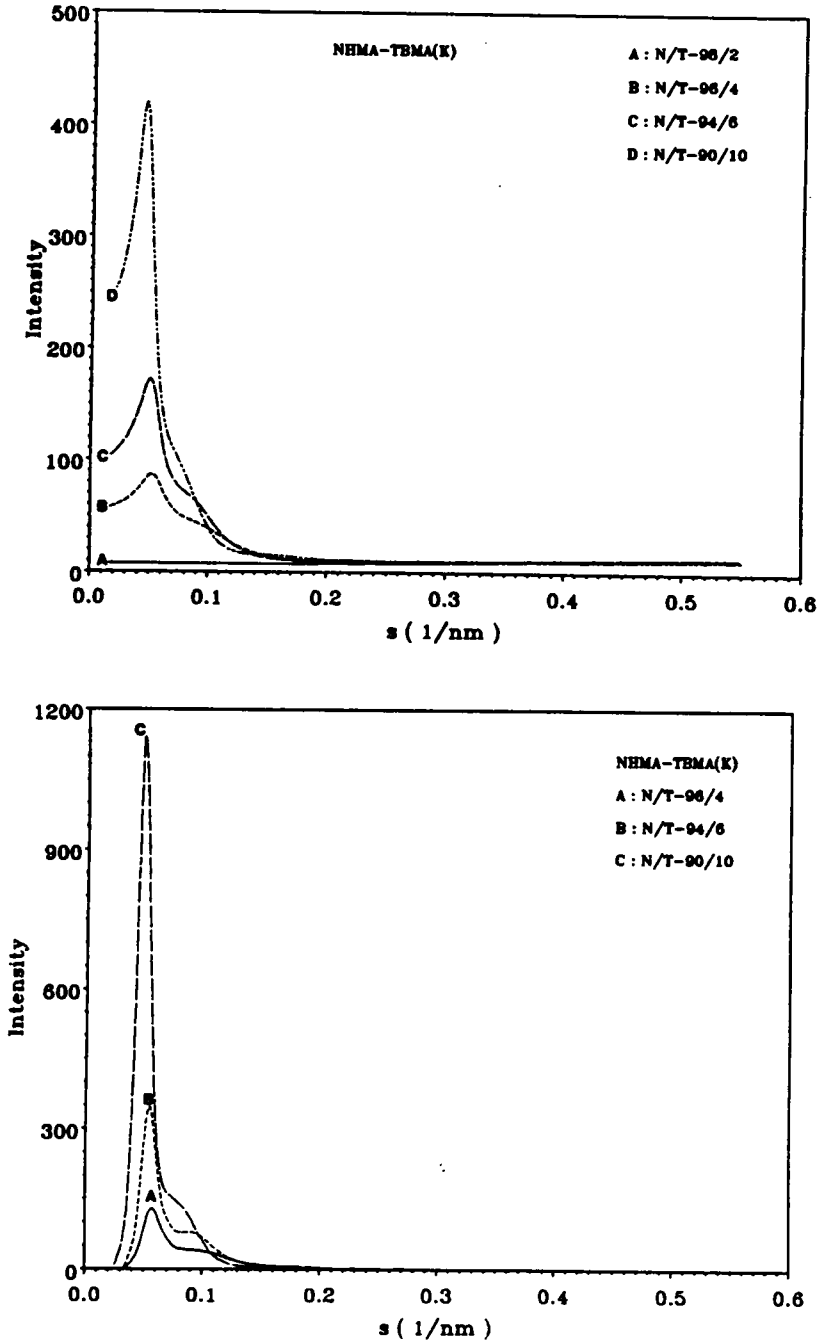

Figure 9.6. Small Angle X-Ray Scattering Profiles of NHMA/TBMA Diblock Ionomers Neutralized with K: (a) smeared, and (b) desmeared

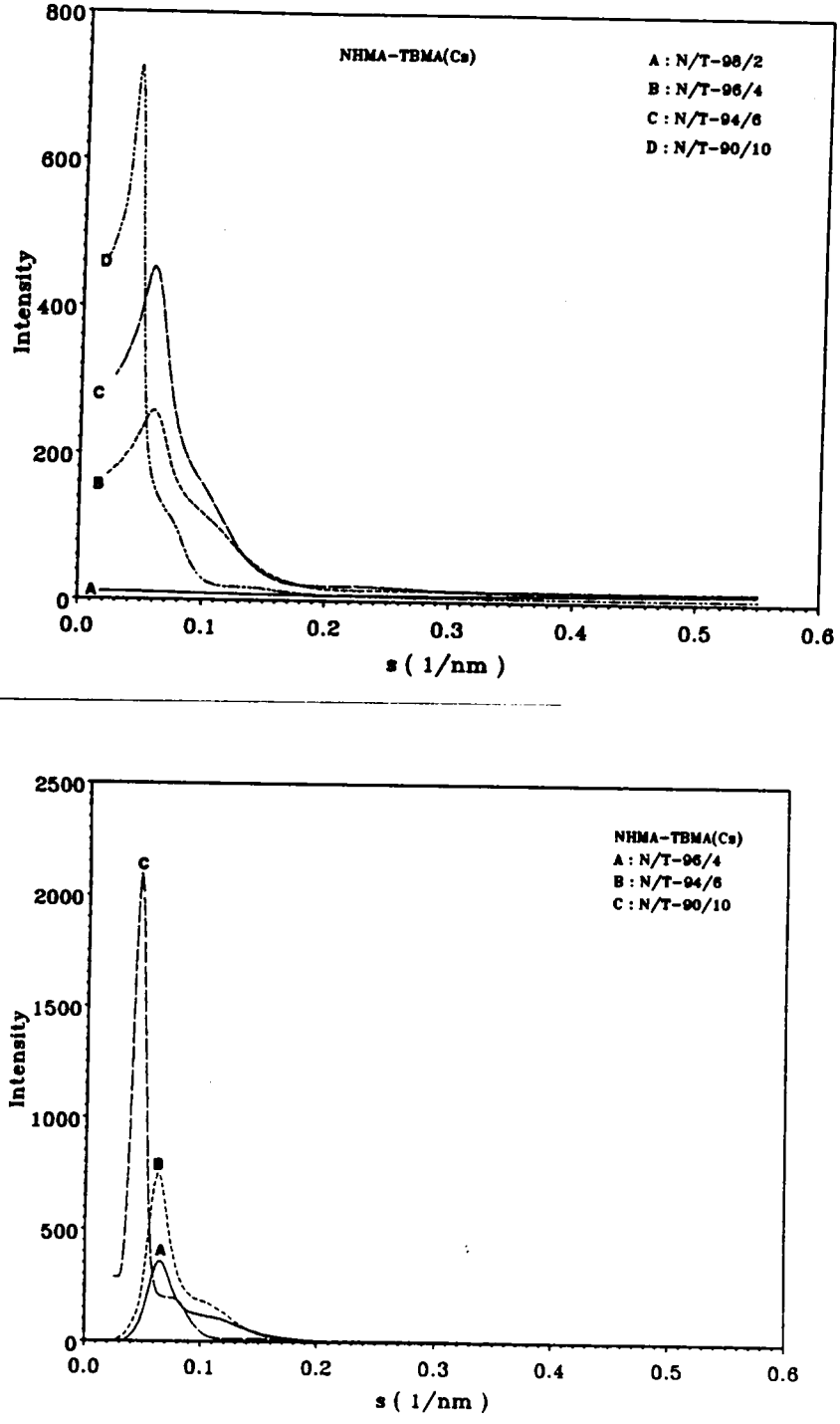

Figure 9.7. Small Angle X-Ray Scattering Profiles of NHMA/TBMA Diblock Ionomers Neutralized with Cs: (a) smeared, and (b) desmeared

Table 9.1. Periodic Spacing between the Ionic Domains in NHMA-TBMA Diblock Ionomers as Determined by SAXS and TEM Analyses

Sample-id	Periodic Spacing between the Ionic Domains, (in nm)							
	$d_{smeared}$		$d_{desmeared}$		$\gamma_1(D)$	$\gamma_3(D)$	TEM	RMS
	I	II	I	II				
TN-98/2 (K)								
TN-96/4 (K)	18.8	10.8	17.4	10.0	17.4	20.8		12.9
TN-94/6 (K)	19.8	11.6	18.3	10.6	18.2	22.1		12.5
TN-90/10 (K)	22.3	13.2	21.0	11.8	20.4	24.8	12.5-17.3	12.4
TN-98/2 (Cs)								
TN-96/4 (Cs)	17.0	8.7	15.5	8.6	14.1	18.4		12.9
TN-94/6 (Cs)	17.4	9.9	15.9	9.2	15.4	18.8	13.0-17.3	12.5
TN-90/10 (Cs)	23.8	12.8	23.0	12.7	22.1	26.7	13.5-18.9	12.4

RMS = unperturbed root mean square end-to-end distance of the NHMA block
I = spacing corresponding to the position of the primary SAXS peak
II = spacing corresponding to the position of the secondary SAXS peak

Table 9.2. Periodic Spacing between the Ionic Domains in TBMA/NHMA/TBMA Triblock Ionomers as Determined by SAXS and TEM Analyses

Sample-id	Periodic Spacing between the Ionic Domains, (in nm)					
	$d_{smeared}$	$d_{desmeared}$	$\gamma_1(D)$	$\gamma_3(D)$	TEM	RMS
TNT-2/96/2 (K)	13.0	11.9	10.0	13.9		13.0
TNT-3/94/3 (K)	13.5	12.2	10.5	13.9		12.3
TNT-5/90/5 (K)	20.4	18.3	17.1	21.4		11.5
TNT-2/96/2 (Cs)	14.3	13.2	12.8	15.1		13.0
TNT-3/94/3 (Cs)	14.5	13.5	12.9	15.8		12.3
TNT-5/90/5 (Cs)	19.8	18.3	17.0	21.2	18.3	11.5

RMS = unperturbed root mean square end-to-end distance of the NHMA block
I = spacing corresponding to the position of the primary SAXS peak
II = spacing corresponding to the position of the secondary SAXS peak

a secondary peak (and even a faint third for the NT-90/10 (Cs) ionomer). The higher angle shoulder is further sharpened on desmearing the slit-smeared SAXS profiles. The scattering peaks represent the periodic spacings between the regions of similar electron density in the material; i.e. the nh-TBMA ionic domains. Tables 9.1 and 9.2 provide the periodic spacings between the ionic domains obtained from SAXS and TEM analysis for diblock and triblock ionomers, respectively. The SAXS spacings were obtained from the desmearing procedure and also from the analysis of the 1-D and the 3-D correlation functions. The root mean square end-to-end distance (RMS) values for the NHMA block is also provided which have been estimated from gaussian statistics for the unperturbed chains. The unperturbed end-to-end distance (RMS) values were calculated from prior knowledge of the characteristic ratio of the NHMA segments using $< R^2 >^{1/2} = (C_\infty nl^2)^{1/2}$ (209). Notice that the positions of both the primary as well as the secondary peaks move to lower scattering angles (therefore larger spacings) with increasing block length although the non-ionic block (NHMA) block length remains nearly the same. There is a significant increase in the spacing corresponding to the position of the primary peak with increasing ionic block length in comparison to the estimated unperturbed root mean square end-to-end distance (RMS) value of the NHMA chains (from Tables 9.1 and 9.2). Of course, it is realized that the presence of the additional nh-TBMA block would cause an increase in this spacing. However, the increase in the spacing is quite significant, 85% for sample NT-90/10 (Cs) and 59% for sample TNT-5/90/5 (Cs) although the molecular weight of the nh-TBMA blocks are relatively small (see Table 5.1). It is, therefore, speculated that the spacing corresponding to the observed scattering peaks is a particularly strong function of the ionic block length. This observation is consistent with that observed by Williams et al. on styrene-4-vinylpyridium ABA block ionomers (99). The line widths of the scattering peaks increase with decreasing ionic block length. The larger line width is indicative of a greater dispersity in either the periodic or characteristic spacing between the scattering centers or due to a decrease in the ordering of the macrolattice. As expected, the intensity of the scattering peaks increase with increasing ionic block length because of an increase in the volume fraction of the scattering entities (ionic moieties). Based on the spacing obtained from SAXS it is believed that the ionic blocks are much more extended possibly due to the ionic effects present in the nh-TBMA blocks. In addition,

a significant increase in the scattered intensity was observed for Cs block ionomers as compared to the K block ionomers because of the apparent increase in the inherent scattering contrast in going from the K ion to the Cs ion.

The invariant and the diffuse boundary analysis could not be performed because all the ionomers exhibited an increase in the scattered intensity (almost "steplike") at larger "s" values - a behavior similar to that observed in the TET block ionomers. Hence, no further quantitative analysis could be performed for the NHMA-TBMA based di- and tri- block ionomers.

The 1-D and the 3-D correlation function for the 90/10 diblock ionomers neutralized with K and Cs are shown in Figure 9.8. In Table 9.1, the spacings obtained from the 1-D and 3-D correlation functions for the diblock ionomers are provided. These spacings are also indicative of the periodic spacing between the ionic domains assuming one-dimensional symmetry for the 1-D correlation function and a spherical (or isotropic) symmetry for the 3-D correlation function. For the diblock ionomers, the desmeared spacings obtained from the SAXS profiles scale more closely to the 1-D correlation function than those from the 3-D correlation function. This suggests that the ionic domains might be geometrically anisotropic and may therefore exist in either a cylindrical or a lamellar morphology. Taking the ratio of the primary to the secondary peak provides information regarding the nature of packing of the ionic domains if indeed they pack in a pseudo-lattice. It is well known that for lamellar systems, the ratio of increasing order peaks scale as 1:2:3 while for a hexagonally packed cylindrical system the ratio scales as 1:1.732:2, etc. From Table 9.1, for the diblock ionomers, this ratio ranges between 1.73-1.80. Since this ratio is close to 1.732, it is believed that the ionic domains may be arranged in a hexagonally packed cylindrical pseudo-lattice. It is also possible that the primary and the secondary peaks may be entirely unrelated and that a dual morphology may indeed exist in these systems. In order to possibly separate these two hypothesis, imaging the ionic domains using transmission electron microscopy was attempted. Sufficient electron density contrast is already available in these block ionomers that selective staining was not necessary.

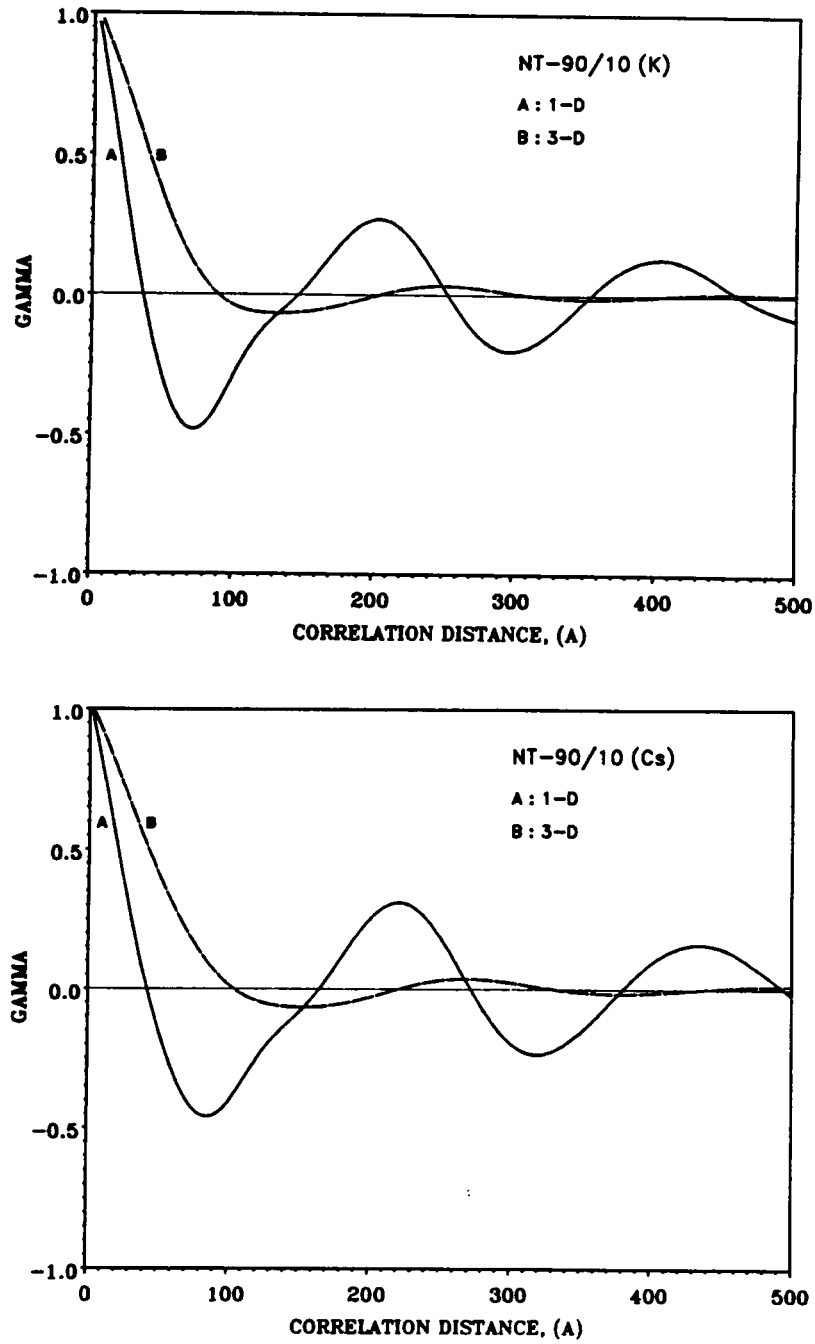

Figure 9.8. The 1-D and the 3-D Correlation Functions of the NT-90/10 Diblock Ionomers: (a) K ionomer, and (b) Cs ionomer

9.3.3 *TEM Analysis of Diblock and Triblock Ionomers*

The TEM analysis was performed on both the di- and the tri- block ionomers by Mr. Greg York from the Department of Materials Engineering at Virginia Tech. The TEM micrographs of the NT-90/10 K and Cs ionomers are shown in Figure 9.9. From the micrographs, both highly ordered as well as somewhat disordered regions can be observed in both the ionomers. A cylindrical or discontinuous lamella type of structure is observed in the highly ordered regions with an average interdomain spacing of ca. 19nm for the NT-90/10 (Cs) ionomer and ca. 17nm for the NT-90/10 (K) ionomer - a bit smaller than the spacing obtained from the position of the primary SAXS peak. However, this estimated value is not a particularly precise number as can be understood from viewing the TEM micrographs. Since the ordered regions were randomly oriented, it was difficult to determine if these regions were strictly of a lamellar or cylindrical morphological in nature. However, one would anticipate in view of the ratio of the primary and secondary scattering peaks being 1.73-1.80 and, in view of the relatively low percentage of the ionic block component, the structure is more likely to be of a cylindrical morphology in nature. In addition, such a structure would be well in line with that observed by Feng on the IB-NS-18 ionene material (refer to Chapter 7 for nomenclature) where a somewhat cylindrical morphological texture was observed for a system that also possessed a small volume fraction of ionic phase, ca. 7%. It therefore seems that the long range order observed here, while not quite as discrete as that observed in the earlier work of Feng, is likely promoted by the strong ionic interactions that will take place in these block systems discussed here.

It was noted that some disordered regions also existed in the same micrographs addressed above. These disordered regions suggested a somewhat spherical morphological texture. This same texture was maintained when the sample was tilted through 45° angle from the plane of the film in the TEM so as to detect any anisotropy. Since these regions showed a somewhat smaller interdomain spacing (13 nm) than the ordered regions, one might attempt to associate this spacing with the secondary peak in the SAXS profile, which is nearly the same value. However, in view of the fact that the long range order exists in much of the sample, it is believed that the multiple scattering

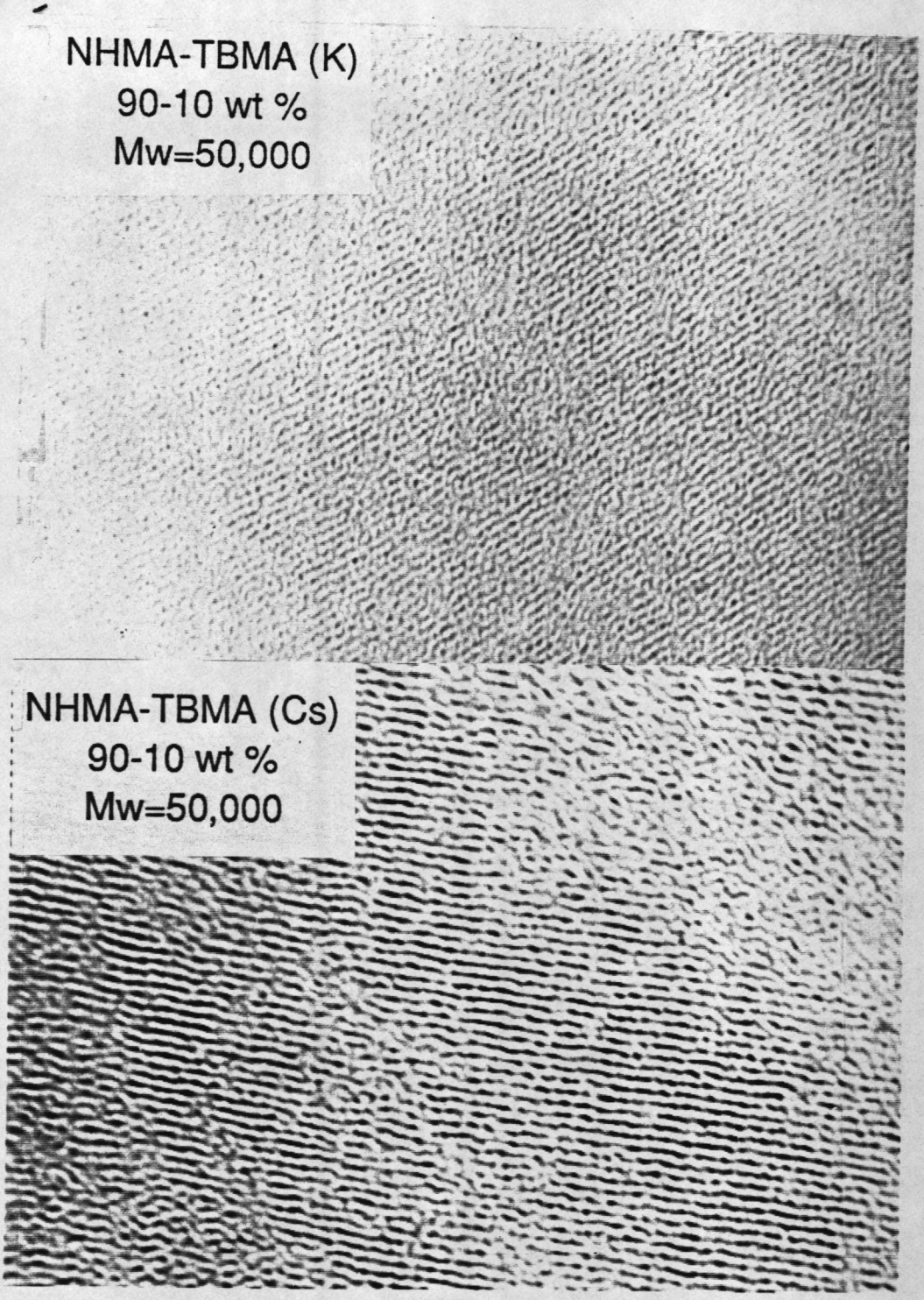

Figure 9.9. TEM Micrographs of NT-90/10 Diblock Ionomers: (a) K ionomer, and (b) Cs ionomer

peaks arise from a long range order in contrast to a dual morphology. Future work should attempt to confirm or disprove the proposed speculation.

Recall that sample NT-90/10 (Cs) exhibited a faint sign of a third peak. Since the line width of the third peak is very broad, no correlation to any of the earlier stated morphologies could be definitively made. In contrast, decreasing the ion content to 6% in the diblock ionomer (sample NT-94/6 (Cs)) shifted the morphology to a more discrete spherical texture (Figure 9.10a) but there still appears to be some regions of interconnected domains. The average spacing for the spherical domains was found to be ca. 15 nm. Keeping the ion content nearly the same as NT-90/10 (Cs) but changing the architecture to a triblock ionomer (TNT-5/90/5 (Cs) - Figure 9.10b), distinctly shifted the morphology to a more disordered spherical structure with the average spacing being ca. 18 nm. With nearly the same ion content, the diblock ionomer exhibits regions of highly ordered morphology but which is surprisingly absent in the corresponding triblock ionomer. The rationale for this observed behavior will be discussed shortly.

9.3.4 SAXS Analysis of the Triblock Ionomers

The slit smeared and the desmeared small angle x-ray scattering profiles of K and Cs neutralized triblock ionomers are shown in Figures 9.11 and 9.12, respectively. All the ionomers exhibit a distinct scattering or an ionic peak with the TNT-5/90/5 material of both K and Cs ionomers showing a faint sign of a higher order scattering. It can be seen from Figures 9.11b and 9.12b that on desmearing, the higher angle shoulder becomes more pronounced. Tables 9.2 provides the periodic spacings between the ionic domains obtained from SAXS and TEM analysis for the triblock ionomers. As mentioned earlier, the SAXS spacings were obtained from the desmearing procedure and also from the analysis of the 1-D and the 3-D correlation functions. As in the diblock ionomer, the scattering peak moves to lower scattering angles (therefore larger spacings) and the peak intensity significantly increases with increasing ionic block length. Also, the intensity of the scattering peaks in the Cs ionomers were substantially higher than the K triblock ionomer. These characteristic features in the scattering profile of triblock ionomers are very similar to that observed in diblock ionomers.

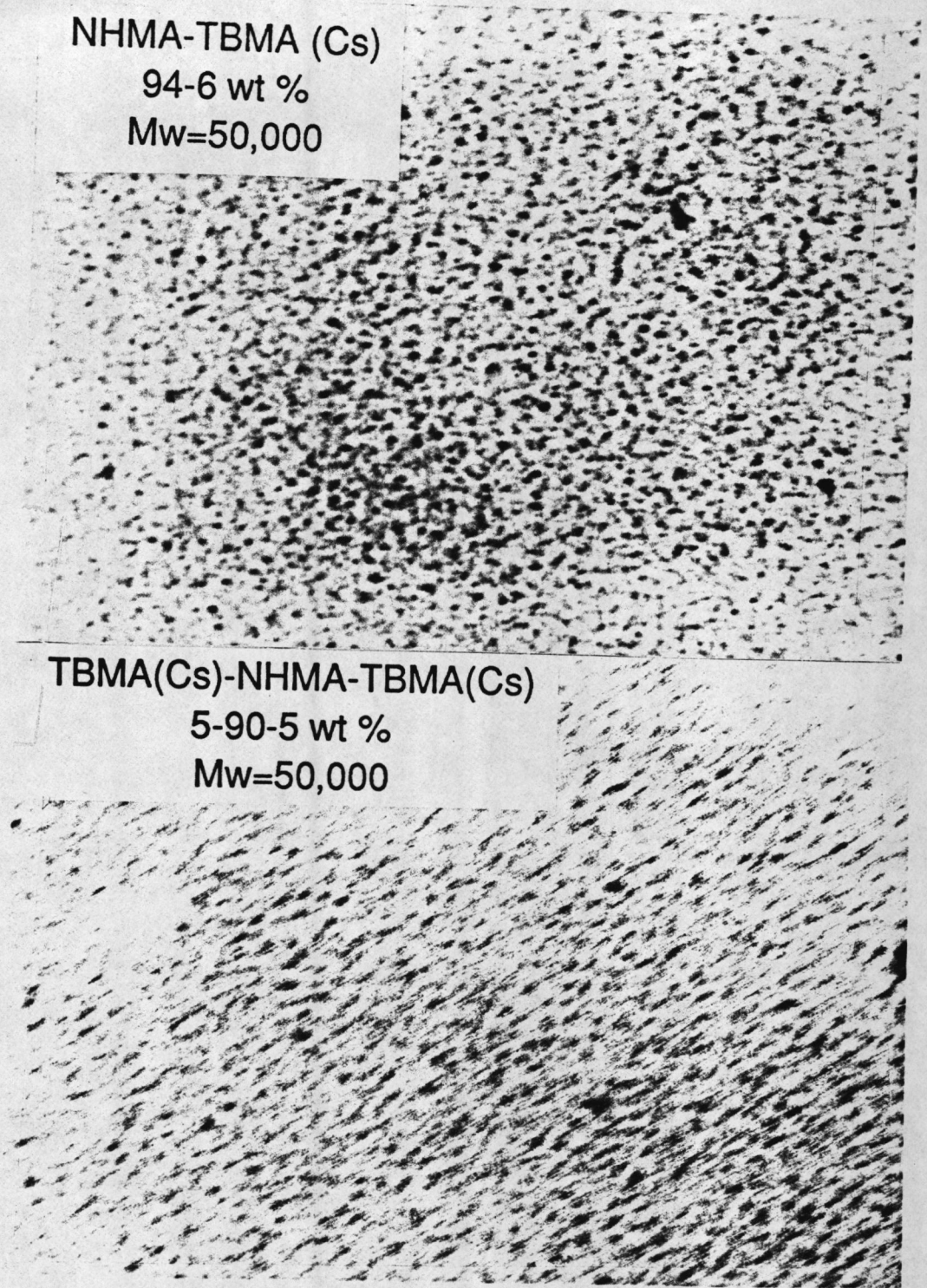

Figure 9.10. TEM Micrographs of Cs Neutralized 6% Diblock and 10% Triblock Ionomers: (a) NT-94/6 diblock ionomer, and (b) TNT-5/90/5 triblock ionomer

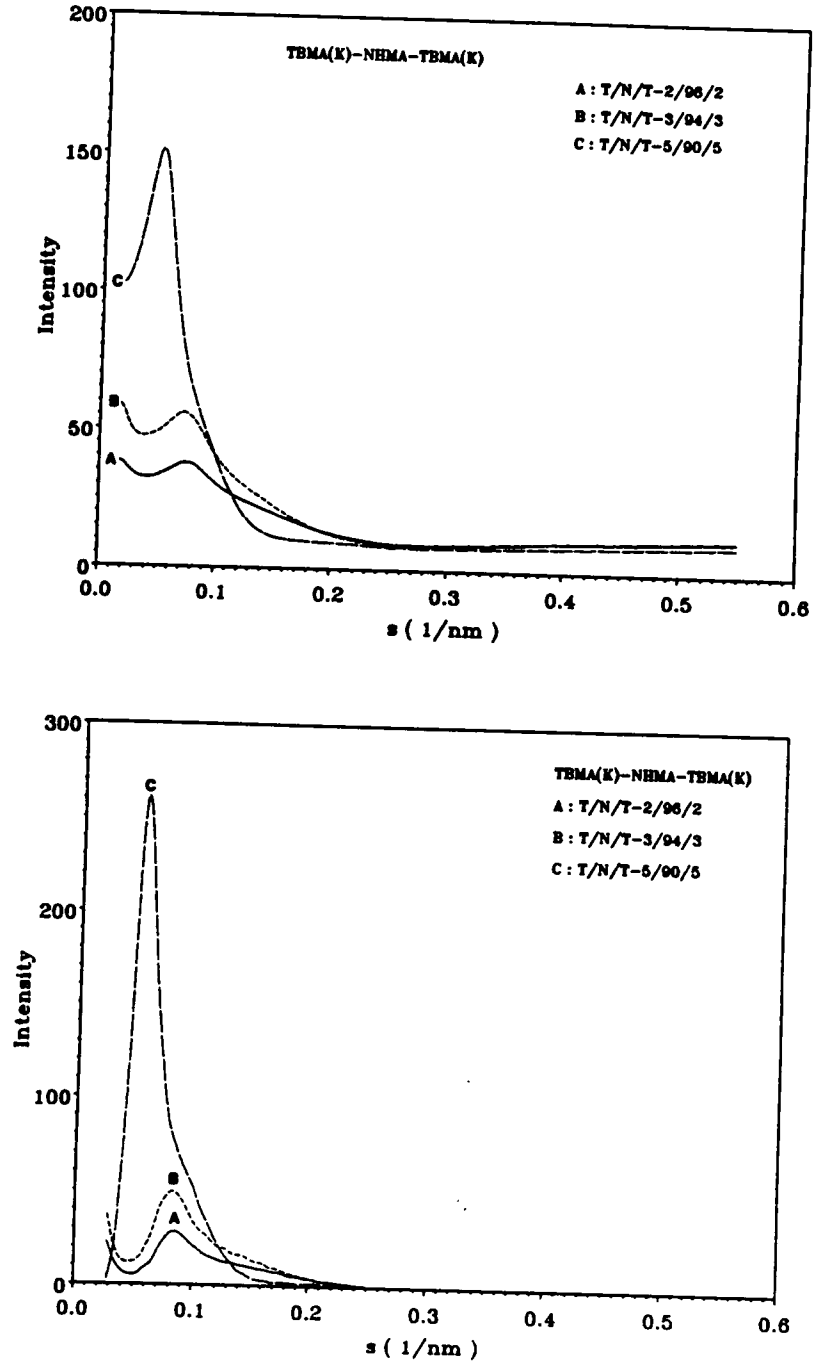

Figure 9.11. Small Angle X-Ray Scattering Profiles of TBMA/NHMA/TBMA Triblock Ionomers Neutralized with K: (a) smeared, and (b) desmeared

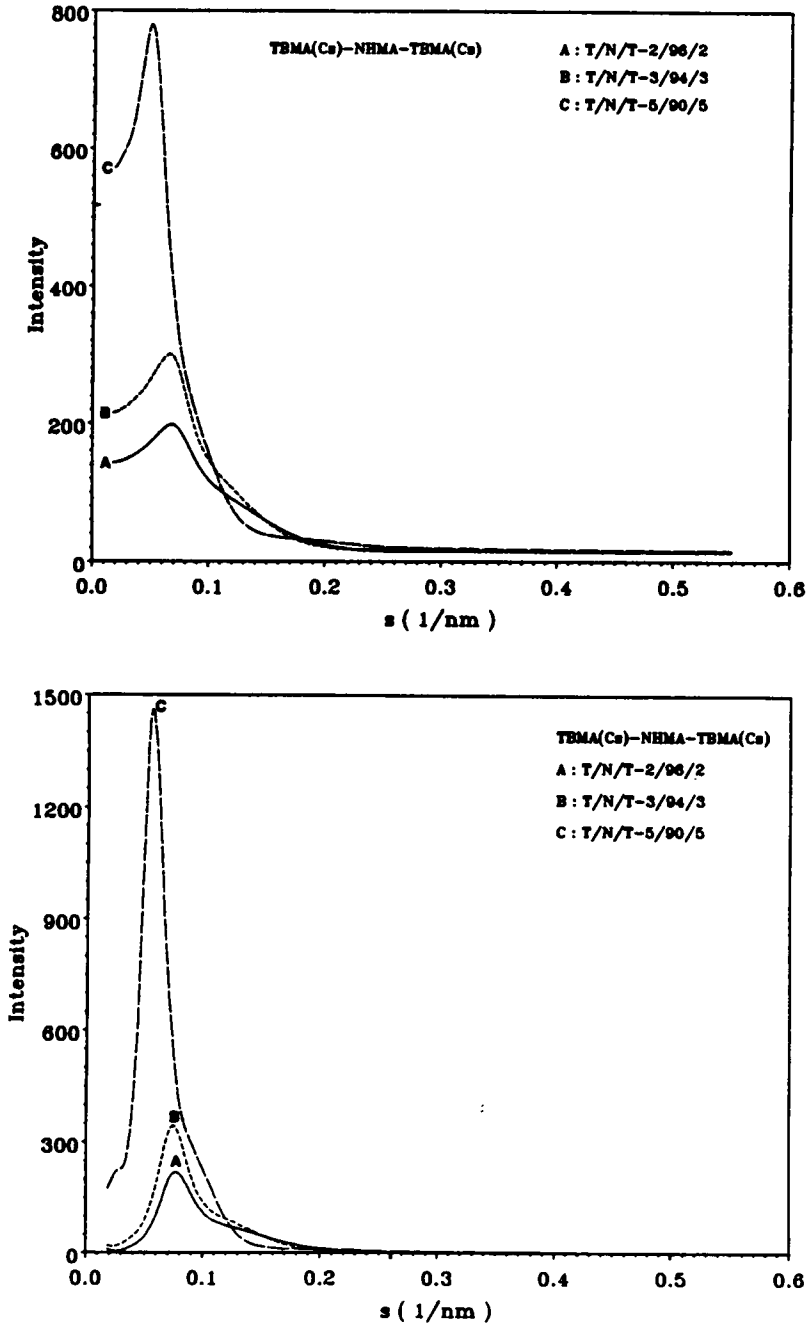

Figure 9.12. Small Angle X-Ray Scattering Profiles of TBMA/NHMA/TBMA Triblock Ionomers Neutralized with Cs: (a) smeared, and (b) desmeared

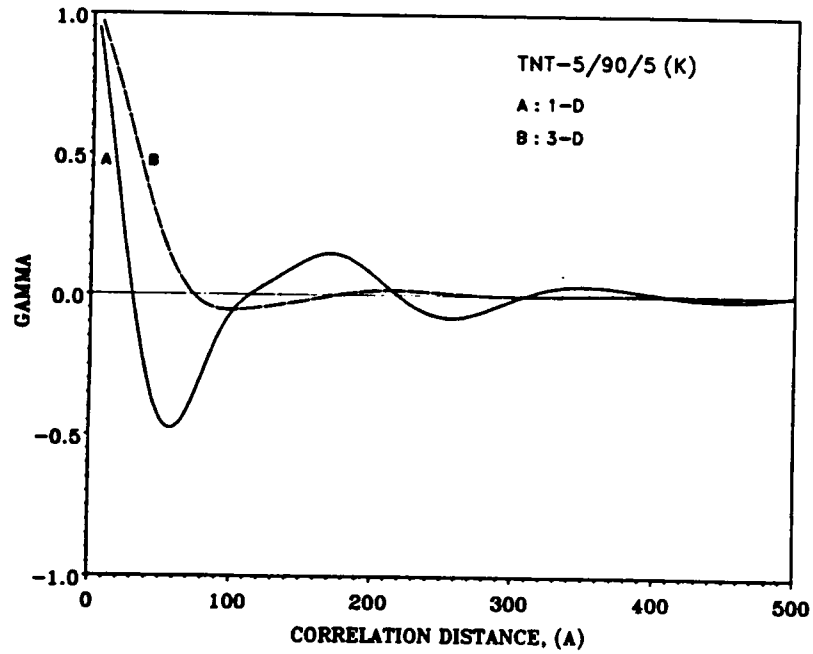

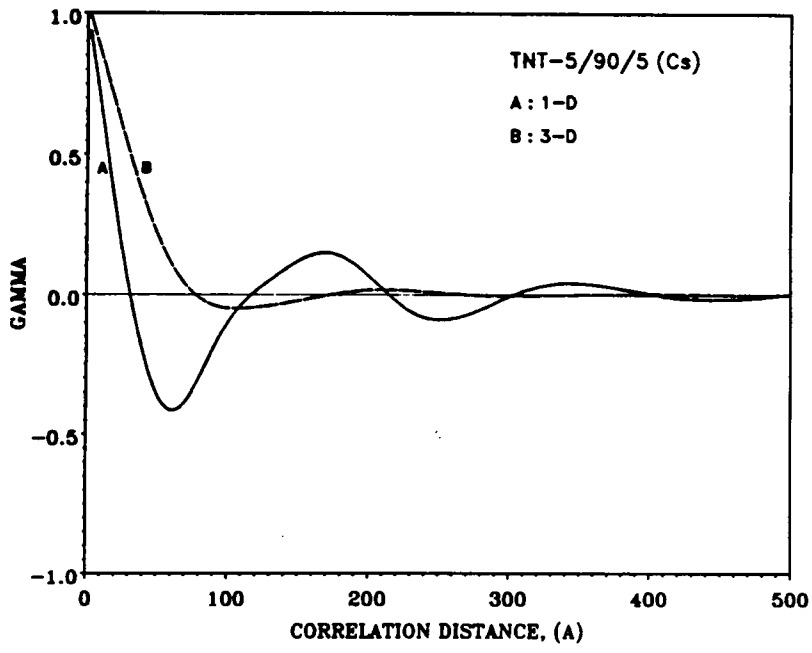

Figure 9.13. The 1-D and the 3-D Correlations Function of the TNT-5/90/5 Triblock Ionomers: (a) K ionomer, and (b) Cs ionomer

The 1-D and the 3-D correlation function of the K and Cs neutralized TNT-5/90/5 triblock ionomers is given in Figure 9.13. The periodic spacings obtained from the 1-D and 3-D correlation functions are also reported in Table 9.2. In the triblock ionomers the desmeared spacings obtained from SAXS profiles lies between the spacings corresponding to 1-D correlation function and the 3-D correlation function. This again suggests that the ionic domains may be geometrically anisotropic in nature. From TEM analysis of the TNT-5/90/5 (Cs) ionomer, mainly spherical domains were observed and there was no indication of any long range ordering. The absence of a distinct secondary scattering peak in the triblock ionomer with the same ion content as that of the diblock ionomer is very surprising. The absence of long range ordering may be attributed to both a larger molecular weight distribution (MWD) and to compositional variations of the nh-TBMA segments in the system (210). Since the compositional distribution of the individual segments is closely related to the MWD of the entire polymer, it is often difficult to specifically obtain the compositional distribution of individual segments in block copolymers. However, the MWD's of the diblock ionomers are distinctly narrower (1.1 to 1.2) than that of the triblocks (1.3 to 1.4) (see Table 5.1). The compositional distribution can be attributed to the sequential addition process where the control over the block sequence in diblock is much better than in the triblock materials because of the additional step involved in the synthesis of the precursors for the triblock ionomers. This compositional distribution can be significantly reduced with the use of an active difunctional initiator.

9.4 Summary

A detailed morphological investigation of the block ionomers has provided some very interesting findings. It was found that considerable reorganization within the material takes place with increasing polarity in the medium. As the polarity of the medium increases, the demixing process is greatly facilitated which is responsible for microphase separation of the ionic domains in the ionomers.

As expected, very poor mechanical properties were observed for the diblock ionomers but the triblock ionomers exhibited some potential in using them as pressure sensitive adhesives. For contrast, even the methacrylate based triblock ionomers exhibited lower tensile strength than the PIB sulfonated ionomers studied earlier in this laboratory (93). Therefore, it can be seen that the potential of using the methacrylate based block ionomers for structural applications, is quite limited. Based on the observed bulk properties, it is expected that the size of the ionic domains in the Cs ionomers to be greater than the K ionomers but the K ionomers forms more cohesive ionic domains as expected from electrostatic considerations.

Multiple scattering peaks were observed from the SAXS experiments for the diblock ionomers which is indicative of an high level of ordering in these systems. This has been confirmed using TEM where highly ordered regions as well as disordered regions were observed. The spacings corresponding to the position of the SAXS peaks appear to correlate very well with the structural features observed from the TEM micrographs. This a yet another study based on an entirely different chemistry where a non-spherical morphology has been observed for a material containing a small volume fraction of the ionic phase. Earlier, Feng et al. (194) had observed a non-spherical or a cylindrical related morphological texture was observed for a system that also possessed a small volume fraction of ionic phase, ca. 7%. Therefore, it seems that the long range order observed here is likely promoted by the strong ionic interactions that takes place in these block systems discussed here as well as noted in the segmented ionene systems. At present, no definitive arguments can be made regarding the morphological texture of the ionic domains in these materials, though there is some evidence that a cylindrical morphology might be present. Finally, it was found that the periodic spacing between the ionic domains appeared to be strong function of the nh-TBMA ionic block length.

10.0 CONCLUSIONS AND RECOMMENDATIONS FOR FUTURE WORK

10.1 Conclusions

The structure-property behavior of model elastomeric ionomers has been investigated for three different materials, though there is an underlying theme connecting all of these systems. The location of the ions in the polymer backbone in all the three systems investigated is very well defined, thus simplifying the task of relating the network microstructure to the observed properties in the material. The studies from each of the three materials has yielded interesting and valuable information which helps in elucidating the nature of ion aggregation in ionomers, in general. The conclusions from each of the studies will be summarized separately.

10.1.1 Structure Property Studies of Telechelic Ionomers

1. *Diffuse Phase Boundary Analysis*

   The primary driving force for the high level of phase separation occurring in these ionomers is believed to be due to coulombic forces in the ionic domains. The phase boundary between the ionic phase and the non-ionic matrix was found to be relatively sharp (< 0.1 nm - i.e. less than the length of the C-C bond) in all the telechelic ionomers studied, irrespective of the nature of the cation, the functionalized acid group or the non-ionic backbone.

2. *Degree of Phase Separation*

   The degree of phase separation or the invariant analysis is believed to be inapplicable to all the telechelic ionomers investigated in this study because of the uncertainty involved in the deter-

mination of the values of $\overline{\Delta\rho_e^2}$. Based on the diffuse phase boundary analysis, it is expected that a high degree of phase separation exists in all the ionomers investigated in this study.

3. *Origin of the zero angle scattering*

The upturn in the intensity near zero angle region was observed in all the ionomers and it increased with increasing levels of neutralization. Based on this information, it was speculated that the upturn may be related to the isolated ion pairs heterogeneously distributed in the backbone material.

4. *Observed bulk Properties*

The observed bulk properties (such as stress-strain, tensile creep or stress-relaxation behavior) were found to be highly dependent on the nature of the cation, its valency, and its ionic radius. The size of the cation not only determined the magnitude of the forces of association but also its cohesiveness from steric considerations. For example, the Mg ion (0.65 Å) displayed higher network stability than the Na ion (0.95 Å). The nature of the cation, i.e. ionic versus covalent, displayed very different behavior. The cations which were ionic in nature (such as Na or Mg) displayed greater network stability than the materials neutralized with cations that are more covalent (or less ionic) in nature (such as Al or Ti).

5. *Sulfonate versus Carboxylate Ionomers*

The nature of aggregation in the sulfonate ionomers was found to be much stronger than the corresponding carboxylated ionomers as determined from bulk properties (such as stress-strain, tensile creep or stress-relaxation behavior). This is consistent with the earlier observation of Lundberg et al. on random polystyrene ionomers (94). For the sulfonate ionomers the spacing corresponding to the ionic peak was found to be about 8-10% larger than in the carboxylate ionomer. No definitive explanation has been given for the observed behavior, although two plausible speculations have been provided.

6. *SAXS Behavior*

Based on the SAXS behavior, it is believed that the nature of the ion aggregation in the telechelic ionomers investigated appear to favor the "interparticle interference" model. In addition, more than one distinct SAXS peak has been observed from the 2000 $\overline{M}_n$ PBD telechelic ionomers. It is speculated that a dual morphology might be responsible for the observed bimodal SAXS behavior.

10.1.2 SAXS Investigations of Novel Ionene Polymers

1. ***Effect of PTMO segment molecular weight***

   The periodic spacing between the ionene domains systematically increases with increasing PTMO segment molecular weight. Based on the SAXS results, a change in the type of morphology is indicated above 3400 $\overline{M}_n$. For materials with PTMO segment molecular weight < 3400 $\overline{M}_n$, multiple scattering peaks were observed. The spacings corresponding to these peaks scale nearly as 1:2:3. It is, however, believed that a cylindrical type of morphology may exist at least in the IB-NS-18 material. At present, no definitive conclusions could be drawn regrading the morphology of these materials. Surprisingly, the diffuse boundary thickness was not significantly affected with increasing PTMO segment molecular weight. Also, no distinct trends could be observed regarding the effect of PTMO segment molecular weight on the degree of phase separation in the system.

2. ***Effect of the Nature of the Counterion***

   The intensity of the scattering peak increases dramatically with increasing atomic number of the counterion (I>Br>Cl). The phase boundaries were relatively sharp (<0.1 nm - i.e. less than the length of the C-C bond) for all the materials investigated and were not dependent on the nature of the cation.

3. ***Effect of the Nature of the Ionene Segment Architecture***

   Based on the chemistry of the ionene segments, it was expected that some degree of phase mixing would occur in the ionene segment containing the aliphatic spacer group (-S- materi-

als). Estimation of the diffuse boundary region could only be made for the IB-S-34 material. All other materials with a spacer in the ionene segment exhibited a small positive deviation from the ideal or Porod behavior. The observed behavior may be due to segmental mixing of one domain in the other. The estimated diffuse boundary thickness for the material investigated was less than the length of a C-C bond which clearly indicates that a sharp boundary exists even in the materials that contain the spacer group in the ionene hard segment.

10.1.3 Selective Plasticization of Segmented Ionene Polymers

It has clearly been shown that zinc stearate functions as an effective ionic plasticizer. With zinc stearate incorporation, the softening temperature of the the ionene materials is lowered to ca. 120 °C. The plasticized materials were shown to be thermally processable (utilizing techniques such as compression molding) without appreciable loss of the bulk properties. It was found that zinc stearate was completely "compatible" with the ionene polymer up to a loading level between 40 and 60 phr with no indication of "blooming" occurring to the surface.

10.1.4 Structure-Property Studies of Block Ionomers

1. ***Polarity of the medium***

   Considerable reorganization within the material takes place with increasing polarity of the glassy segment. As the polarity of the medium increases, i.e. in going from the ester to the acid and finally to the ionomer form, the demixing process between the polar and the non-polar segments is greatly facilitated. This is believed to be responsible for the microphase separation of the ionic domains from the non-ionic matrix.

2. ***Effect of the Ionic Block Length***

   The position of the scattering peaks was found to be a particularly strong function of the ionic block length. Both, the scattering intensity and the spacing corresponding to the ionic peak

increased significantly with increasing ionic block length. The scattering intensity was also enhanced with increasing atomic number of the cation.

3. *Effect of the Block Segment Architecture*

As expected, the tensile properties of the diblock ionomers were very poor (< 2 MPa). Significant improvements were observed in the tensile properties (reaching upto 4 MPa) in changing the architecture to the triblock ionomer. Even these triblock ionomers compared quite poorly to the PIB sulfonated ionomer studied earlier in this laboratory (93). Multiple scattering peaks were observed from SAXS measurements for the diblock ionomers which is indicative of a high level of ordering in the system. The high level of ordering has been confirmed using TEM but no conclusions could be made regarding the morphological features observed. Surprisingly, the high level of ordering that was seen in the diblock ionomers was not observed in the triblock ionomers with similar ion content.

10.2 Recommendations for Future Work

This research has provided some valuable information regarding the nature of ion aggregation in ionomers. Though this investigation has provided many answers regarding the nature of ion aggregation, there are still many unanswered questions. The recommendations for future work are provided below;

1. In this investigation, extensive SAXS data has been obtained for a number of ionomer systems. The data from this investigation could be utilized as a database for the purposes of applying the different models proposed in the literature to the experimental data. Most of the earlier modelling work has been conducted on the random ionomers which contains one main limitation - lack of knowledge regarding the placement of the ions. For example, the recently proposed Lee and Cooper model could be used to determine the applicability of that model to the model systems investigated in this study.

2. It was observed that the spacing of the sulfonate ionomers was consistently higher than the carboxylated ionomers. Small angle neutron scattering can be used to obtain information regarding the conformation of the intervening non-ionic segment which could be used in conjunction with SAXS data to determine the cause for the observed behavior.

3. The origin of the upturn in the intensity near the zero angle region still remains a controversial issue. A systematic study, particularly the effect of neutralization using both SAXS and ASAXS (anomalous small angle x-ray scattering) techniques may provide some indication regarding its origin.

4. A dual morphology was proposed for the 2000 $\overline{M}_n$ PBD ionomer based on the observed SAXS behavior. Careful examination using TEM may provide indications regarding the origin of the different scattering peaks. The selection of a proper solvent to float the microtomed samples must be made carefully so that the actual morphology is not affected by the carrier solvent.

5. The mathematical modelling of the spiral lattice model proposed for the IB-NS-18 material should be attempted. If suitable parameters for the model could be identified, then the morphological texture of the highly ordered regions can be established using graphic modelling packages such as Chem-X, etc.

6. In the II-NS-15 ionomer, an additional peak was observed at lower "s" values. The origin of this peak needs to be identified. Again, a systematic investigation using TEM of the II-NS-15 sample should be carried out.

7. In the dynamic mechanical analysis, an increase in the modulus was observed for the IB-NS-14 material above 80 °C. Real time SAXS measurements should be performed in a synchotron as a function of temperature. The sample should be scanned at a rate close to 2 °C per minute (the rate utilized in the rheovibron). It has been speculated that this phenomenon might be due to an ordering mechanism of the ionene segments. If this were to occur, at elevated tem-

peratures, a maxima would be observed in a plot of the scattering invariant as a function of temperature.

8. From the TEM analysis, highly ordered regions were observed for the NT-90/10 (Cs) ionomer. Detailed investigation of this material using SAXS equipped with 2-D detector should be attempted. Indication of any azimuthal dependence can be determined by this method.

9. The lack of long range order in the triblock material has been attributed to both MWD as well as to compositional distribution in the TBMA segments. Possibly, NMR or FTIR could be utilized to obtain information regarding the compositional distribution of the TBMA segments in the triblock polymer after conducting a series of fractination steps in a suitable solvent.

11.0 REFERENCES

1. R. W. Rees, *Modern Plastics*, 42, 98, (1965).

2. H. A. Al-Salah, K. C. Frisch, H. X. Xiao and J. A. McLean, Jr., *J. of Polym. Sci., Polym. Chem. Ed.*, 25, 2127 (1987).

3. E. P. Otocka, *J. of Macromol. Science* Chem., 5, 275 (1971).

4. C. G. Bazuin and A. Eisenberg, *Ind. Eng. Chem. Prod. Res. Dev.*, 20, 271 (1981).

5. M. Tant and G. L. Wilkes, *J. of Macromol. Science - Rev. Chem. Phys.*, C28, 1 (1988).

6. A. Eisenberg, *Adv. Polym. Sci*, 5, 59 (1967).

7. W. J. MacKnight and T. R. Earnest, Jr., *J. of Polym. Sci., Macromol. Rev.*, 16, 41 (1981).

8. J. J. Fitzgerald and R. A. Weiss, *J. of Macromol. Science - Rev. Chem. Phys.*, C28, 99 (1988).

9. L. Holliday, Ed., *"Ionic Polymers"*, Halstead-Wiley, New York, 1975.

10. A. Eisenberg, Ed., *"Ions in Polymers", Adv. in Chem. Ser., No. 187*, ACS Washington D.C., 1980.

11. A. Eisenberg and M. King, Eds, *"Ions Containing Polymers"*, Academic Press, New York, 1977.

12. A. D. Wilson and H. J. Prosser, Eds., *"Developments in Ionic Polymers - 1"*, ACS Symp. Ser. No. 302, American Chemical Society, Washington D.C., 1986.

13. M. Pineri and A. Eisenberg, Eds. *"Structure and Properties of Ionomers"*, D. Reidel Pub. Co., Dordrecht, Holland (1987).

14. A. Eisenberg and F. E. Bailey, Eds., *"Coulombic Interactions in Macromolecular Systems"*, ACS Symp. Ser. 302, American Chemical Society, Wahington D.C., 1986.

15. A. Eisenberg and H. J. Yaeger, Eds., *"Perflorinated Ionomer Membranes"*, ACS Symp. Ser. No. 180, American Chemical Society, Washington D.C., 1982.

16. H. P. Brown, ***Rubber Chem. Technol.***, 30, 1347 (1957).

17. E. P. Otocka, M. Y. Hellman, and L. L. Blyler, ***J. Appl. Phys.***, 40, 4221 (1969).

18. S. Bonotto and E. F. Bonner, ***Polym. Prepr.***, 9, 537 (1968).

19. A. Eisenberg, ***Macromol.***, 3, 147 (1970).

20. R. Longworth and D. J. Vaughan, ***Polym. Prepr.***, 9, 525 (1968).

21. C. L. Marx, D. F. Caulfield, and S. L. Cooper, ***Macromol.***, 6, 344 (1973).

22. W. J. MacKnight, T. P. Taggart, and R. S. Stein, ***J. Polym. Sci., Polym. Symp.*** 45, 113 (1974).

23. M. Fujimura, T. Hashimoto, and H. Kawai, ***Macromol.***, 15, 136 (1982).

24. D. J. Yarusso and S. L. Cooper, ***Macromol.***, 16, 1871 (1983).

25. P. Debye, ***Phys. Z.***, 28, 135 (1927).

26. D. J. Yarusso and S. L. Cooper, ***Polymer***, 26, 371 (1985).

27. D. Lee, R. A. Register, C. Yang, and S. L. Cooper, ***Macromol.***, 21, 998 (1988).

28. P. Chu,D. Wu, W. J. MacKnight, C. Wu, J. C. Phillips, A. Legrand, C. W. Lantman, and R. D. Lundberg, *Macromol.*, 21, 525 (1988).

29. S. Kumar and M. Pineri, *J. of Polym. Sci., Polym. Lett. Ed.*, 24, 1767 (1986).

30. Y. S. Ding, S. R. Hubbard, K. O. Hodgson, R. A. Register, and S. L. Cooper, *Macromol.*, 21, 1698 (1988).

31. C. W. Lantman, W. J. MacKnight, D. G. Peiffer, R. D. Lundberg, J. S. Higgins, A. M. Pedley, B. G. Gabrys, A. R. Rennie, and A. F. Galambos, - to be published

32. A. F. Galambos, W. B. Stockton, J. T. Koberstein, A. Sen, R. A. Weiss and T. P. Russell, *Macromol.*, 20, 3094 (1987).

33. R. A. Weiss and J. A. Lefelar, *Polymer*, 27, 3 (1986).

34. D. G. Peiffer, R. A. Weiss and R. D. Lundberg, *J. of Polym. Sci., Polym. Phys. Ed.*, 20, 1503 (1982).

35. D. L. Handlin, W. J. MacKnight, and E. L. Thomas, *Macromol.*, 14, 795 (1981).

36. D. Graiver, M. Litt, and E. Baer, *J. of Polym. Sci., Polym. Chem. Ed.*, 17, 3573 (1979).

37. D. Feng, G. L. Wilkes, C. M. Leir and J. E. Stark, - to be published

38. T. Hashimoto, M. Shibayama, M. Fujimura and H. Kawai, *Memoirs of the Faculty of Engineering*, Kyoto University, 43 (1981).

39. M. Pineri, C. T. Meyer, A. M. Levelut and M. Lambert, *J. of Polym. Sci., Polym. Phys. Ed.*, 12, 115 (1974).

40. C. T. Meyer and M. Pineri, *J. of Polym. Sci., Polym. Phys. Ed.*, 13, 1057 (1975).

41. M. Pineri, C. T. Meyer, and A. Bourret, *J. of Polym. Sci., Polym. Phys. Ed.*, 13, 1881 (1975).

42. C. T. Meyer and M. Pineri, *J. of Polym. Sci., Polym. Phys. Ed.*, 16, 569 (1978).

43. W. C. Forsman, *Macromol.*, 15, 1032 (1982).

44. W. C. Forsman, W. J. MacKnight and J. S. Higgins, *Macromol.*, 17, 490 (1984).

45. B. Dreyfus, *Macromol.*, 18, 284 (1985).

46. E. Squires, P. Painter, and S. Howe, *Macromol.*, 20, 1740 (1987).

47. J. Mauritz, *J. of Macromol. Science - Rev. Chem. Phys.*, 28, 65 (1988).

48. M. Drzewinski and W. J. MacKnight, *J. of Appl. Polym. Sci.*, 30, 4753 (1985).

49. M. Hara and P. Jar, *Polymer Communications*, 28, 52 (1987).

50. M. Hara and P. Jar, *Macromol.*, 21, 3187 (1988).

51. A. Eisenberg, *J. of Poly. Sci.*, Polym. Symp. No. 45, 99 (1974).

52. A. Eisenberg, *Macromol.*, 4, 125 (1971).

53. H. Matsuura and A. Eisenberg, *J. of Polym. Sci., Polym. Phys. Ed.*, 11, 2079, (1973),

54. A. Eisenberg, H. Matsuura and Yokoyama, *J. Polym. Sci. Part A*, 29, 2131 (1971).

55. R. Longworth and D. J. Vaughan, *Nature*, 218, 85 (1968).

56. A. Eisenberg and M. Navratil, *Macromol.*, 6, 604 (1973).

57. A. Eisenberg and M. Navratil, *Macromol.*, 7, 84 (1974).

58. A. Eisenberg and M. Navratil, *Macromol.*, 7, 90 (1974).

59. A. Eisenberg and M. Navratil, *J. of Polym. Sci., Polym. Lett. Ed.*, 10, 537 (1972).

60. A. Eisenberg, H. Matsuura and T. Tsutsui, *J. of Polym. Sci., Polym. Phys. Ed.*, 38, 4208 (1967).

61. M. Rigdahl and A. Eisenberg, *J. of Polym. Sci., Polym. Phys. Ed.*, 9, 1641 (1981).

62. D. K. Jenkins and E. W. Duck, in *"Ions in Polymers"*, L. Holliday, Ed., Halsted-Wiley, New York, 1975.

63. R. D. Lundberg and H. S. Makowski, *Polym. Prepr.*, 19, 287 (1978).

64. N. H. Canter, U.S. Patent 3642728 (1974).

65. C. P. O. Farrel and G. E. Jernick, U. S. Patent 3836511 (1974).

66. H. S. Makowski, R. D. Lundberg, and G. S. Singhal, U. S. Patent 3870841 (1975).

67. H. S. Makowski, R. D. Lundberg, L. Westerman, and J. Bock, in *"Ions in Polymers"*, A. Eisenberg, Ed., Adv. Chem. Ser., No. 187, American Chemical Society, Washington D.C., Chapter 1, 1980.

68. P. K. Agarwal, H. S. Makowski, R. D. Lundberg, *Macromol.*, 13, 1980 (1679).

69. L. R. G. Treloar, *"The Physics of Rubber Elasticity"*, 2nd Ed., Oxford Univ. Press, London, 1958.

70. G. Broze, R. Jerome, Ph. Teyssie and C. Marco, ***Polym. Bull.***, 4, 241 (1981).

71. R. Jerome, J. Horrion, R Fayt, and Ph. Teyssie, ***Macromol.***, 17, 2447 (1984).

72. G. Broze, R. Jerome and Ph. Teyssie, ***Macromol.***, 14, 224 (1981).

73. G. Broze, R. Jerome and Ph. Teyssie, ***Macromol.***, 15, 920 (1982).

74. G. Broze, R. Jerome and Ph. Teyssie, ***Macromol.***, 15, 1300 (1981).

75. G. Broze, R. Jerome and Ph. Teyssie, ***J. of Polym. Sci., Polym. Lett. Ed.***, 19, 415 (1981).

76. G. Broze, R. Jerome, Ph. Teyssie and C. Marco, ***Macromol.***, 16, 1771 (1983).

77. G. Broze, R. Jerome and Ph. Teyssie, ***J. of Polym. Sci., Polym. Phys. Ed.***, 21, 2205 (1983).

78. G. Broze, R. Jerome and Ph. Teyssie, ***Macromol.***, 15, 996 (1983).

79. G. Broze, R. Jerome and Ph. Teyssie, ***J. of Polym. Sci., Polym. Phys. Ed.***, 21, 237 (1983).

80. G. Broze, R. Jerome, Ph. Teyssie, and C. Macro, ***Macromol.***, 18, 1376 (1985).

81. G. Broze, R. Jerome, Ph. Teyssie and C. Marco, ***J. of Polym. Sci., Polym. Phys. Ed.***, 20, 259 (1982).

82. R. Jerome and G. Broze, ***Rubber Chem. Technol.***, 58, 223 (1985).

83. M. Tant, J. H. Song, G. L. Wilkes, J. Horrion and R. Jerome, ***Polymer***, 27, 1815 (1986).

84. C. E. Williams, T. P. Russell, R. Jerome and J. Horrion, *Macromol.*, 19, 2877 (1986).

85. M. Laleg, Y. Camberlin, G. Boiteus-Steffan, G. Seytre, and J. P. Pascault, *J. of Macromol. Science* - Phys. B23, 223 (1984).

86. Y. Mohajer, D. Tyagi, G. L. Wilkes, R. F. Storey and J. P. Kennedy, *Polym. Bull.*, 8, 47 (1982).

87. S. Bagrodia, Y. Mohajer, G. L. Wilkes, R. F. Storey and J. P. Kennedy, *Polym. Bull.*, 8, 281 (1982).

88. S. Bagrodia, Y. Mohajer, G. L. Wilkes, R. F. Storey and J. P. Kennedy, *Polym. Bull.*, 9, 174 (1983).

89. Y. Mohajer, S. Bagrodia, G. L. Wilkes, R. F. Storey and J. P. Kennedy, *J. of Appl. Polym. Sci.*, 29, 1943 (1984).

90. S. Bagrodia, G. L. Wilkes, and J. P. Kennedy, *J. of Appl. Polym. Sci.*, 30, 2179 (1985).

91. M. R. Tant, G. L. Wilkes, R. F. Storey and J. P. Kennedy, *Polym. Bull.*, 13, 541 (1985).

92. M. R. Tant, G. L. Wilkes, M. D. Read and J. P. Kennedy, *J. of Polym. Sci., Polym. Lett. Ed.*, 24, 619 (1986).

93. S. Bagrodia, M. R. Tant, G. L. Wilkes, and J. P. Kennedy, *Polymer*, 28, 2207 (1987).

94. R. D. Lundberg and H. S. Makowski, in *"Ions in Polymers"*, A. Eisenberg, Ed., Adv. Chem. Ser., No. 187, American Chemical Society, Washington D.C., Chapter 2, 1980.

95. R. D. Allen, T. L. Huang, D. K. Mohanty, S. S. Huang, H. D. Qin, and J. E. McGrath, *Polym. Prepn.*, 24(2), 41 (1983).

96. R. D. Allen I. Yilgor, and J. E. McGrath in *reference 14*, 79.

97. T. E. Long, Ph.D. Dissertation, Department of Chemistry, Virginia Polytechnic Institute and State Univeristy, Blacksburg, July 1987.

98. S. Gauthier and A. Eisenberg, *Macromol.*, 20, 760 (1987).

99. J. P. Gouin, C. E. Williams, and A. Eisenberg - to appear in *Macromol.*

100. B. Lee, Ph.D. Dissertation, Department of Chemistry, Virginia Polytechnic Institute and State Univeristy, Blacksburg, 1987.

101. K. K. S. Hwang, C. Yang, and S. L. Cooper, *Polym. Eng. & Sci.*, 21, 1027 (1981).

102. J. A. Miller, K. K. S. Hwang, and S. L. Cooper, &jmsp. B22, 321 (1983).

103. K. K. S. Hwang, T. A. Speckhard and S. L. Cooper, &jmsp. B23, 153 (1984).

104. D. Dieterich, W. Keberle, and H. Witt, *Angew. Chem. Int. Ed.*, 9, 40 (1970).

105. M. Rutkowska and A. Eisenberg, *Macromol.*, 17, 822 (1984).

106. M. Rutkowska and A. Eisenberg, *J. of Appl. Polym. Sci.*, 29, 755 (1984).

107. E. R. Littmann and C. S. Marvel, *J. Amer. Chem. Soc.*, 52, 287 (1930).

108. A. Rembaum, W. Baumgartner and A. Eisenberg, *J. Polym. Sci. B*, 6, 159 (1968).

109. H. Noguchi and A. Rembaum, *J. of Polym. Sci., Polym. Lett. Ed.*, 7, 383 (1969).

110. A. Rembaum, S. Singer, and H. Keyzer, *J. of Polym. Sci., Polym. Lett. Ed.*, 7, 395 (1969).

111. D. Carson and A. Rembaum, *Macromol.*, 5, 75 (1972).

112. T. P. Klun, L. A. Wendling, J. W. C. van Bogart, and A. F. Robbins, *J. of Polym. Sci., Polym. Chem. Ed.*, 25, 87 (1987).

113. A. Eisenberg, H. Matsuura and T. Yokoyama, *Polym. J.*, 2, 117 (1971).

114. T. Tsutsui, R. Tanaka, and T. Tanaka, *J. of Polym. Sci., Polym. Phys. Ed.*, 13, 2091 (1975).

115. E. G. Knapick, J. A. Hirsch, and P. Ander, *Macromol.*, 18, 1015 (1985).

116. C. M. Leir and J. E. Stark, to be published in *J. of Appl. Polym. Sci.*

117. M. Watanabe, N. Toneaki, Y. Takizawa, and I. Shinohara, *J. of Polym. Sci., Polym. Chem. Ed.*, 20, 2669 (1982).

118. M. Watanabe, N. Toneaki, and I. Shinohara, *Polym. J.*, 14, 189 (1982).

119. M. Watanabe, K. Nagaoka, M. Kanba and I. Shinohara, *Polym. J.*, 14, 877 (1982).

120. S. Kohjiya, T. Ohtsuki, and S. Yamashita, *IUPAC 6th International Symposium on Cationic Polymerization and Related Processes,* Ghent, Belgium, 169 (1983).

121. S. Kohjiya, T. Ohtsuki, and S. Yamashita, *Macromol. Chem., Rapid Commun.*, 2, 417 (1981).

122. S. Kohjiya, T. Hashimoto, and S. Yamashita, and M. Irie, *Chem. Lett.*, 1497 (1985).

123. S. Smith and A. J. Hubin, &jmsc., A7, 1399 (1973).

124. S. Yamashita, M. Itoi, S. Kohjiya and A. Kidera, *J. of Appl. Polym. Sci.*, 35, 1927 (1988).

125. C. M. Paleos, G. Margomenon-Leonidopoulou and C. Christias, *Mol. Cryst. Liq. Cryst.*, 137, 391 (1986).

126. E. Shohamy and A. Eisenberg, *J. of Polym. Sci., Polym. Phys. Ed.*, 14, 1211 (1976).

127. K. Sakamoto, W. J. MacKnight, and R. Porter, *J. Polym. Sci., Pt. A-2*, 8, 277 (1970).

128. T. R. Earnest and W. J. MacKnight, *J. of Polym. Sci., Polym. Phys. Ed.*, 16, 143 (1978).

129. J. D. Ferry, *"Viscoelastic Properties of Polymers"*, 3rd Ed., Wiley, New York, 1980, Chapter 11.

130. S. Bagrodia, R. Pisipati, G. L. Wilkes, R. F. Storey and J. P. Kennedy, *J. of Appl. Polym. Sci.*, 29, 3065 (1984).

131. S. Bagrodia, G. L. Wilkes and J. P. Kennedy, *Polym. Eng. Sci.*, 26, 62 (1986).

132. H. S. Makowski and R. D. Lundberg, in *"Ions in Polymers"*, A. Eisenberg, Ed., Adv. Chem. Ser., No. 187, American Chemical Society, Washington D.C., Chapter 3, 1980.

133. R. D. Lundberg, H. S. Makowski, M. L. Westerman, in *"Ions in Polymers"*, A. Eisenberg, Ed., Adv. Chem. Ser., No. 187, American Chemical Society, Washington D.C., Chapter 5, 1980.

134. I. Duvdevani, R. D. Lundberg, C. Wood-Lordova and G. L. Wilkes, in *"Coulombic Interactions in Macromolecular System"*, A. Eisenberg and F. E. Bailey, Eds., *ACS Symp. Ser. No. 302*, ACS WashingtonD.C., 184 (1986).

135. J. J. Fitzgerald, D. Kim, and R. A. Weiss, *J. of Polym. Sci., Polym. Lett. Ed.*, 24, 263 (1986).

136. R. A. Weiss, A. Sen, A. F. Galambos, and J. T. Koberstein, *Polym. Mater. Sci. Eng.*, 59, 176 (1988).

137. B. D. Cullity, "Elements of X-Ray Diffraction", Addison-Wiley Publishing Co., Reading, MA (1959).

138. O. Glatter and O. Kratky, "Small Angle X-ray Scattering", Academic Press, New York (1982).

139. L. E. Alexander, "X-Ray Diffraction Methods in Polymer Science", Wiley-Interscience, John Wiley & Sons, Inc., New York (1969).

140. M. Kakudo and N. Kasai, "X-Ray Diffraction of Polymers", Kodansha Ltd. & Elsevier Publishing Co., New York (1972).

141. A. Guinier and G. Fournet, "Small Angle Scattering of X-Rays", John Wiley and Sons, Inc., New York (1955).

142. A. Guinier, "X-Ray Diffraction in Crystals, Imperfect Crystals, and Amorphous Bodies", W. H. Freeman and Co., San Francisco (1963).

143. H. Brumberger, Proceedings of the Conference held in Syracuse University on "Small-Angle X-Ray Scattering", Gordon and Breach, New York (1967).

144. Reviews, Papers and Abstracts from the 4th International Conference on "Small Angle Scattering" in Gatlinburg, USA - appeared in *J. of Appl. Cryst.*, 11, 295 (1978).

145. J. S. Higgins and R. S. Stein, *J. of Appl. Cryst.*, 11, 346 (1978).

146. D. S. Brown and R. E. Wetton in "Developments in Polymer Characterization - 1", J. A. Dawkins (ed.), Allied Sci. Pub. Ltd., London

147. O. Kratky and I. Pilz, *Quarterly Reviews in Biophysics*, 5, 481 (1972).

148. O. Kratky, *Progress in Biophysics*, 13, 105 (1963).

149. G. L. Wilkes, *J. Macromol. Sci.-Revs. Macromol. Chem.*, C10(2), 149 (1974).

150. A. H. Compton and S. K. Allison in "X-Ray in Theory and Experiment", D. Van Nostrand Co. Inc., New York (1935).

151. J. W. C. Van Bogart, Ph.D. Dissertation, University of Wisconsin, Department of Chemical Engineering, 1981 (University Microfilms 81-7545).

152. D. Tyagi, Ph.D. Dissertation, Department of Chemical Engineering, Virginia Polytechnic Institute & State University, March 1985.

153. R. W. Hendricks and P. W. Schmidt, *Acta. Phys. Austriaca*, 24, 97 (1967).

154. J. T. Koberstein, B. Morra, and R. S. Stein, *J. of Appl. Cryst.*, 13, 34 (1980).

155. J. A. Lake, *Acta Cryst.*, 23, 191 (1967).

156. O. Glatter, *J. of Appl. Cryst.*, 7, 147 (1974).

157. C. G. Vonk, *J. of Appl. Cryst.*, 4, 340 (1971).

158. P. W. Schmidt and R. Hight, Jr., *Acta Cryst.*, 13, 480 (1960).

159. P. W. Schmidt, *Acta Cryst.*, 19, 938 (1965).

160. T. R. Taylor and P. W. Schmidt, *Acta Physica Austriaca*, 25, 293 (1966).

161. J. S. Lin, C. R. Von Bastian and P. W. Schmidt, *J. of Appl. Cryst.*, 7, 439 (1974).

162. C. G. Vonk, *J. of Appl. Cryst.*, 8, 340 (1975).

163. P. Debye and A. M. Bueche, *J. of Appl. Phys.*, 20, 518 (1949).

164. D. Tyagi, J. L. Hedrick, D. C. Webster, J. E. McGrath and G. L. Wilkes, ***Polymer***, 29, 833 (1988).

165. P. Debye, H. R. Anderson, Jr. and H. Brumberger, ***J. of Appl. Phys.***, 28, 279 (1957).

166. C. G. Vonk and G. Kortleve, ***Kolloid-Z***, 220, 19 (1967).

167. D. Tyagi, J. E. McGrath and G. L. Wilkes, ***Polym. Eng. & Sci.***, 26, 1371 (1986).

168. G. Porod in "Small Angle X-Ray Scattering", H. Brumberger Ed., Gordon and Breach, Sci. Publishers, Inc., New York (1967).

169. G. Porod, ***Kolloid-Z***, 124, 83 (1951).

170. G. Porod, ***Kolloid-Z***, 125, 51 (1952).

171. G. Porod, ***Kolloid-Z***, 125, 108 (1952).

172. W. Ruland, ***Kolloid-Z***, 255, 29 (1977).

173. J. Rathje and W. Ruland, ***Kolloid Polym. Sci.***, 254, 358 (1976).

174. W. Weigand and W. Ruland, ***Prog. Colloid Polym. Sci.***, 66, 355 (1979).

175. J. Goodisman and H. Brumberger, ***J. of Appl. Cryst.***, 4, 347 (1971).

176. W. Ruland, ***J. of Appl. Cryst.***, 4, 70 (1971).

177. J. T. Koberstein and R. S. Stein, ***J. of Polym. Sci., Polym. Phys. Ed.***, 21, 2181 (1980).

178. A. Todo, T. Hashimoto and H. Kawai, ***J. of Appl. Cryst.***, 11, 558 (1978).

179. C. G. Vonk, *J. of Appl. Cryst.*, 6, 81 (1973).

180. J. T. Koberstein and R. S. Stein, *J. of Polym. Sci., Polym. Phys. Ed.*, 21, 1439 (1983).

181. R. Bonart and E. H. Muller, *J. Macromol. Sci. Phys.*, B10, 177 (1974).

182. R. Bonart and E. H. Muller, *J. Macromol. Sci. Phys.*, B10, 345 (1974).

183. J. T. Koberstein and R. S. Stein, *Polym. Eng. & Sci.*, 24, 293 (1984).

184. O. Kratky and G. Porod, *J. Colloid Sci.*, 4, 35 (1949).

185. W. S. Rothwell, *J. of Appl. Phys.*, 41, 4459 (1970).

186. O. Glatter, *J. of Appl. Cryst.*, 13, 7, (1980).

187. M. R. Tant, Ph.D. Dissertation, Department of Chemical Engineering, Virginia Polytechnic Institute and State Univeristy, Blacksburg, September 1986.

188. Y. Mohajer, S. Bagrodia, G. L. Wilkes, R. F. Storey and J. P. Kennedy, *J. of Appl. Polym. Sci.*, 29, 1943 (1984).

189. Z. Ophir and G. L. Wilkes, *J. of Polym. Sci., Polym. Phys. Ed.*, 18, 1469 (1980).

190. F. Fontaine, M. Foucart, J. Ledent, R. Sorby and R. Jerome, Conference Proceedings of the 10th Discussion on *Small Angle Scattering and Related Methods*, Prague, July 13-16 (1987).

191. J. Ledent, F. Fontaine, H. Reynaers, and R. Jerome, *Polym. Bull.*, 14, 461 (1985).

192. P. Molyneux, in *Water-Soluble Synthetic Polymers : Properties and Behavior*, Vol. II, CRC Press Inc., Boca Raton, Florida, 1984.

193. A. Douy, and B. Gallot, *Makromol. Chem.*, 156, 81 (1972).

194. D. Feng, Ph.D. Dissertation, Department of Chemical Engineering, Virginia Polytechnic Institute & State University, April 1989.

195. D. Feng, L. N. Venkateshwaran, G. L. Wilkes, J. E. Stark and C. M. Leir, to appear *J. of Appl. Polym. Sci.*

196. A. Douy, and B. Gallot, *Makromol. Chem.*, 165, 297 (1973).

197. L. Leibler, *Macromol.*, 13, 1602 (1980).

198. G. N. Ramachandran and V. Sasisekharan, *Arch. Biochem. Biophys.* 63, 25 (1956).

199. V. Sasisekharan and G. N. Ramachandran, *Proc. Ind. Acad. Sci.*, 45, 363 (1957).

200. P. Dreyfuss, *"Poly(tetrahydrofuran)"*, Gordon Breach Sci. Pub. Inc., New York, 1982.

201. A. H. Willbourn, *Trans. Faraday Soc.*, 54, 717 (1958).

202. C. B. Wood, Masters Thesis, Department of Chemical Engineering, Virginia Polytechnic Institute & State University, March 1982.

203. I. Duvdevani, P. K. Agarwal and R. D. Lundberg, *Polym. Eng. & Sci.*, 22, 500 (1982).

204. J. Selb and Y. Gallot, in *Developments in Block Copolymers - 2*, I. Goodman., Ed., Elsevier Applied Science, London, (1985).

205. T. E. Long, R. Subramanian, T. C. Ward, and J. E. McGrath, *Polym. Prepn.*, 27(2), 258 (1986).

206. C. D. DePorter, L. N. Venkateshwaran, G. A. York, G. L. Wilkes, and J. E. McGrath, ***Polym. Prepn.***, 30(1), 201 (1989).

207. C. D. DePorter, unpublished results

208. A. Eisenberg and D. Wollmann, ***Polym. Prepn.***, 30(1), 408 (1989).

209. J. W. Mays and N. Hadjichristidis, ***JMS-Rev. Macromol. Chem. Phys.***, C28, 371 (1988).

210. J. Podesva, J. Stejskal, and P. Kratochvil, ***Macromol.***, 20, 2195 (1987).

CALCULATION OF ELECTRON DENSITY

In ionomers the calculation of the true electron density variance presents a particularly difficult problem since the composition of the ionic domains is not clearly defined. Furthermore, since the position of the counterion is not fixed, it further complicates the determination of the electron density of the ionic domains. However, an approximate value of the electron density of the ionic phase can be calculated by the following procedure. The same calculations are also applicable to non-ionic systems. First, the chemical structure of the segment under consideration must be determined or assumed. From the chemical structure of the segment, calculate its molecular weight and the total number of electrons present in that segment. Let than be M and n, respectively. If ρ is the mass density of the segment in g/cm^3, then the electron density for the segment, ρ_e, is given by :

$$\rho_e = (\rho * n)/M$$

The units for the electron density determined in this manner would be in m-elec/cm^3.

EXAMPLE

Determination of the electron density of ionene hard segment based on dibromo-p-xylene

Molecular weight of dibromo-p-xylene = 263.89 g/mol

Number of electrons/ionene segment = 126

Density of dibromo-p-xylene = 2.102 g/cm^3

Therefore,

Electron density of the ionene hard segment = 1.0036 m-elec/cm^3

(based on dibromo-p-xylene)

The vita has been removed from the scanned document